Searching for new very high energy emitting AGN among the unclassified and unassociated *Fermi*-LAT sources

Johannes Petrus Marais

Submitted in fulfillment of the requirements for the degree

Magister Scientiae

in the Faculty of Natural and Agricultural Sciences

Department of Physics

University of the Free State

South Africa

28 January 2019

Supervised by: Dr. B. van Soelen, Department of Physics

The financial assistance of the National Research Foundation (NRF) towards this research is hereby acknowledged. Opinions expressed and conclusions arrived at, are those of the author and are not necessarily to be attributed to the NRF.

Abstract

Jet dominated Active Galactic Nuclei (AGN) are the most energetic persistent sources of emission in the universe, emitting radiation across the entire electromagnetic spectrum. When these jets are pointed towards the observer, they become known as blazars. Blazar emission is dominated by the beamed non-thermal emission from the relativistic jet and are the brightest sources in the extragalactic sky. Blazars, sub-categorized into BL Lacertae objects (BL Lacs) and Flat Spectrum Radio Quasars (FSRQs) exhibit variability at all wavelengths on diverse timescales, high polarization and weak or featureless optical spectra. These extreme sources provide a laboratory to test some of the most energetic physical processes in the known universe. In order to study the processes responsible for the highest energy emission originating from blazar jets, more Very High Energy (VHE) emitting blazars must be found and studied with Imaging Air Cherenkov Telescopes (IACTs). The small sample of currently known VHE emitting blazars, studied for many years, has not yet provided a complete understanding of blazar physics. A study to monitor 17 VHE blazars detected by the High Energy Stereoscopic System (H.E.S.S.) with the Watcher Robotic Telescope has been underway since May 2015. A fast reduction and analysis pipeline, written in `python` and using `PyRAF` to interface with `IRAF`, was developed to perform aperture photometry on 14 of these sources and search for long-term variability (LTV). In addition, to search for new VHE emitting blazars observable with IACTs, a sample of 11 Blazar Candidates of Uncertain Type (BCUs) listed in the Third *Fermi* Large Area Telescope Source Catalog (3FGL), 11 BCUs and an unassociated source listed in the Third Catalogue of Hard Large Area Telescope sources (3FHL), selected based on hard γ-ray spectra and lack of redshift measurements were identified for spectroscopic follow-up with the aim of classifying them. The selected sources were observed with the SpUpNIC grating spectrograph mounted on the SAAO 1.9-m telescope. A selection of 6 3FHL sources identified for spectroscopic study were also observed with the Sutherland High-speed Optical Camera (SHOC) mounted on the SAAO 1.0-m telescope to search for intra-day variability (IDV). All 22 of the BCUs were classified as BL Lac objects based on the absence of strong emission lines and a diluted Ca break (less than 40%). Further, redshifts were calculated for 11 BCUs and potential redshifts for 4 BCUs. Further searches for photometry variability were undertaken for all sources. Spectral Energy Distributions (SEDs) were constructed to determine which of the observed BCUs were good candidates to be observed with IACTs. The 50h H.E.S.S. and Cherenkov Telescope Array (CTA) South sensitivity curves were overlayed on the SEDs. Of the BCUs observed, 8 of the sources have γ-ray emission above the CTA detection threshold and are good candidates for VHE observation.

Key words: techniques: photometry; spectroscopy — active galaxies: BL Lac objects; FSRQ; redshift — instruments: Watcher; SHOC; SpUpNIC

Opsomming

Spuitstraal gedomineerde Aktiewe Galaktiese Kerne (AGN) is die mees energieke permanente stralingsbronne in die heelal en produseer straling wat strek oor meeste van die elektromagnetiese spectrum. Wanneer die spuitstraal in die rigting van die waarnemer georiënteer is, staan die AGN as blazars bekend. Blazar straling word gedomineer deur nie-termiese straling vanaf die relativistiese spuitstraal en is die helderste voorwerpe in in die buitegalaktiese hemelruim. Blazars, verdeel in BL Lacertae voorwerpe (BL Lacs) en Plat Spectrum Radio Kwasars (FSRQ), varieer op diverse tydskale, het hoë polarisasie en swak of afwesige optiese emissielyne. Hierdie eksotiese voorwerpe verskaf 'n laboratorium om die mees energieke fisiese prosesse in die heelal te toets. Om die prosesse verandwoordelik vir die hoogste energie uitstraling van die spuitstraal te toets, moet meer Baie Hoë Energie (VHE) bronne ondek word en met Beelding Atmosferiese Cherenkov Teleskope (IACT) bestudeer word. Die klein populasie reeds bekende VHE blazars wat al vir baie jare bestudeer word het nog nie 'n volledige begrip van blazar Fisika openbaar nie. 'n Studie om 17 VHE blazars wat voorheen deur die Hoë Energie Stereoskopiese Sisteem (H.E.S.S.) waargeneem is te monitor met die Watcher robotiese teleskoop is al besig vanaf Mei 2015. 'n Vinnige analiese pyplyn, ontwikkel in **python**, wat gebruik maak van **PyRAF** om met **IRAF** te kommunikeer, was gebruik om die lang-termyn variasie van 14 van die blazars gemonitor deur Watcher te ondersoek. 'n Soektog na nuwe blazars wat deur IACTs waargeneem kan word is ook begin. 11 blazars van onbekende tipe (BCU) gelys in die "Third *Fermi* Large Area Telescope Source Catalog" (3FGL), 11 BCUs gelys in die "Third Catalogue of Hard Large Area Telescope sources" (3FHL) en 'n 3FHL voorwerp sonder enige genootskap met bronne by ander golflengtes wat gekies is gebaseer op hulle harde γ-straal emissie en afwesige rooiverskuiwing is waargeneem met die SAAO 1.9-m SpUpNIC spektrograaf met die doel om hulle te klasifiseer. 'n Groep van 6 3FHL bronne was ook waargeneem met die SAAO 1.0-m Hoë Spoed Optiese Kamera (SHOC) om hulle intra-dag variasie (IDV) te ondersoek. Al 22 van die BCUs is as BL Lac voorwerpe geklasifiseer, gebaseer op die afwesigheid van sterk emissie lyne en 'n swak Ca breuk. Rooiverskuiwings was vir 11 BCUs bepaal en potensiale rooiverskuiwings vir 4 BCUs. Spectraal Energie Verspreidings was gebou vir die BCUs om te bepaal of hulle sigbaar mag wees met IACTs. Die 50 uur instrument sensitiwiteit kurwes van die Cherenkov Teleskoop Opstelling (CTA) is op die SEDs gepas om te bepaal watter BCUs helder genoeg is om sigbaar te wees. Net 8 van die BCUs se γ-straal emissie is helder genoeg om deur CTA waargeneem te word.

Sleutelwoorde: tegnieke: fotometrie; spektroskopie – aktiewe galaxies: BL Lac voorwerpe; FSRQs, rooiverskuiwings – instrumente: Watcher; SHOC; SpUpNIC

Acknowledgements

I hereby wish to acknowledge the following parties for their contributions towards the completion of this study:

- Dr. B. van Soelen for his role as supervisor, and for all the motivation and guidance that I have received from him during the completion of this study.
- My family for their love and support throughout all of my endeavours. Without them my studies would not be possible.
- Ms. Hélène Szegedi, Dr Alida Odendaal and Dr. Richard Britto for assisting in the data gathering for this project.
- Prof. Lorraine Hanlon, Dr. Antonio Martin-Carrillo and David Murphy for providing the Watcher data.
- The financial assistance of the National Research Foundation (NRF) towards this research is hereby acknowledged. Opinions expressed and conclusions arrived at, are those of the author and are not necessarily to be attributed to the NRF. This research has made use of the NASA/IPAC Extragalactic Database (NED), which is operated by the Jet Propulsion Laboratory, California Institute of Technology, under contract with the National Aeronautics and Space Administration. This research has made use of the VizieR catalogue access tool, CDS, Strasbourg, France. Part of this work is based on archival data, software or online services provided by the Space Science Data Center (SSDC). This work uses observations made at the South African Astronomical Observatory (SAAO). pyRAF is a product of the Space Telescope Science Institute, which is operated by AURA for NASA. This work uses observations made with the Watcher robotic telescope, operated by the University College Dublin, Dublin, Ireland.

Contents

1 Introduction **9**

2 Active Galactic Nuclei (AGN) **13**

2.1 The Unified AGN model 15

2.1.1 The central source: a supermassive black hole 17

2.1.2 Accretion disc 18

2.1.3 The emission line regions 19

2.1.4 The dusty torus 22

2.1.5 The jet 23

2.2 AGN classification 29

2.2.1 Radio-quiet AGN 31

2.2.2 Radio-loud AGN 34

3 Multi-wavelength observation of blazars **39**

3.1 γ-ray observations of blazars 40

3.1.1 Energetic Gamma-ray Experiment Telescope (EGRET) . . . 40

3.1.2 The *Fermi* Large Area Telescope (LAT) 41

3.1.3 The H.E.S.S. telescope 42

3.1.4 Active Galactic Nuclei in γ-rays 44

3.1.5 Using γ-rays to probe the Extragalactic Background Light . 46

3.2 X-ray observations of blazars 47

3.3 Optical observations of blazars 48

3.3.1 Variability and long-term monitoring 49

3.3.2 Spectroscopy 50

3.3.3 Spectropolarimetry 51

3.4 Radio observations of blazars 53

3.5 Multi-wavelength modelling of blazars 55

4 Selection of γ-ray sources for optical follow-up 59
4.1 Selection of TeV blazars observed with the Watcher robotic telescope 60
4.2 Selection of *Fermi* blazars for spectroscopic classification 61
4.2.1 Observability 62
4.2.2 Photon spectral index 63
4.2.3 Blazar classification 63
4.2.4 Potential multi-wavelength counterparts 63
4.3 Selected blazar candidate sources 65
4.4 Selection of *Fermi* blazars for photometric observation 67

5 Photometric observations of blazars 71
5.1 Instrumentation 71
5.1.1 The Watcher robotic telescope 72
5.1.2 The SAAO 1.0-m telescope 72
5.1.3 The Sutherland High Speed Optical Cameras (SHOC) . . . 74
5.2 Data reduction of CCD images 77
5.2.1 Flat field correction 78
5.3 The SHOC pipeline 79
5.4 Watcher pipeline 80
5.4.1 WatReduction 81
5.4.2 WatCombiner 81
5.4.3 WatPhotometry 82
5.4.4 WatPipeplot 85
5.5 Differential photometry 86
5.6 Watcher long-term observations 87
5.7 SHOC light-curves of 3FHL BCUs 92
5.8 Variability statistical analysis 95
5.8.1 Statistical tests 96
5.8.2 Results of the variability statistical tests 99
5.8.3 Watcher discussion 99
5.8.4 SHOC discussion 104

6 Optical spectroscopic observations of the blazar candidates 109
6.1 Instrumentation 109
6.1.1 SAAO 1.9-m telescope 110
6.1.2 The SpUpNIC grating spectrograph 110
6.1.3 The SpUpNIC control software 112

6.2 Data reduction of CCD spectroscopy . . . 114
6.2.1 Pre-reduction . . . 114
6.2.2 Flat correction . . . 115
6.2.3 Wavelength calibration . . . 115
6.2.4 Cosmic ray removal . . . 116
6.2.5 Background subtraction . . . 116
6.2.6 Extracting the spectra . . . 117
6.2.7 Flux calibration . . . 117
6.2.8 Spectral analysis methods . . . 118
6.3 Results . . . 120
6.3.1 3FHL BCUs and unassociated sources . . . 121
6.3.2 3FGL BCUs . . . 132
6.4 Summary of the spectroscopic observations of *Fermi* BCUs . . . 140

7 Discussion **143**
7.1 Photometry using the reduction and analysis pipeline . . . 144
7.2 Source classification . . . 145
7.2.1 3FGL J0051.2-6241 . . . 146
7.2.2 3FHL J0305.2-1609 . . . 146
7.2.3 3FHL J1130.5-7801 . . . 147
7.2.4 3FGL J1406.0-2508 . . . 148
7.2.5 3FGL J1842.3-5841 . . . 150
7.2.6 3FGL J1944.1-4523 . . . 150
7.2.7 3FGL J1954.9-5640 . . . 151
7.2.8 3FGL J1959.8-4725 . . . 152

8 Conclusion **155**
8.1 Sample selection . . . 156
8.1.1 Photometric results . . . 156
8.1.2 Spectroscopic results . . . 157
8.1.3 Detectability of BCUs by IACTs . . . 158
8.2 Future studies . . . 158

Bibliography **161**

Appendices **175**

A 3FHL and 3FGL BCUs not detectable by IACTs **175**

B Peer-reviewed contributions **189**

Long-term monitoring of TeV Blazars with the Watcher Robotic Telescope. 190

Characterising the Fermi-LAT BCUs: Optical Spectroscopy and Neural Networks. 197

Observations of the flaring Fermi-LAT blazar 4C +01.02 and prospects in spectro-polarimetry with SALT-RSS. 203

Studies of optical/gamma-ray flares of blazar 4C +01.02: recent updates from the 2016-2017 observations. 212

Searching for new TeV blazars in the 3rd Fermi-LAT catalogue of hard gamma-ray sources. 219

New Discoveries and Surprises Revealed through SALT Spectroscopy of the Unclassified Fermi-LAT Sources. 228

SALT Spectropolarimetry and Self-Consistent SED and Polarization Modeling of Blazars. 235

SALT Spectropolarimetry and Self-Consistent SED and Polarization Modeling of Blazars. 241

List of Acronyms

1RXS	ROSAT All-Sky Bright Source Catalogue
1SXPS	Swift X-ray telescope point source catalogue
2FHL	Second Catalogue of Hard LAT sources
2RXS	Second ROSAT all-sky survey
ADU	Analog-to-digital Unit
AGN	Active Galactic Nuclei
BAL	Broad Absorption Line
BCU	Blazar Candidate of Uncertain type
BL Lac	BL Lacertae object
BLR	Broad Line Region
BLRG	Broad Line Radio Galaxies
CCD	Charge Coupled Device
CGRO	Compton Gamma-ray Observatory
CMB	Cosmic Microwave Background
CTA	Cherenkov Telescope array
DACF	Discrete Auto Correlation Function
EBL	Extragalactic Background Light
EC	External Compton
EGRET	Energetic Gamma-ray Experimental Telescope
FITS	Flexible Image Transport System
FLWO	Fred Lawrence Whipple Observatory
FR	Fanaroff-Riley
FSRQ	Flat Spectrum Radio Quasar
GRB	Gamma-ray Burst
H.E.S.S.	High Energy Stereoscopic System
HAWC	High Altitude Water Cherenkov
HBL	High synchrotron peaked BL Lacs

HIPPO HIgh speed Photo-POlarimeter
HSP High Synchrotron Peaked
HST Hubble Space Telescope
IACT Imaging Air Cherenkov Telescopes
IBL Intermediate synchrotron peaked BL Lacs
IC Inverse Compton
IDV Intra-day Variability
IGMF Intergalactic Magnetic Fields
IR Infrared
ISM Interstellar Medium
ISMF Interstellar Magnetic Fields
LBAS LAT Bright AGN Sample
LBL Low synchrotron peaked BL Lacs
LCO Las Cumbres Observatory
LINER Low Ionization Nuclear Emission-line Regions
LLAGN Low-Luminosity AGN
LSP Low Synchrotron Peaked
LTV Long-term Variability
MAGIC Major Atmospheric Gamma Imaging Cherenkov
MHD magnetohydrodynamic
NED NASA/IPAC Extragalactic Database
NLR Narrow Line Region
NLRG Narrow Line Radio Galaxies
NOMAD Naval Observatory Merged Astrometric Dataset
NVSS NRAO VLA Sky Survey
OGS Optical Guidance Systems
OTA Optical Tube Assembly
PKS Parkes Radio Sources
PMN Parkes-MIT-NRAO
QE Quantum Efficiency
RASS ROSAT all-sky survey faint source catalogue
RBS ROSAT Bright Survey
RG Radio Galaxies
RQQ Radio-Quiet Quasars
S/N Signal-to-Noise Ratio
SAAO South African Astronomical Observatory

SED Spectral Energy Distributions
SF Star Forming
SFG Star Forming Galaxies
SHOC Sutherland High-speed Optical Camera
SMBH Supermassive Black Hole
SpUpNIC Spectrograph Upgrade: Newly Improved Cassegrain
SSC Synchrotron Self Compton
SSDC Space Science Data Center
STV Short-term Variability
SUMSS Sydney University Molonglo Sky Survey
TCS Telescope Control Software
UCD University College of Dublin
UV Ultra-Violet
VERITAS Very Energetic Radiation Imaging Telescope Array System
VLBA Very Long Baseline Array
WCS World Coordinate System
WISE Wide-field Infrared Survey Explorer
WMAP Wilkinson Microwave Anistropy Probe

Chapter 1

Introduction

The Large Area Telescope (LAT) onboard the *Fermi* Gamma-ray Space Telescope has been in operation since August 2008. The LAT, the primary instrument aboard is sensitive to γ-rays in the 20 MeV to 300 GeV energy range, has a large field of view (FoV = 2.4 sr) covering 20% of the sky at any instance (Atwood et al., 2009). The LAT's sensitivity allows many sources to be identified which could not be identified by the Energetic Gamma-ray Experimental Telescope (EGRET), providing an immense opportunity to increase the number of high energy sources that can be studied by telescopes observing in other energy regimes.

The third *Fermi* Large Area Telescope Source Catalog (3FGL) lists 3033 sources in the 100 MeV to 300 GeV energy range. Of the sources listed 642 are classified as BL Lacertae (BL Lac) objects, 446 as Flat Spectrum Radio Quasars (FSRQ), while 568 are classified as Blazar Candidates of Uncertain Type (BCU; Acero et al., 2015). The Third Catalog of Active Galactic Nuclei detected by the *Fermi* Large Area Telescope (3LAC) is a complementary catalogue, listing 1563 Active Galactic Nuclei (AGN) with a Test Statistic (TS) greater than 25, and high Galactic latitudes ($|b| > 10\,\mathrm{deg}$; Ackermann et al., 2015). The 3LAC is an invaluable resource to search for extragalactic objects to study with current ground based Imaging Air Cherenkov Telescopes (IACT) such as the High Energy Stereoscopic System (H.E.S.S.) and the future Cherenkov Telescope Array (CTA).

Another catalogue that can be used to search for Very High Energy (VHE, > 1 TeV) emitting extragalactic objects is the Third Catalogue of Hard LAT sources (3FHL), which lists 1556 objects detected in the 10 GeV to 2 TeV energy range. Of the 1556 objects listed in the 3FHL, 56% are classified as blazars, while a further 19% are classified as BCUs. There are 177 sources that do not have any association at other wavelengths (Ajello et al., 2017).

Blazars are jet dominated AGN which emit radiation over the entire electromagnetic regime, from radio to the very highest energy γ-rays. The jet is powered by accretion onto a supermassive black hole (SMBH) and is orientated close to the observer's line of sight, Doppler boosting the emitted radiation. Blazars are characterized by variability at all wavelengths, from hours to years. The multi-wavelength variability is often correlated, indicating that the observed emission originates from the same volume in the jet. The extreme and fast variability that is observed from blazars, originating from a compact region, is a testament to the extreme environment present in the jet and provides an opportunity to study processes in environments too extreme to reproduce in laboratories, such as the effect that an AGN has on the host galaxy, how AGNs evolve and the effect the jet has on the intra-galactic medium.

The environments of AGN are still not completely understood, therefore, a larger sample size is extremely important to increase our understanding of AGN and their environments. Finding rare AGN classes will be important in refining the models used to explain the properties of AGN. Finding non-blazar AGN that emit at very high energies will provide a better understanding of the environment near the SMBH. By finding and classifying the BCUs in the LAT catalogues, rare AGN classes can be found and studied further, with ground based telescopes, such as radio and optical telescopes, IACTs such as H.E.S.S. and the upcoming CTA and space based telescopes such as the *Fermi*, XMM-Newton and Chandra X-ray observatories.

Additionally, to observe blazars and other extragalactic γ-ray emitting sources with IACTs, the distance to the source needs to be less than $z \lesssim 1$, beyond which the universe becomes opaque to VHE γ-ray due to $\gamma\gamma$ absorption from the extragalactic backgound light (EBL). Observing AGN in the VHE regime provides important clues as to the nature of the emitting particles responsible for the γ-ray emission.

Unfortunately, while the LAT catalogues provide candidate sources, the LAT's point spread function (PSF) can only constrain a source location to within a few arcminutes, making a positive identification at other wavelengths difficult, especially if the source is faint in γ-ray, with few counterparts at other wavelengths. It is therefore necessary to constrain the source location at other wavelengths, before a serious multiwavelength study can be performed.

The aim of this project is to find candidate AGN that emit in the TeV range which can be further studied with IACTs. By finding more AGN to study in the

VHE energy, the current models explaining the dominant jet emission mechanisms and the environment around the SMBH can be better constrained and improved. To compliment this, a longterm study is also underway with the Watcher Robotic Telescope to monitor the optical variability of TeV detected blazars for follow-up studies of flaring events.

To find AGN that possibly emit in the VHE range and are close enough to observe with IACTs, I selected a sample of hard γ-ray unclassified and unassociated AGN from the 3FGL and 3FHL catalogues for optical follow-up and identification. Further, AGN were selected based on the presence of multiwavelength counterparts within or near the LAT 68% and 95% error circles. The source list was further narrowed by using ALLWISE colours to separate stars and AGN and their observability with the SAAO telescope. The final AGN selection were classified with the SAAO 1.9-m telescope SpUpNIC grating spectrograph. A further subset of the 3FHL sources were also observed with the 1.0-m telescope to look for intra-day variability.

This study is structured as follows: In Chapter 2, an overview is given of the different classes of AGN and their properties. In Chapter 3, the multiwavelength observation strategies employed to study AGN are reviewed. Chapter 4 discusses the criteria used to select the Watcher TeV detected blazars and the 3FGL and 3FHL BCUs and unassociated sources. In Chapter 5, optical photometric observations of the target sample are outlined, the reduction and analysis pipeline developed for this project discussed and the variability statistical tests utilized to detect variability in the optical light curves of the sources are presented. In Chapter 6 the optical spectroscopic observation of the 3FGL and 3FHL sources are discussed and the results presented. In Chapter 7 I discuss the results of the photometry and spectroscopy on the sources observed during this project and which sources could be detected with IACTs. Finally the conclusion is presented in Chapter 8 and the prospects of future work regarding the continued long-term monitoring of TeV detected blazars and further multiwavelength analysis of the targets observed during this project are outlined. The BCUs classified during this project that are not observable with IACTs are presented in Appendix A. This research has been presented at both national and international conferences and published in peer-reviewed conference proceedings and are presented in Appendix B.

Chapter 2

Active Galactic Nuclei (AGN)

In 1943, Karl Seyfert described a number of galaxies with high excitation nuclear emission lines originating from compact and brighter than normal cores, superimposed on typical G-type solar spectra. The measured emission lines were broadened and differed significantly between objects. In some of the spectra the Hydrogen lines showed wing broadening, corresponding to velocities of up to 8500 km s^{-1}, while other lines showed no evidence of wing broadening. Also noted was the correlation between the Hydrogen emission line widths, the absolute magnitude of the emitting galaxy and the galaxy/core luminosity. This suggested that there was a correlation between the properties of the galaxy nucleus and the width of the emission lines (Seyfert, 1943). These sources, subsequently called Seyfert galaxies, were the first discovered class of Active Galactic Nuclei (AGN).

Since this first discovery other AGN classes have since been found. A series of lunar occultations of the quasar 3C 273, studied at the Parkes radio observatory, allowed Maarten Schmidt to associate the strong radio source with a stellar object with a redshift of $z = 0.16$ (Schmidt, 1963). The large redshift to 3C 273 forced researchers to abandon preconceived ideas about the nature of strong radio emitters. Before the measurements of 3C 273 at Parkes in 1962, the high luminosities of distant AGN was inconceivable. Today, quasars have been detected up to $z \sim 7.5$ (Bañados et al., 2018).

The different AGN classes all share similar properties. These include the high velocities of gas in the central regions, small emitting regions and their extremely bright cores. These shared properties would indicate that the different AGN classes share the same underlying physical processes. Today it is understood that many of the observed differences in the properties of AGN are produced by the inclinations of these systems to the observer, i.e. the angle between the jet (or the angle of

the galaxy plane) and the observer (Antonucci, 1993). In addition to this, the properties of the central Supermassive Black Hole (SMBH) powering the AGN and the host galaxy also play a role in the AGN class.

With the advent of multi-wavelength astronomy, covering radio to γ-rays, AGN are now studied in many different energy regimes, all of which study different aspects of AGN. Observations of AGN in the radio regime measure the synchrotron emission which gives insight into the particle distribution and the magnetic field at the emission regions. Radio observations also indicate if a relativistic jet is present in the system. One complication of studying AGN in the radio regime is that the contribution of synchrotron emission from supernova remnants in the host galaxy can significantly add to the low frequency radio emission. This excess radio emission is an indicator of the star Star Forming (SF) in the galaxy hosting the AGN and needs to be taken into account when determining the properties of the AGN (Maini et al., 2016). Observations in the infrared, optical and ultraviolet allow measurements of the size of the Broad Line Region (BLR), using the reverberation mapping technique to measure light travel time delays inside the BLR and determine its size and morphology. Observations in the X-ray regime are used to measure the properties of the accretion disc (Done, 2010; Mushotzky et al., 1993), while observations in the X-ray and γ-ray regimes allow us to study the non-thermal high energy particle population and the size of the emitting region through measurements of the variability time-scales. Since the cooling times of the highest energy electrons are significantly shorter than the lower energy electron population, measurements of variability time-scales at higher energies places stricter limits on the size of the emitting region (see e.g Brown, 2013; Nakagawa & Mori, 2013; Tramacere et al., 2009).

With so many energy regimes being studied, the classification of AGN has evolved from the simple picture hinted at by the study of extragalactic "nebulae" by Karl Seyfert to one where AGN classification is affected by the wavelengths they are studied at. Radio selected AGN include Radio Galaxies (RG), steep and flat spectrum AGN and radio-loud quasars. Optically selected AGN can be classified, for example, as Seyfert galaxies, Low Ionization Nuclear Emission-line Regions (LINER) or quasars. AGN selected in the γ-ray regime are dominated by blazars (Flat Spectrum Radio Quasars and BL Lacertae objects) since the large Doppler factors of the relativistic jets and small viewing angles, drastically increases the intensity of the non-thermal γ-ray emission.

This chapter will briefly summarize the different components of AGN in the

context of the Unified AGN model (Section 2.1) and the classification of AGN (Section 2.2), while the observational multiwavelength view will be presented in Chapter 3.

2.1 The Unified AGN model

Figure 2.1 shows a schematic illustration of the central components of an AGN in the Unified AGN model. In the Unified AGN model, AGN are powered by a central accreting SMBH, with a mass of $\sim 10^6 - 10^9$ $M_\odot$. The SMBH and surrounding regions are continually supplied with gas infalling from the outer regions of the host galaxy (see e.g Carmona-Loaiza et al., 2015, and references therein). The infalling material forms an accretion disc, extending from an inner radius of $R_{\rm in} \sim 0.01 - 60$ AU to an outer radius of $R_{\rm out} \sim 1000$ AU. The accretion disc is surrounded by fast moving clouds, the Broad Line Region (BLR), which produces broad emission lines.

Surrounding the accretion disc and the BLR is a $\sim 1 - 100$ pc scale dusty torus, which can obscure the inner regions of the AGN depending on the viewing angle. Outside the torus is the Narrow Line Region (NLR), with a radius of $R_{\rm NLR} \sim 10^2 - 10^4$ pc. The BLR and NLR are both powered by ionizing radiation (UV to soft X-rays) from the hot accretion disc.

Accreting material can extract energy from the central rapidly rotating SMBH and be launched in the form of relativistic jets that can extend up to megaparsec scales (Blandford & Znajek, 1977). The jet is the main site where the non-thermal emission is produced. The low energy synchrotron emission, emitted from radio through X-rays is produced by non-thermal electrons accelerating in the jet's magnetic field. The high energy emission, from X-rays to the highest energy γ-rays, is believed to be produced by leptonic Inverse Compton (IC) emission, but the possibility remains that the emission can be produced by hadronic processes such as proton synchrotron or pion decay (see e.g Böttcher et al., 2013).

The Unified AGN model explains the differences in the observed properties of AGN by attributing them to the viewing angle, accretion rate and the presence or absence of a jet. AGN with significant radio emission compared to their optical emission are known as *radio-loud* AGN and include Fanaroff-Riley galaxies, radio-loud quasars and blazars (see Section 2.2.2). Radio-quiet AGN comprise Seyfert galaxies, radio-quiet quasars and LINERs. It should be noted that radio-quiet AGN are not radio silent, but only have a low radio flux when compared to their

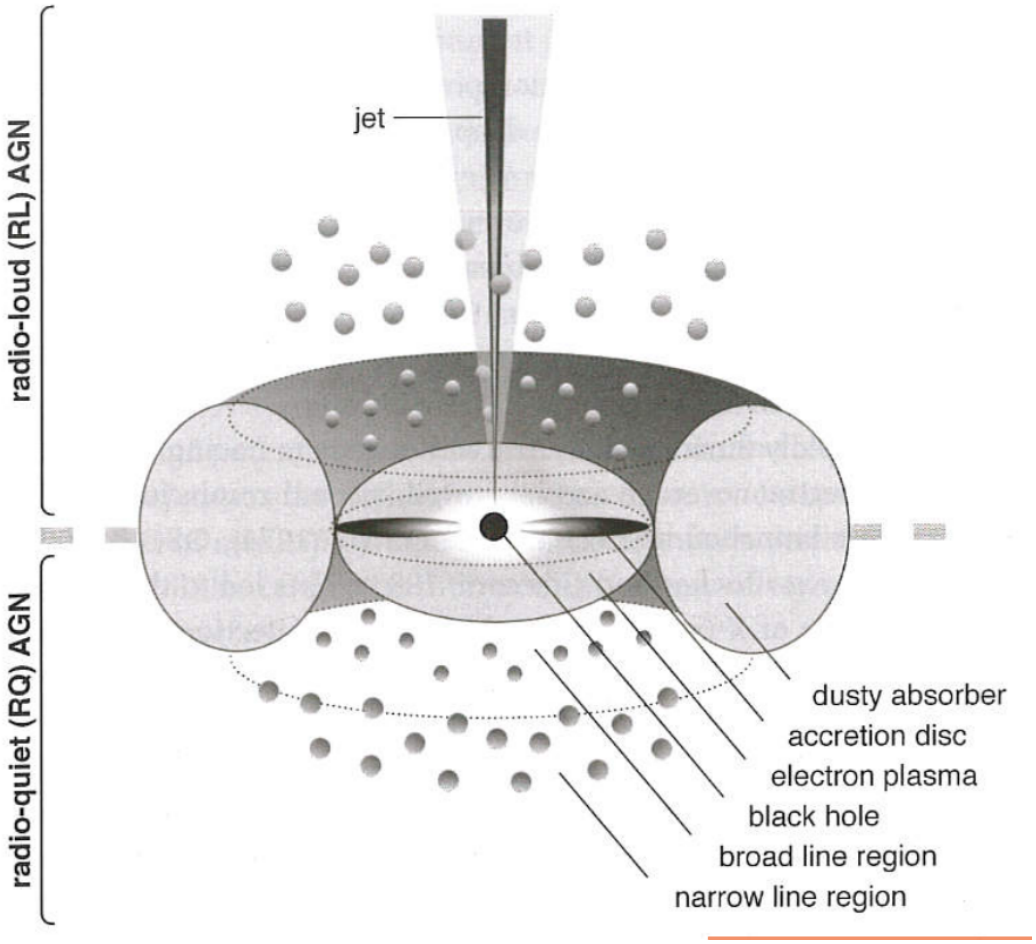

Figure 2.1: A simple schematic featuring the important central components in the Unified AGN model. Adapted from Beckmann & Shrader (2012, p. 5).

optical flux. Various schemes have been used to define whether AGN are radio-quiet or radio-loud (as discussed in Section 2.2, p. 29).

Large-scale jet structures can be studied in Fanaroff-Riley galaxies, while small-scale jet structures can be studied in blazars by making use of, for example, variability studies. Many blazars also exhibit large-scale radio jets, suggesting they are essentially Fanaroff-Riley galaxies viewed at smaller angles (see e.g Kharb et al., 2010; Landt & Bignall, 2008; Stanley et al., 2015).

In the following subsections I will briefly summarize the properties of the main components of AGN. In Subsection 2.1.1, I will give a brief description of the effects of the SMBH, Subsection 2.1.2 will detail the properties of the accretion disc, Subsection 2.1.3 will discuss the Emission line regions. Subsection 2.1.4 will briefly describe the dusty torus surrounding the AGN and Subsection will 2.1.5 will describe the jets observed in some AGN and the relativistic effects arising from them.

2.1.1 The central source: a supermassive black hole

The rapid variability of AGN, where the luminosity sometimes changes by more than 50% on daily times scales, requires that the spatial extent of the emission region must be small enough to be in causal contact. This requires that the emission region must have a radius $R \lesssim 1$ lightday or $R \lesssim 10^{15}$ cm. The high luminosity, $L \gtrsim 10^{47}$ erg s^{-1}, and rapid variability of AGN suggest a very small and efficient energy source, most likely a black hole (see e.g Schneider, 2015, pp 224-225). AGN are believed to be powered by accreting matter from the host galaxy onto a SMBH. The infalling matter converts the gravitational potential energy into kinetic energy. This conversion of gravitational potential energy to kinetic energy is highly efficient, since the bolometric luminosity of the accretion disc scales as

$$L_{\rm acc} = \eta \dot{M} c^2,$$

where η is the *energy efficiency parameter*, $\dot{M}$ the mass accretion rate and c the speed of light. The *energy efficiency parameter* is defined as the radiated energy per unit accreted rest mass and can reach $\eta \leqslant e_{\rm bin}$, where $e_{\rm bin}$ is the binding energy of the orbiting material (see Böttcher et al., 2012, sect. 4.1.2 for a detailed discussion). The SMBHs in AGN have masses in the range between $10^6 - 10^9$ M$_\odot$ (Urry & Padovani, 1995), although smaller $\sim 10^5$ M$_\odot$ (e.g Barth et al., 2005) and larger $\sim 10^{9.5}$ M$_\odot$ (e.g Jun et al., 2017) SMBHs have also been found.

Black holes are described by only three parameters, namely mass, global charge and angular momentum (Ruffini & Wheeler, 1971). The mass of the black hole will determine the size of the event horizon while the angular momentum plays a crucial role in the interaction between the black hole and the surrounding space-time, i.e. frame-dragging. Black holes have no solid surface for accretion, so the last stable orbit determines the size of the inner accretion disc: for a non-rotating black hole, the last stable orbit is located at $R = 6R_g$, where R_g is the gravitation radius, given by

$$R_g = \frac{GM}{c^2},$$

where G is the gravitational constant and M the mass of the black hole. The size of the last stable orbit of a maximally rotating Kerr black hole is $R = R_g$ for a prograde accretion disc and $R = 9R_g$ for a retrograde accretion disc. Particles inside the last stable orbit will freefall onto the massive object (see Böttcher et al.,

2012, pp 84-85).

2.1.2 Accretion disc

Galactic matter falling towards the central regions of the galaxy will accumulate into an accretion disc around the SMBH since the infalling matter conserves angular momentum. As the material in the accretion disc spirals inwards to the SMBH it transports angular momentum outwards through various processes, including turbulence, viscosity, shear and magnetic fields.

There is still some uncertainty regarding AGN accretion processes, such as how momentum transfer and energy dissipation govern their thickness and emission profile (see e.g Czerny & You, 2016; Yuan & Narayan, 2014). An approximation for geometrically thin but optically thick accretion discs with constant accretion was proposed by Shakura & Sunyaev (1973), in which the accretion disc radiates a blackbody spectrum, with the disc temperature T, scaling with disc radius R, as $T \propto R^{-3/4}$. The peak emission from the thin, optically thick accretion disc occurs in the Optical-UV spectrum. Many AGN Spectral Energy Distributions (SED) show a Optical-UV excess, referred to as the Big Blue Bump, which originates from the accretion disc.

Typical examples of SEDs for both jetted and non-jetted AGN are shown in Fig. 2.2 with the major accretion disc components illustrated. The various emission components include the infrared emission from the torus and outer regions of the accretion disc, the Big Blue Bump in the optical-UV produced by the accretion disc black body radiation, the soft X-ray excess from the inner disc regions and the Compton reflection from the hot corona surrounding the accretion disc (e.g Koratkar & Blaes, 1999).

The X-ray emission from the accretion disc can be separated into thermal X-ray emission from the inner regions of the accretion disc and non-thermal X-ray emission from IC scattering of accretion disc photons by the corona surrounding the accretion disc (see Fig. 2.3d). X-ray spectra show broad Fe Kα emission at 6.4 keV (see Fig. 2.3a), attributable to the fluorescence of cold ($< 10^6$ K), optically thick and slow moving gas (≤ 7500 km s^{-1}) (Mushotzky et al., 1993). The Fe Kα line originates from the inner regions of the accretion disc and the shape of the line is severely influenced by frame-dragging effects, Doppler and transverse Doppler shifts, relativistic beaming, and gravitational redshifting near the SMBH (see e.g Ingram & Done, 2012). Figure 2.3b shows the different effects this has on the Fe Kα line. Panel 1 shows the shape the line will have if only Newtonian processes

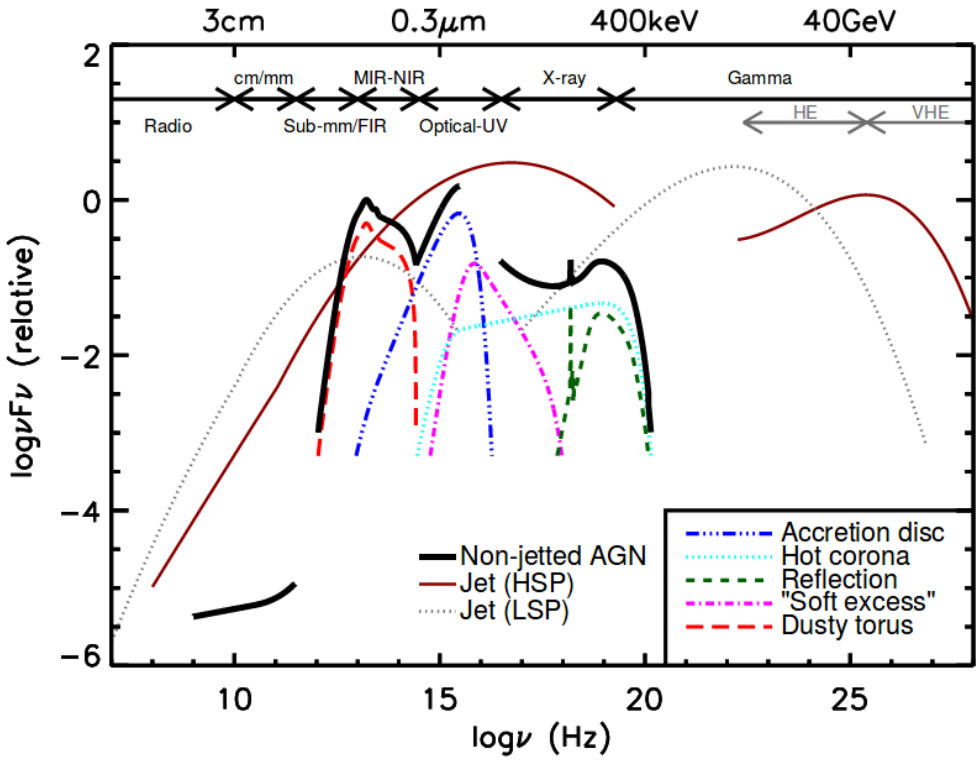

Figure 2.2: A schematic representation of an AGN SED, illustrating the contribution of the different accretion disc components. The black solid line represents a Seyfert galaxy SED, while the dashed and thin solid lines represent the radio-loud galaxies. Adopted from Koratkar & Blaes (1999).

effect the Fe Kα line. Panel 2 adds the effects of special relativity to the Fe Kα line and panel 3 shows the effects of general relativity. Panel 4 integrates multiple Fe Kα lines at different distance from the SMBH, which is what will be measured by an observer. Limits can be set on the black hole spin using the Fe Kα emission line as a diagnostic tool (see e.g. Brenneman et al., 2011).

2.1.3 The emission line regions

One of the defining AGN classification schemes depends on the ultra-violet/optical spectra. AGN are customarily divided into Type I & II, with Type I AGN showing broad and narrow emission lines, while the Type II AGN show only narrow lines. The broad emission lines display velocities between $\sim 10^3 - 10^4$ km s^{-1}, while the narrow emission lines only display velocities between $\sim 200 - 700$ km s^{-1}. The emission lines originate from two different regions surrounding the SMBH, the BLR and NLR (see e.g. Netzer, 2006; Rees et al., 1989; Schneider, 2015; Urry & Padovani, 1995). A summary of the emission lines most commonly observed in

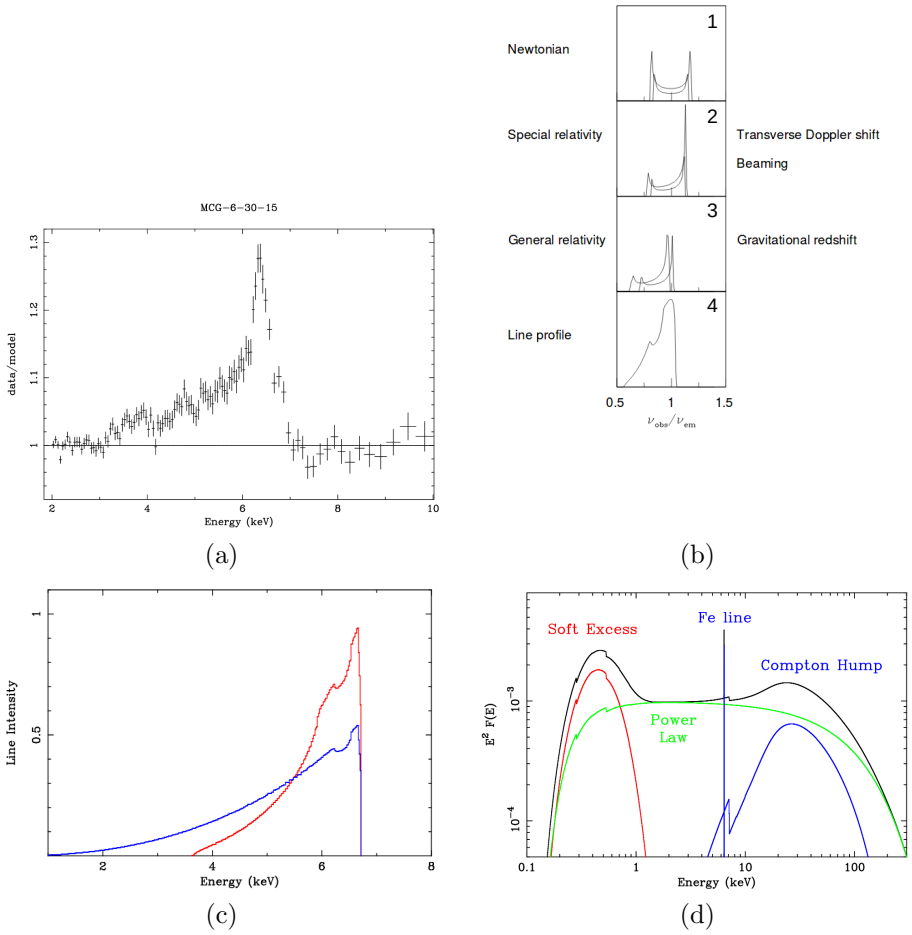

Figure 2.3: a) The broad iron line in MCG6-30-15 from XMM-Newton observations. The flux is shown relative to the continuum model (Fabian et al., 2002). b) A schematic diagram highlighting the different effects of Doppler and transverse Doppler shifts, relativistic beaming and gravitational redshifting on the profile of the broad Fe Kα emission at 6.4 keV (Fabian et al., 2000). c) Computed Fe Kα profiles for a non-rotating black hole (narrow, inner disc radius at 6 R_g) and a maximally rotating Kerr black hole (broad, inner disc radius at $1.24 \simeq R_g$). d) The main components of the X-ray spectrum of an unobscured accreting black hole . The main components are the soft X-ray excess from the accretion disc, Comptonization of the soft X-rays in the corona above the accretion disc and narrow Fe line due to reflection of the hard X-ray emission from dense gas. Figures adopted from Fabian (2008).

AGN is given in Table 2.1.

2.1.3.1 The Broad Line Region (BLR)

The BLR consists of gas moving with velocities between $\sim 10^3 - 10^4$ km s^{-1}, which lies beyond the accretion disc and can extend from ~ 0.01 pc for low luminosity

Table 2.1: Typical emission and absorption lines observed in AGN. The permitted and forbidden lines are tabulated, with their corresponding rest wavelength, λ_0 (Beckmann & Shrader, 2012, p. 91).

Line	λ_0 (Å)	Line	λ_0 (Å)	Line	λ_0 (Å)	Line	λ_0 (Å)
Lyβ	1026	Ne V	3346	Hδ	4101	[Ca V]	5309
O VI	1032	[He I]	3587	G-band	4306	[Fe VII]	5721
Ly α	1216	[O II]	3727	H γ	4340	H I	5876
N V	1240	[Fe VII]	3760	[O III]	4363	Na I-D	5894
Si IV	1400	H η	3835	[He II]	4471	[O I	6300
C IV	1549	[Ne III]	3869	[Fe II]	4570	[N II]	6548
He II	1640	H ζ	3889	[He II]	4686	H α	6563
[C III]	1909	Ca II H	3935	H β	4861	[N II]	6584
[C II]	2326	Ca II K	3970	[O III]	4959	[S II]	6716
[Mg II]	2798	H η	3970	[O III]	5007	[S II]	6731
[Ne V]	3346	[S II]	4071	[Mg I]	5174	[Ar III]	7136

AGN, up to ~ 1 pc for high luminosity AGN such as quasars (Netzer, 2006; Urry & Padovani, 1995). The gas in the BLR is photo-ionized and excited by the Ultra-Violet (UV) and soft X-ray emission from the accretion disc and hot corona above the accretion disc, giving rise to the observed high velocity emission lines when the electrons recombine or transition back to their ground states (see e.g. Schneider, 2015, p. 240).

The precise kinematics of the BLR region around AGN is still uncertain. Reverberation mapping has gone a long way towards studying the properties of the BLR. This technique involves near-continuous observations of AGN spectra to study the change in continuum luminosity and emission line strengths. Since the central continuum source heats and ionizes the gas in the BLR, reverberation mapping can use the changes in the continuum source to study changes in the emission line strengths after a time lag. This time lag corresponds to the light travel time to the different emission regions, which allows a measure of the extent and structure of the BLR to be made. The structure of the BLR can be explained by clouds of clumpy material or an outflowing disc wind. Reverberation mapping results strongly suggest that the BLR is not dominated by strong outflows but rather consist of high velocity clouds gravitationally bound to the SMBH (see e.g Gaskell, 1988; Korista et al., 1995; Sergeev et al., 1999).

2.1.3.2 The Narrow Line Region (NLR)

The NLR consist of gas with a lower column density ($\sim 10^{20} - 10^{21}$ cm^{-2}) and a lower gas density ($\sim 10^4$ cm^{-3}) than the BLR. The NLR extends up to $\sim 10^2 - 10^4$

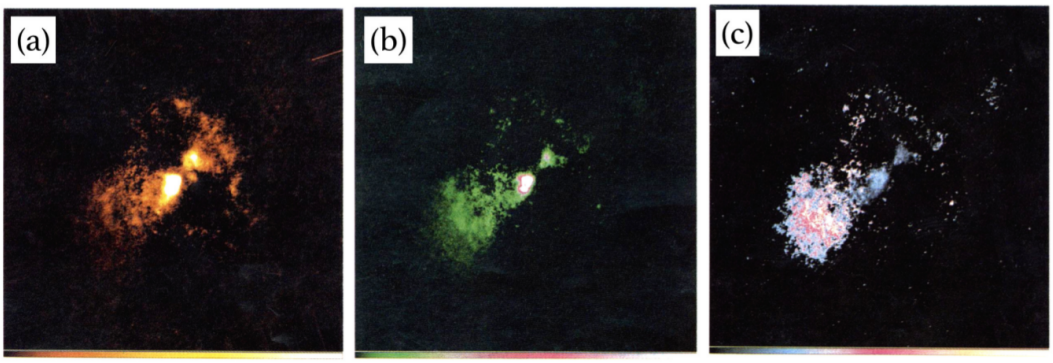

Figure 2.4: HST images of NGC 5728. (a) Hα + [II]emission line image. (b) [OIII] image. (c) Ionization map with the flux ratio [OIII]/Hα+[II]. Two cones are projected, a cone approaching the observer from the South-East, and a cone projected toward the North-West, moving away from the observer. In the images, North is up and East is to the left. Adapted from Wilson et al. (1993)

pc from the SMBH and as a result of the larger distance, displays emission lines with lower velocities ($\sim 200 - 700$ km s^{-1}) than those from the BLR (Bennert et al., 2002; Netzer, 2006; Osterbrock, 1989, see e.g.). Both the forbidden (e.g. [O III] and [NII]) and permitted lines (e.g. Hα and HeII) are detected from the NLRs of many AGN (e.g. Osterbrock, 1989, 1991; Veilleux et al., 2003).

The NLR is studied using ionization maps constructed from continuum-subtracted images made from [O III] and Hα filters. The continuum-subtracted images sample the ionization cones of the NLR, which extends well beyond the inner AGN regions. Figure 2.4 shows Hubble Space Telescope (HST) ionization maps of the NLR of NGC 5728 which show an extensive ionization cone (in the South-East direction) and a smaller, 0.270 kpc cone extending in the opposite (North-West) direction. The differences in the ionization cones are most likely due to dust obscuration of the receding North-West cone from the star forming ring and galaxy disc in NGC 5728 (Wilson et al., 1993).

2.1.4 The dusty torus

In the Unified AGN model, a number of the differences in the measured properties are explained by the presence of a dusty absorber that obscures the emission from the central regions of the AGN (Antonucci, 1984). Evidence for the presence of an absorber is found in the spectra of some Type II AGN: in unpolarized light, Type II spectra only display narrow emission lines, but when observed in polarized light, some display broad emission lines like those found in Type I AGN. The dusty torus (column density 10^{25} cm^{-2}), absorbs the emission emitted towards an observer, but

a scattering source which is present above the BLR scatters and polarizes the BLR emission into the line of sight of the observer (e.g. Schneider, 2015, pp 252-254). Observations by Corbett et al. (2000) suggest that the emission can be scattered and polarized towards an observer by either the torus, or by a region directly above the BLR.

The torus, with a temperature of ~ 1400 K dominates the AGN SED from $\sim 1\mu$m up to a few tens of micron (see Fig. 2.2). The emission is due to reprocessing of the accretion disc emission into mid-infrared wavelengths. Torus models have come a long way from the first picture of a uniformly distributed obscuring gas (see e.g. Feltre et al., 2012; Fritz et al., 2006; Granato & Danese, 1994; Pier & Krolik, 1992; Stenholm, 1994) and newer torus models now assume a clumpy structure, with the torus clumps obscuring the central regions for certain viewing angles (see e.g. Hönig et al., 2006; Rowan-Robinson, 1995; Stalevski et al., 2016). Figure 2.5 shows a simplified representation of the clumpy torus in the Unified AGN model. More realistic torus models include a clumpy torus with a polar outflow (Hönig & Kishimoto, 2017).

2.1.5 The jet

For radio-loud AGN, the SED is dominated by a relativistic jet emitting radiation over the entire electromagnetic regime, from radio to γ-rays. The energy required to launch the relativistic jet can be extracted from a rotating black hole and transferred to particles near the SMBH (see e.g Blandford, 1976; Blandford & Znajek, 1977). General relativistic hydrodynamical simulations by Tchekhovskoy et al. (2011) found that for a rotating SMBH with a spin parameter of $a = 0.99$, an outflow can be launched with as much as 140% of the available accretion energy. The outflow becomes relativistic, with the bulk flow obtaining typical Lorentz factors of $\Gamma \sim 20$, with the most energetic quasars reaching values of up to $\Gamma \sim 50$ (Jorstad et al., 2005).

The initial outflow may not be in the form of a collimated jet since, for example, observations of M87 show a gradually collimated jet with an opening angle of 60° on scales of ~ 0.01 pc to $\sim 5°$ on kpc scales. An explanation for the highly collimated jet at large distances may be due to the jet itself: the sideways expansion of a moving fluid increases the speed of the bulk flow of the fluid. Since the bulk flow of the jet must be less than the speed of light, this constrains the rate of the sideways expansion. This limits the jet opening angle to $< 1/\Gamma$, which for most AGN, with $\Gamma < 10$ yields opening angles of $< 18°$. The jet collimation could be

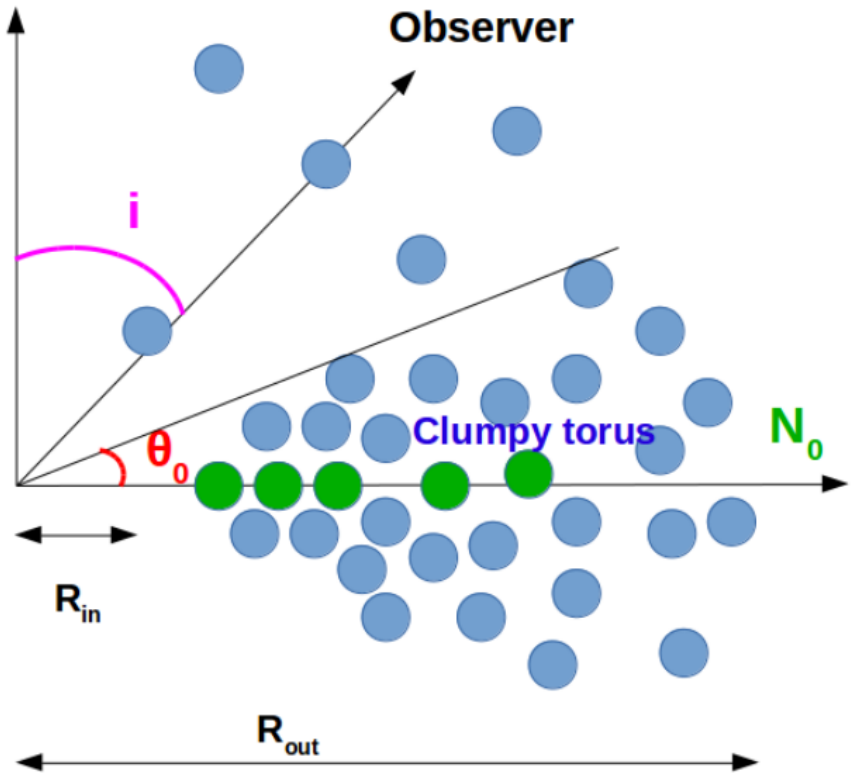

Figure 2.5: Simplified schematic of a clumpy torus model. The torus consist of clumpy obscuring material that covers a substantial part of the AGN, although most of the material is concentrated near the equatorial regions (θ_0 line). Adopted from García-González et al. (2017).

further enhanced by factors such as the disc wind, magnetic fields anchored in the disc and at larger distances the Interstellar (ISMF) and Intergalactic Magnetic Fields (IGMF) (see Böttcher et al., 2012, chapter 4.3 and references therein).

A magnetohydrodynamic (MHD) simulation by Barniol Duran et al. (2017) is shown in Fig. 2.6 with the collimating magnetic fields included. They found that the jet can dissipate its energy either via magnetic reconnection events when the jet "drills" a hole through the ambient medium (magnetic kink instabilities) or when jets form during repeated cycles of AGN activity and escape through a pre-existing hole in the ambient medium (collimation shocks). Both energy dissipation mechanisms accelerate electrons in the jet. These accelerated electrons cool by radiating their energy by e.g. synchrotron and IC emission, resulting in a dominant non-thermal component in the overall emission of the AGN. The IC radiation can arise from either the Synchrotron Self Compton (SSC) process or from the External Compton (EC) process, scattering photons from background radiation fields such as the Cosmic Microwave Background (CMB), accretion disc

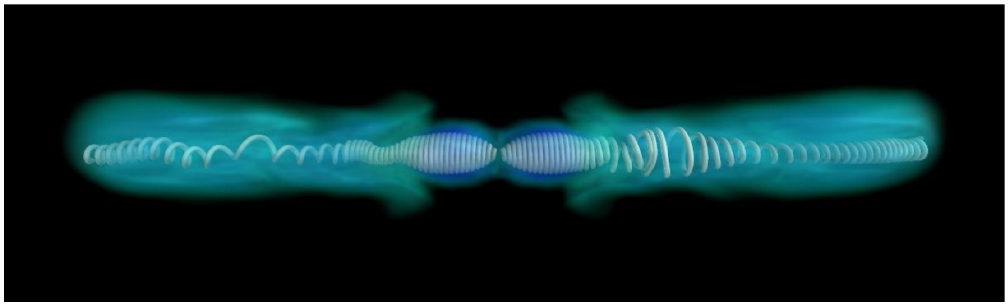

Figure 2.6: Simulation of a relativistic AGN jet with the magnetic field lines shown. Adopted from Barniol Duran et al. (2017)

photons or photons from the BLR and dusty torus (see e.g. Yang et al., 2009).

2.1.5.1 Relativistic effects observed in AGN jets

Jets launched from the cores of AGN often appear one sided and can exhibit apparent superluminal velocities. In cases where the jets are non-relativistic, there are several explanations for the one-sided appearance of the jets, including flip-flop behavior of the jet, where the central source oscillates between emitting a one-sided jet for $\sim 10^6$ years, before switching the jet direction. Another explanation for the one-sided appearance of the jet introduces asymmetric internal dissipation, where the conditions in the jet and counter-jet are different. In such a scenario one of the jets dissipates its energy in extended radio lobes, while the other jet emits from collimated regions (see e.g Rees, 1982).

For relativistic jets, Doppler boosting can explain the one-sided appearance of AGN jets. Below, the effects of Doppler boosting are briefly summarized, following the discussion in Böttcher et al. (2012, pp. 25-29).

If an emitting region in the jet is moving at a relativistic velocity then the bulk Lorentz factor of the emitting region can be expressed as

$$\begin{aligned} \Gamma &= \frac{1}{\sqrt{1-\frac{v^2}{c^2}}} \\ &= \frac{1}{\sqrt{1-\beta_\Gamma^2}}, \end{aligned} \tag{2.1}$$

where v is the velocity of the flow, c is the speed of light and $\beta_\Gamma = v/c$. Radiation from relativistic particles within this flow is beamed in the direction of movement. The radiation emitted in the co-moving frame of the jet will be Lorentz transformed when received in the observer's (rec) frame. The Doppler factor, δ, determines the

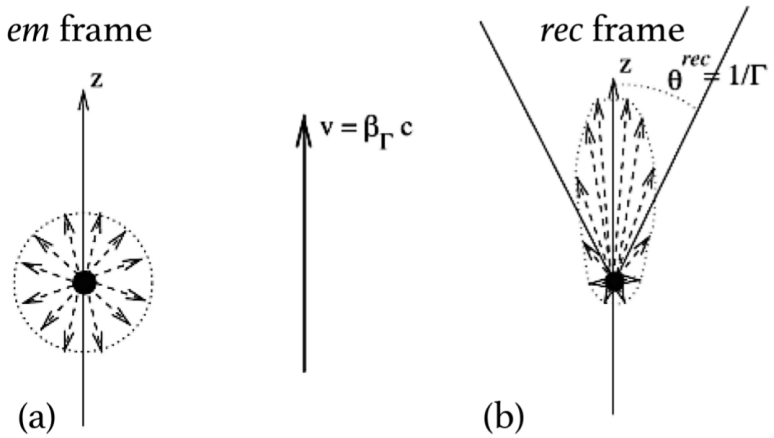

Figure 2.7: Illustration of the beaming effect for emitting relativistic particles. Isotropically emitted radiation in the particle's rest frame is beamed into a forward cone with opening angle $\theta^{\rm rec} \sim 1/\Gamma$ in the observer's frame. The length of the arrows represents the intensity in the emitted radiation in a given direction (Böttcher et al., 2012, p.28)

boosting in the photon energies, and is given by

$$\delta = \frac{1}{\Gamma\left(1 - \beta_\Gamma \mu^{\rm rec}\right)}, \tag{2.2}$$

where $\mu^{\rm rec} = \cos\theta^{\rm rec}$ where $\theta^{\rm rec}$ is the angle of the line-of-sight with respect to the direction of the moving emitter, as measured in the the receiver's reference frame. The aberration formulas governing the radiation pattern are given by (e.g. Rybicki & Lightman, 2008, pp. 109-110),

$$\sin\theta^{\rm rec} = \frac{\sin\theta^{\rm em}}{\Gamma\left(1 + \beta_\Gamma \cos\theta^{\rm em}\right)}, \quad \cos\theta^{\rm rec} = \frac{\cos\theta^{\rm em} + \beta_\Gamma}{1 + \beta_\Gamma \cos\theta^{\rm em}}, \tag{2.3}$$

where $\theta^{\rm em}$ is the angle of the emission in the emitter's reference frame. For ultra-relativistic particles with $\Gamma \gg 1$, the emission is emitted into a cone with $\theta^{\rm rec} \sim 1/\Gamma$. This effect is illustrated in Fig. 2.7.

Because the radiation is only beamed into a narrow cone with opening angle $\theta^{\rm rec} \sim 1/\Gamma$, the intensity is much brighter in the forward direction compared to the backward direction. The ratio between the forwards and backwards boosting is

$$\frac{\delta_{\text{forward}}}{\delta_{\text{back}}} = \frac{(1+\beta_\Gamma)^2}{(1-\beta_\Gamma^2)}$$
$$= \Gamma^2 (1+\beta_\Gamma)^2 \sim 4\Gamma^2 \quad (2.4)$$
$$= \sim 4\Gamma^2 \text{ for } \beta \to 1. \quad (2.5)$$

It is obvious that for closely orientated AGN jets, the counter-jet is deboosted by a significant amount, making it very difficult to detect (see e.g. Jones & Wehrle, 1994; Wardle & Aaron, 1997; Wilson et al., 2001; Xu et al., 2000). The transformation of flux, F_ν, between the receiver and emitter frames is

$$F^{\text{rec}}_{\nu^{\text{rec}}} = F^{\text{em}}_{\nu^{\text{em}}} \delta^3,$$

where ν is the frequency. If we assume the emitted flux follows a power-law of the form $F_\nu \propto \nu^{-\alpha}$, where α is the spectral index of the emission, the emitted flux, measured in the receiver's reference frame is

$$F^{\text{rec}}_{\nu^{\text{rec}}} = F^{\text{em}}_{\nu^{\text{rec}}} \left(\frac{\nu^{\text{rec}}}{\nu^{\text{em}}}\right)^{\alpha} = F^{\text{em}}_{\nu^{\text{rec}}} \delta^{\alpha},$$

which leads to a flux transformation

$$F^{\text{rec}}_{\nu^{\text{rec}}} = F^{\text{em}}_{\nu^{\text{rec}}} \delta^{3+\alpha}.$$

The increase in flux as observed in the receiver and emitter frames is very significant for blazars whose jets are closely aligned towards an observer.

2.1.5.2 Apparent superluminal motion in AGN jets

Apparent velocities higher than the speed of light are often seen in astrophysical jets (see e.g. Hummel et al., 1992; Jorstad et al., 2005; Kharb et al., 2010; Shen et al., 2001). Figure 2.8 shows a 43 GHz VLBA radio image of 3C 11 detected over a 3 year period, ejecting several radio knots moving at apparent velocities of $\sim$ 3c. The apparent superluminal motion can be explained by regarding a relativistic blob, moving along the jet between two points in a time Δt with a constant velocity v, emitting photons towards an observer, as shown in Fig. 2.9. The time difference upon arrival of photons emitted between the two points is

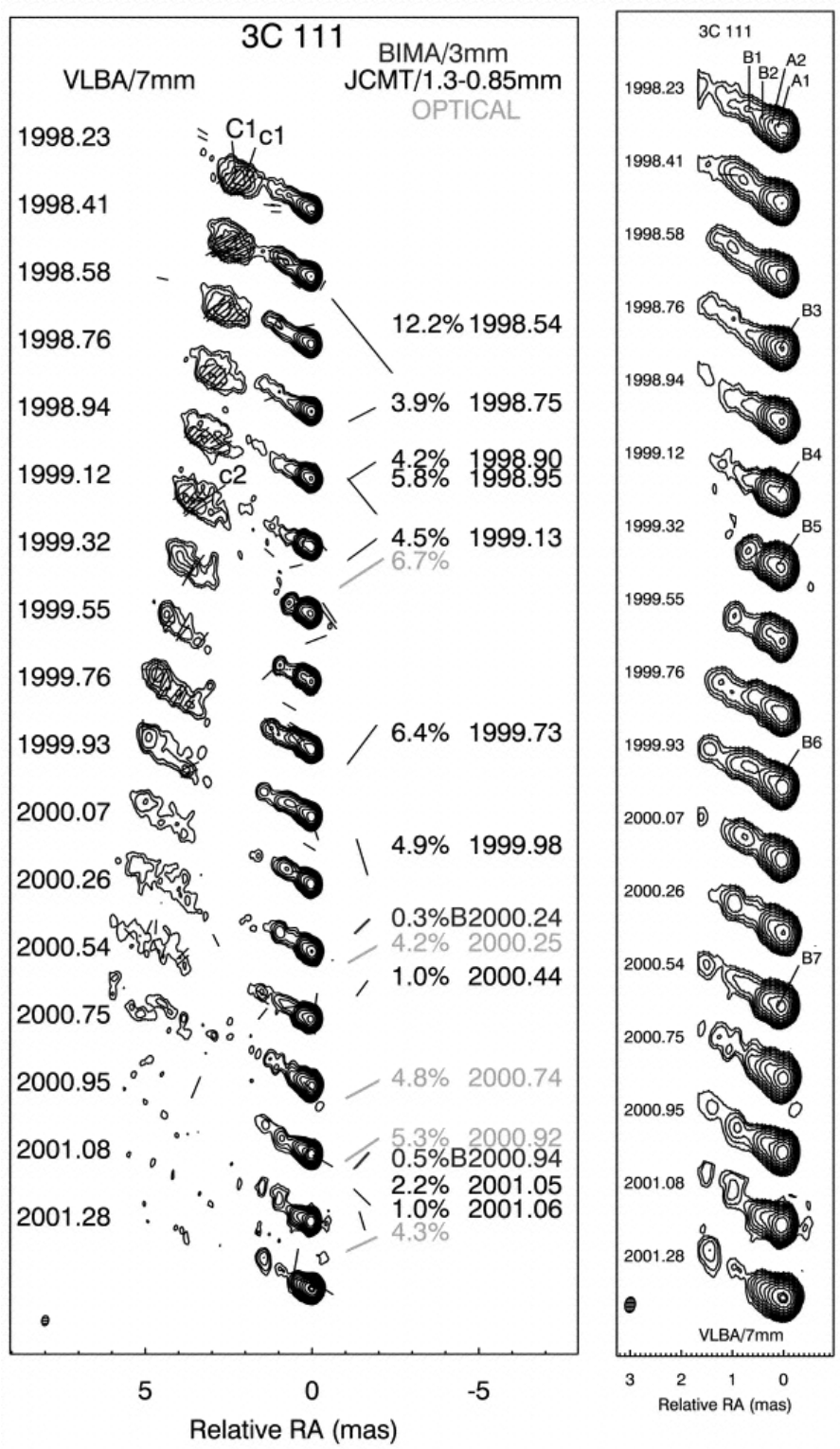

Figure 2.8: VLBA 43 GHz radio observations of the jet of 3C 111. The jet shows superluminal motion of $\sim 3c$. Adopted from Jorstad et al. (2005)

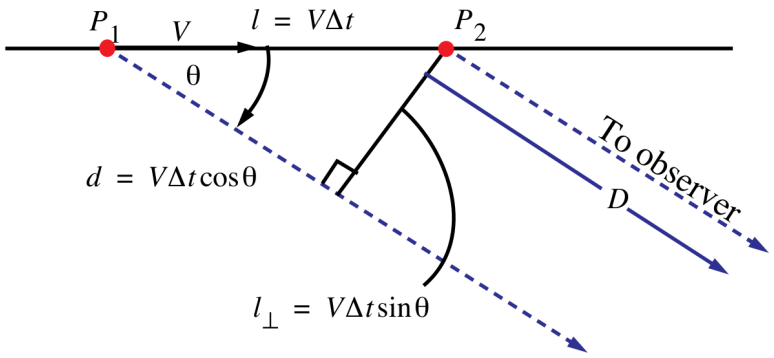

Figure 2.9: Diagram illustrating a blob propagating along a jet at relativistic velocity.

$$\delta t_{\rm rec} = (1 - \beta_\Gamma \cos\theta)\, \Delta t, \tag{2.6}$$

where θ is the angle between the jet propagation direction and the observer's line of sight. The projected distance the blob travelled during the time Δt is

$$l_\perp = v \Delta t \sin\theta. \tag{2.7}$$

The apparent velocity is then

$$v_{\rm app} = \frac{l_\perp}{\delta t_{\rm rec}}, \tag{2.8}$$

which can be simplified using Eq. 2.6 and 2.7, becoming

$$\beta_{\rm app} = \frac{v_{\rm app}}{c} = \frac{\beta_\Gamma \sin\theta}{1 - \beta_\Gamma \cos\theta}. \tag{2.9}$$

The apparent velocity of the relativistic blob will reach a maximum when $\cos\theta = \beta$. Therefore, jets closely aligned to the line of sight of an observer can display velocities up to $\beta_{\rm app} \approx \beta_\Gamma \Gamma$. Since $\Gamma \gg 1$ and $\beta_\Gamma \leq 1$, the apparent superluminal velocity of the jet is just a relativistic abberation effect.

2.2 AGN classification

AGN all share certain characteristics, such as a compact centres with a high luminosity and variability over a wide wavelength range. However, certain char-

acteristics separate them into different classes. AGN can be classed based on their radio-properties (i.e radio-loudness), the ratio of radio and X-ray luminosity, bolometric luminosity and viewing angles (see e.g. Tadhunter, 2008).

Radio loudness, has historically been based on the radio-to-optical ratios. One of the methods used by Sramek & Weedman (1980), parametrizes radio-loudness as

$$R^* = \left(\frac{f_{5\ \mathrm{GHz}}}{f_{2500\ \text{Å}}} \right), \tag{2.10}$$

which is the flux ratio between the 5 GHz radio band and optical band.[1]. A source is considered radio-loud when $R^* > 10$ or if $L_r > 10^{33}$erg s^{-1}Hz^{-1}. Another method measures the spectral slope between the optical and radio bands (della Ceca et al., 1994), defined as

$$\alpha_{\mathrm{r}_0} = \frac{\log\left(\frac{f_{5\ \mathrm{GHz}}}{f_{2500\text{Å}}}\right)}{\log\left(\frac{\nu_{\mathrm{r}}}{\nu_0}\right)} = \frac{R^*}{5.38}. \tag{2.11}$$

In Eq. (2.11), sources are regarded as radio-loud if $\alpha_{\mathrm{r}_0} > 0.35$, corresponding to $R^* \gtrsim 76$ in Eq. (2.10). Radio-loud AGN are typically found in giant elliptical galaxies, while radio-quiet AGN are normally found in spiral galaxies.

The radio-quiet AGN classes, include Seyfert type I and II galaxies, Radio-Quiet Quasars (RQQ) and LINERs. Radio-loud AGN constitute $\sim 15 - 20\%$ of AGN (Urry & Padovani, 1995) and include radio galaxies, radio-loud quasars and blazars.

AGN can also be classified as low power AGN (i.e Seyfert galaxies, Fanaroff-Riley type I galaxies and BL Lacertae objects) or high power AGN (i.e Fanaroff-Riley type II and Flat Spectrum Radio Quasars). Figure 2.10 illustrates the major components of the Unified AGN model contributing to the class of AGN that an observer will see. The observational differences between different AGN classes depends largely on the angle at which they are observed at and the presence or absence of a radio jet.

As previously mentioned, AGN are divided into Type I and II AGN based on their optical spectra. Type I AGN show broad and narrow emission lines, while Type II AGN exhibit only narrow emission lines in unpolarized light. Radio-quiet AGN can be divided into Seyfert I and II galaxies respectively. Radio-loud AGN are also divided into Type I AGN and Type II AGN. In addition to these two main

[1]The 2500 Å flux is actually at ultraviolet wavelengths. However, the convention is to refer to this as the radio-to-optical ratio.

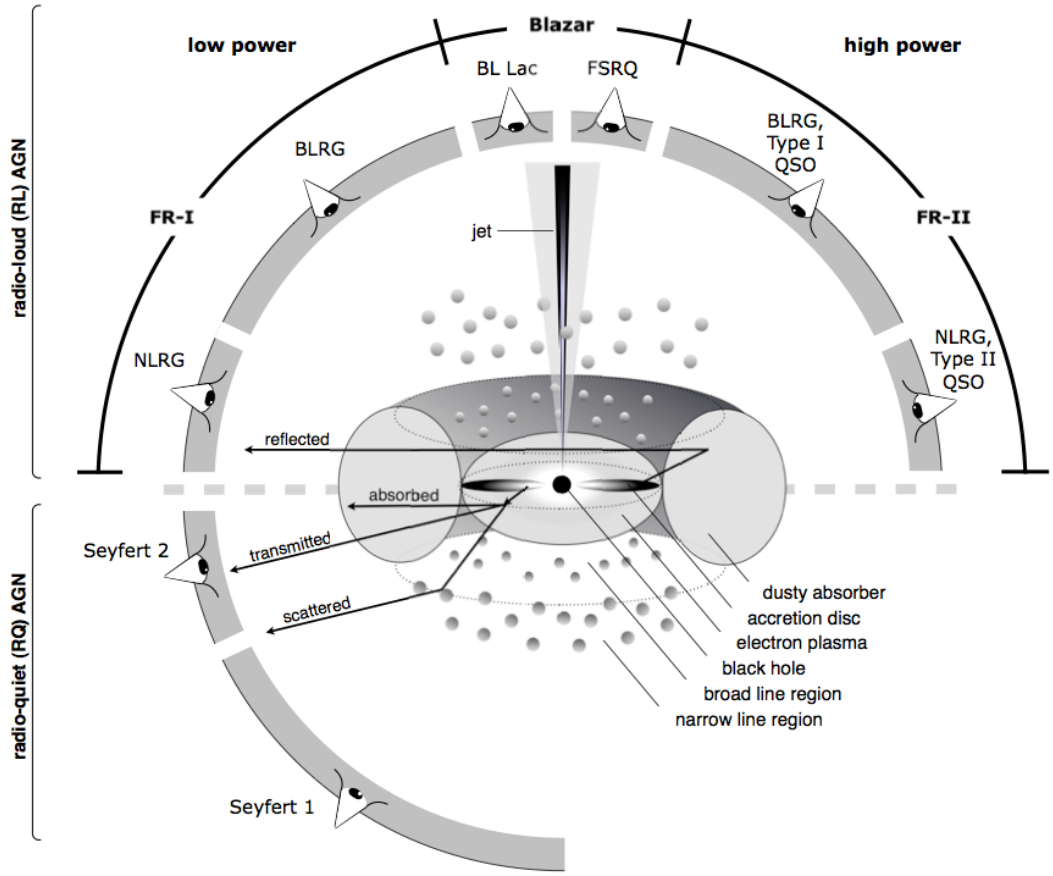

Figure 2.10: Illustrative diagram of the nomenclature of the Unified AGN model. The classification strongly depends on the viewing angle. In the radio-loud cases, jet-like structures emerge from the central core. Adopted from Beckmann & Shrader (2012, p. 132, fig. 4.16).

AGN classes, another class also exists, the Type 0 AGN. These AGN have non-existent or very weak emission lines and sometimes show weak absorption lines (e.g. BL Lacertae objects). Some sources also show broad P-Cygni-like lines in their optical and ultraviolet spectra, these are known as Broad Absorption Line AGN (BAL Urry & Padovani, 1995). The optical spectrum of a few different AGN classes are compared to that of a normal galaxy in Fig. 2.11.

Below, a brief overview of the different subclasses of radio-quiet and radio-loud AGN is given.

2.2.1 Radio-quiet AGN

In the Unified AGN model, radio-quiet AGN lack strong radio jets. Radio-loud and radio-quiet AGN accrete material, but it is still unclear why some AGN reprocess

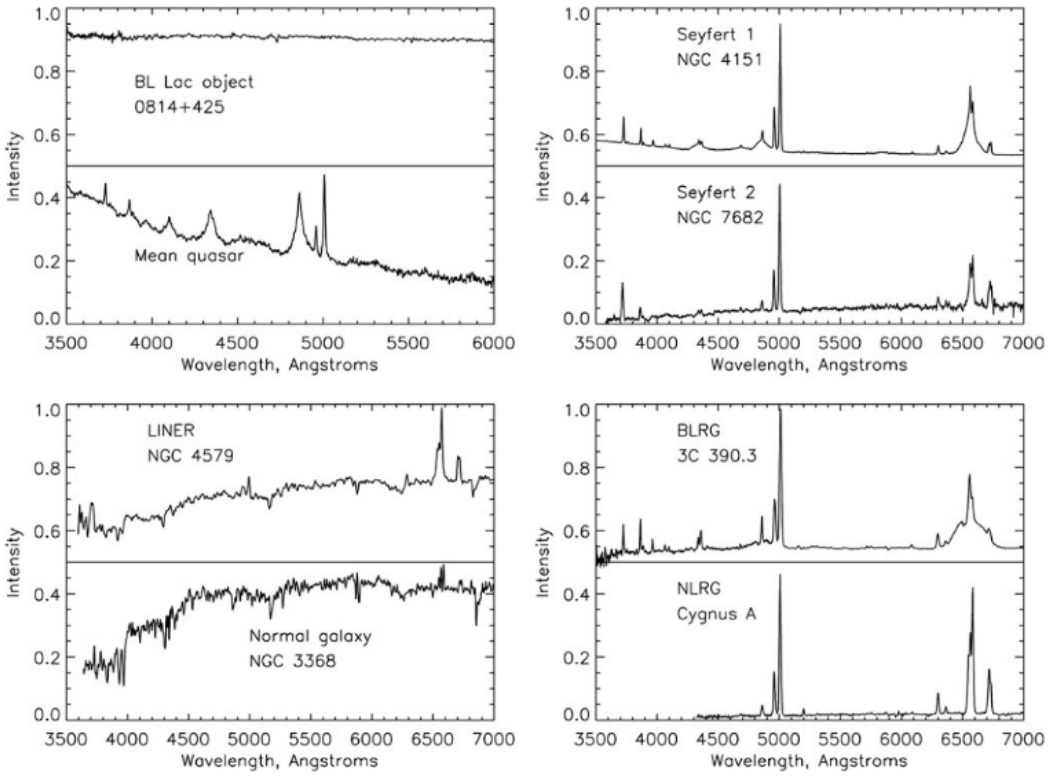

Figure 2.11: A comparison of optical spectra for various AGN classes. The differences between all the spectra can be explained by the Unified AGN model. Adopted from Schneider (2015, p. 220).

part of the accreting material into a radio jet. One of the possibilities is that the SMBHs in the centres of radio-quiet AGN do not rotate fast enough for significant energy to be extracted via the Blandford-Znajek process (see e.g. Blandford & Znajek, 1977; Tchekhovskoy et al., 2011; Teukolsky, 2015). SMBHs are inefficient at being spun-up via accretion, and will be more efficiently spun-up during mergers with similar-mass black holes. The resulting fast rotating SMBH will then be able to launch a relativistic jet. Not all galaxy mergers will lead to the production of a fast rotating SMBH and, therefore, the expected number of radio-loud galaxies is low. Most radio-quiet AGN will reside in spiral galaxies which have not undergone a recent major merger (see e.g. Wilson & Colbert, 1995). The most prominent radio-quiet AGN are the Seyfert, LINERs and RQQS.

2.2.1.1 Seyfert galaxies

Seyfert galaxies, first described by Seyfert (1943), are identified as spiral galaxies with extremely luminous cores. Seyfert galaxies exhibit strong emission lines that are broader than the typical velocities in galaxies. They can be distinguished into

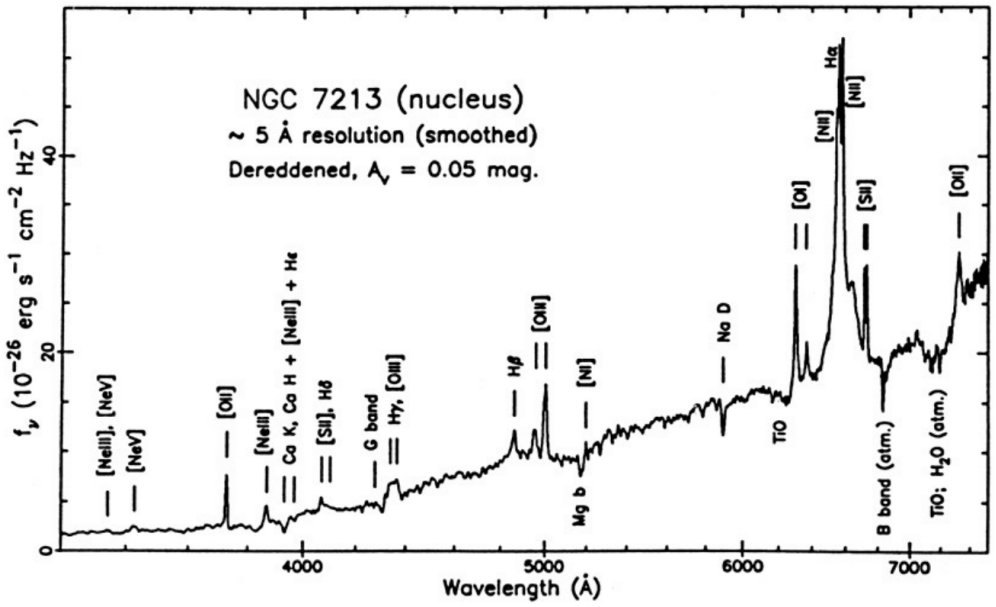

Figure 2.12: A spectrum of the LINER 7213 with broad wings in the Hα emission (Filippenko & Halpern, 1984).

Type I and Type II galaxies, although intermediate type are also found. Seyfert I galaxies both show broad and narrow emission lines, while Seyfert II galaxies only exhibit narrow emission lines. The top right panels in Fig. 2.11 compares the spectra of a Seyfert I (NGC 4151) and a Seyfert II (NGC 7682).

The difference between Seyfert Type I and Type II galaxies can be explained by the Unified AGN model: the broad emission lines are produced in the BLR, while the narrow emission lines are produced in the NLR. Seyfert Type I galaxies are aligned so that the observer sees both the BLR and NLR emission from the AGN. Seyfert Type IIs are viewed at angles such that only emission from the NLR reaches the observer, while the emission from the BLR is obscured by the dusty torus.

2.2.1.2 LINERs

LINERs resemble Seyfert Type II galaxies but exhibit strong low-ionization emission lines (e.g [O I λ6300] and [N II λ6548, λ6583]), which are also detected in H II regions and star forming galaxies, making the identification of LINERs difficult. Figure 2.12 shows as an example the spectrum of the LINER NGC 7213.

LINERs are Low-Luminosity AGN (LLAGN), exhibiting lower luminosities than other AGN, but higher core luminosities than regular galaxies. Distinguishing between LINERs, Seyfert II galaxies and star forming galaxies can be accom-

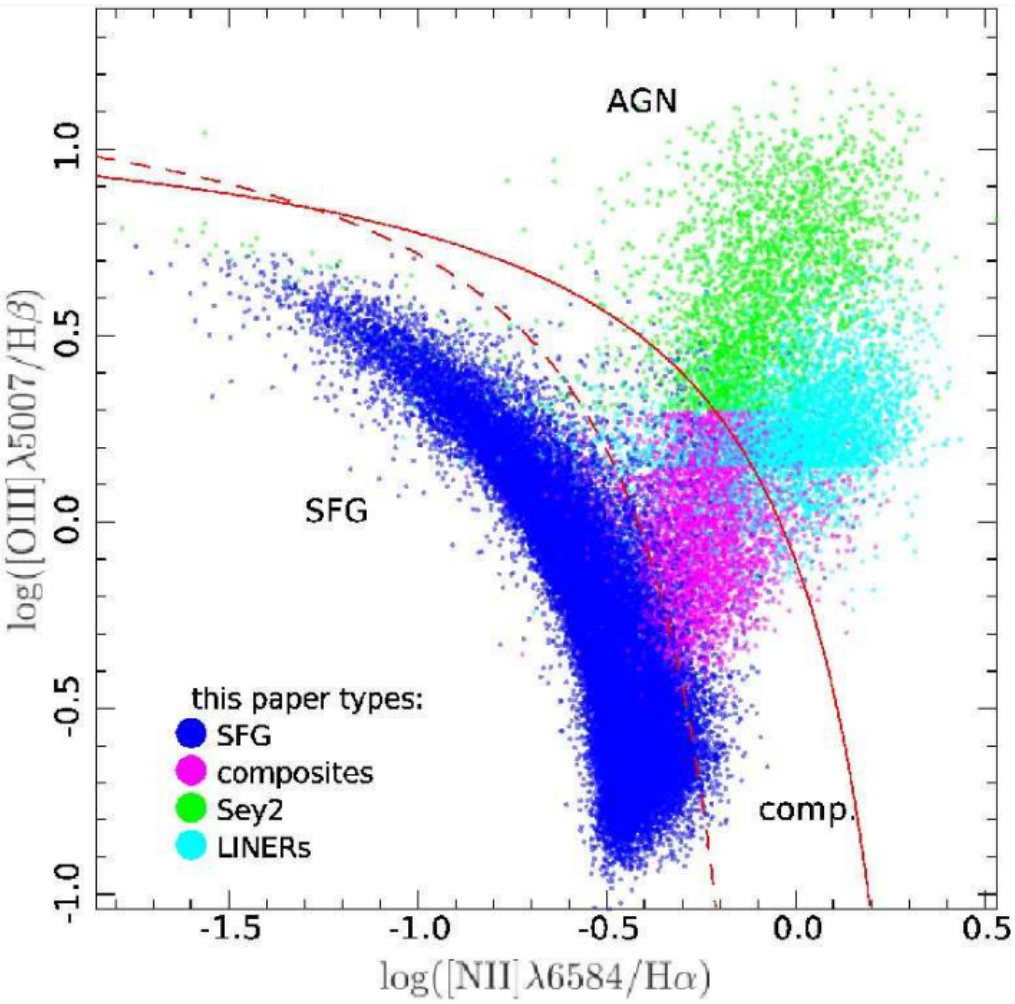

Figure 2.13: Illustration of a BPT diagram for the identification of different line emitting galaxies. The BPT diagram uses the OIII/Hβ vs. [NII6583]/Hα line ratios to distinguish between LINERs (cyan), Seyfert II galaxies (green) and star forming regions (blue). The composite (pink) galaxies, i.e. galaxies showing features from multiple classes, are also represented. Adopted from Marocco et al. (2011).

plished with the use of a Baldwin, Phillips & Terlevich (BPT) diagram (Baldwin et al., 1981), which uses the ratios between different emission lines (OIII/Hβ vs. [NII6583]/Hα) to classify the nature of the objects emitting the lines. An example of a BPT diagram is shown in Fig. 2.13.

2.2.2 Radio-loud AGN

Radio-loud AGN are found in giant elliptical galaxies with an active nucleus. Like radio-quiet AGN, they can be separated into two classes based on their emission line properties. Radio-loud AGN with broad emission lines are classified as Broad

Line Radio Galaxies (BLRG) and those with narrow emission lines as Narrow Line Radio Galaxies (NLRG).

Radio-loud AGN are characterized by the presence of a bi-directional jet originating from the centre of the AGN. These jets can extend up to hundreds of kpc, often terminating at a radio lobe. The relativistic jets from radio-loud AGN often display different luminosities for the receding and approaching jets, a result of Doppler boosting as discussed in Section 2.1.5.1.

2.2.2.1 Radio-galaxies

AGN with relativistic jets not closely aligned with an observer's line-of-sight often display extended radio emission. These radio jets can have a wide variety of morphologies (see e.g. Miley, 1980). These morphologies are a product of both intrinsic and extrinsic influences on the radio jet. Extrinsic effects could, for example, produce large scale bending of the jet. Intrinsic effects are associated with knots, shocks and bends in the jet structure caused by the precession of the jet and variable particle injection into the jet. Because the jet is not closely orientated toward the observer, there is minimal relativistic boosting. The emission is often only seen at radio and microwave frequencies, caused by synchrotron emission from low energy particles emitting radiation into a wider emission cone than the higher energy particles.

Relativistic jets transport extreme amounts of energy over very large distances. Energy dissipation, in the form of synchrotron emission, produces radio emission that can trace the jet to hundreds of kpc, with some extending even further (Strom & Willis, 1980). A radio contour map of 3C 236, a radio galaxy whose two radio jets extend to almost 4 Mpc is shown in Figure 2.14.

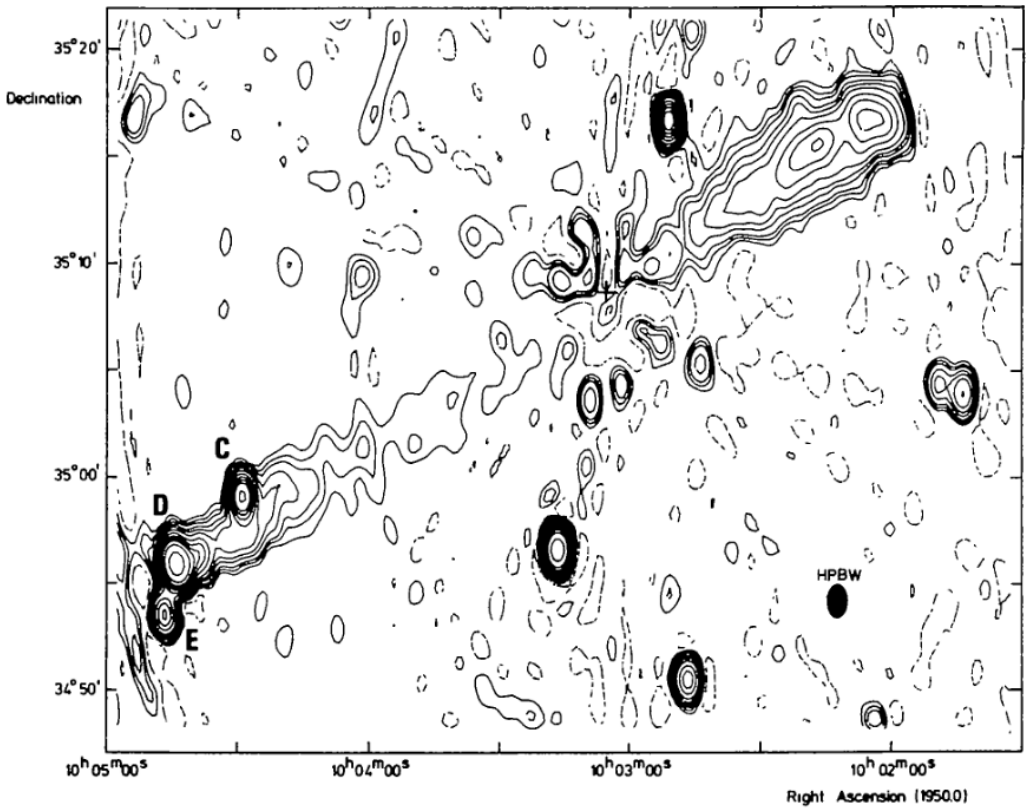

Figure 2.14: Westerbork 49 cm radio contour map of the radio galaxy 3C 236, whose two radio jets extend a combined 4 Mpc from the central AGN. Adopted from Strom & Willis (1980).

Radio galaxies are classified based on their radio morphology. Radio galaxies that display decreasing jet luminosity from the core are classified as low-power Fanaroff-Riley (FR) I radio galaxies, while FR II are high powered AGN whose radio jet increases in luminosity away from the core of the galaxy (Fanaroff & Riley, 1974). Figure 2.15 illustrates the difference between an FR I and FR II type radio galaxies.

2.2.2.2 Blazars

When the propagation direction of the jet lies close to the observer's line of sight, there is a large Doppler boosting of the emission (see Section 2.1.5.1) and such sources are collectively called blazars. The dramatic increase in brightness results in blazars being the most numerous objects detected in the extragalactic γ-ray sky (e.g. Acero et al., 2015; Ackermann et al., 2015; Ajello et al., 2017).

Blazar SEDs are subsequently dominated by the non-thermal emission from the beamed jet, which can extend up to TeV energies. Blazar SEDs display two broad

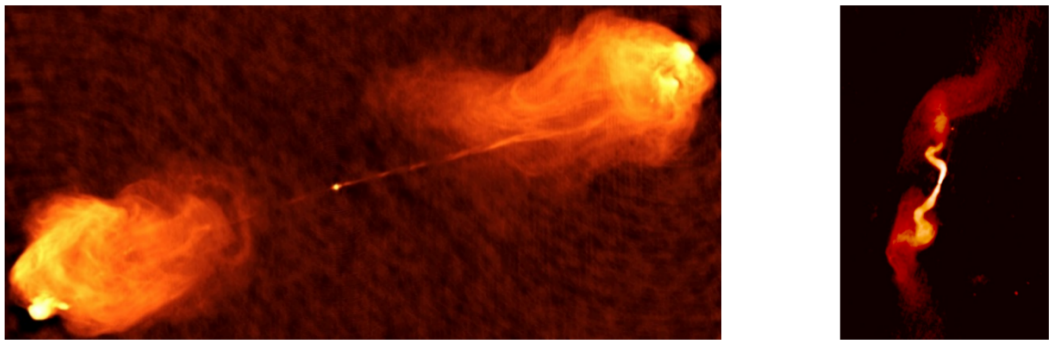

(a) (b)

Figure 2.15: (a) The FR II type radio galaxy Cyg A, imaged by the VLA at 5 GHz. The bright lobes and faint core are characteristic of FR II type radio-galaxies. (b) FR I type radio galaxy 3C 31 as imaged by the VLA at 1.4 GHz. The radio brightness of FR I radio galaxies decreases from the radio core. Adapted from `http://images.nrao.edu/AGN/Radio_Galaxies`.

components, a low energy component (radio to X-ray) produced by synchrotron emission, while the high energy component (X-ray to TeV) is the result of either leptonic IC emission or hadronic processes.

Blazars are divided into Flat Spectrum Radio Quasars (FSRQ, high powered AGN) and BL Lacertae objects (BL Lac, low powered AGN). The distinction between FSRQs and BL Lacs is based on their emission line equivalent widths, although the division correlates with the SED properties of these objects. BL Lacs lack strong emission lines and often have absorption lines, while FSRQs have strong emission lines. The dividing line between BL Lacs and FSRQs is often set by the equivalent width (EW, in the galaxy's rest frame) of the emission lines, with BL Lacs having EW < 5 Å and FSRQs EW > 5 Å (Stickel et al., 1991; Urry & Padovani, 1995).

FSRQs have radiative efficient accretion discs which photo-ionizes the BLR and NLR. The high luminosities of the accretion disc and BLR provides seed photons that the electrons in the jet can upscatter to γ-rays via the IC process. BL Lacs, with radiative inefficient accretion discs, cannot sustain luminous line regions and so the dominant high energy component is SSC emission. BL Lacs are effectively divided into three different subclasses based on the position of their synchrotron peaks. Low synchrotron peaked BL Lacs (LBL) have synchrotron peaks below $\nu^{\rm syn}_{\rm peak} < 10^{14}$ Hz, Intermediate synchrotron peaked BL Lacs (IBL) between $10^{14} < \nu^{\rm syn}_{\rm peak} < 10^{15}$ Hz and High synchrotron peaked BL Lacs (HBL) peak at $\nu^{\rm syn}_{\rm peak} > 10^{15}$ Hz (Abdo et al., 2010a).

The different classes of blazars can be explained, in the leptonic scenario, by

the different cooling rates in their jets. The FSRQs, with their radiative efficient accretion discs emit the most seed photons into the jets. The relativistic electrons in the FSRQ jets experience the largest radiative cooling rates due to the larger number of seed photons, preventing them from accelerating to the highest energies. The HBLs on the other hand, with their radiative inefficient accretion discs and low luminosity line regions, have less seed photons emitted into their jets, allowing the electrons to reach higher energies, resulting in less luminous, but higher IC peak emission (see e.g. Ghisellini et al., 1998). This leads to the expectation that the high energy component of HBLs will be of a similar or lower luminosity compared to the lower energy component of the SED. Indeed, this can be observed in the blazar sequence, a collection of the average SEDs of blazrs detected by the EGRET γ-ray telescope (Donato et al., 2001; Fossati et al., 1998). A more detailed picture of blazar physics will be presented in Chapter 3.

Chapter 3

Multi-wavelength observation of blazars

Multi-wavelength observations of blazars, coupled with detailed modelling, are crucial to understanding the physics in these sources. Blazars contain relativistic jets, with the emission highly Doppler boosted towards us and, therefore, observations probe the particle acceleration in extremely relativistic regions. Observations of high energy (HE, 20 MeV $< E_\gamma <$ 10 GeV) and very high energy (VHE, $E_\gamma >$ 10 GeV) blazar emission with the *Fermi* Large Area Telescope (*Fermi*-LAT) and High Energy Spectroscopic System (H.E.S.S) γ-ray telescopes are an important tool to study blazars. However, only studying blazars in one limited energy regime provides an incomplete picture. Therefore observations in all energy regimes are required to expand our understanding of the physics of blazars.

For example, variability studies at optical and γ-ray energies provide information on the size of the emission regions (see e.g. Goyal et al., 2017); observing blazar jets, which are closely aligned to us and highly Doppler boosted, in radio allow us to study the rapid parsec scale evolution of the jets; optical spectroscopy is used to classify blazars, based on their emission properties; spectropolarimetry is used to place constraints on the contribution of polarized synchrotron emission to the total emission from blazars, which can then be used to help constrain multi-wavelength emission models (see e.g. Smith et al., 2011). These observations all provide a partial look into blazar physics, but have the potential to provide a deeper understanding if combined into a complete multi-wavelength picture. This chapter will present a brief overview of the current picture of blazars in the multiwavelength regime.

3.1 γ-ray observations of blazars

The highest energy emission detected from AGN, produced by non-thermal processes, is believed to originate in the relativistic jet. The γ-rays can be produced by the up-scattering of lower energy photons to γ-ray energies via the IC processes in leptonic scenarios, or by hadronic processes such as proton synchrotron or pion decay (see e.g. Böttcher et al., 2013). The energy requirements to sustain continuous γ-ray emission means that the γ-rays are emitted only in compact regions, allowing the study of processes on the smallest scales in the jet.

Two γ-ray telescopes have significantly improved our understanding of the HE universe. These two telescopes, the Energetic Gamma-ray Experimental Telescope (EGRET) and its successor, the *Fermi*-LAT, both provided insights into Galactic and extragalactic γ-ray emission and changed our understanding of the most powerful persistent events in the universe. The all-sky coverage of the two telescopes and large number of detected sources provides a large dataset of γ-ray loud blazars to study with Imaging Air Cherenkov Telescopes (IACT)s, such as the H.E.S.S telescopes and Cherenkov Telescope array (CTA).

3.1.1 Energetic Gamma-ray Experiment Telescope (EGRET)

The Compton Gamma-ray Observatory (CGRO) operated from 1991 to 2000, when it was intentionally de-orbited. The CGRO had four HE detectors on board, among which was the the Energetic Gamma-ray Experiment Telescope (EGRET), capable of detecting γ-rays in the energy range between 30 MeV and 30 GeV. The instrument (Fig. 3.1a) detected single γ-rays using a multi-level spark chamber, triggered by a scintillator coincidence system (Thompson et al., 1993). The system used Tantalum foil to convert γ-rays into electron-positron pairs, which were detected by a series of scintillation counters which in turn triggered the spark chamber, recording the positron-electron path. The calorimeter used Nal(TI) to measure the energy of the electron-positron pairs.

EGRET performed the first all-sky survey of the HE sky and detected 271 γ-ray sources, of which 170 sources remained unidentified in the final EGRET catalogue (Hartman et al., 1999). The source list was split between 80 low Galactic latitude ($|b| < 10°$) and 181 high Galactic latitude ($|b| > 10°$) sources. The large number of sources that remained unidentified at the end of the mission highlighted the need for further observations, not just in the γ-ray regime, but the entire electromagnetic spectrum, to find sources that are capable of producing high energy radiation.

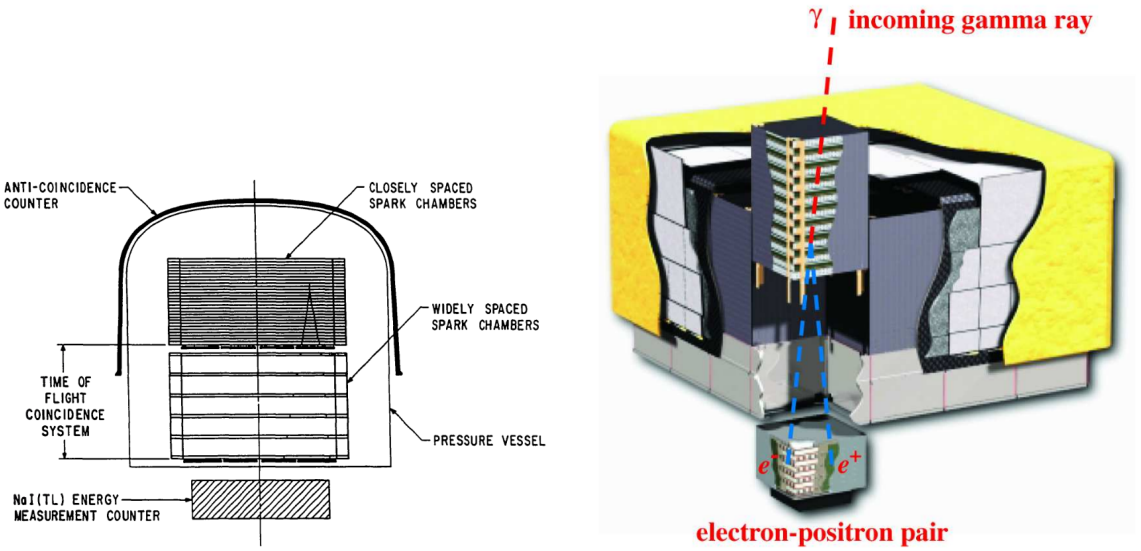

(a) EGRET consisted of a multi-level spark chamber and measured the direction and energy of single γ-rays entering the telescope. It measured γ-rays with energy between 30 MeV and 30 GeV. Adopted from Thompson et al. (1993).

(b) The LAT is a pair-conversion telescope with a 2.4 sr field-of-view able to measure γ-rays with energy between 20 MeV and 300 GeV. Adopted from Atwood et al. (2009).

Figure 3.1: Schematics of the EGRET and LAT γ-ray detectors.

EGRET also discovered a large population of extragalactic γ-ray emitting sources, which opened up new avenues in high energy research. Using a sample of multi-wavelength detected blazars, Fossati et al. (1998) constructed the blazar sequence using data from the EGRET telescope (Fig. 3.2a), providing the first hints that differences in the observed characteristics between blazar classes are due in part to fundamental differences of just a few properties, such as the strength of their BLR emission and jet power (see e.g. Ghisellini et al., 1998, and Chapter 2.2.2.2).

3.1.2 The *Fermi* Large Area Telescope (LAT)

The *Fermi Gamma-ray Space Telescope* is the successor to EGRET and was launched in 2008 aboard a Delta II Heavy launch vehicle. The telescope was inserted into a low earth orbit (altitude $\sim$ 565 km, 1.5 hours per orbit) that allows the telescope's 2.4 sr field of view (FoV) to cover the entire sky every 3 hours. The primary instrument on *Fermi* is the Large Area Telescope (LAT), an imaging, wide field-of-view, pair-conversion telescope, covering the energy range from below 20 MeV to more than 300 GeV (Fig. 3.1b Atwood et al., 2009). As part of the scientific goals of the LAT, the instrument has contributed significantly to our understanding of AGN and transient phenomena in HE environments. This includes

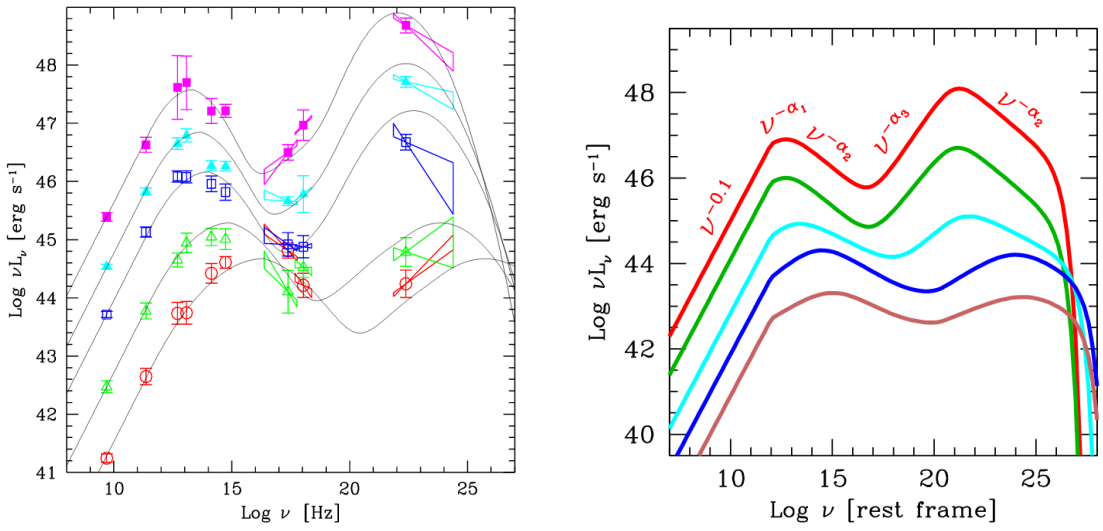

(a) The original blazar sequence, constructed using blazars detected by EGRET (Donato et al., 2001; Fossati et al., 1998).

(b) The updated blazar sequence. This updated blazar sequence was fitted with two smoothly broken power laws using blazars from the LAT 3LAC with established redshifts. The SEDs show a correlation between the synchrotron peak, luminosity and HE peaks. The HE peak tends to shift towards lower energies for more luminous blazars. Adopted from Ghisellini (2016)

Figure 3.2: A comparison between the original blazar sequence by Fossati et al. (1998) and the updated one by Ghisellini (2016).

the discovery that blazars are the most numerous extragalactic HE objects.

Fermi also discovered a γ-ray counterpart to the Wilkinson Microwave Anistropy Probe (WMAP) haze, a feature that remains after all other galactic emission have been subtracted from the WMAP data; these are the so-called *Fermi* bubbles. The *Fermi* bubbles consist of 2 lobes extending $\sim 50^{\circ}$ above and below the galactic center (Dobler et al., 2010). The LAT has so far discovered 3033 γ-ray sources with energies between 100 MeV and 300 GeV, 1010 of which still need to be associated to objects at other wavelengths. The large blazar population observed with the LAT, allowed Ghisellini (2016) to present an updated version of the blazar sequence, presented in Fig. 3.2b. The new results confirm the initial predictions made with the EGRET data, that the HE peak tends to shift towards lower energies for more luminous blazars.

3.1.3 The H.E.S.S. telescope

The High Energy Stereoscopic System(Pühlhofer, 2018, H.E.S.S.) is an IACT located in the Khomas region in Namibia, undertaking observations of VHE γ-ray

photons in the energy range of tens of GeV up to TeV energies. H.E.S.S. observes γ-rays by measuring the Cherenkov light produced by high energy secondary particles created when VHE γ-rays interact with atmospheric particles. A VHE γ-ray will interact with the particles in the atmosphere ($12 - 15$ km above sea level), producing an electron-positron pair. The electron-positron pair will then undergo Bremsstrahlung breaking, producing more γ-rays, which in turn produces more electron-positron pairs until the energy of the particles become small enough so their energy loss is dominated by ionization losses. This process is known as an electromagnetic air shower. The particles constituting the air shower produce Cherenkov radiation which travels to the surface with very little absorption. The light pool produced by the Cherenkov radiation has a diameter of ~ 250-m at sea level (see e.g. Völk & Bernlöhr, 2009).

The H.E.S.S. telescope consists of four 12-m reflectors arrayed in a square with 120 m sides and a 28-m reflector in the center, aimed at lowering the energy threshold of the array to below 100 GeV (e.g. Cerruti et al., 2017). The telescopes measure the flashes of Cherenkov light using photomultiplier tube arrays, which allows an image of the Cherenkov light to be reconstructed. If multiple detectors measure a Cherenkov flash, the direction of the air shower can be determined, using the stereoscopic technique, which in turn provides the direction of the incoming γ-ray. Fig. 3.3 indicates how the direction of a γ-ray can be determined using data from multiple detectors. The intersection of multiple images from different detectors converges at the point where the air shower originated. Another advantage of using multiple detectors is the almost complete elimination of unwanted background muon detections. Since muons interact with the atmosphere much closer to the ground than γ-rays and hadrons, the air shower results in a much smaller light pool and is able to illuminate only one of the detectors (Völk & Bernlöhr, 2009).

Other large IACTs exist in the Northern Hemisphere: the Major Atmospheric Gamma Imaging Cherenkov telescopes (MAGIC; Aleksić et al., 2016), the Very Energetic Radiation Imaging Telescope Array System (VERITAS; Holder, 2017) and the High Altitude Water Cherenkov (HAWC; Abeysekara et al., 2013). MAGIC and VERITAS work on the same principles as the H.E.S.S telescope, measuring the Cherenkov radiation of VHE γ-ray air showers. MAGIC is comprised of two 17m telescopes located in La Palma, Canary Islands and is sensitive to γ-rays above $\gtrsim 30$ GeV. VERITAS is located at the Fred Lawrence Whipple Observatory (FLWO) in Arizona, USA and consists of four identical 12-m telescopes, sensitive

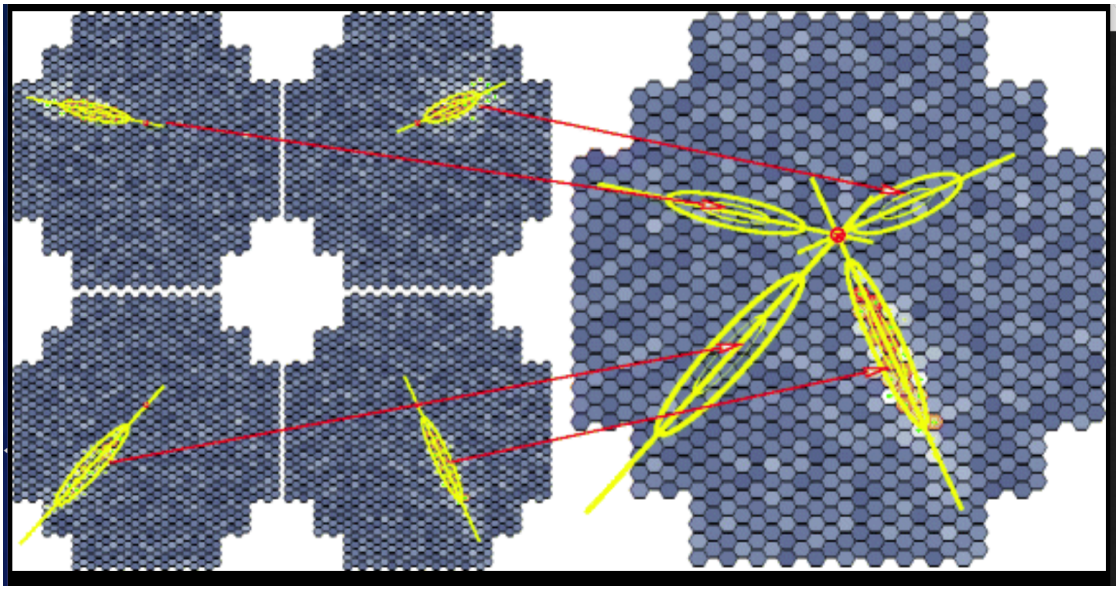

Figure 3.3: Projection of multiple images can be used to reconstruct the direction of a electromagnetic particle shower using the stereoscopic technique. Adopted from Völk & Bernlöhr (2009).

to γ-rays above $\gtrsim$ 85 GeV. The HAWC observatory, located in the Sierra Negra, Mexico, 4100 m above seal level, is an array of water Cherenkov detectors, sensitive to γ-rays above $\gtrsim$ 100 GeV. HAWC measures Cherenkov radiation from secondary particles reaching the water-based detectors when a γ-ray interacts with the atmosphere.

3.1.4 Active Galactic Nuclei in γ-rays

The large sky coverage and near continuous observation strategy has allowed LAT to provide long-term γ-ray data of more than 3033 sources.[1] These include $\sim$ 1750 AGN, allowing detailed studies of AGN variability in the HE regime. Using sources in the LAT Bright AGN Sample (LBAS), Abdo et al. (2010b) studied the variability of 106 AGN during the first 11 months of the *Fermi* mission and found that FSRQs are more variable than BL Lacs. They also found the light crossing times for 53 of the brightest and most variable blazars with known redshifts using the Discrete Auto Correlation Function (DACF). The results of their DACF analysis are shown in Fig. 3.4. The average light crossing times for their sample was $\Delta t_{\rm cross} \sim 7$ weeks in the observer's frame and when corrected for relativistic effects, was $\Delta t^{\rm rest}_{\rm cross} < 50$ weeks, indicating that the HE and VHE emission is produced within regions with diameters $\lesssim 0.3$ pc.

[1]Fermi data products are accessible at `https://fermi.gsfc.nasa.gov/ssc/data/access/`

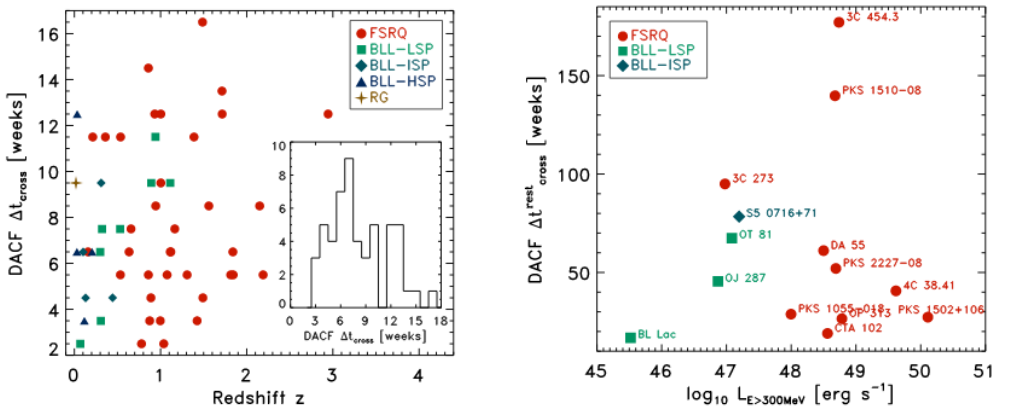

(a) Plot of the DACF crossing times in weeks, versus the redshift for the 53 brightest and most variable blazars with known redshift in the LBAS dataset.

(b) Plot of the DACF crossing times in weeks in the rest frame corrected for redshift and relativistic beaming

Figure 3.4: These two figures show the light crossing times during blazar flares as calculated by the DACF algorithm, in the observers time frame and corrected for redshift and relativistic beaming from the sources. The fast variability seen during blazar flaring states are largely a result of the relativistic beaming from the jets, which drastically shortens the flaring timescales in the observers frame. The data was taken from variable blazars in the LBAS catalogue. Adopted from Abdo et al. (2010b)

Long-term γ-ray observations of γ-ray-loud AGN reveal both dramatic short-term flaring and long-term variability of AGN over the course of a few years (Fig. 3.5). Kushwaha et al. (2017) constructed long-term γ-ray light curves for four LAT detected γ-ray-loud AGN, namely the FR I radio galaxy NGC 1275, the BL Lac MRK 421 and the FSRQs B2 1520+31 and PKS 1510-089. All four sources exhibited long-term variability, while MRK 421, B2 1520+31 and PKS 1510-089 exhibited several flaring periods during the observations.

During flaring periods blazars typically display a harder-when-brighter trend (Abdollahi et al., 2017). This behaviour means that blazar emission extends to higher energies during flares, possibly allowing blazars which are not normally detected by IACTs to become visible. For example, the distant FSRQ 3C 279 (z = 0.54), first seen by MAGIC in 2007 (Berger et al., 2009), normally undetected by IACTs, was observed by H.E.S.S during a very bright flare in 2015. The source was detected using $\sim$ 3 hours of observations during the flare (Romoli et al., 2017). The harder-when-brighter nature of blazar flares means that many blazars can potentially be detected by IACTs, provided that they are close enough to not be severely obscured by the Extragalactic Background Light (EBL). A more detailed understanding of blazars is therefore needed to predict which blazars are potential

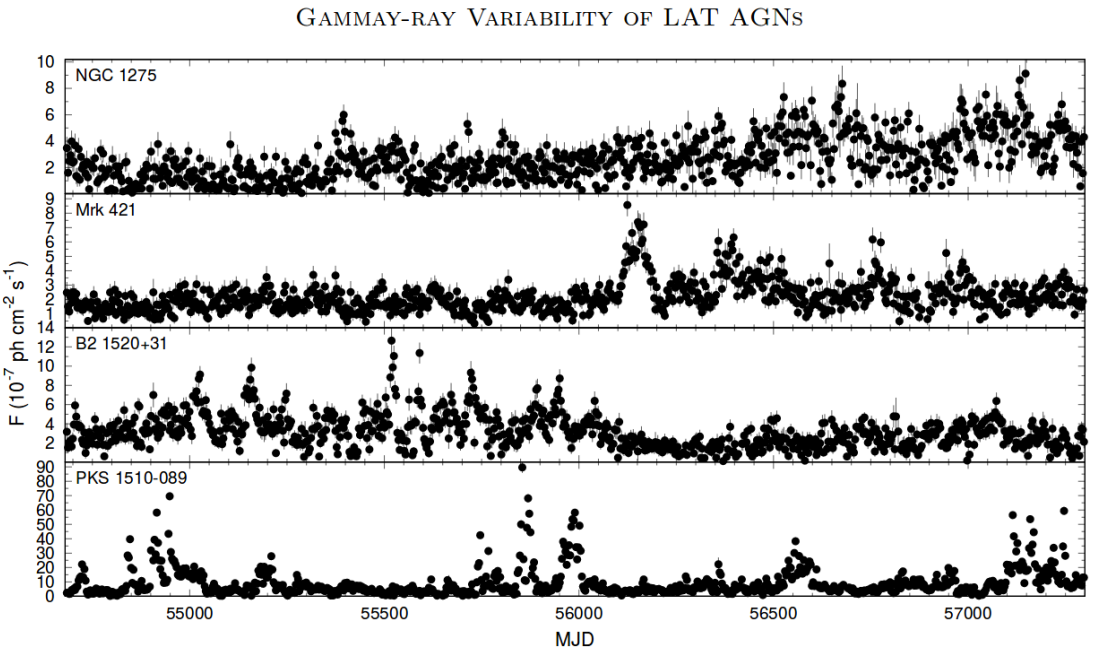

Figure 3.5: LAT 0.1-300GeV γ-ray light curves of NGC 1275, Mrk 421, B2 1520+31 and PKS 1510-089 showing the long-term variability displayed by AGN. Adopted from Kushwaha et al. (2017).

VHE emitters detectable by IACTs. An overview of our current understanding of blazar emission models is presented at the end of this chapter.

3.1.5 Using γ-rays to probe the Extragalactic Background Light

The detailed study of distant γ-ray sources is hindered by the presence of the EBL which attenuates the γ-ray emission ($\gtrsim$ 10 GeV) through $\gamma\gamma$ absorption. The EBL is comprised of the combined emission from all resolved and unresolved extragalactic sources, including all truly diffuse background sources, excluding the Cosmic Microwave Background (CMB). This attenuation of the γ-rays by the EBL alters the intrinsic γ-ray spectrum of distant blazars. Therefore, to study the emission from distant blazars requires an understanding of the EBL spectrum (see Dwek & Krennrich, 2013, for a recent review). Fig. 3.6 shows the spectrum of the EBL. The spectrum was obtained from direct observations of the EBL in the UV to far-infrared bands. The spectrum was fitted with a semi-analytical model, taking into account galaxy formation, evolution and reprocessing of starlight by dust (Gilmore et al., 2012).

The difficulty of directly measuring the EBL introduces large uncertainties,

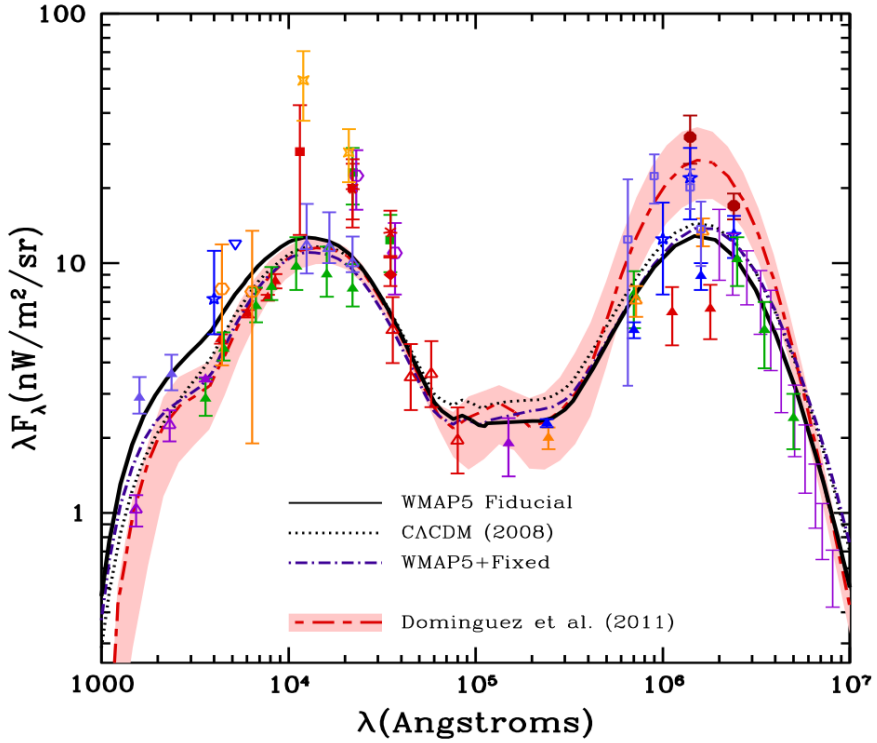

Figure 3.6: The predicted ($z = 0$) EBL spectrum, obtained from direct observations and model predictions. Adopted from Gilmore et al. (2012)

which cannot be easily resolved. Therefore, using γ-ray to indirectly measure the EBL through $\gamma\gamma$ absorption studies can place constraints on the EBL spectrum: extrapolating the $\lesssim$ 10 GeV power-law spectrum of distant blazars to 300 GeV allows the EBL absorption to be estimated, in effect measuring the EBL density between the distant blazar and Earth, assuming that the VHE spectrum is produced by the same population of particles responsible for the HE emission (see e.g. Armstrong et al., 2017).

Very different HE and VHE spectra are calculated from different EBL models for distant ($z > 1$) blazars (see e.g. Aleksić et al., 2014; Manganaro et al., 2016; Singh et al., 2014). Further, the choice of EBL can influence the redshift calculations made using VHE emission (see e.g. Abeysekara et al., 2017).

3.2 X-ray observations of blazars

X-ray emission from blazars is produced by both thermal accretion disc processes and non-thermal processes. While the X-ray emission produced by IC scattering of accretion disc photons is the dominant component in non-jetted AGN, the emis-

sion is dominated by the jet in jetted AGN. In LSP blazars, the origin of the X-ray emission is IC emission from the lowest energy particles in the jet, while in HSP blazars the X-ray emission is produced by the highest energy synchrotron emission. The better resolution from X-ray observations can be used in conjunction with radio and γ-ray emission to constrain the position of unidentified/unclassified blazars.

3.3 Optical observations of blazars

The UV, optical and Infrared (IR) emission from AGN provides essential clues to the physical processes taking place in the inner regions of AGN. UV emission gives insight into accretion processes, while the IR emission primarily provides information about the cold dusty torus surrounding the AGN. The optical to UV emission probes the accretion disc. In non-jetted AGN, this is the dominant contribution to the optical continuum from the AGN (e.g. Schneider, 2015, p. 223). The UV radiation ionizes the gas in the BLR and NLR, which gives rise to the broad and narrow optical emission lines from these regions. The strength of the BLR emission lines is an indication of the radiative cooling efficiency of the disc, while the Doppler broadening of the BLR emission can be used to calculate the mass of the SMBH.

In blazars, the synchrotron emission from the jet provides a significant amount of optical/UV emission which, in some cases, can dominate over the thermal emission. Optical emission from blazars will often display a non-thermal continuum with weak or absent emission lines. For example, the featureless spectrum of the BL Lac object PKS 1424+240 is shown in Fig. 3.7. One piece of evidence for the synchrotron origin of the emission is the presence of significant polarization in blazar spectra. Modelling the polarization can provide a means to disentangle the thermal emission from the non-thermal emission (see e.g. Böttcher et al., 2017).

Two different blazar classes can be distinguished based on their optical properties. FSRQs, which show strong emission lines with EW $\gtrsim$ 5Å and BL Lac objects which have weaker, EW $\lesssim$ 5Å, or no emission lines (Urry & Padovani, 1995). The difference in emission line strengths can be attributed to the nature of their accretion discs and BLR strength, which have consequences for the non-thermal emission produced by the blazars (see Fig. 3.2 and Chapter 2.2.2.2).

Blazars often show highly correlated multiwavelength variability, suggesting a single particle population is the origin of both the low energy and the high energy

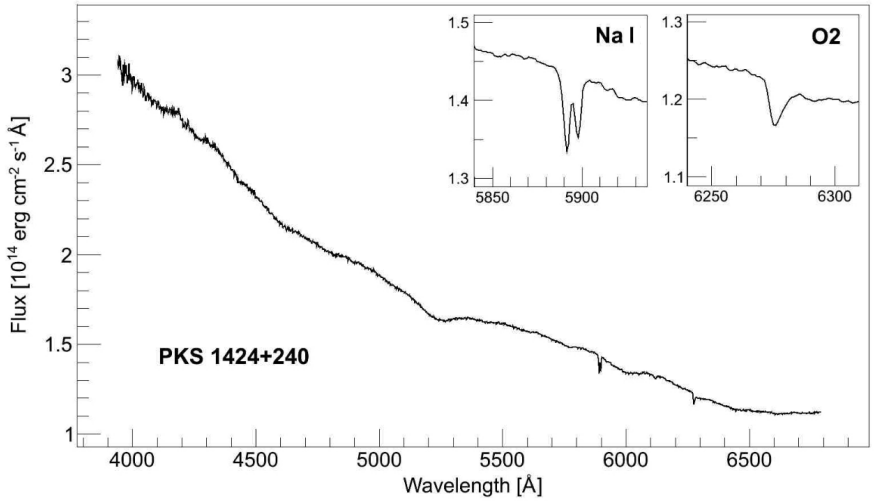

Figure 3.7: Optical spectrum of PKS 1424+240. The insets show the Galactic Sodium lines and the molecular Oxygen telluric absorption. The featureless BL Lac spectra prevents a redshift from being calculated. Adopted from Rovero et al. (2015)

emission. The variability is usually faster and more pronounced in the higher frequency tails of the low and high energy SED components, a result of the rapid particle cooling in the higher energy regimes (see e.g. Gupta et al., 2016).

3.3.1 Variability and long-term monitoring

Studying AGN variability provides insight into the location, size, structure, and dynamics of the non-thermal emitting regions (Ciprini et al., 2003). Using the variability timescale an upper limit for the size of the emitting region can be inferred from simple light travel time considerations. The variability is usually more pronounced for higher energies compared to lower energies, usually attributed to the shorter cooling timescales of the higher energy particles.

More advanced approaches can be used to analyse the properties of the variability and determine the size and origin of the optical emission. Goyal et al. (2017) was able to use 18 years of optical observations of PKS 0735+178, in conjunction with LAT data to constrain the radius of the jet at the emission region to $R_{\rm jet} \leq 0.03$ pc, with the emission emitted a distance of $R_{\rm core} \leq 1$ pc from the core. Similar methods were used to constrain the size and location of the emission regions for PKS 150-089 and BL Lacertae (Yan et al., 2017).

Blazars typically show significant variability over periods from hours (see e.g. Rani et al., 2011) to years (see e.g. Carnerero et al., 2017) in all wavelengths (see e.g. Castignani et al., 2017). Variability on the order of hours to a day is called

Intra-day Variability or microvariability (IDV, see e.g. Wagner & Witzel, 1995). Short-term Variability (STV) occurs on the order of days to a few months, while Long-term Variability (LTV) is variability lasting months to years. All blazars exhibit STV and LTV when viewed for a sufficiently long time. Gupta & Joshi (2005) found that $80 - 85\%$ of blazars show IDV when observed for longer than 6 hours.

Blazar monitoring on diverse timescales has revealed the trends of the different blazar classes. In general, High Synchrotron Peaked (HSP) BL Lacs exhibit less pronounced optical IDV than Low Synchrotron Peaked (LSP) BL Lacs and FSRQs (see e.g. Gaur et al., 2012a; Gupta et al., 2016). The highest electron energies present in HSPs and LSPs emit, via synchrotron emission, at different wavelengths: in LSPs at optical and IR wavelengths, while in HSPs, at X-ray energies. Gupta et al. (2016) examined 12 LSPs observed with the XMM-Newton and found that only $\sim 4\%$ showed true IDV in the X-ray energy band. Similarly Gaur et al. (2012a) examined 144 optical lightcurves of HSPs in the optical band and found that only $\sim 4\%$ exhibited IDV in optical wavelengths. These results suggest that the IDV originates from the highest energy electrons in the jet. If optical and X-ray IDV originated from the accretion disc, it would have been independent of the type of blazar.

Optical observations have revealed that STV and LTV are most likely caused by variations of the blazar jet, such as changes to the line-of-sight of the jet (see e.g. Raiteri et al., 2017) or emitting regions in the jet varying their orientation with respect to the line of sight (see e.g. Carnerero et al., 2017).

3.3.2 Spectroscopy

In AGN astronomy, optical spectroscopy provides a look into the inner regions of AGN, allowing the BLR, NLR and SMBH to be probed (Landt et al., 2017).

Studying how the BLR emission changes in relation to the continuum intensity is the basis of reverberation mapping. Measuring the time delays between continuum changes and the corresponding changes in the BLR after a time delay, can provide information about the morphology of the AGN emission regions (see e.g. Blandford & McKee, 1982). The reverberation mapping technique uses almost continuous spectroscopic observations of type I AGN lasting months to years (see e.g Peterson et al., 2004). Type I AGN are used for reverberation mapping campaigns since the inner regions of the AGN are visible to observers. Also, changes in the BLR happen over much shorter timescales than in the NLR (months-years vs.

decades), making Type I AGN attractive candidates for reverberation mapping campaigns. Over the last $\sim$ 30 years, reverberation mapping has been performed for $\sim$ 60 AGN. The results have been used to help constrain the SMBH mass and BLR geometry and kinematics. For instance, reverberation mapping has been used to derive a relationship between the Hβ emission line and 5100 Å continuum (see e.g. Bentz et al., 2013).

Spectroscopic observations of blazars can prove challenging, since the jet emission can overwhelm the AGN continuum and BLR emission. FSRQs are easier to study than BL Lacs, since they have a brighter emission region and so display emission lines from the BLR in their spectra.

Optical observations are also crucial for determining the redshift to blazars, a vital component for modelling their emission and for determing their observability with IACTs. Measuring the distance to FSRQs is a trivial process due to the presence of the emission lines in their spectra. The distance to BL Lacs, on the other hand, is sometimes impossible to measure due to the lack of any features in their spectra. However, the optical emission from the jet in some BL Lac objects do not completely overpower their host galaxies' thermal emission and they exhibit faint absorption lines from the host galaxy (see e.g. Álvarez Crespo et al., 2016).

3.3.3 Spectropolarimetry

Modern spectropolarimeters consist of a normal spectrograph in conjunction with polarizing optics to enable the measurement of the polarization state of the measured photons. Specifically, light entering the spectrograph first passes through one or two rotating waveplates, consisting of a birefringent crystal that alters the polarization state of light waves passing through it. Next, a prism consisting of one or more birefringent crystals, such as calcite or quartz, is used to separate the light into two orthogonally polarized beams, known as the extraordinary and ordinary polarization beams. The two polarized light beams are then directed towards the spectrograph grating or grism before being recorded by a CCD (see e.g. Kawabata et al., 1999). Rotating the polarizing waveplates changes the intensity of the ordinary and extraordinary polarized beams, which in turn allows the original polarized state of the incoming light to be reconstructed. A schematic diagram of a spectropolarimeter is shown in Fig. 3.8.

Spectroplarimetry provides a means to measure energy resolved polarization of astrophysical sources. Polarization measurements can provide insights into extrinsic effects such as reflection and scattering (see e.g. Goodrich, 1989; Hansen &

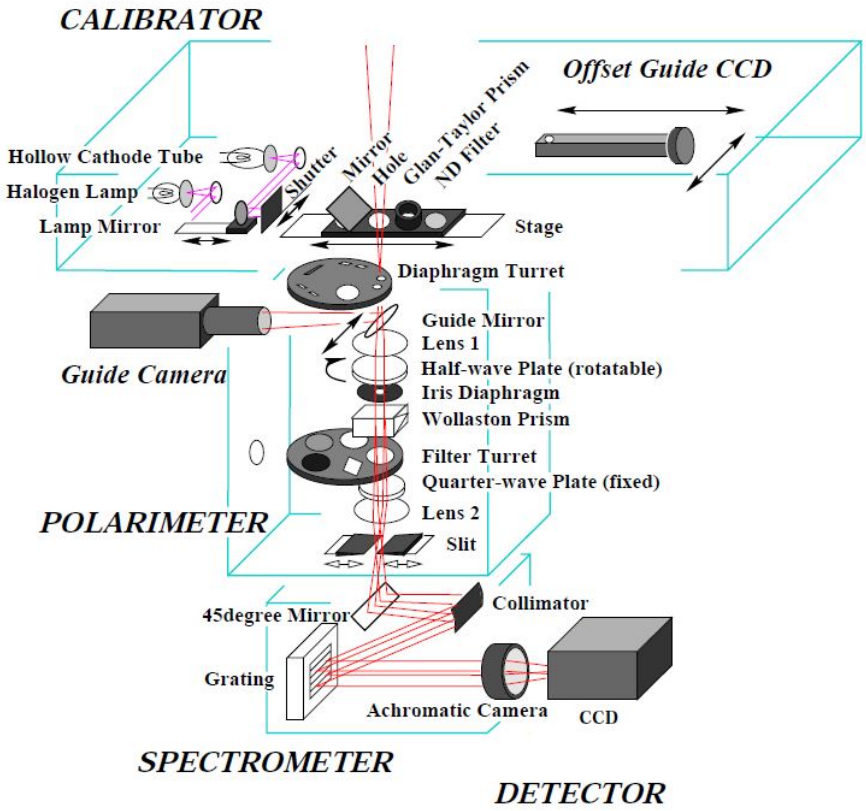

Figure 3.8: A schematic of a spectropolarimeter. The polarizing optics have been added to a normal spectrometer, thus enabling the spectrometer to function as a spectropolarimeter. Adopted from Kawabata et al. (1999).

Travis, 1974) or intrinsic effects such as the polarized radiation from synchrotron emission (see e.g. Rybicki & Lightman, 2008, Chapter 6). Spectropolarimetry is used to study the polarized emission from AGN, among other astrophysical sources, which is believed to be dominated by synchrotron emission in the optical regime (see e.g. Schmidt & Smith, 2000; Smith et al., 2011).

Different emission models are able to fit the same blazar SEDs, making it difficult to distinguish between them. However, since these models predict different polarization properties, this provides a possible method to differentiate them. Böttcher et al. (2017) measured the synchrotron contribution to the flux of 4C +01.02 during an optical outburst. The synchrotron model and thermal emission are fitted to the spectopolarimetry data during the 2016 November outburst and is shown in Fig. 3.9 and Appendix B. The emission consists of a stable unpolarized thermal component from the accretion disc and BLR and variable polarized non-thermal synchrotron emission produced by the relativistic jet. The increased polarization during flaring periods indicate that synchrotron emission is the origin

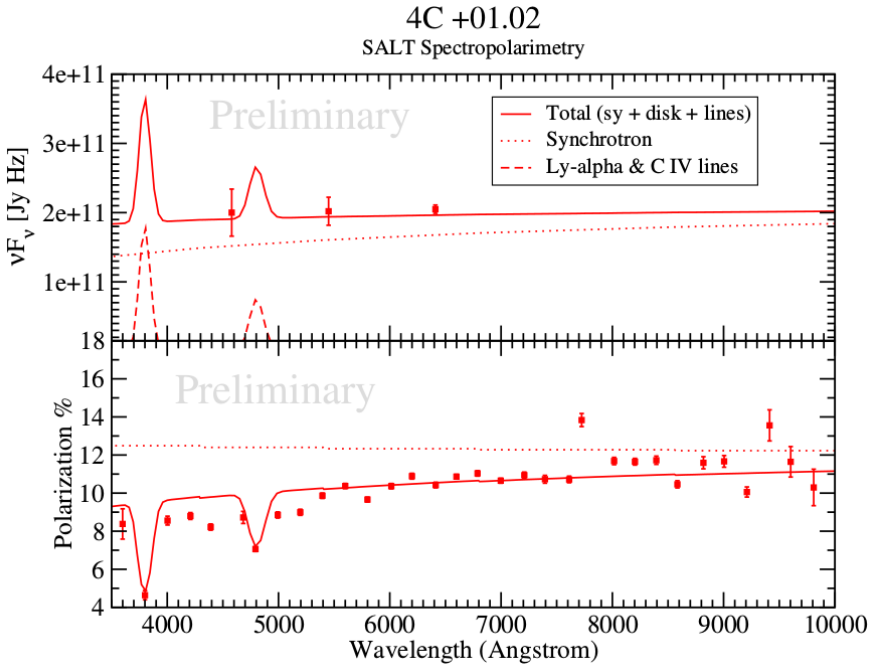

Figure 3.9: *Top Panel* SALT RSS optical spectrum of 4C +01.02 with 3 semi-contemporaneous LCO photometry (data points). *Bottom Panel*: SALT spectropolarimetry (data points) of 4C +01.02 along with a model prediction of the total polarization (solid red line), and the degree of polarization of the synchrotron radiation component (red dotted). Adopted from Böttcher et al. (2017).

of the increased optical flux and not the unpolarized thermal component (see e.g. Smith et al., 2011).

3.4 Radio observations of blazars

The extragalactic radio sky is dominated by Star Forming Galaxies (SFG), and AGN. While the radio emission from SFGs is produced mostly by supernova remnants, the radio emission originating from AGN is produced by the relativistic jets (see e.g. Condon, 1992; Miley, 1980). The non-thermal synchrotron emission typically follows a power-law in the form of $S_\nu \propto \nu^{-\alpha}$, where S_ν is the flux density, usually expressed in Jy or mJy, ν is the frequency and α the spectral index. Based on their radio spectra, AGN can be divided into steep spectrum ($\alpha < 0.5$) and flat spectrum ($\alpha > 0.5$) radio sources. FSRQs and BL Lacs belong to the flat spectrum source class, which tend to also be compact radio objects, with most of the radio emission originating near the AGN core (see e.g. Kimball & Ivezić, 2008).

Very Long Baseline Array (VLBA) observations are capable of resolving parsec

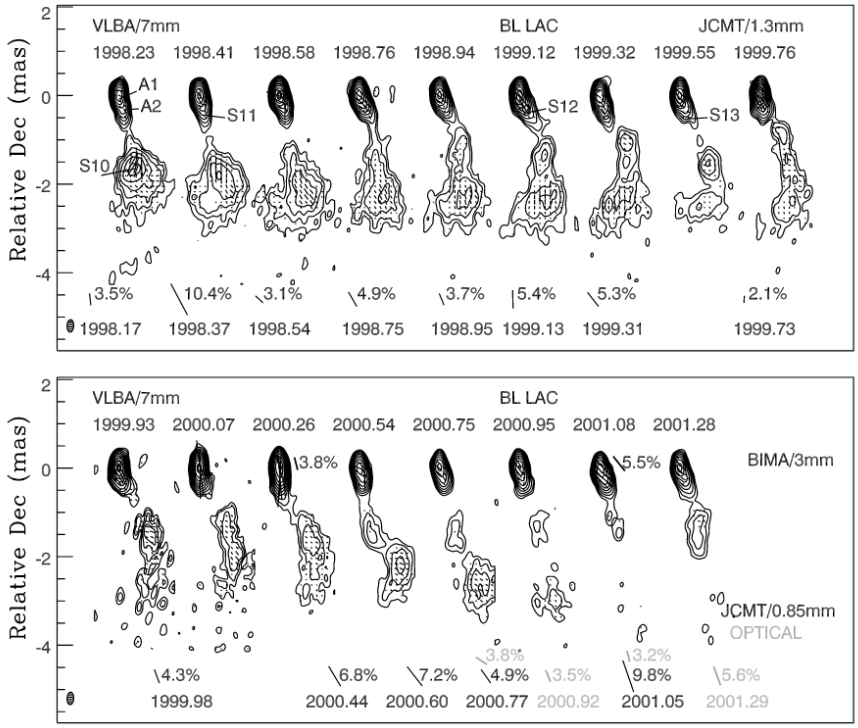

Figure 3.10: VLBA images of BL Lacertae at 43 GHz and polarization measurements at 7, 3, and 1.3/0.85 mm and optical wavelengths. Adopted from Jorstad et al. (2005).

scale structures and providing insights into AGN jet formation and evolution. This can trace events such as large injections of new particles in the form of knots into the jet. The ejection of radio knots is usually accompanied by radio flares. The evolution of the light curves of radio flares suggests that the flux variability is controlled by light-travel delays across the shocked region (see e.g. Sokolov et al., 2004). Radio images of AGN jets show stationary and moving knots. The stationary knots remain at a constant separation from the core. The stationary knots seen in radio images can be interpreted as standing shocks or re-collimation shocks, while the moving knots can be interpreted as traveling shocks in the jet (see e.g. Daly & Marscher, 1988). These knots are regions where particles are accelerated and can lead to emission across the electromagnetic spectrum.

Long-term VLBA studies have shown that the radio jets from blazars can change significantly on short timescales, with radio blobs forming and dissipating in a few years. VLBA 43 GHz radio images of BL Lacertae are shown in Fig. 3.10, illustrating the highly variable nature of the radio jet, with new radio knots launching and dissipating in the span of 3 years.

A consequence of the small viewing angle of blazar jets is the strong relativistic boosting and apparent superluminal velocities associated with the relativistic

jets, which allows us to study changes that could normally only be observed on timescales of decades and centuries for non-boosted sources. As such, VLBA studies of the FSRQ PKS 1510-089 shows two stationary features, one of which shifts downstream when a moving knot approaches and shifts back when the knot has passed. Such behaviour has been demonstrated for stationary shocks in computational simulations of relativistic jets (see e.g. Aloy et al., 2003).

3.5 Multi-wavelength modelling of blazars

In order to connect the multitude of multi-wavelength data gathered from a source with physical processes driving the emission, modelling of the multi-wavelength data is essential. As previously mentioned (see Chapter 2.2.2.2), SEDs of blazars consist of two broad components, a low energy component produced by synchrotron emission, and a high energy component, thought to be produced either leptonic or hadronic processes.

In the leptonic scenario, the HE and VHE emission is often described by a one-zone synchrotron self-compton (SSC) model, where the γ-ray emission is the result of the upscattering of the synchrotron photons by the same electron population that produces them, or by the External Compton (EC) model, where the γ-ray emission is the result of the upscattering of photons which originate externally to the jet (e.g. from the accretion disc or BLR). The leptonic model can be used to explain the blazar sequence (Fig. 3.2), where the choice between the two models depend on the strength of the accretion disk, BLR emission and the subsequent electron cooling rate (see e.g. Ghisellini et al., 1998). In hadronic models, the HE and VHE emission is produced by proton synchrotron, π^0 decay, synchrotron and IC emission from charged pion decay products and emission from pair cascades initiated by high energy photons absorbed by $\gamma\gamma$ pair production. Both leptonic and hadronic models can fit the emission, but very different jet conditions are required (see e.g. Abdo et al., 2011; Böttcher, 2007; Böttcher et al., 2009, 2013; Cerruti et al., 2011).

For example, Abdo et al. (2011) modelled Mrk 421 using both a leptonic SSC and a hadronic model (Fig. 3.11). Both models fit the SED reasonably well, although the parameters describing the jet are very different. The hadronic model requires that the particle energy density is about a factor of ~ 5 higher than the magnetic field energy density, while in the SSC model the electron energy density dominates that of the magnetic field by a factor of 10. For Mrk 421, with a SMBH

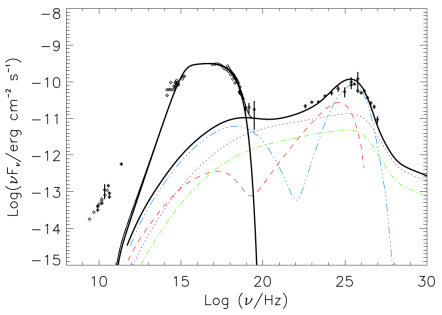

(a) SED of Mrk 421 with a hadronic model fit. The components of the fit are: π^0-cascade (dotted line), $\pi^{\pm}$ cascade (dashed dotted line, ν-synchrotron and cascade (dashed-triple-dotted line), proton synchrotron and cascade (dashed line)) and sum of all the emission components, including synchrotron emission from the primary electrons (solid line).

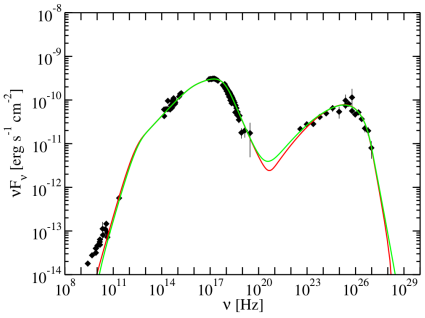

(b) SED of Mrk 421 with two 1-zone SSC model fits with different minimum variability timescales: $t_{\rm var} = 1$ day (red curve) and $t_{\rm var} = 1$ hour (green curve).

Figure 3.11: Hadronic and Leptonic SSC model fits for MRK 421. Adopted from Abdo et al. (2011).

with mass $\sim 2 \times 10^8$ $M_\odot$, the hadronic model predicts the emitting region has a radius $R_{\rm emit} = 4 \times 10^{14}$ cm, which is comparable to the gravitational radius of the SMBH, $R_g \approx 0.5 - 2.0 \times 10^{14}$ cm. This small emission region has a dense synchrotron photon energy density, which softens the spectrum below 100 MeV through reprocessing of the HE emission. On the other hand, using the variability timescale of $t_{\rm var} \sim 1$ day, the leptonic SSC model predicts an emitting region much larger than the gravitational radius, $R_{\rm emit} \gtrsim 10^3 - 10^4 R_g$.

The model degeneracy can be overcome by modelling the emission using multiple approaches, i.e. modelling the emission using time-dependent models, (e.g. Böttcher, 2010), or including polarization at HE and VHE in the modelling (e.g. Zhang & Böttcher, 2013; Zhang et al., 2014). Polarization measurements of HE emission can be used to directly discern between hadronic and leptonic emission. HE leptonic emission is expected to be unpolarized, making a positive polarization measurement in the HE bands a sure sign that the HE and VHE is caused by hadronic processes instead of leptonic ones. Fig. 3.12 shows the simulated leptonic and hadronic polarization signatures of the FSRQ 3C 279. Unfortunately, *Fermi*-LAT does not provide polarization data, but see Giomi et al. (2017) for a discussion of this possibility.

In order for emission models to work, the emitting particles need to be constrained to the emitting region, i.e. the jet. This poses almost no problem for

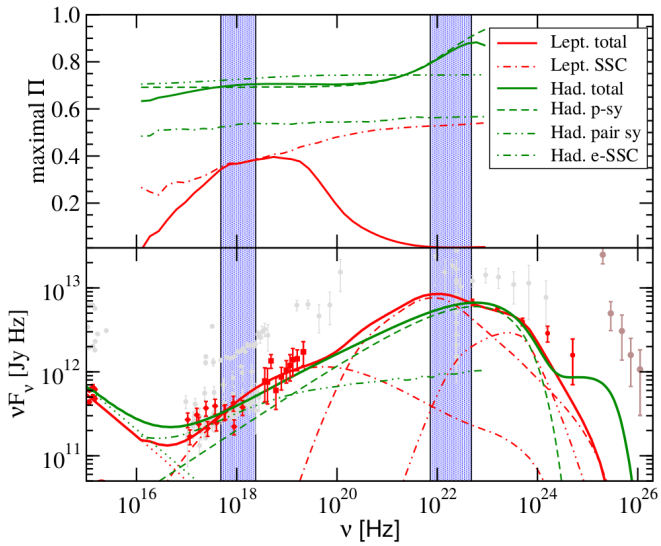

Figure 3.12: UV through γ-ray SED (lower panel) and expected maximal degree of polarization (upper panel) of the FSRQ 3C 279. The HE polarization expected from leptonic (red) and hadronic (green) models are plotted against frequency. The shaded areas, $2-10$ keV and $30-300$ MeV, indicate the energies where the X-ray polarimeters and LAT are sensitive. Adopted from Zhang & Böttcher (2013).

leptonic models, which require small magnetic field strengths ($B \lesssim 1$ G) in order to constrain the electron's Larmor radius to be small enough to trap the electrons inside the emitting region. In hadronic models, on the other hand, the HE emission is produced primarily by proton synchrotron emission. This requires that the magnetic field strength reach values of $B > 10$ G (see e.g. Abdo et al., 2011; Böttcher, 2010).

In order to test model results against actual blazars, a large sample of blazars are needed. In order to increase the sample size, I undertook a campaign to optically classify a selection of unclassified and unassociated blazar candidates detected by the LAT telescope. The selection criteria used for my campaign is presented in Chapter 4.

Chapter 4

Selection of γ-ray sources for optical follow-up

The launch of *Fermi* opened up a new avenue to search for very high energy (VHE) emitting objects beyond our galaxy. VHE emitting blazars are a rare class of radio loud AGN whose emission extends beyond 1 TeV and provides a laboratory to examine the most energetic processes in the known universe. The all-sky γ-ray survey undertaken by the LAT has resulted in a number of γ-ray catalogues in the energy range between 100 MeV and 300 GeV. These catalogues are subdivided into general γ-ray catalogues such as the Fermi Large Area Telescope Third Source Catalogue (3FGL) (Acero et al., 2015) and high energy catalogues, such as the Second and Third Catalogues of Hard LAT Sources (2FHL and 3FHL) (Ackermann et al., 2016; Ajello et al., 2017). A few source specific catalogues also exist, such as the Third Catalogue of Active Galactic Nuclei Detected by the LAT (3LAC Ackermann et al., 2015).

The 2FHL lists 360 detected above 50 GeV utilizing the first 80 months of LAT data. The catalogue contains 271 AGN and AGN candidates, with 60 listed as Blazar Candidate of Uncertain type (BCU). These are sources that do not have a published high-quality optical spectrum necessary to determine a redshift or classification. There are also 48 sources with no association at other wavelengths. At the time of publishing the 2FHL, only 25% of the 2FHL sources were detected in VHE, implying a reservoir of very high energy candidates (Ackermann et al., 2016). The 3FHL catalogue utilizes the first 7 years of LAT data and lists 1556 objects detected above 10 GeV. It includes 937 classified AGN and 290 BCUs. The larger amount of data and broader energy range allowed more sources with better resolution to be included in the catalogue (Ajello et al., 2017).

The 3LAC catalogue is an extension of the 3FGL and contains 1591 high galactic latitude ($|b| > 10^{\circ}$) AGN detected between 100 MeV and 300 GeV. Of the 1951 detected AGN and AGN candidates, 460 are listed as BCUs with no confident redshift or classification (Ackermann et al., 2015). The *Fermi* catalogues provide important resources to study the blazar population and their γ-ray properties. The catalogues also provide important resources to search for new and novel TeV blazars that can be studied with IACTs.

This study consists of two parts, the first is a long-term photometric study of known TeV blazars in order to examine their short-term and long-term variability, using the Watcher Robotic Telescope. The second involves spectroscopic observations with the South African Astronomical Observatory (SAAO) 1.9-m Cassegrain Spectrograph (SpUpNIC) of *Fermi* 3FHL and 3FGL unclassified and unassociated blazars in order to determine their class and redshift. Further, a sub-sample of the *Fermi* blazars were selected for follow-up optical photometry with SAAO Sutherland High-speed Optical Camera (SHOC) in order to measure their intra-night variability. This chapter will present the criteria used to select the sources used in this study. Section 4.1 will list the criteria used to select the known TeV blazars that are currently being observed by the Watcher Robotic Telescope. Section 4.2 will present the criteria used to select sources studied with the SAAO 1.9-m spectrograph and the 1.0-m SHOC photometer.

4.1 Selection of TeV blazars observed with the Watcher robotic telescope

The Watcher Robotic Telescope, a 16 inch (40 cm) Casssegrain reflector located at the Boyden Observatory, South Africa, has been observing Southern TeV detected blazars periodically as part of a long-term observing campaign underway since 2014. Sources that have been detected by H.E.S.S., with an upper magnitude limit of $V_{mag} < 18$ mag are currently being observed. These sources are listed in Table 4.1

Table 4.1: List of Watcher monitored sources analyzed during this project.

Name[a]	Class[b]	Ra[c] hh:mm:ss	Dec[c] dd:mm:ss	z[d]	Syn_{pk}[e] Hz	Mag[f] V
SHBL J001355.9-185406	BLL	00 13 56.1	-18 54 06.7	0.095	5.26E+16	
KUV 00311-1938	BLL	00 33 34.4	-19 21 33.1	0.61	8.32E+15	16.3
RGB J0152+017	BLL	01 52 39.6	+01 47 17.4	0.08	2.66E+15	15.12
PKS 0301-243	BLL	03 03 26.5	-24 07 11.5	0.266	2.06E+15	16.18
PKS 0447-439	BLL	04 49 24.7	-43 50 08.9	0.205	3.89E+15	15.24
1RXS J101015.9-311909	BLL	10 10 16.0	-31 19 08.4	0.143	1.78E+16	
1ES 1101-232	BLL	11 03 37.6	-23 29 31.1	0.186	1.32E+17	16.55
3C 279	FSRQ	12 56 11.2	-05 47 21.5	0.536	8.32E+12	17.75
1ES 1312-423	BLL /BCU	13 15 03.4	-42 36 49.7	0.105	1.91E+16	16.6
PKS 1510-089	FSRQ	15 12 50.5	-09 05 59.8	0.36	3.67E+13	16.54
AP Librae	BLL	15 17 41.8	-24 22 19.5	0.048	1.46E+14	14
PG 1553+113	BLL	15 55 43.0	+11 11 24.4	0.36	2.93E+15	14.57
PKS 2005-489	BLL	20 09 25.4	-48 49 53.7	0.071	1.81E+16	12.81
PKS 2155-304	BLL	21 58 52.1	-30 13 32.1	0.116	8.32E+15	13.09

[a] Name of the Source, from different catalogues
[b] Blazar class. Described in the *Fermi* 3LAC catalogue
[c] Optical coordinates of the source in J2000
[d] Measured redshift of the source
[e] Redshift-corrected Synchrotron peak frequency
[f] Visual magnitude of the optical source

4.2 Selection of *Fermi* blazars for spectroscopic classification

The low resolution of the LAT requires broadband data in order to constrain the position of the γ-ray sources. This study utilized multiple *Fermi* catalogues (3LAC, 3FGL, & 3FHL) in order to classify blazars from the unassociated and unclassified extragalactic γ-ray sources listed in these catalogues. The criteria used to select sources during this study are mostly identical, therefore, the listed criteria include all the LAT catalogues used in this study, except where mentioned. The selection criteria are summarized below.

High galactic latitude sources: Only sources that are located at high Galactic latitudes ($|b| > 10^{\circ}$) were selected.

Observability: Only sources observable from South African telescopes were included in this study.

Photon Spectral index: The blazars listed in the *Fermi* catalogues which have γ-ray photon indexes $1.2 \lesssim \Gamma \lesssim 3$. The blazars listed in the 3FHL catalogue have hard γ-ray photon indexes, extending their emission to higher energies than the blazars with softer γ-ray photon indexes, which suggest that the emission could extend up to VHE energies. I selected sources with the $\Gamma < 2.6$ for 3FHL sources and $\Gamma < 2.2$ for 3FGL sources.

Classification: I selected sources that were listed as BCU in the LAT catalogues, with no later classification or redshift measurements, thus ensuring that already classified blazars were not observed. The selection criteria used for sources from the 3FHL also included sources with no association at other wavelengths.

Potential multi-wavelength counterparts: I selected potential optical counterparts that were located within the 95% error circles of the 2FHL and 3FGL catalogues. The Wide-field Infrared Survey Explorer (WISE) is a NASA Medium Class Explorer mission that performs all-sky mid infrared observations (2009 - present; Wright et al., 2010). An extended WISE catalogue, the ALLWISE catalogue, extends the original catalogue, with increased data and improved analysis (Cutri & et al., 2014). The selected counterparts included sources with ALLWISE infrared colours representative of blazars (see e.g. D'Abrusco et al., 2012, and Section 4.2.4) and radio/X-ray sources inside the error circles.

Based on the above criteria, I initially selected 58 blazar candidates from the different LAT catalogues considered. However, due to observing time constraints, 31 of the sources were observed. Below, I expand on the criteria used and motivate the chosen limits.

4.2.1 Observability

The source density in the Galactic plane is high and diffuse background emission is present. The likelihood of detecting extragalctic sources rises sharply away from the Galactic plane. Therefore, I limited the search for candidates to sources away from the Galactic plane, namely sources with high galactic latitude $|b| > 10^{\circ}$. This is the same constraint used in the *Fermi*-LAT AGN catalogues.

The observing campaign was carried out from the SAAO Sutherland observatory with the 1.9-m and 1.0-m telescopes, which have declination limits of $-90^{\circ} \leqslant \delta < +20^{\circ}$. The aim of the study was to classify γ-ray emitting blazars that could potentially be observed by southern latitude IACTs, such as the H.E.S.S. telescopes in Namibia (16°30′00″E, 23°16′18″S) and the upcoming CTA South in Chile (70°18′58.8″W, 24°41′00″S). I, therefore, only chose sources that could be viewed from southern latitudes.

All of the sources considered are optically faint, so I applied an upper magnitude limit of $V_{mag} < 20$ mag, as taken from the Naval Observatory Merged Astrometric Dataset (NOMAD). The NOMAD database makes use of data derived from the Hipparcos, Tycho-2, UCAC2, and USNO-B catalogues and is supplemented by

2MASS near-infrared photometry. Making use of the NOMAD magnitudes, originating from different surveys published at different times, as absolute indicators is difficult for highly variable objects such as AGN. Therefore, I only used the NOMAD magnitudes as a guide when more recent magnitudes were not available.

4.2.2 Photon spectral index

The 3FHL list blazars with photon spectral index distributions between $\sim 1.2 - 6.8$. The blazars with harder, i.e. lower photon indices, will have stronger γ-ray emission at higher energies, potentially extending to energies that can be observed by IACTs. Therefore, to find blazars that can potentially be observed by IACTs, I selected blazars from the different catalogues considered that have γ-ray photon indexes below $\Gamma \sim 2.6$.

4.2.3 Blazar classification

I selected unclassified LAT blazars in the 3LAC, 3FGL and 3FHL catalogues. The SIMBAD Astronomical Database[1] and NASA/IPAC Extragalactic Database[2] (NED) were used to confirm the BCU positions and that they did not have published classifications and redshift measurements.[3]

4.2.4 Potential multi-wavelength counterparts

Synchrotron emission indicates that a population of HE and VHE electrons are present. Therefore, to constrain the optical positions of the selected LAT blazars, I used the NED and SIMBAD databases to search for radio and X-ray sources inside the LAT position error circles, since it is expected that the γ-ray sources will also be bright in radio and X-ray. If the radio and X-ray sources are spatially coincident, there is a high probability that the emission originates from the same source and I therefore included the optical source coincident to the radio/X-ray source in the observations. Some of the sources I selected did not have any obvious counterparts inside the LAT error circles, in which case I selected multiple candidates, i.e. sources inside or near the LAT error circles with multiwavelength counterparts.

The search for radio counterparts were done using the 1.4GHz NRAO VLA Sky Survey (NVSS Condon et al., 1998), the Sydney University Molonglo Sky Survey

[1] `http://simbad.u-strasbg.fr/simbad/`
[2] `https://ned.ipac.caltech.edu/`
[3] During an extensive literature search during the final analysis I found that the 3FGL counterpart to 3FHL 0305.2-1609 was already classified.

(SUMSS Mauch et al., 2003), the Parkes-MIT-NRAO (PMN Wright et al., 1994) and the Parkes Radio Sources (PKS Wright & Otrupcek, 1990) Catalogues.

The X-ray catalogues included the ROSAT All-Sky Bright Source Catalogue (1RXS Voges et al., 1999), the Second ROSAT all-sky survey (2RXS Boller et al., 2016), the ROSAT all-sky survey faint source catalogue (RASS Voges et al., 2000), the ROSAT Bright Survey (RBS Fischer et al., 1998) and the Swift X-ray telescope point source catalogue (1SXPS Evans et al., 2013).

To further constrain the optical position of the LAT blazars, I also searched for sources whose ALLWISE colours were the same as those found inside the so-called blazar strip. D'Abrusco et al. (2012) showed, using all the LAT detected ROMA-BZCAT[4] blazars with an ALLWISE detection, that γ-ray-loud blazars inhabit a small and well defined region in the ALLWISE colour-space. The blazar-strip is a direct result of the non-thermally dominated emission. I used the ALLWISE [3.4]-[4.6]-[12] μm colour-space to select candidates that were inside the blazar strip. A colour-colour diagram indicating where the selected blazars lie in the ALLWISE colour space is presented in Fig. 4.1.

Many of these potential counterparts were low Signal-to-Noise Ratio (S/N) sources in the ALLWISE data and were not located on optically detectable sources. I, therefore, further constrained the candidates to ALLWISE sources that coincided with optically detectable sources with magnitudes brighter than an upper magnitude limit of $V_{mag} < 20$ mag. If these candidates were coincident with radio/X-ray sources, I selected them as probable candidates for observation. For two sources, 3FHL J0813.7-0353 and 3FHL J1212.1-2328, the most probable counterpart was too faint to be detected during the observation campaign. For these two sources, I therefore, observed secondary candidate sources to exclude their association. 3FHL J0813.7-0353 was constrained to 5 optical candidates in the blazar strip, of which two were also coincident with radio sources inside and near the the LAT error circle, but the optical counterpart coincident with the radio source inside the error circle was not detected during observations. I therefore included the other 4 detected ALLWISE sources in the observations to exclude them from possible association. I limited the other source, 3FHL J1212.1-2328, to 2 candidates, one outside the LAT error circle, the other inside. The candidate inside the LAT error circle was too faint to observe, so I was only able to observe the less likely candidate to exclude a potential association.

[4]http://www.asdc.asi.it/bzcat/

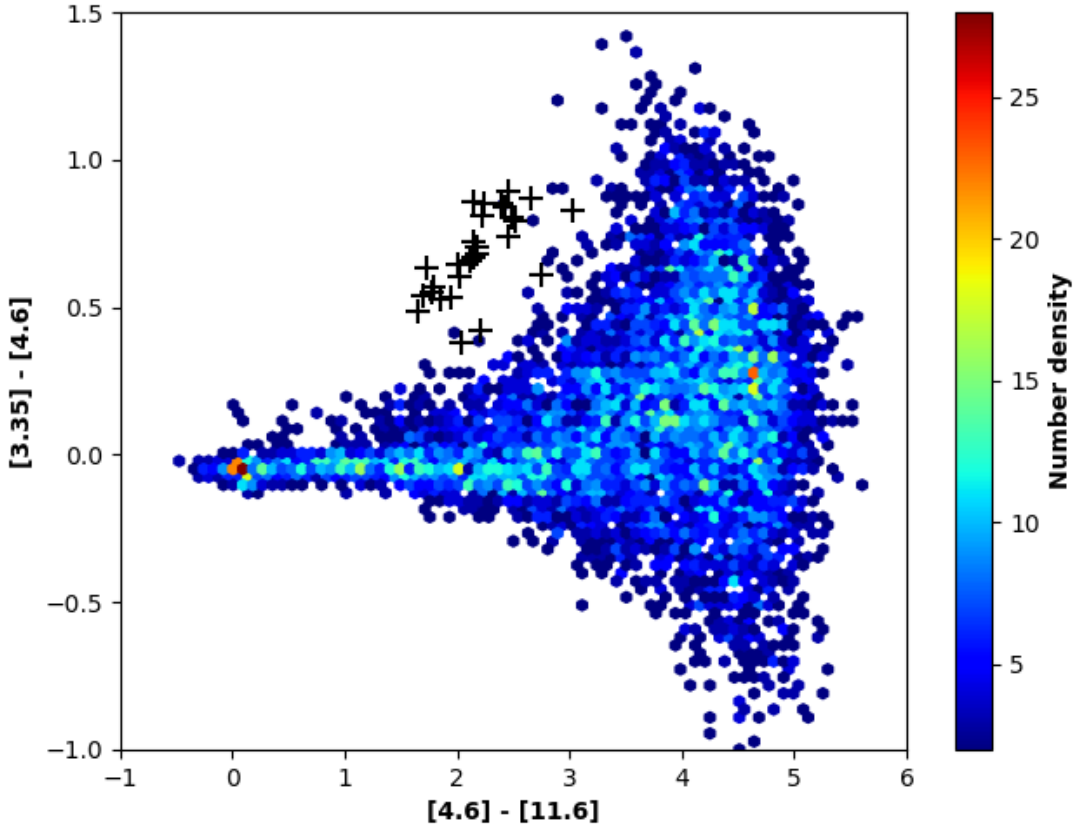

Figure 4.1: The ALLWISE $2.35-4.6$ μm versus $4.6-11.6$ μm colour diagram indicating where the selected blazars (crosses) lie in the ALLWISE colour sapce.

4.3 Selected blazar candidate sources

From the *Fermi*-3FHL and 3FGL catalogues a subset of sources was selected for spectroscopic observations. The candidate 3FHL and 3FGL sources are listed in Tab 4.2 and Tab 4.3 respectively. The tables list their various properties from the respective catalogues on which the selection was based. These include the source type, integral γ-ray flux, γ-ray photon index (SpI), Synchrotron peak frequency ($\mathrm{Sy_{Peak}}$) and association at other wavelengths listed in the catalogues. All the 3FHL sources, except 3FHL J0813.7-0353 are listed as BCUs. Also, all the 3FGL sources are listed as BCUs, however, four of the sources lack an association at other wavelengths.

All sources observed lacked a classification and redshift measurement during the source selection, except for 3FHL J0305.2-1609. During the final analysis it was found that the 3FGL counterpart of 3FHL J0305.2-1609, 3FGL J0305.2-1607, was observed by Paiano et al. (2017) and classified as a BL Lac.

Multiple radio sources and no overlapping X-ray sources were present in the

Table 4.2: Twelve blazar candidates selected among the *Fermi* 3FHL sources.

3FHL name[a]	RA[b] hh:mm:ss	Dec[b] dd:mm:ss	Class[c]	Flux[d] 10^{-12} erg cm^{-2} s^{-1}	SpI[e] Γ	Sy_{Peak}[f] log Hz	Assoc[g]
J0001.9-4155	00:01:33	-41:55:25	bcu	3.49 ± 1.83	1.94	15.80	1RXS J000135.5-415519
J0002.1-6728	00:02:15	-67:26:53	bcu	2.31 ± 0.96	2.43	15.65	SUMSS J000215-672653
J0003.3-5248	00:03:20	-52:47:27	bcu	2.29 ± 1.11	2.25	16.85	RBS 0006
J0115.9-2746	01:15:55	-27:44:32	bcu	1.63 ± 1.21	2.03		1RXS J011555.6-274428
J0305.2-1609	03:05:15	-16:08:18	bcu	2.22 ± 1.13	2.41	15.57	PKS 0302-16
J0647.0-5138	06:47:10	-51:35:46	bcu	1.54 ± 0.95	2.26	16.45	1ES 0646-515
J0813.7-0353	08:13:38	-03:57:17		2.48 ± 1.65	1.93		
J0935.2-1735	09:35:15	-17:36:59	bcu	2.70 ± 1.25	2.39		NVSS J093514-173658
J1042.2-4128	10:42:03	-41:29:30	bcu	1.55 ± 0.94	2.27	15.35	1RXS J104204.1-412936
J1130.5-7801	11:30:32	-78:01:05	bcu	7.54 ± 2.3	2.02		SUMSS J113032-780105
J1212.1-2328	12:11:50	-23:32:26	bcu	1.54 ± 0.85	2.6	15.16	PMN J1212-2327
J1223.5-3033	12:23:37	-30:32:50	bcu	2.10 ± 1.28	2.03	15.95	NVSS J122337-303246

[a] Name of the Source (3FHL)
[b] Optical coordinates of the source in J2000
[c] γ-ray source class
[d] Integral γ-ray photon flux obtained with spectral fitting
[e] γ-ray photon index
[f] Synchrotron peak frequency
[g] Association with source at other wavelengths

Table 4.3: Eleven blazar candidates selected among the *Fermi* 3FGL sources.

3FHL name[a]	RA[b] hh:mm:ss	Dec[b] dd:mm:ss	Class[c]	Flux[d] 10^{-12} erg cm^{-2} s^{-1}	SpI[e] Γ	Sy_{Peak}[f] log Hz	Assoc[g]
J0051.2-6241	00:51:16	-62:42:04	bcu	16.5 ± 1.7		15.90	1RXS J005117.7-624154
J0256.3+0335	02:56:28	+03:33:31	bcu	4.0 ± 1.0		15.62	PKS B0253+033
J1344.5-3655	13:44:24	-36:56:28	bcu	4.4 ± 1.0	2.18		
J1406.0-2508	14:06:10	-25:08:10	bcu	6.7 ± 1.1	1.89		1FHL J1406.3-2509
J1507.6-3710	15:07:21	-37:09:03	bcu	4.9 ± 1.0	2.13		
J1842.3-5841	18:42:30	-58:41:57	bcu	6.4 ± 1.1		16.48	1RXS J184230.6-584202
J1855.1-6008	18:54:52	-60:09:23	bcu	2.3 ± 0.7	1.81		
J1944.1-4523	19:44:22	-45:23:27	bcu	2.5 ± 0.9	1.56		
J1954.9-5640	19:55:03	-56:40:28	bcu	5.3 ± 1.0	1.88		2FGL J1955.0-5639
J1959.8-4725	19:59:46	-47:25:19	bcu	11.1 ± 1.4	1.81		2FGL J1959.9-4727
J2338.7-7401	23:39:21	-74:04:36	bcu	6.3 ± 1.0		16.20	1RXS J233919.8-740439

[a] Name of the Source (3FHL)
[b] Optical coordinates of the source in J2000
[c] γ-ray source class
[d] Integral γ-ray photon flux obtained with spectral fitting
[e] γ-ray photon index
[f] Synchrotron peak frequency
[g] Association with source at other wavelengths

error regions of 3FGL J1507.6-3710 and 3FHL J0935.2-1735. I, therefore, observed the only optical counterpart located inside the radio error regions for these two sources. In the case 3FGL J2338.7-7401, a 3LAC source, the most likely optical counterpart was located just outside the 3FGL error region, but inside the 3FHL error circle, with a coincident radio and X-ray counterpart.

3FHL J0647.0-5138 has radio and X-ray counterparts just outside the 3FHL error circle, with multiple optical sources inside the radio error regions. I, therefore observed the optical source inside the X-ray error region, which is more localized than the radio error region.

There were five optical candidates for J0813.7-0353, with two coincident radio sources, one inside the 3FHL error circle, the other outside. Both of the radio sources coincided with optical candidates. The optical candidate coinciding with

Table 4.4: Six blazar candidates among the selected *Fermi* 3FHL sources observed with the SAAO 1.0-m SHOC instrument

3FHL name[a]	RA[b] hh:mm:ss	Dec[b] dd:mm:ss	b[c] deg	θ_{95}[d] deg	Class[e]	SpI[f] Γ	Sy_{Peak}[g] log Hz	Assoc[h]
J0802.2-0943	08 02 15.71	-09 43 01.70	10.94	0.0396	bcu	2.48		NVSS J080216-094215
J0813.7-0353	08 13 46.48	-03 53 57.22	16.33	0.0567		1.93		
J0953.3-7659	09 53 23.60	-76 59 35.58	-17.54	0.0527	bcu	2.23	14.92	1RXS J095306.1-765755
J1042.2-4128	10 42 12.64	-41 28 08.58	15.17	0.0399	bcu	2.27	15.35	1RXS J104204.1-412936
J1130.5-7801	11 30 35.69	-78 01 33.52	-15.83	0.0217	bcu	2.02		SUMSS J113032-780105
J1223.5-3033	12 23 35.71	-30 33 34.64	31.93	0.035	bcu	2.03	15.95	NVSS J122337-303246

[a] Name of the Source (3FHL)
[b] Optical coordinates of the source in J2000
[c] Galactic latitude
[d] Radius of 95% error circle (degrees)
[e] γ-ray source class
[f] γ-ray photon index
[g] Synchrotron peak frequency
[h] Association with sources at other wavelengths

the radio source inside the 3FHL was to faint to observe. Therefore, I observed the other four optical candidates to exclude them from the association. In order to select the most probable optical counterpart for the 3FHL and 3FGL sources I constructed finder charts indicating the radio (green ellipses) and X-ray (black ellipses) sources within 7.5 arcmin of the 3FHL (dashed red circles) and 3FGL (dashed blue ellipses) coordinates. The optical coordinates of the observed source are indicated by the crosses. The finder charts are shown in Fig 4.2.

4.4 Selection of *Fermi* blazars for photometric observation

During the observing campaign in February/March 2017, I selected a subset of the 3FHL sources I was observing with SpUpNIC and observed them with the SHOC camera on the 1.0-m telescope in order to search for variability and to aid in the identification of the unassociated 3FHL source and study their IDV. Therefore, they used the same selection criteria as the sources observed with SpUpNIC. The sources are listed in Tab. 4.4.

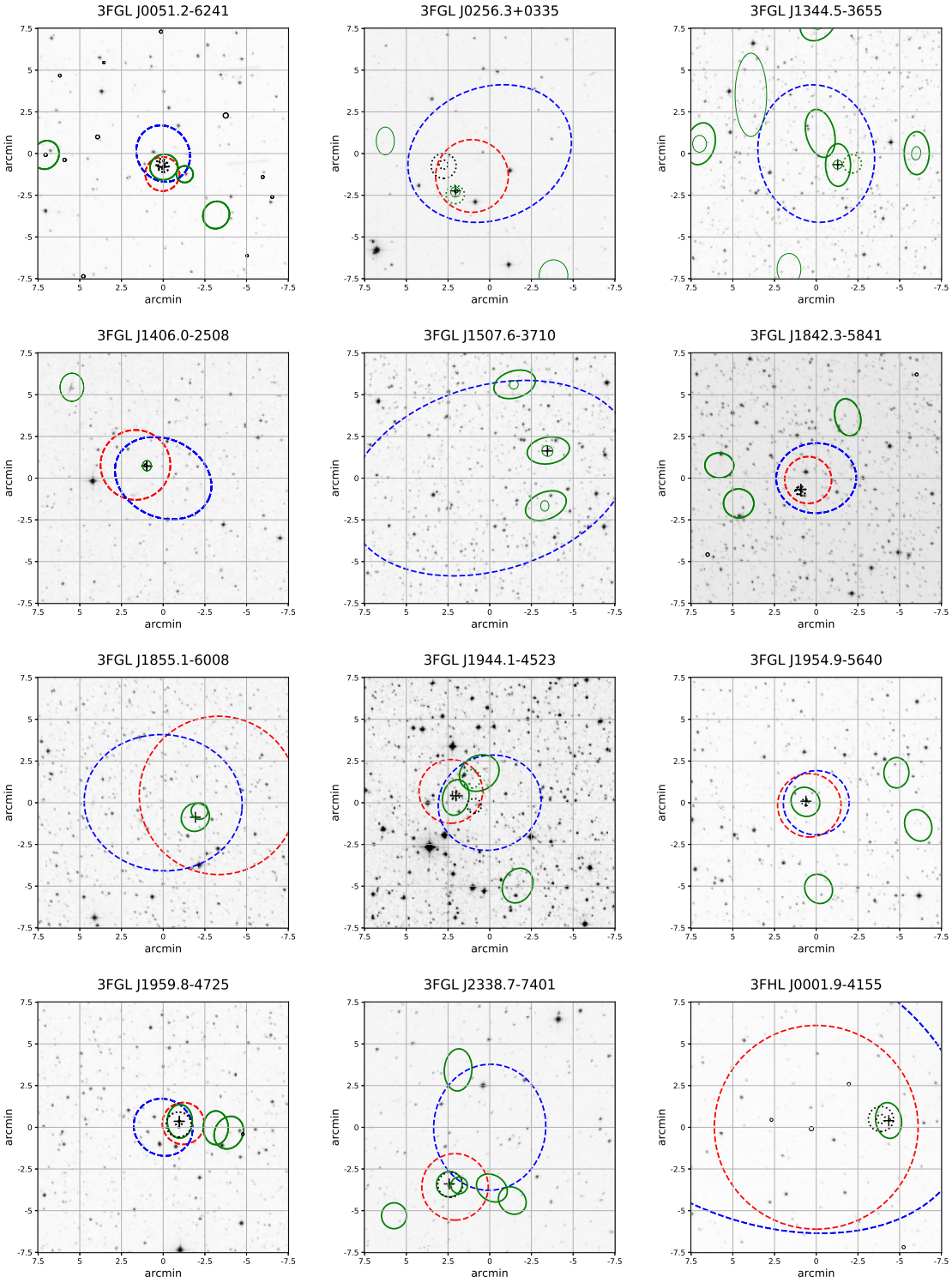

Figure 4.2: Multiwavelength finder charts used to constrain the optical coordinates of the *Fermi*-3FHL and 3FGL sources observed. The finder charts are centered on the 95% 3FHL or 3FGL error regions. The radio (solid green ellipses) and X-ray (black ellipses and circles) sources within 7.5 arcmin of the 3FHL (dashed red circles) and 3FGL (dashed blue ellipses) error regions are indicated. The optical coordinates of the observed source is indicated by the crosses.

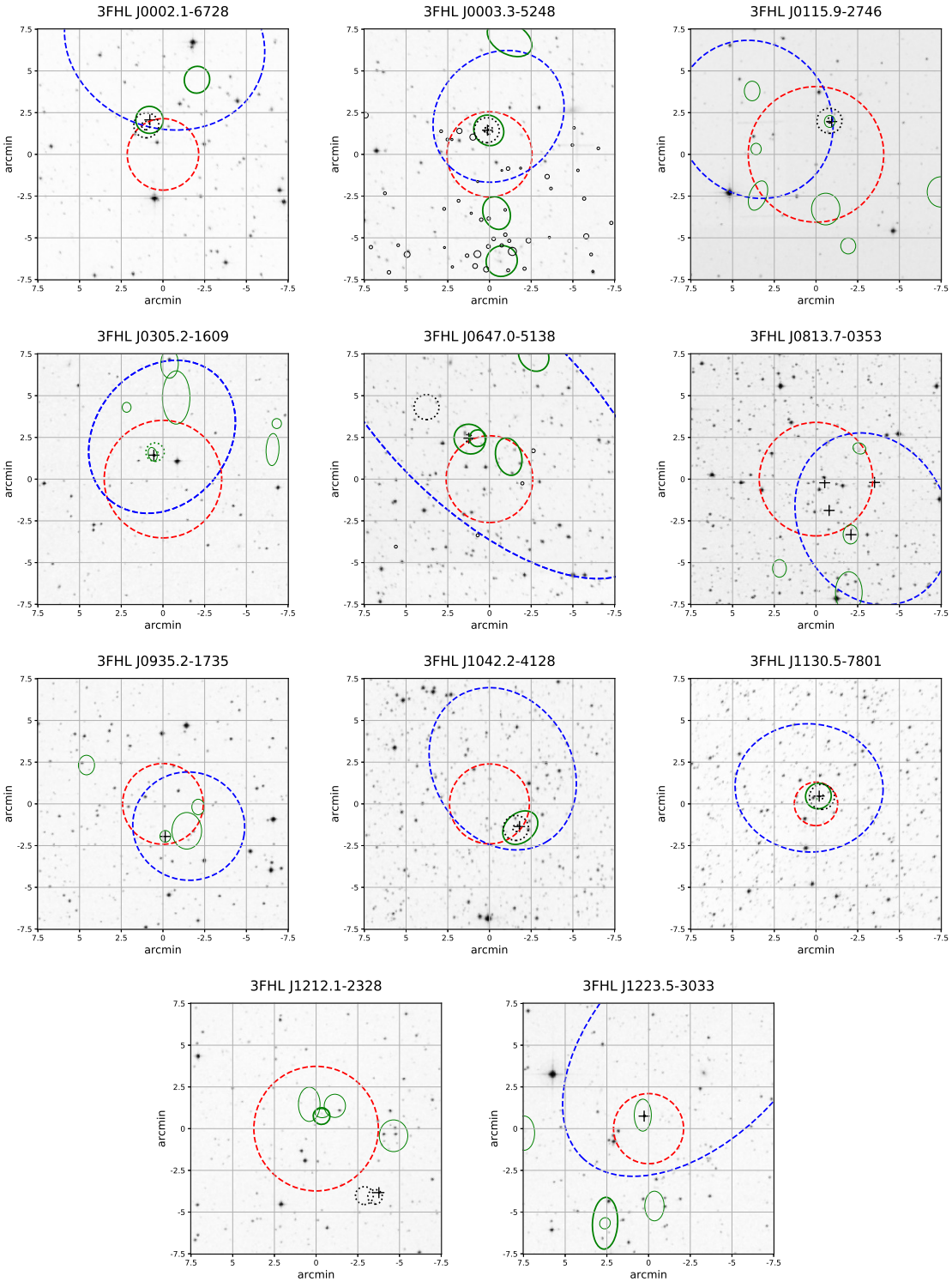

Figure 4.2: *continued.*

Chapter 5

Photometric observations of blazars

The focus of this chapter is to apply optical photometry techniques in order to analyse the intra-day (IDV), short-term (STV) and long-term variability (LTV) of the sources observed with the Watcher Robotic Telescope (hereafter Watcher) and the SAAO 1.0-m SHOC instrument. The detection of IDV in the blazar candidates, provides motivation for further follow-up observations and study of a source. The detection of STV and/or LTV in the TeV detected blazars observed with Watcher, provides justification for continued monitoring. This chapter is structured as follows: in Section 5.1, the technical details of the SAAO 1.0-m SHOC and Watcher are reviewed; in Section 5.2 general Charge Coupled Device (CCD) reduction techniques are presented; Sections 5.3 and 5.4 present the data reduction pipelines of the SAAO 1.0-m SHOC instrument and Watcher; Section 5.5 presents the differential photometry techniques used in the analysis; Section 5.6 and 5.7 presents the results of the Watcher and SAAO 1.0-m SHOC campaigns respectively; Section 5.8 presents the statistical techniques used to search for IDV and LTV and their results.

5.1 Instrumentation

We undertook two separate observation campaigns, namely a long-term monitoring campaign of H.E.S.S. detected blazars with Watcher, located 26 km east of Bloemfontein (Free State, South Africa; 26°24′17.0″E, 29°02′19.8″S) at an altitude of 1372 m above sea level and an intra-night observation campaign of 3FHL unclassified BCUs with the SHOC instrument mounted on the SAAO 1.0-m telescope,

located at the SAAO Sutherland Observatory 18 km east of Sutherland (Northern Cape, South Africa; 20°48′38.5″E; 32°22′46″S) at an altitude of 1798 m above sea level. For this project we utilized the optical data from the Watcher campaign between June 2015 and July 2017. The SAAO 1.0-m SHOC data was obtained during a two week observing campaign in February/March 2017.

5.1.1 The Watcher robotic telescope

Watcher is a fully robotic 16" Cassegrain reflector mounted on a Software Bisque Paramount ME mount which is hosted at the Boyden Observatory and operated by the University College of Dublin (UCD) Space Science group (PI: Lorraine Hanlon). The Optical Tube Assembly (OTA) is an Optical Guidance Systems (OGS) 16" Classic Cassegrain reflector with a 16" parabolic mirror and hyperbolic secondary mirror. The OTA has a 5.7-m focal length and a f-number of f/14.25. The telescope uses an Andor iXon+ 888 CCD with 1024×1024 pixels, resulting in a $10' \times 10'$ FoV with the focal reducer installed. Watcher has eight Astrodon filters installed, which are listed in Tab. 5.1.[1]

Table 5.1: List of the Astrodon Filters installed on the Watcher Robotic Telescope.

Pos.	Filter	Model	Production run	Wavelength	FWHM
0	Clear	(C2 27R)	2102-19104/19109		
1	g	(g2 27R)	1017-17522/17528	4770 Å	1490 Å
2	V	(V* 27R)	2102-12226/12229	5448 Å	840 Å
3	H	(HA5 27R)	2102-22451/22465	6560 Å	50 Å
4	r	(r2 27R)	2102-18234/18244	6231 Å	1450 Å
5	OIII	(OIII5 27R)	2102-22457/22490	5010 Å	50 Å
6	R	(Rc* 27R)	2102-22158/22162	6407 Å	1580 Å
7	i	(i2 27R)	2102-20009/20017	7625 Å	1300 Å

Watcher is designed for the rapid optical follow-up of γ-ray burst (GRB) events, but it also performs regular observations of non-GRB sources, in particular long-term monitoring of blazars.

5.1.2 The SAAO 1.0-m telescope

The SAAO 1.0-m telescope, built by Grubb Parsons in 1964, is located at the SAAO Sutherland Observatory. It has an equatorial mount and all observations

[1] `http://watchertelescope.ie/files/Watcher_Hardware.pdf` (Accessed on 12/06/2018)

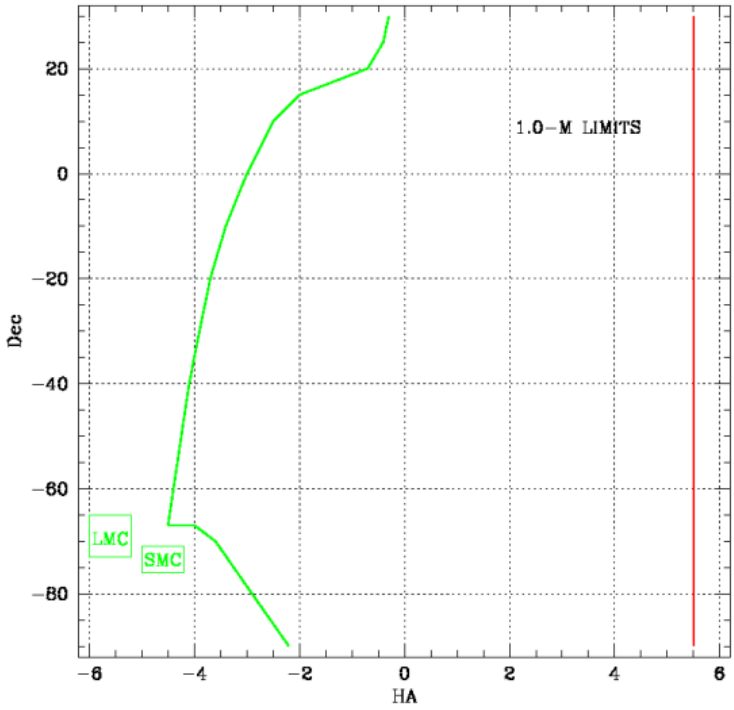

Figure 5.1: The SAAO 1.0-m telescope observing limits in terms of hour angle and declination `http://www.saao.ac.za/science/facilities/telescopes/1-0m/` (accessed on 12/06/2018).

were carried out with the telescope on the East side of the pier. The observing limits of the 1.0-m telescope are affected by the telescope and building designs as is shown in Fig. 5.1. The two available instruments are mounted at the Cassegrain focus (f/16, plate scale $\sim$ 12.94 arcsec/mm). Instruments available are the SHOC and the SAAO CCD. The telescope has an acquisition box comprising of two mirrors orientated at 45° from the incident beam, an offset guide mirror and rear view mirror. A dye coated EEV CCD, with a broad wavelength response from roughly 0.35 to 1.0 μm and an image scale of 0.35 arcsec/mm, is used for both guide star acquisition and guiding during observations. A schematic of the 1.0-m acquisition and guide box is shown in Fig. 5.2.

The SAAO 1.0-m Telescope Control Software (TCS) User Manual[2] was consulted for the use of the 1.0-m acquisition and guiding procedures. A suitably bright star was used for tracking during all observations.

[2]Available at `www.saao.ac.za/science/observing/operating-manuals/1-0m-manuals`

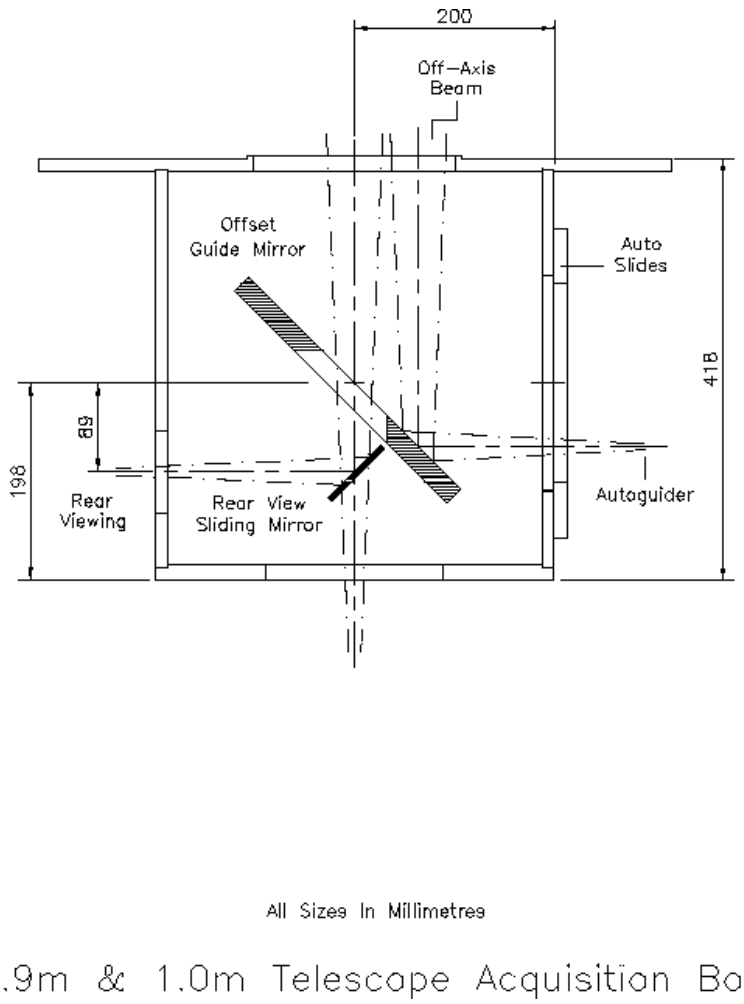

Figure 5.2: Schematic illustration of the 1.0-m acquisition and guide box `http://www.saao.ac.za/science/facilities/telescopes/1-0m/` (accessed on 12/06/2018).

5.1.3 The Sutherland High Speed Optical Cameras (SHOC)

The SHOC instruments are two nearly identical instruments that can be mounted at the Casseggrain focus below the filter wheels of the SAAO 1.0-m, 1.9-m and the Lesedi telescope as shown in Fig. 5.3. They both comprise of an Andor iXon 888 EM CCD with 2048×1024 pixels operated in frame transfer mode (imaging area 1024×1024 pixels), a GPS system (*Inc. Intelligent Reference/TM-4*^{TM}) and a control computer: SHOCnawe (SHOC 1, 1.9-m), SHOCndisbelief (SHOC 2, 1.0-m) and SHOCnhorror(development system). In both SHOC 1 and 2, the GPS antenna is attached to the end of the telescope tube, inside the domes, allowing the signal from three GPS satellites to be measured. This does not allow for position information, which requires at least four satellites to be visible to the GPS antenna, to be calculated, but does allow for accurate time information from

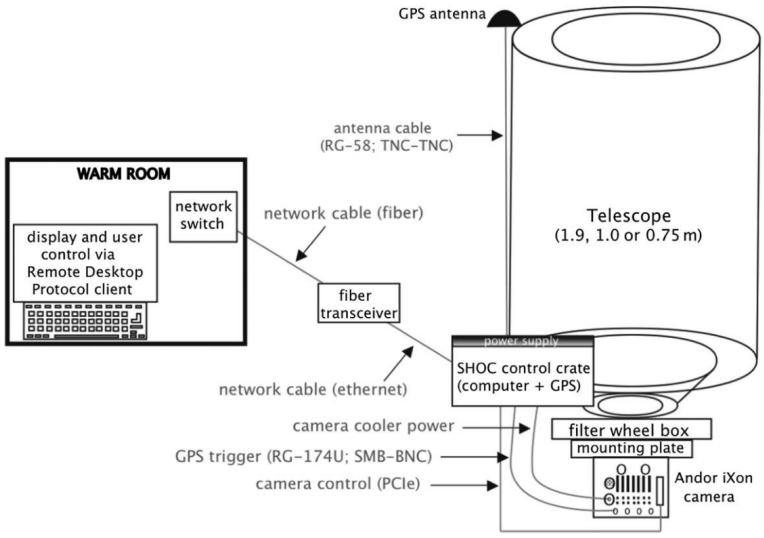

Figure 5.3: Schematic diagram of SHOC mounted at the Cassegrain focus below the filter wheel on the SAAO telescopes (Coppejans et al., 2013, fig. 1).

the satellites.

The camera mode is defined in term of three parameters, *Readout Rate*, *Pre-Amplifier Gain* and the *Output Amplifier*. The available output amplifier modes available are the EM[3] and CON[4] modes. There are also different electron to ADU[5] gains (*Pre-Amplifier Gain*) available for different pre-amp values, i.e. 1.0x, 2.4x or 4.9x on SHOC 1 and 1.0x, 2.5x and 5.2x on SHOC 2. The following readout speed to the storage area are also available: 1 MHz 16bit CON, 3 MHz 14bit CON, 1 MHz 16bit EM, 3 MHz 14bit EM, 5 MHz 14bit EM or 10 MHz 14bit EM. The read noise, electron to ADU gain and saturation for SHOC 2 are shown in Tab. 5.2. The Read Noise and Electron to ADU gain are similar for SHOC 1 and 2, but they have very different full well saturations (Coppejans et al., 2013). It takes 6 milliseconds for the topmost row of pixels to be read out to the register, and since neither SHOC 1 nor 2 has a camera shutter, care should be taken not to take exposures which are less than a hundredth of a second long.

Coppejans et al. (2013) provided predicted S/N ratios in the V filter for the SHOC systems in order to determine with which telescope, camera mode, exposure times and moon conditions sources with specific magnitudes should be observed.[6] Bessel B, V, R and I filters are available for use with the SHOC systems, as well as an empty slot in the filter wheel to enable white light exposures. It is only possible

[3]EM = Electron Multiplying
[4]CON = Conventional
[5]ADU = analog-to-digital units
[6]An online signal-to-noise calculator is available at `http://shoc.saao.ac.za/SHOCsnr.html`

Table 5.2: Electron to ADU gain, read noise and saturation for SHOC 2. Adapted from Coppejans et al. (2013).

Mode	Pre-amp Value	Gain (Electrons/ADU)	Read Noise (Electrons)	Saturation (Counts/ADU)
1 MHz 16bit CON	1.0x	3.79	8.22	20 888
	2.5x	1.53	6.52	51 744
	5.2x	0.68	6.03	65 536
3 MHz 14bit CON	1.0x	9.92	13.99	7 980
	2.5x	3.96	10.85	16 384
	5.2x	1.77	9.79	16384
1 MHz 16bit EM	1.0x	18.61	32.20	4 254
	2.5x	7.43	19.62	10 655
	5.2x	3.39	16.54	23 353
3 MHz 14bit EM	1.0x	44.32	51.85	1 786
	2.5x	19.07	33.18	4 151
	5.2x	8.59	26.29	9 216
5 MHz 14bit EM	1.0x	44.92	69.63	1 762
	2.5x	19.24	45.02	4 114
	5.2x	8.6	35.69	9 205
10 MHz 14bit EM	2.5x	21.97	52.07	3 603
	5.2x	10.05	46.33	7 877

to perform high-speed photometry with one filter at a time, since the filter wheel control is not integrated into the camera control software. Filters must therefore be manually changed and recorded between exposures.

The SHOC systems are read out by two timing modes, internal triggering controlled by an internal clock signal and external triggering controlled by GPS. The internal timing mode, when synchronized with the GPS, has an accuracy of ± 0.5 sec, since the recorded time stamp on the headers are rounded to the nearest second. The internal timing mode should be used with long exposures where extremely accurate timing is not required. The external triggering mode should be used when microsecond (± 5 μs) accurate timing is required. In the external triggering mode, the readout trigger is received from a GPS clock signal. This enables more accurate exposure times than the internal triggering mode, but suffers from the absence of an absolute readout time. This results in some limitations regarding exposures.

The iXon cameras used by SHOC accept an external input from the GPS in order to trigger a readout. When the cameras are used in external triggering mode, they run a "keep clean" cycle, where a readout is done proximately every 23 μs in order to prevent charge build up on the CCD. When a GPS pulse is received, the current "keep clean" cycle completes, after which the CCD is immediately read out again. The GPS pulses are independent of the camera state and therefore when the next pulse arrives, the CCD will be read out to early. This second exposure will therefore be shorter than the required exposure time due to the first exposure being readout late. The third GPS pulse will result in the correct exposure length,

because the second exposure was read out at the correct time. Therefore, the first two exposure in the observation series need to be removed from the data when the external triggering mode is selected (Coppejans & Gulbis, 2017).

5.2 Data reduction of CCD images

Raw CCD data contain an accumulated signal from different wanted and unwanted sources. This signal comprises information from actual sources such as the background sky and target, as well as an artificial signal originating from the telescope and CCD itself, i.e. the CCD bias signal, the CCD thermal current, pixel sensitivity variations across the CCD, hot pixels, cosmic rays, readout noise, dust or internal reflections in the telescope. These unwanted signals need to be removed before analysing the data.

An unexposed CCD is expected to have zero collected photoelectrons, but after the CCD is read out, a non-zero signal is recorded. This signal is caused by two additive effects, a bias signal and a signal produced by thermal electrons caused by the non-zero temperature of the CCD. The bias signal is introduced by CCD readout and electronic noise and a voltage added to the CCD to introduce an artificial signal (Howell, 2006, pp. 52-54). A bias frame can be obtained by taking an exposure where the integration time of the CCD is as close to zero as possible and no photoelectrons are recorded. This bias image measures the pixel-to-pixel variation in the ADU conversion and readout noise, and should be subtracted from all further exposures in order to remove this bias level signal.

The other unwanted signal, caused by thermal noise, is the dark current (Howell, 2006, pp. 47-50). The dark current can be measured by taking a sufficiently long exposure, with no light reaching the CCD and subtracting the bias signal. The dark current can be minimized by cooling the CCD to a very low temperature, e.g. using liquid Helium, liquid Nitrogen or thermo-electric cooling.

Watcher bias and dark correction procedure

Watcher does not take bias exposures. The Andor iXon+ 888 CCD attached to Watcher is factory calibrated to add ~ 400 counts at $-75°$C to the readout. This is subtracted from the data, instead of performing bias reductions. The very low temperature of the CCD during use makes any dark current negligible, therefore no dark corrections are needed during the data reduction procedure.

SHOC bias and dark correction procedure

SHOC has no shutter and therefore bias frames must be taken with the dome and telescope shutter closed. Further, the U filter should be used to prevent any stray light from reaching the CCD. The same mode and binning as the science frames should be used in order to keep the camera characteristics unchanged. In order to take bias frames with SHOC, the lowest integration time should be selected. This can be done by setting the exposure time to zero, in which case the camera control software will change the exposure time to the lowest possible value given the camera binning and mode settings. A series of bias frames should be taken, so that a master bias frame can be constructed and used to perform the bias reductions.

The operating temperature of SHOC is $-50°$C. Therefore, the dark current is negligible and no dark frames were taken.

5.2.1 Flat field correction

A series of images must be taken of a uniformly illuminated source (either a lit area inside the dome, or the twilight sky after sunset) in order to calibrate for the non-uniformity of the recorded image. Large non-uniformities are caused by differences in the thickness of the CCD, non-uniform illumination across the CCD caused by the telescope optics (known as vignetting) or dust particles in the optical path (normally on the filter itself), while small-scale non-uniformities are caused by differences in the size of the pixels (Wodaski, 2002, pp. 238-244).

In order to correct for these effects, a master flat can be constructed using multiple flat frames to increase the S/N of the master flat frame. The science frames, after being corrected for bias and dark current are divided by the normalized master flat frame in order to remove the non-uniformities in the science frames.

Flat frames can be taken using the twilight sky opposite the setting or rising Sun, in order to obtain a uniformly illuminated exposure across the CCD. An illuminated screen inside the dome can also be used to obtain flat frames, but several concerns arise, which include that the artificially lit screen is redder than the sky.

Flat fields taken with SHOC have two prominent features, diagonal diamond shaped lines caused by the CCD thinning process; and a bright centre fading towards the edges, which is likely caused by vignetting (Coppejans & Gulbis,

2017, p. 23). Both these features are removed by the flat field corrections.

5.3 The SHOC pipeline

The SHOC pipeline, reduces SHOC data using a `python`[7] developed pipeline (Kotze, 2013). SHOC saves exposures using a multi-extension Flexible Image Transport System (FITS) cube, with a single header. The SHOC pipeline facilitates the extraction of the FITS cubes and creates new headers (`PyFITS`) based on user-provided information. It performs bias and flat corrections, standard aperture photometry (using `IRAF` - `PyRAF` tasks), differential photometry and constructs light curves (`GNUPLOT`). Only the reduction script of the SHOC pipeline was used to correct the headers and reduce the raw data. The aperture photometry and differential photometry was performed using a reduction and analysis pipeline written to analyse the Watcher data (Section 5.4).

The SHOC instrument creates a single data-cube during an observation run, containing a single header describing all the exposures. The pipeline splits the cube into individual files and calculates their properties, e.g. airmass, exposure time, exposure date, CCD gain and readout noise.

In order to use the pipeline, the user needs to create separate directories containing the bias, flat and science cubes. The SHOCpipeline.tar[8] is then extracted into the directory and the **mkiraf** task is run to initialize `IRAF`. The *SHOCpipeline.py* is run to create the **SHOCscript**, **PHOTscript** and **PLOTscript** scripts, which

- correct the header information using user supplied input,
- create the correct time information in the headers (UT, JD and HJD),
- perform bias corrections,
- perform flat field corrections,
- inform the user if an error occurred and the pre-reductions could not be completed,
- execute aperture photometry, and
- extract and plot raw light curves.

[7] Available at `https://www.python.org/`

[8] `http://shoc.saao.ac.za/Pipeline/` accessed 22/02/2017

The pre-reductions are performed by **SHOCscript**, which includes the header corrections, splitting of data cubes, bias and flat correction (including construction of the master bias and flat frames) and applying the bias and flat corrections to the science frames.

5.4 Watcher pipeline

In order to analyse the long-term observations undertaken by Watcher, a reduction and analysis pipeline was developed as part of this dissertation in order to reduce the data, perform aperture photometry and differential photometry with minimal user input. The Watcher pipeline performs bias subtractions, flat field corrections, aperture photometry, aperture corrected photometry and differential photometry.

The Watcher pipeline is programmed in `python`, using `PyRAF` to interface with `IRAF` and `SEP`, a `python` implementation of `Source Extractor (SE)` (Barbary, 2016; Bertin & Arnouts, 1996). `SEP` allows the pipeline to determine the background statistics and ideal aperture size for each individual frame, without any user interaction. The Watcher pipeline:

- subtracts the bias counts,
- performs flat field corrections,
- combines frames to increase the signal-to-noise ratio,
- calculates source properties using the `SE` detection algorithms,
- reject frames with no usable data (e.g. high background noise, smeared frames),
- calculates the ideal aperture based on the previously calculated source properties,
- performs aperture photometry and aperture corrections using `IRAF/PyRAF`,
- performs differential photometry,
- rejects outlier photometric points using sigma clipping, and
- plots light curves using `python/matplotlib`.

The Watcher pipeline consist of three `python` classes, namely **WatReduction**, **WatCombiner** and **WatPhotometry** and the `python` script **WatPipeplot**. These classes should be called inside a small, user generated `python` script, in conjunction with any user commands, in order to perform the reductions and photometry. The scripts are designed to perform batch operations, i.e they reduce all raw data and perform aperture photometry on all the available frames for a selected source.

5.4.1 WatReduction

The WatReduction class is used to perform bias, dark and flat reductions. The reductions are performed in batch mode, reducing all non-reduced images the user supplies. The class accepts as input an `IRAF` instrument file, a dictionary setting the folder name where a frame type is stored, the shallowest directory where the files are located and optional parameters defining the location of the instrument file and directory structure.

The script writes out a log of the steps followed to the file headers so that steps are not repeated. This is normally done by `IRAF` after each reductions step, but since the bias subtractions were not done by the standard `ccdred/zerocombine` task, the information is added to the header by the script.

The reduction functions can be called, after the class is imported, following the usual `python` syntax without any parameters specified to run it using the default parameters, or, if the user desires, using non-default parameter inputs. In order to increase performance when additional data is added to an already large dataset, the script creates a file with a list of the already reduced data frames. These frames are ignored during reductions, so that only the new data is reduced. The user is free to add or remove entries in this file if data are replaced. Because different CCD/telescope properties are included as parameters, the script can be used to reduce data from other telescopes as well. An example of the execution of WatReduction is shown in Fig. 5.4.

5.4.2 WatCombiner

The WatCombiner class is used to combine FITS files. It will stack frames within user defined time bins, with the option of specifying a maximum exposure time for any stacked frame. The frames are combined using the methods available in the `immatch/imcombine` task and the headers are updated in the new frames. The

```
# Import the Reduction class
from Pipeline import WatReduction as Reduction

# Create the Reduction class instance
reduction = Reduction.Reduction(pwd='Photometry',
                                telescope='watcher',
                                site='custom',
                                verbose='v')

# Perform the flat reductions
reduction.flat(imarith=400,
               flat_options={'mode': 'h', 'combine':'average',
                             'reject': 'crreject', 'process': 'no',
                             'subset':'yes', 'delete':'no',
                             'scale': 'mean',
                             'rdnoise': 8.4,  'gain': 3.8})
```

Figure 5.4: Example code to perform flat reductions on Watcher data.

script also correctly updates the gain and readnoise values based on the number of combined frames and combining method (Massey & Lindsey, 1992, p. 41). It is run as a single function, with the desired parameters set when the function is called. It also takes as an optional variable, a `Astropy` coordinate object, that sets the desired coordinate that offsets are calculated from, for example, when the target is offset on the frame because a bright star near the target might saturate the CCD. This script requires that the frames have a World Coordinate System (WCS) defined in the header in order to calculate offsets for the combining operations. An example of the execution of the code to perform image stacking with offsets for Watcher observations of PKS 1510-089 is presented in Fig. 5.5.

5.4.3 WatPhotometry

The WatPhotometry class performs aperture photometry, aperture correction photometry and differential photometry. It consists of three main functions, **run_phot**, **phot_tab** and **phot_diff**. The script can be run on photometric data from different telescopes, the main requirements being a consistent coordinate system between frames and a coordinate file containing the coordinates of the stars the user want to analyse. An example of the code execution to perform aperture corrected photometry on the stacked frames of PKS 1510-089 observed with Watcher is presented in Fig. 5.6.

```
import WatCombiner
from astropy.coordinates import SkyCoord
import astropy.units as u

# Construct a valid SkyCoord coordinate object for PKS 1510-089
coordinate = SkyCoord(ra=['15:12:50.53'],
         dec=['-09:05:59.82'],
         unit=(u.hourangle, u.deg))

WatCombiner.wcombine('Target',
                     output_dir='Combine/PKS1510_089',
                     pwd='Watcher',
                     coords=coordinate,
                     bin_type='average',
                     binning=300 * u.second,
                     max_offset=3 * u.arcmin,
                     max_time_sep = 12 * u.hour)
```

Figure 5.5: Example code to perform image stacking for PKS 1510-089 with 300 second frame binning and a maximum of 12 hour separation between the first and last stacked frame.

```
# Import the Photometry class
from Pipeline import WatPhotometry as Photometry

# Create the Photometry class instance
photometry = Photometry.Photometry(pwd='Combine', verbose='v')

# Run aperture corrected photometry using 15 apertures
photometry.run_phot(PKS1510_089, ccdread='NRDNOISE', gain='NGAIN',
                    naperts=15, reject_eccentricity=0.7,
                    exposure='EXPTIME', obstime='MID_MJD',
                    aper_cor=True, flux_frac=0.9,
                    zeromag=10)

# Transform the output files into single table-like file
photometry.phot_tab(PKS1510_089, aper=True)
# Perform differential photometry (Everett and Howell, 2001)
photometry.phot_diff(PKS1510_089, method='EV_HO')
```

Figure 5.6: Example code to perform aperture corrected photometry and differential photometry on PKS 1510-089 observed with Watcher.

5.4.3.1 run_phot

In order to perform aperture photometry or aperture correction photometry, **run_phot** is run on the data. It has only one required variable, the source name, which will be used to select only files whose path includes the source name. All other variables are optional. In order for aperture photometry to be performed, the function requires that a coordinate file exists which has the coordinates of the target and one or more comparison stars. The coordinate file must use coordinates that are consistant between frames, the WCS coordinate system works best, but a physical (x, y) system also works if the targets do not move around significantly between frames.

The function sets the parameters used by the `digiphot/phot` task and sub tasks. The frame properties, i.e. background noise and FWHM of the stars in the frame are automatically calculated using the `Source Extractor (SE)` algorithms.

The SE detection algorithm does not provide the PSF FWHM value of a star, but rather the semimajor and semiminor values for an ellipse that contains a fraction of the object flux. These values allow the script to reject frames where the objects do not approximate a circular footprint (by default a maximum eccentricity of $\epsilon \sim 0.7$ is allowed) on the frame. Stars with a highly eccentric footprint will have a significant portion of their flux outside the circular aperture `digiphot/phot` uses to calculate a magnitude. Setting the aperture to have arbitrarily large sizes will include more background noise in the calculations and can result in unacceptably large errors. Instead of calculating the FWHM of the sources in the frame, the script instead uses an aperture size that contains 90% of the average flux of the stars in the coordinate file.

The run_phot function has an option to perform aperture correction photometry, in which case the single aperture is replaced by multiple apertures and the aperture correction task `photcal/mkapfile` is run.

After the photometry is performed the individual `digiphot/phot` output files are extracted using the `ptools/txdump` task. The function **phot_tab** is used to transform the list-like structure of these output files into a table-like structure.

5.4.3.2 phot_tab

This function reorganizes the `txdump` output files from a list-like format into a table-like format that is easier to use in spreadsheet programs. If aperture correction photometry has been used, the uncorrected magnitude list needs to be cross-matched to the potentially shorter aperture corrected list. The `photcal/mkapfile`

task is not able to calculate a curve-of-growth for every star and also does not record the time of observation in the output. Cross-matching the two lists is a slow process when many entries need to cross-matched. Therefore, to increase performance, an algorithm that simultaneously steps through and cross-match both lists only once was implemented.

The newly created list needs to be reorganized into a table-like structure. The list is converted to a `numpy` array and sorted by the filter, observation time and star ID fields. The function then reorganizes the magnitude list into a table-like format so that it is easier to load into third-party spreadsheet programs.

This function saves the raw photometric data into a new file, which the user can use in their own analysis scripts. Differential photometry can then be performed on the data using the function **phot_diff**.

5.4.3.3 phot_diff

This function performs differential photometry on a table-like input file using the algorithm developed by Everett & Howell (2001) and Burdanov et al. (2014). The function takes as input a table-like file (created by the **phot_tab** function), performs the differential photometry and saves the results in a new file. The algorithm used will be presented Section 5.5.

5.4.4 WatPipeplot

The WatPipeplot script is used to plot the results of either the raw photometry or the differential photometry results produced by the Watcher Pipeline. It is written in `python` and uses `matplotlib` to plot the results. By default, it assumes the first three columns contain the observation date (in JD or MJD), the target magnitude and target magnitude error respectively. The following columns contain the magnitude, error for each of the comparison stars. The stars to plot can be changed by the user when the script is run. By default, the script plots the first three stars, i.e. the target and two comparisons. If desired, the user can select different stars to plot. A short manual page can be called by running the script with the **-h/- -help** options.

5.5 Differential photometry

The differential photometetry was performed using comparison stars that were present in the same frame as the target and of a similar magnitude to correct for atmospheric and observational effects.[9] The raw photometric data points were filtered to ensure that only frames where all the comparisons were present (implemented in `WatPhotometry.phot_tab`) and with magnitudes within a few standard deviations of the mean (to eliminate spurious data) were used in the differential photometry.

Instrumental magnitudes were calculated using the weighted differential photometry discussed by Everett & Howell (2001) and Burdanov et al. (2014). This differential photometry method uses the variance of the comparison magnitude errors to assign weights to the comparison stars used to correct the frames. The weighted average instrumental magnitude $\langle m_j \rangle$ of the comparison stars is calculated for each frame as

$$\langle m_j \rangle = \frac{\sum_{k=1}^{K} m_{kj}\omega_k}{\sum_{k=1}^{K} \omega_k},$$

where

$$\omega_k = \frac{1}{\langle \mathrm{m}_{err,k}^2 \rangle}$$

and k is the number of the star in the ensemble with size K, j is the frame number, m_{kj} is the magnitude of the k-th ensamble star in the j-th frame and $\langle \mathrm{m}_{err,k}^2 \rangle$ is the mean squared error of the measured magnitude m_k of the ensemble star.

The mean magnitude M of all ensemble stars is then found by averaging over all the frames:

$$M = \frac{\sum_{k=1}^{K} m_j}{N},$$

where N is the total number of frames.

To correct the magnitude of the stars for atmospheric effects, the difference between the weighted averaged magnitude $\langle \mathrm{m}_j \rangle$ of the ensemble stars and the mean magnitude M of all ensemble stars, averaged over all frames, is subtracted

[9] The colour of the comparison stars were not taken into account. Using a large ensemble of comparison stars with different colours will help to reduce the correction uncertainties caused by atmospheric extinction, which is colour dependant.

from the observed magnitude of the stars:

$$m_{corr,ij} = m_{ij} - (\langle m_j \rangle - M)\,,$$

where $m_{corr,ij}$ and m_{ij} are the corrected and initial magnitudes of the i-th star in frame j.

The error in the corrected magnitudes are given by

$$m_{\rm err,comp} = \frac{1}{\sqrt{\sum_{k=1}^{K} \frac{1}{m_{err,k}^2}}},$$

where $m_{err,k}^2$ is the error of the k-th comparison star. The error in the corrected magnitude can then be calculated as

$$m_{\rm err} = \sqrt{m_{err,i}^2 + m_{err,comp}^2}$$

5.6 Watcher long-term observations

The observations of the TeV detected sources were stacked to exposure times of 300 seconds to increase the S/N of the data (see Sect.5.4.2) and aperture corrected photometry performed (see Sect.5.4.3). Differential photometry was performed using a minimum of 5 comparison stars.

In Fig 5.7 to 5.11 I present the Differential Light-curves (DLC) on LTV timescales for 14 of the TeV detected blazars observed by Watcher. The data has been corrected so that only data that are within 2σ of the mean are included. In all cases the target is indicated in black, and only two of the comparisons are included in each plot.

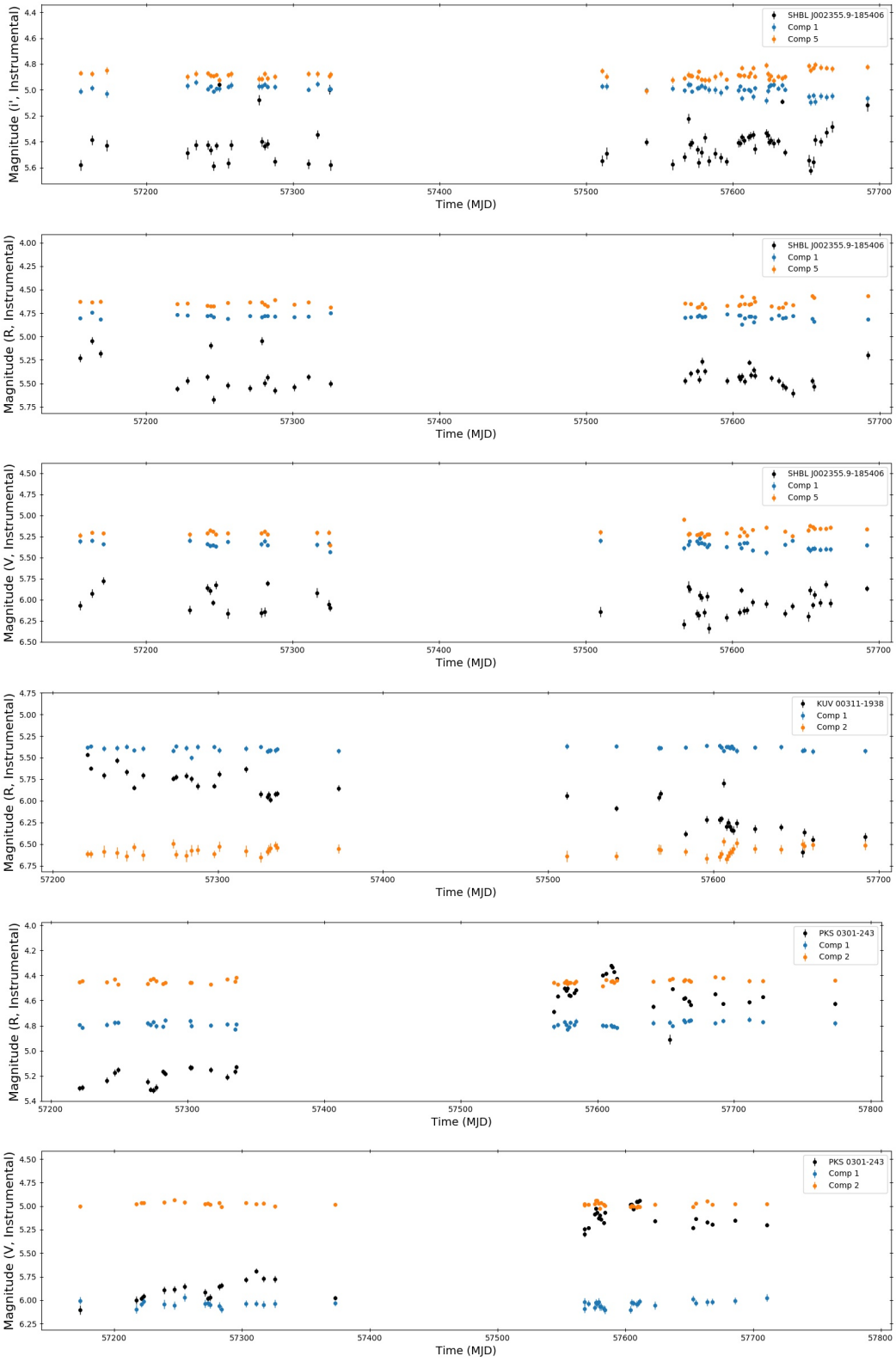

Figure 5.7: DLCs of SHBL J001355.9-185406 (May 2015 - October 2016), KUV 00311-1938 (July 2015 - October 2016) and RGB J0152+017 (July 2015 - January 2017) taken with the Watcher Robotic Telescope.

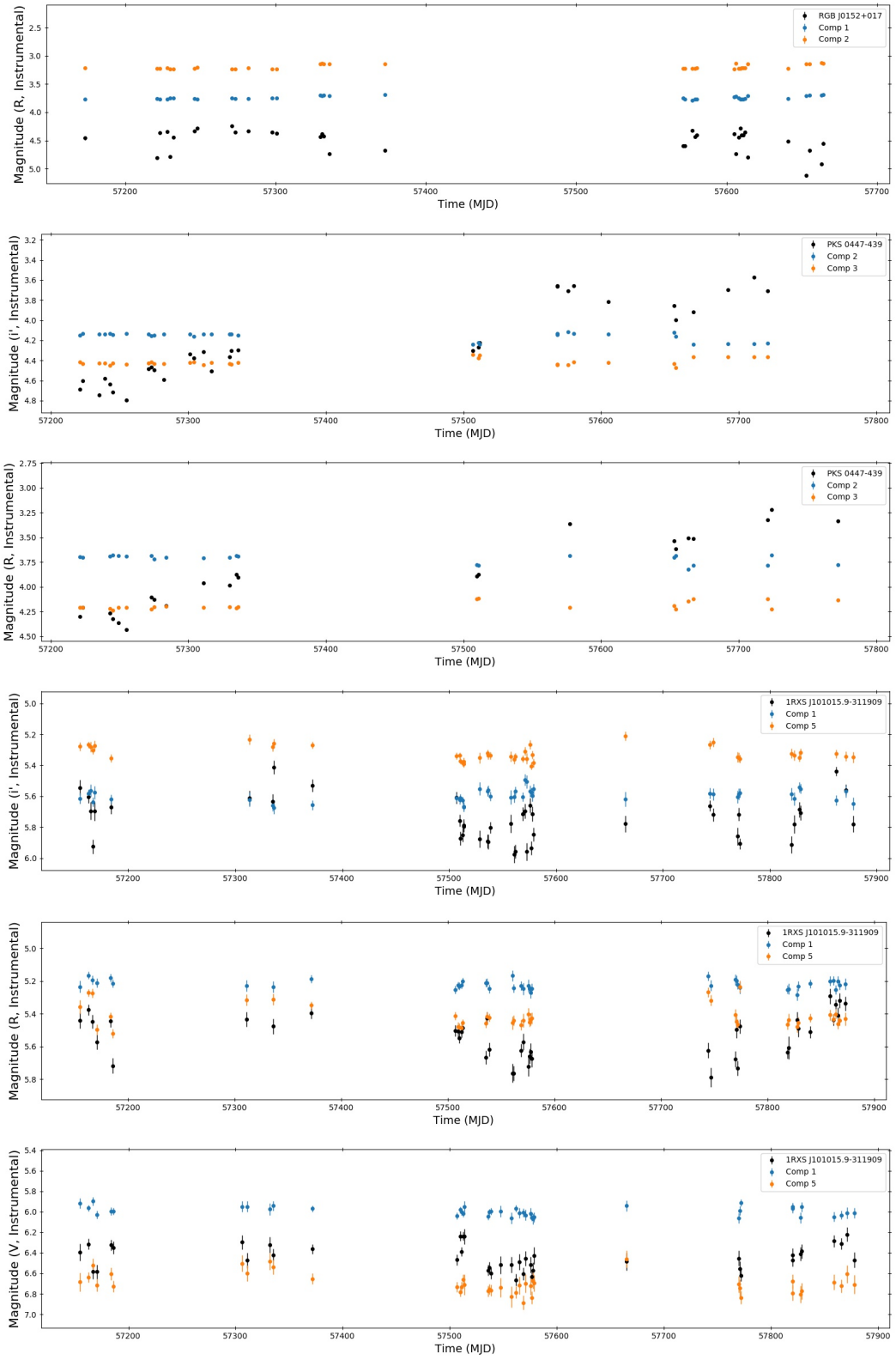

Figure 5.8: DLCs of RGB J0152+017 (May 2015 - October 2016), PKS 0447-439 (July 2015 - November 2016) and 1RXS J101015.9-311909 (May 2015 - May 2017) taken with the Watcher Robotic Telescope.

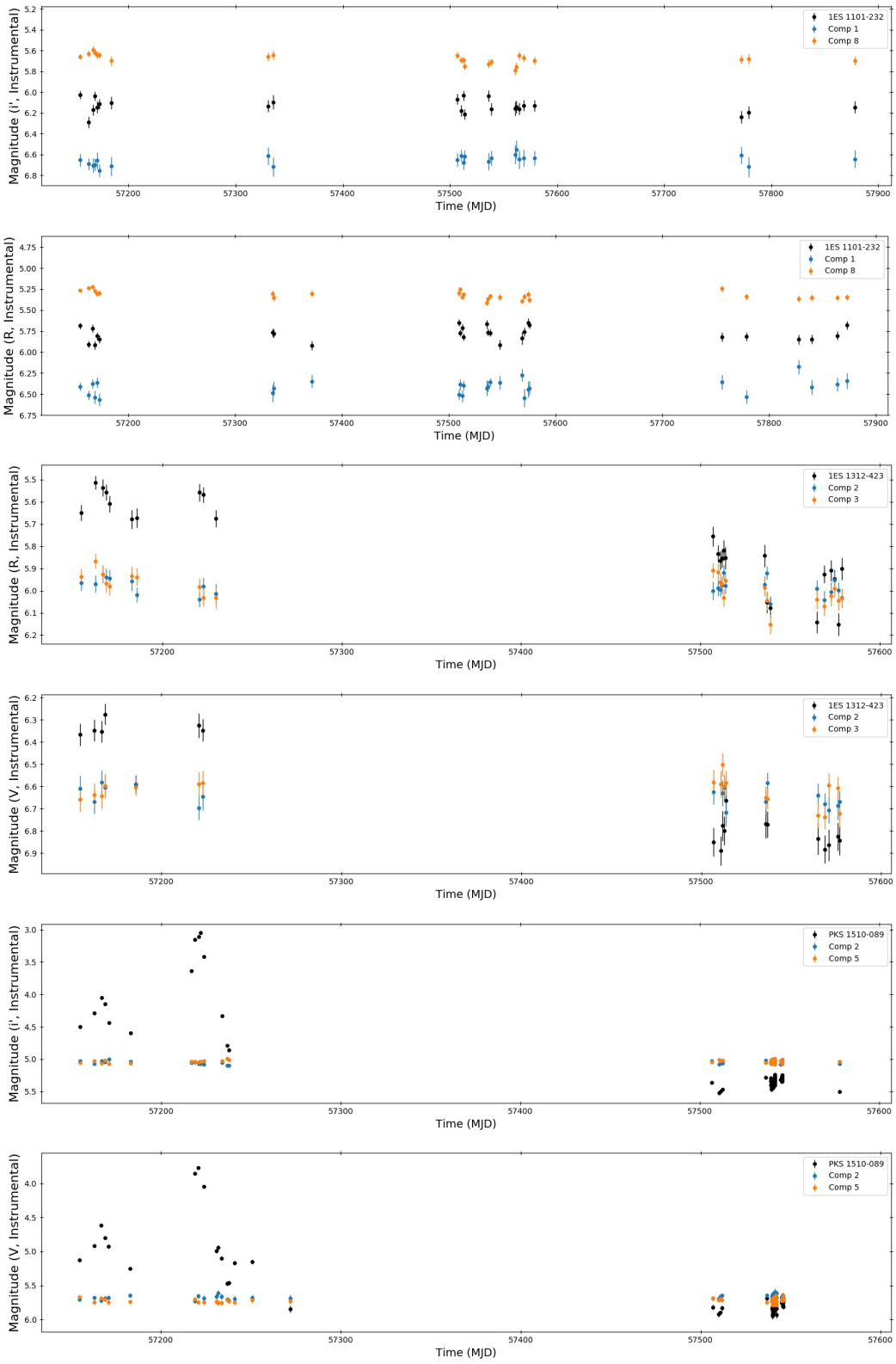

Figure 5.9: DLCs of 1ES 1101-232 (May 2015 - May 2017), 1ES 1312-423 (May 2015 - July 2016) and PKS 1510-089 (May 2015 - July 2016) taken with the Watcher Robotic Telescope.

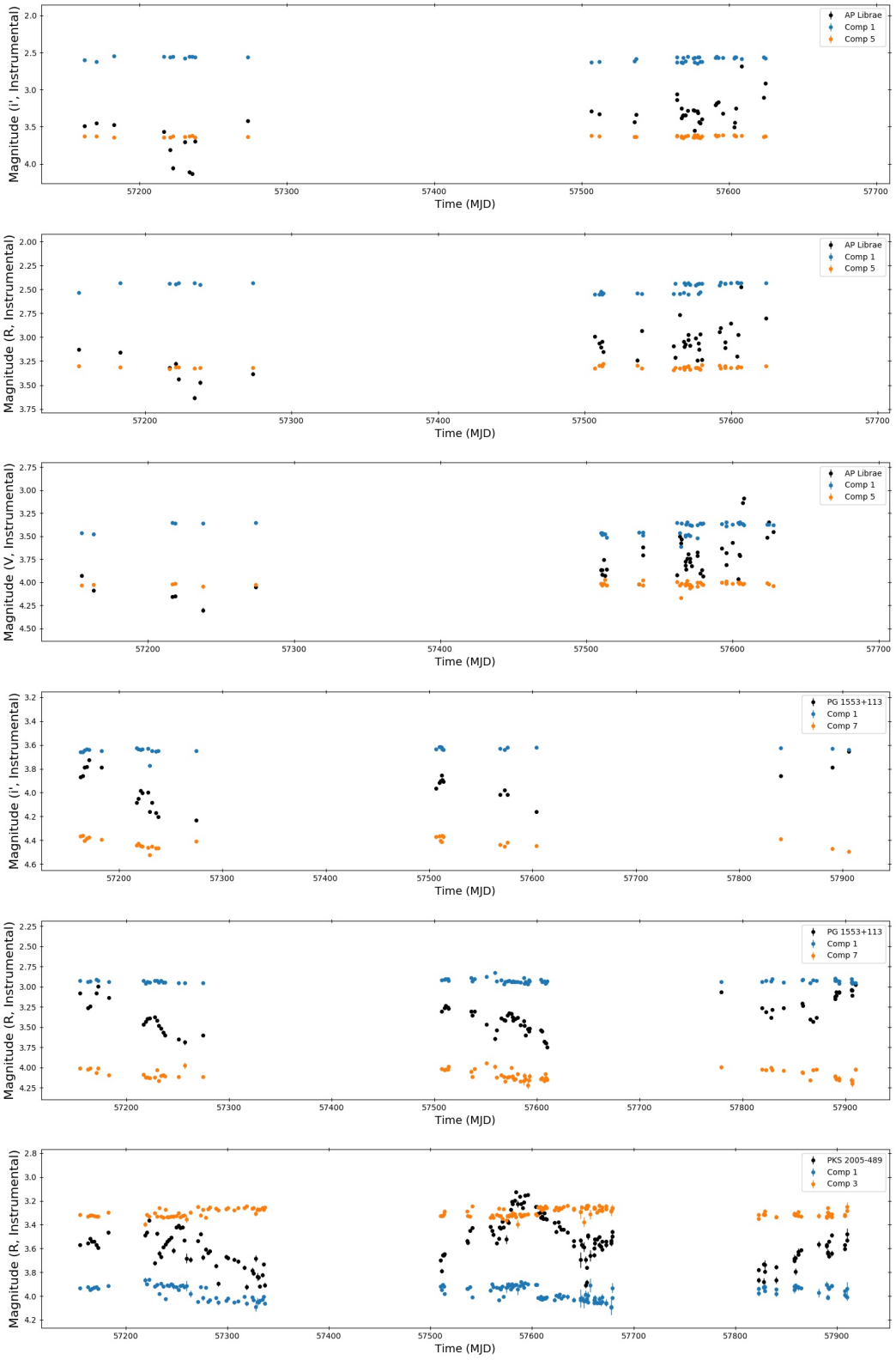

Figure 5.10: DLCs of AP Librae (May 2015 - August 2016), PG 1553+113 (May 2015 - June 2017) and PKS 2005-489 (May 2015 - June 2016) taken with the Watcher Robotic Telescope.

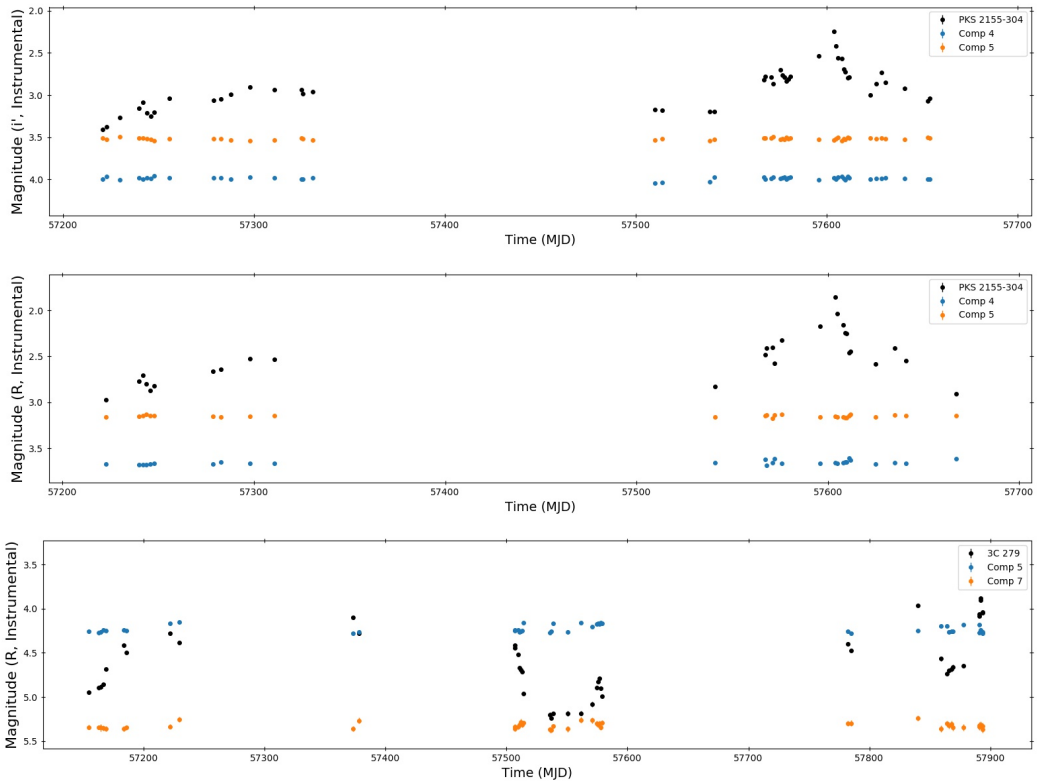

Figure 5.11: DLCs of PKS 2155-304 (July 2015 - October 2016) and 3C 279 (May 2015 - May 2017) taken with the Watcher Robotic Telescope.

5.7 SHOC light-curves of 3FHL BCUs

A total of five unidentified 3FHL BCUs and one unassociated 3FHL source was observed with the SAAO 1.0-m SHOC instrument to help in the identification of the sources for spectroscopic classification and study their possible IDV. Each source was localized to 1 optical candidate using multiwavelength archival data, except 3FHL J0813.7-0353, which could only be localized to 5 optical candidates, 4 of which could be detected with the SHOC instrument (as discussed in Section 4.2.4). The log of the observations are given in Tab. 5.3. Each source was observed for 1 to 4 hours (depending on the telescope track length and available observing time) in the clear filter to study their IDV. Differential photometry was performed using at least 3 comparison stars in order to correct for atmospheric effects in the data. The DLCs of the observable candidates of 3FHL J0813.7-0353 are shown in Fig. 5.12. The DLCs of the observed BCUs are shown in Fig. 5.13. In all cases the target is indicated in black, and only two of the comparisons are included in each plot.

Table 5.3: The observation log of the SAAO 1.0-m SHOC observations. The Source name, observation date and optical candidate are listed. Also listed are the exposure times, total number of exposures, the total length of the observing run and the average seeing.

Source	Obs date y/m/d	Candidate	Exp time sec	Exposures	Obs length h m s	Seeing arcsec
3FHL J0802.2-0943	2017/03/03		30	400	3 h 24.5 m	1.1
	2017/02/25	C1	20,30	350	2 h 27 m	2.8
	2017/02/25	C2	20,30	350	2 h 27 m	2.8
3FHL J0813.7-0353	2017/02/25	C3 1	30	171	1 h 55 m	1.7
	2017/02/27	C3 2	30	240	2 h	2.1
	2017/02/27	C4	15,20	362	1 h 55 m	1.5
3FHL J0953.3-7659	2017/03/02		30	500	4 h 10 m	1.0
3FHL J1042.2-4128	2017/03/05		30	300	2 h 30 m	1.3
3FHL J1130.5-7801	2017/03/01		30	500	4 h 15 m	2.9
3FHL J1223.5-3033	2017/02/24		15	281	1 h 10 m	1.4

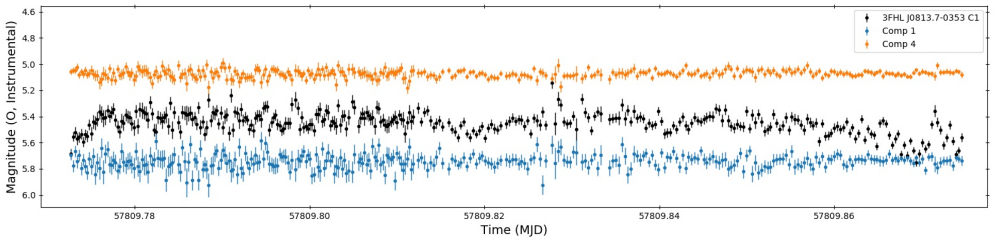

(a) Candidate 1.

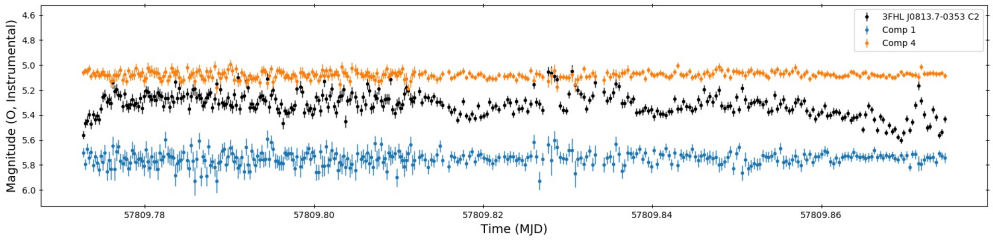

(b) Candidate 2.

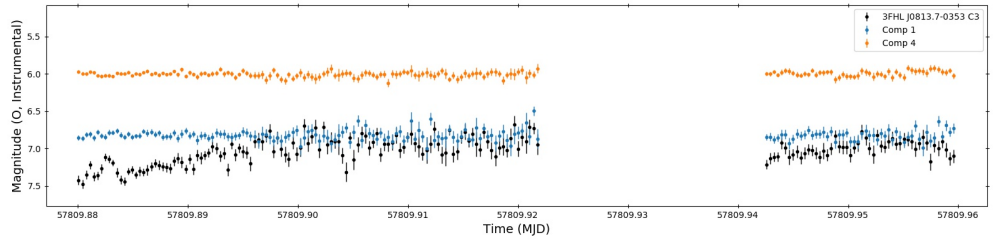

(c) Candidate 3, Observation 1.

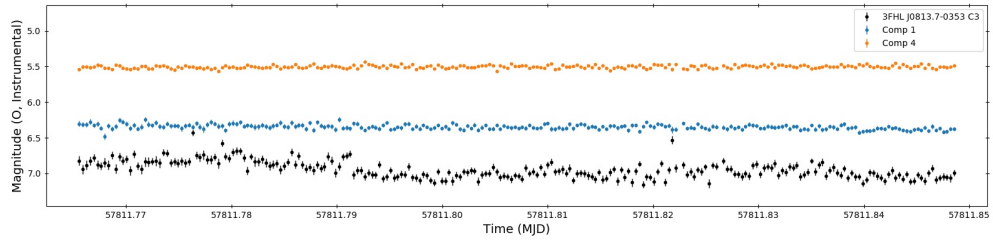

(d) Candidate 3, Observation 2.

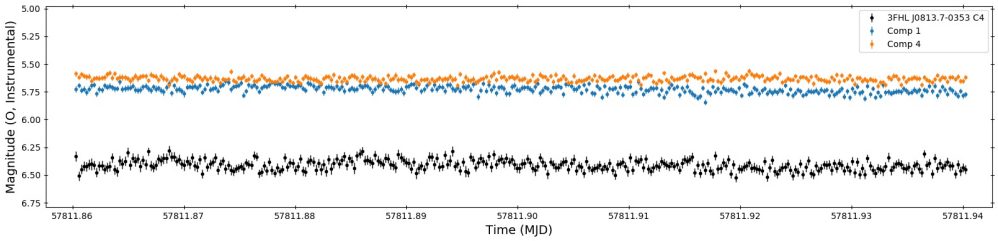

(e) Candidate 4.

Figure 5.12: DLCs of the 4 optical candidates of 3FHL J0813.7-0353 that was detectable with SHOC. The candidates were observed on 2017/25/02 (5.12a, 5.12b and 5.12c) and 2017/02/27 (5.12d and 5.12e). The data has been corrected so that only data that are within 2σ of the mean are included.

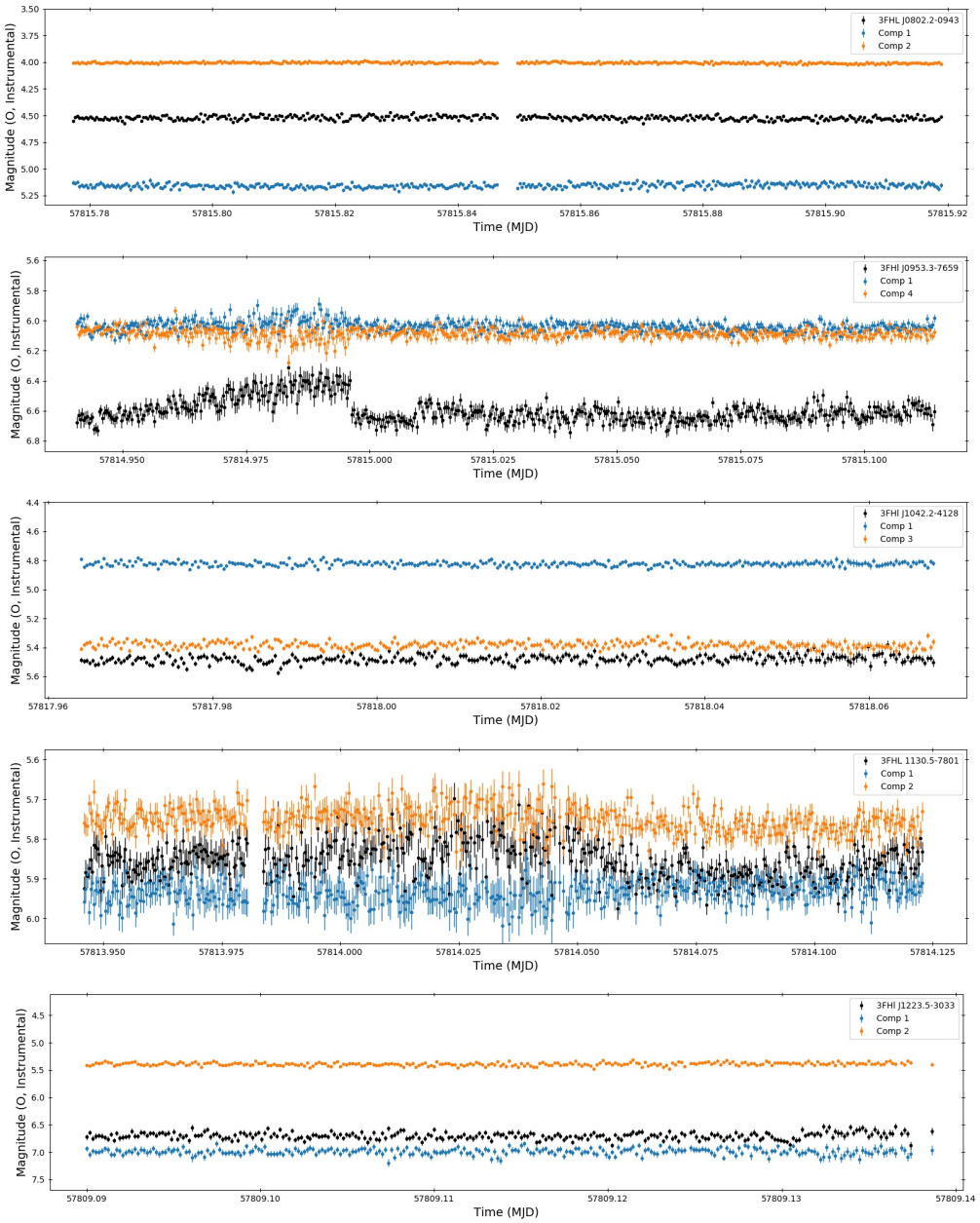

Figure 5.13: DLCs of 3FHL J0802.2-0943 (2017/03/03), 3FHL J0953.3-7659 (2017/03/02) 3FHL J1042.2-4128 (2017/03/05) 3FHL J1130.5-7801 (2017/03/01) and 3FHL J1223.5-3033 (2017/02/24). The data has been corrected so that only data that are within 2σ of the mean are included.

5.8 Variability statistical analysis

Various statistical tests are used to search for IDV and LTV in the lightcurves of blazars. These tests include the χ^2-distibition test, the F-test, scaled F-test and the power enhanced F-test (see e.g. Agarwal & Gupta, 2015; Gaur et al., 2012b;

Goyal et al., 2012; Joshi et al., 2011). The reliability and limitations of different variability tests have been investigated in detail by de Diego (2010, 2014).

5.8.1 Statistical tests

The various statistical tests used to search for variability on intra-day and long-term time-scales in the sources observed by Watcher and the SAAO 1.0-m SHOC instrument are presented below.

5.8.1.1 The *F*-test

The F-test compares the variance of the suspected variable source and the non-variable comparisons stars (Howell et al., 1988). The F-test, is defined by (Howell et al., 1988) as

$$F_1 = \frac{Var\,(V-C)}{Var\,(C-K)} \qquad F_2 = \frac{Var\,(V-K)}{Var\,(C-K)}, \tag{5.1}$$

where $Var\,(V-C)$, $Var\,(V-K)$ and $Var\,(C-K)$ are the variances in the difference in magnitude between the variable and star$_1$, the variable and star$_2$ and between star$_1$ and star$_2$ light-curves respectively. The suspected variable is denoted by V, while the two non-variable comparison stars are denoted by C (star$_1$) and K (star$_2$). In order to claim variability, the results of the F-test are compared against F-distribution tables, which provide critical F-values for different significance values. The critical F-value, $F^{(\alpha)}_{\nu_B \nu^*}$ depends on the degrees of freedom of the data set, which for the F-test is the same for the target and comparison stars and is given by

$$\nu_{\rm B} = \nu^* = N - 1$$

where N is the number of data points considered. The critical F-values normally used are $\alpha = 0.001$, $\alpha = 0.01$ and $\alpha = 0.05$, which correspond to the 99.9%, 99% and 95% confidence levels respectively. In order to claim variability, the average critical value $F_{\rm avg}$ is compared to the critical value or, alternatively, comparing F_1 and F_2 to the critical value separately. The source is considered variable (V) if $F \geq F_{\rm crit}$ for a confidence level of $\alpha = 0.01$, possibly variable (PV) for a F-value in the range $0.05 < \alpha \leq 0.01$ and not variable (N) if $F < F_{\rm crit}$ for a confidence $\alpha = 0.05$.

5.8.1.2 The scaled *F*-test

The scaled F-test compensates for the brightness mismatches between the comparison and suspected variable sources, which may cause spurious variations as a result of different photon statistic between sources (see e.g. Howell et al., 1988; Joshi et al., 2011). The correction factor is given by

$$\kappa = \left[\frac{\sum_{i=0}^{N} \sigma_{i,err}^{2}\left(V-C\right)/N}{\sum_{i=0}^{N} \sigma_{i,err}^{2}\left(C-K\right)/N}\right] \equiv \frac{\langle \sigma^{2}\left(V-C\right)\rangle}{\langle \sigma^{2}\left(C-K\right)\rangle}, \tag{5.2}$$

where $\sigma_{i,err}^{2}\left(V-C\right)$ and $\sigma_{i,err}^{2}\left(C-K\right)$ are the errors in the Variable−star and star−star DLCs respectively. The scaled F-test is then calculated as

$$F^{s} = \frac{Var\left(V-C\right)}{\kappa^{2}\left(Var\left(C-K\right)\right)}. \tag{5.3}$$

The κ term normalizes the variances of the DLC by the mean of the squared errors (i.e. $\langle\sigma^{2}\rangle$) of individual points returned by **daophot**.

5.8.1.3 The power-enhanced *F*-test

The F-test, while a powerful statistical test, becomes less powerful for small variations or smaller degrees of freedom (see e.g. de Diego, 2014). The power of the F-test can be increased by including multiple comparison stars in the analyses, effectively increasing the degrees of freedom of the denominator in the F-distribution. To perform this power-enhanced F-test, the light-curves of multiple comparison stars are stacked. Suppose there are N observations (frames) of a suspected variable, along with k comparison stars. The scaled square deviation of comparison j in frame i is then

$$s_{j,i}^{2} = \left(m_{j,i} - \bar{m}_{j}\right)^{2}, \tag{5.4}$$

where $\bar{m}_{j}$ is the mean magnitude of comaprison j. Stacking all the $s_{j,i}^{2}$ for all N frames and all k comparisons, the combined variance of the comparison stars is given by

$$s_{c}^{2} = \frac{1}{\left(\sum_{j=1}^{k} N_{j}\right) - k} \sum_{j=1}^{k} \sum_{i=1}^{N_{j}} s_{j,i}^{2} \tag{5.5}$$

If all the comparisons have the same number of observations, as is usually the case in CCD observations, the degrees of freedom in the denominator is then $\nu_c = k\,(N-1)$. The increase in the degrees of freedom, either in the numerator or denominator, yields an increase in the power of the F-test. The power enhanced F-test is then calculated as

$$F_{\rm enh} = \frac{s_B^2}{s_c^2}, \tag{5.6}$$

where s_B^2 is the variance of the variable and s_c^2 the stacked variances of the suspected variable and comparison stars used in the test. $F_{\rm enh}$ was compared to the $F_{\rm crit}$ with the numerator (target) degrees of freedom $\nu_B = N_B - 1$ and denominator (stacked comparison stars) degrees of freedom $\nu_c = k\,(N-1)$. Variability (V) was claimed if $F_{\rm enh} > F_{\alpha=0.001}$ (see e.g. de Diego et al., 2015; Gaur et al., 2017). Possible variability (PV) was claimed for $F_{\alpha=0.01} < F_{\rm enh} < F_{\alpha=0.001}$ and the source was regarded as non-variable (N) if $F_{\rm enh} < F_{\alpha=0.01}$.

5.8.1.4 The χ^2-distribution

The χ^2-test, first utilized by Pica & Smith (1983) to measure variability in quasars and blazars, is now regularly used to detect variability on various timescales (see e.g. Agarwal & Gupta, 2015; Gaur et al., 2012b). The χ^2-distribution is defined as

$$\chi^2 = \sum_{i=1}^{N} \frac{\left(V_i - \bar{V}\right)^2}{\sigma_i^2}, \tag{5.7}$$

where N is the number of data points, V_i, the i-th data point's magnitude, $\bar{V}$ the average of V_i over all data points N, and σ_i is the root mean square (rms) error of V_i as calculated by the `daophot/phot`. It is recommended that σ_i be increased by a factor $\eta \approx 1.5$ to correctly estimate the rms error of the data points (see e.g. Agarwal & Gupta, 2015; Gaur et al., 2012b). The result is then compared to a critical value $\chi^2_{\alpha,\nu}$ with a significance level α and $\nu = N - 1$ degrees of freedom. Variability can be claimed if $\chi^2 \geq \chi^2_{\alpha=0.001}$, while the source can be claimed possibly variable if $\chi^2_{\alpha=0.01} < \chi^2 < \chi^2_{\alpha=0.001}$ (Agarwal & Gupta, 2015; de Diego, 2010).

However, since the χ^2-test does not test for variability against a non-variable reference source, variability may be found where there is none. This can occur, for example, when the seeing is not ideal for photometry, which will tend to increase the variance of the measured magnitude. If this extrinsic variability is larger than

the rms errors calculated by `IRAF`, variability may be wrongly detected by the χ^2-test.

5.8.2 Results of the variability statistical tests

As discussed in the previous sections, long-term optical monitoring was performed with Watcher for several H.E.S.S detected blazars. Many of the monitored sources exhibit large magnitude changes due to outbursts and flares during the observation period, that show, even by eye, clear variability. The statistical tests described in Sect. 5.8.1 are typically used to quantify or search for low amplitude variability. However, they can also be used to determine from the data when a source starts to show large amplitude changes. This can be used, in future work, to provide alerts the onset of flare events. The variability timescales were not calculated for the sources, since with the low cadence of the Watcher data during flares, a variability timescale would not be reliable, while no significant brightness changes were recorded with SHOC.

The results of the variability tests (see Sect. 5.8) performed for the sources observed with Watcher are presented in Tab. 5.4.

The results of the variability tests performed for the data taken with the SAAO 1.0-m SHOC instrument are presented in Tab. 5.5. Many of the sources observed showed variability or potential variability.

5.8.3 Watcher discussion

In this section I discuss the results of the long-term monitoring of the Watcher sources. The statistical tests used to consider variability were the χ^2-test, F-test, scaled F-test and the power-enhanced F-test. The tests generally agree with each other, although the χ^2-test may detect variability the other tests might not (see Sect. 5.8.1.4). The different F-test are well in agreement with each other for the majority of DLCs. The power-enhanced F-test appears to be the most robust method for detecting variability, which can be attributed to the increased degrees of freedom included in the test.

5.8.3.1 SHBL J001355.9-185406

A BL Lac object ($z = 0.09485$), SHBL J001355.9-185406 was observed during 2015 - 2016 in the R, V and i' filters. It was found to be variable in the i', R and V filters by the χ^2-test, F-test and power-enhanced F-test. The scaled F-test,

Table 5.4: Results of the variability tests performed on the Watcher monitored blazars. The variability tests performed were the χ^2-test, F-test, scaled F-test and the power-enhanced F-test for the observation periods (Obs Start-End), and filters (Filter), with an indication whether the source displays variability (V), possible variability (PV) or no variability (N).

Name	Observation		Filter	χ^2-test		F-test			Scaled F-test			Enhanced F-test	
	Start	End		χ^2-value	Variable?	F_1	F_2	$F_{\rm avg}$	Variable?	F_2^s	$F_{\rm avg}^s$	Variable?	$F_{\rm enh}$	Variable?
SHBL J001355.9-185406	2015/05	2016/10	i'	975.89325	V	4.98540	5.07946	5.03243	V,V,V	2.69758	2.79723	V,V,V	23.85131	V
	2015/05	2016/10	R	533.05313	V	7.79459	7.42112	7.60785	V,V,V	2.85150	2.74014	V,V,V	41.35892	V
	2015/05	2016/10	V	383.22101	V	4.28726	4.33964	4.31345	V,V,V	1.95889	2.01967	PV,PV,PV	10.04940	V
KUV 00311-1938	2015/07	2016/10	R	2683.39327	V	16.21311	17.40535	16.80923	V,V,V	26.61726	14.71036	20.66381	V,V,V	14.54042	V
RGB J0152+017	2015/05	2016/10	R	2006.90781	V	128.16249	137.07384	132.61816	V,V,V	19.02986	21.12574	20.07780	V,V,V	11.94451	V
PKS 0301-243	2015/06	2017/01	R	15977.90335	V	239.97421	239.70542	239.83982	V,V,V	186.62781	228.27533	207.45157	V,V,V	48.21607	V
PKS 0447-439	2015/07	2017/01	i'	47159.38457	V	31.50713	28.20231	29.85472	V,V,V	33.69346	28.47282	31.08314	V,V,V	116.86522	V
	2015/07	2017/01	R	42004.15262	V	23.60670	19.39586	21.50128	V,V,V	26.78937	19.10407	22.94672	V,V,V	4.69346	V
	2015/05	2017/05	i'	467.24676	V	6.10119	3.69927	4.90023	V,V,V	3.59542	2.52350	3.05946	V,V,V	12.31638	V
IRXS J101015.9-311909	2015/05	2017/05	R	349.01278	V	6.10119	3.69927	4.90023	V,V,V	2.52960	2.53338	2.53149	V,V,V	7.47451	V
	2015/05	2017/05	V	176.84902	V	1.94983	1.85707	1.90345	N,N,N	2.25515	1.40437	1.82976	V,N,PV	4.83564	V
	2015/05	2017/05	i'	38.68781	N	1.13107	0.88445	1.00776	N,N,N	0.93259	1.41143	1.17201	N,N,N	0.62293	N
IES 1101-232	2015/05	2017/05	R	77.05780	V	1.36489	0.87654	1.12072	N,N,N	1.15646	1.75987	1.45817	N,N,N	1.00090	N
3C 279	2015/05	2017/05	R	16488.67152	V	77.85352	72.14444	74.99898	V,V,V	138.89218	64.89083	101.89151	V,V,V	50.47133	V
	2015/05	2017/03	R	539.03103	V	9.02203	6.70835	7.86519	V,V,V	8.64039	6.00638	7.32339	V,V,V	13.08140	V
IES 1312-423	2015/05	2017/03	V	321.19751	V	10.27869	10.24933	10.26401	V,V,V	9.17759	9.23222	9.20491	V,V,V	16.69890	V
PKS 1510-089	2015/05	2016/06	i'	98287.95300	V	278.94975	274.18598	276.56786	V,V,V	263.42557	265.10250	264.26404	V,V,V	458.60421	V
	2015/05	2016/06	V	35346.58818	V	121.00390	119.53368	120.26879	V,V,V	127.25512	125.07596	126.16554	V,V,V	8.64615	V
	2015/05	2016/08	i'	17286.05263	V	88.87866	82.55936	85.71901	V,V,V	25.70423	21.02004	23.36214	V,V,V	29.18038	V
AP Librae	2015/05	2016/08	R	10115.77262	V	20.19511	18.87961	19.53736	V,V,V	5.47734	4.61221	5.04477	V,V,V	3.86107	V
	2016/05	2016/08	V	29236.61363	V	2.80788	4.46413	3.63600	PV,V,V	1.69498	2.23898	1.96698	PV,V,V	2.16179	V
	2015/05	2017/06	i'	5846.47027	V	11.82661	10.76975	11.29818	V,V,V	19.12995	9.75247	14.44121	V,V,V	15.92624	V
PG 1553+113	2015/05	2017/06	R	23321.79333	V	11.23840	11.40203	11.32021	V,V,V	25.04420	10.28415	17.66418	V,V,V	9.01282	V
	2015/05	2017/06	V	5848.53848	V	9.49420	8.21361	8.85391	V,V,V	34.34861	7.74804	21.04832	V,V,V	10.07449	V
PKS 2005-489	2015/05	2017/06	R	22175.30503	V	3.65757	4.60345	4.13051	V,V,V	2.77198	4.91270	3.84234	V,V,V	11.66837	V
	2015/07	2016/09	i'	98673.20436	V	200.06956	203.69710	201.88333	V,V,V	229.64415	313.58632	271.61524	V,V,V	87.69645	V
PKS 2155-304	2015/07	2016/09	R	68925.58090	V	154.03347	157.91184	155.97265	V,V,V	176.39525	236.29689	206.34607	V,V,V	46.08234	V

Table 5.5: Results of the variability tests performed on the 3FHL BCUs and unassociated sources observed with the SAAO 1.0-m SHOC instrument. The variability tests performed were the χ^2-test, F-test, scaled F-test and the power-enhanced F-test for the observation dates (Obs date), and filters (Filter), with an indication whether the source displays variability (PV) or no variability (N).

Name	Obs date	Candidate	χ^2-test		F-test				Scaled F-test				Enhanced F-test	
			χ^2-value	Variability	F_1	F_2	$F_{\rm avg}$	Variability	F_1^s	F_2^s	$F_{\rm avg}^s$	Variability	$F_{\rm enh}$	Variability
3FHL J0802.2-0943	2017/03/03		908.84122	V	1.17537	0.68328	0.92932	N,N,N	1.02132	1.03151	1.02642	N,N,N	1.32695	PV
3FHL J0813.7-0353	2017/02/25	C1	1679.39812	V	2.37437	1.93086	2.15262	V,V,V	2.00709	2.77284	2.38997	V,V,V	5.28313	V
	2017/02/25	C2	2589.72698	V	2.83703	2.46835	2.65269	V,V,V	2.64696	4.23450	3.44073	V,V,V	6.78132	V
	2017/02/25	C3 1	999.06686	V	5.43184	5.22592	5.32888	V,V,V	2.90910	3.91619	3.41264	V,V,V	16.86380	V
	2017/02/27	C3 2	1271.18140	V	6.32495	7.88623	7.10559	V,V,V	2.21170	3.31444	2.76307	V,V,V	26.72271	V
	2017/02/27	C4	453.20086	V	1.34253	1.46598	1.40426	N,PV,PV	0.68739	0.78027	0.73383	N,N,N	3.77339	V
3FHL J0953.3-7659	2017/03/02		1211.97230	V	1.82163	2.64114	2.23139	V,V,V	1.15541	1.64592	1.40066	N,V,V	5.06711	V
3FHL J1042.2-4128	2017/03/05		538.14452	V	0.94494	1.18226	1.06360	N,N,N	0.84058	0.86089	0.85074	N,N,N	2.42984	V
3FHL J1130.5-7801	2017/03/01		469.08987	N	1.34577	0.72810	1.03693	PV,N,N	1.21649	0.75994	0.98822	PV,N,N	2.72255	V
3FHL J1223.5-3033	2017/02/24		419.27878	V	1.59899	0.89679	1.24789	V,N,N	1.08074	1.17213	1.12644	N,N,N	2.38697	V

however showed variability in the i' and R filters, but only possible variability in the V filter.

5.8.3.2 KUV 00311-1938

KUV 00311-1938, also a BL Lac object ($z = 0.61$), was observed in the R filter from 2015/07 - 2016/10. During the 15 month observing period, KUV 00311-1938 decreased in brightness by ΔR $\sim$ 1 mag.

5.8.3.3 RGB J0152+017

RGB J0152+017 is a galaxy-dominated BL Lac ($z = 0.08$) that was observed in the R filter during 2015/05 - 2016/10. Variability has been detected by all the tests considered.

5.8.3.4 PKS 0301-243

PKS 0301-243 is a BL Lac object ($z = 0.260$) and was observed in the V and R filters from 2015/07 - 2017/01. PKS 0301-243 transitioned from a low to high brightness state (ΔV $\sim$ 1 mag, ΔR $\sim$ 0.8 mag) sometime during 2015/11 - 2016/06, when it was below the horizon during the night.

5.8.3.5 PKS 0447-439

PKS 0447-439 is a BL Lac object with a possible redshift of $z = 0.107$ or $z = 0.343$, was observed in the R and i' filters during 2015/07 - 2016/11. During the observation period, the source showed a steady increase in brightness of ΔR $\sim$ 1.25 and Δi$'$ $\sim$ 1.25 mag.

5.8.3.6 1RXS J101015.9-311909

1RXS J101015.9-311909, a BL Lac ($z = 0.143$), was observed from 2015/05 - 2017/05 in the V, R and i' filters. Variability was found by the tests considered only for the i' and R filters. The χ^2-test and power-enhanced F-test showed variability in the V filter, while no variability and possible variability were found by the F-test and scaled F-test respectively. Therefore, no conclusive results concerning the variability in the V filter can be given.

5.8.3.7 1ES 1101-232

Also a BL Lac object ($z = 0.186$), 1ES 1101-232 was observed by Watcher during 2015/05 - 2017/05 in the R and i' filters. Variability was rejected by all the tests for all filters, except by the χ^2-test in the R filter. It can therefore be concluded that the source showed no variability during the observing period.

5.8.3.8 3C 279

3C 279 is a highly variable FSRQ (see e.g. Isler et al., 2017) at $z = 0.536$that was observed during 2015/05 - 2017/05 in the R filter. The source underwent several flares during this period, but observing conditions did not allow those flares to be observed in detail. Nevertheless, hints of the flares can be seen in the DLC, e.g. MJD = 57200 and MJD = 57500. All the tests considered found variability.

5.8.3.9 1ES 1312-423

1ES 1312-423 is a galaxy-dominated BL Lac ($z = 0.105$) that was observed during 2015/05 - 2017/03 in the V and R filters. The DLC has large magnitude errors of the order of ± 0.1 mag, while the comparison stars are not very stable. Nevertheless, the source shows a clear decrease in brightness of ΔR ~ 0.6 and ΔV ~ 0.6 mag during the observing period.

5.8.3.10 PKS 1510-089

PKS 1510-089 is a FSRQ ($z = 0.36$) that was observed during 2015/05 - 2016/06 in the V and i' filters. The source underwent two large flares during 2015/05 and 2015/07 brightening by Δi‘ $\sim 1.5-2.5$ and ΔV $\sim 1.5-2.5$ mag from the quiescent state respectively.

5.8.3.11 AP Librae

AP Librae is a BL Lac object ($z = 0.049$) that was observed during 2015/05 - 2016/08 in the V, R and i' filters. Variability in all the filters were found by the tests considered.

5.8.3.12 PG 1553+113

PG 1553+113 is a BL Lac object ($z = 0.36$) that was observed in the V, R and i' filters during 2015/05 - 2017/06. Variability in all the filters were found by all the

tests. Magnitude differences of $\Delta i' \sim 0.6$, $\Delta R \sim 0.7$ and $\Delta V \sim 0.6$ were observed during the entire observing period.

5.8.3.13 PKS 2005-489

A BL Lac ($z = 0.017$), PKS 2005-489 was observed in the R filter during 2015/05 - 2017/06. PKS 2005-489 exhibited a large brightness change of $\Delta R \sim 0.8$ mag during the observation period. An extensive $\Delta R \sim 0.6$ mag brightening can also be seen starting MJD ≈ 57500 and lasting ~ 5 months, before returning to quiescent brightness levels.

5.8.3.14 PKS 2155-304

PKS 2155-304, a BL Lac object ($z = 0.116$) was observed during 2015/07 - 2016/09 in the R and i' filters. PKS 2155-304 underwent a $\Delta i' \sim 0.5$ and $\Delta R \sim 0.45$ mag flare near MJD ≈ 57600. During the observation period, PKS 2155-304 exhibited a $\Delta i' \sim 0.9$ and $\Delta R \sim 0.75$ mag brightness change, calculated to just before the flare.

5.8.4 SHOC discussion

In this section I discuss the search for IDV in the five 3FHL BCUs and one unassociated 3FHL source that was observed with the SAAO 1.0-m SHOC instrument. The sources were observed in order to help identify their optical counterpart and confirm their AGN nature. This was especially important for 3FHL J0813.7-0353, which could only be localized to five optical candidates. However, only four of the optical candidates were detectable with SHOC.

5.8.4.1 3FHL J0802.2-0943

IDV of 3FHL J0802.2-0943, observed on 2017/03/03, was accepted only for the χ^2-test. Possible IDV was found by the power-enhanced F-test. The F-test and scaled F-test did not find any IDV.

5.8.4.2 3FHL J0813.7-0353

Four optical candidates for 3FHL J0813.7-0353 were observed on 2017/02/25 (C1, C2 and C3) and 2017/02/27 (C3 and C4). IDV for all four candidates, including both observations of candidate C3, were found by the χ^2-test and power-enhanced

F-test. In addition, IDV for candidates C1, C2 and both observations of candidate C3 were found by the F-test and scaled F-test as well. Possible IDV was found for candidate C4 by the F-test, while no IDV was found by the scaled F-test. This, unfortunately means the optical counterparts could not be directly identified from the photometry since all shown blazar-like behaviour.

5.8.4.3 3FHL J0953.3-7659

IDV was found for 3FHL J0953.3-7659, observed on 2017/03/02, by all the tests. Although the average F-value for the scaled F-test detected IDV, it did not find IDV with respect to the target and the first comparison star.

5.8.4.4 3FHL J1042.2-4128

IDV for 3FHL J1042.2-4128, observed on 2017/03/05, was found only by the χ^2-test and power-enhanced F-test. IDV was not found by the F-test and scaled F-test.

5.8.4.5 3FHL J1130.5-7801

IDV for 3FHL J1130.5-7801, observed on 2017/03/01, was found only by the power-enhanced F-test. The other tests did not find IDV, possibly due to the unstable DLCs of the comparison stars.

5.8.4.6 3FHL J1223.5-3033

IDV for 3FHL J1223.5-3033, observed on 2017/02/24, was only found by the χ^2-test and power-enhanced F-test. IDV was not found by the F-test and scaled F-test.

A summary of the variability statistical tests for the Watcher and SHOC observations of the TeV detected blazars and 3FHL BCUs are given in Tables 5.6 and 5.7 respectively.

In this chapter, two sets of data have been analysed for variability. The results of a long-term study between 2015 and 2017 by Watcher have been presented and searched for LTV. The observing periods for individual sources typically lasted for no less than a year. Several of the sources monitored by Watcher experienced flares, outbursts and state changes during the observing period. Further, all the sources tested for LTV, except 1ES 1101-232, exhibited variability, as is expected

Table 5.6: Summary of the variability tests for the TeV detected blazars observed with Watcher. The results show which sources display variability (V), possible variability (PV) or no variability (N).

Name	Obs time		Filter	χ^2-test	F-test	Scaled F-test	Enhanced F-test
SHBL J001355.9-185406	2015/05	2016/10	i'	V	V	V	V
	2015/05	2016/10	R	V	V	V	V
	2015/05	2016/10	V	V	V	PV	V
KUV 00311-1938	2015/07	2016/10	R	V	V	V	V
RGB J0152+017	2015/05	2016/10	R	V	V	V	V
PKS 0301-243	2015/06	2017/01	R	V	V	V	V
PKS 0447-439	2015/07	2017/01	i	V	V	V	V
	2015/07	2017/01	R	V	V	V	V
1RXS J101015.9-311909	2015/05	2017/05	i'	V	V	V	V
	2015/05	2017/05	R	V	V	V	V
	2015/05	2017/05	V	V	N	PV	V
1ES 1101-232	2015/05	2017/05	i'	N	N	N	N
	2015/05	2017/05	R	V	N	N	N
3C 279	2015/05	2017/05	R	V	V	V	V
1ES 1312-423	2015/05	2017/03	R	V	V	V	V
	2015/05	2017/03	V	V	V	V	V
PKS 1510-089	2015/05	2016/06	i'	V	V	V	V
	2015/05	2016/06	V	V	V	V	V
AP Librae	2015/05	2016/08	i'	V	V	V	V
	2015/05	2016/08	R	V	V	V	V
	2016/05	2016/08	V	V	V	V	V
PG 1553+113	2015/05	2017/06	i'	V	V	V	V
	2015/05	2017/06	R	V	V	V	V
	2015/05	2017/06	V	V	V	V	V
PKS 2005-489	2015/05	2017/06	R	V	V	V	V
PKS 2155-304	2015/07	2016/09	i'	V	V	V	V
	2015/07	2016/09	R	V	V	V	V

for AGN. Further, results obtained with the SAAO 1.0-m SHOC instrument as part of a campaign to classify 3FHL BCUs and unassociated sources were presented. The results were used to test for IDV in these sources, since this provides strong evidence that these sources are indeed blazars, which are known to be variable on short timescales. Further, the non-detection of optical IDV in an unclassified blazar, can provide clues to the nature of the source, for example whether the blazar is low or high synchrotron peaked (see e.g. Gaur et al., 2012a; Gupta et al., 2016), which in turn can help with spectroscopic classification. In the next chapter, optical spectroscopic results are presented for a sample of 3FGL and 3FHL BCUs and unassociated sources that were observed with the SAAO 1.9-m SpUpNIC instrument in order to classify them as BL Lacs or FSRQs.

Table 5.7: Summary of the variability tests for the 3FHL BCUs observed with SHOC. The results show which sources display variability (V), possible variability (PV) or no variability (N).

Name	Obs time	Candidate	χ^2-test	F-test	Scaled F-test	Enhanced F-test
3FHL J0802.2-0943	2017/03/03		V	N	N	PV
3FHL J0813.7-0353	2017/02/25	C1	V	V	V	V
	2017/02/25	C2	V	V	V	V
	2017/02/25	C3 1	V	V	V	V
	2017/02/27	C3 2	V	V	V	V
	2017/02/27	C4	V	PV	N	V
3FHL J0953.3-7659	2017/03/02		V	V	V	V
3FHL J1042.2-4128	2017/03/05		V	N	N	V
3FHL J1130.5-7801	2017/03/01		N	N	N	V
3FHL J1223.5-3033	2017/02/24		V	N	N	V

Chapter 6

Optical spectroscopic observations of the blazar candidates

This chapter presents the results of the spectroscopic observations of the sample of 3FHL BCUs, the 3FHL unassociated source and 3FGL blazar candidates undertaken with the SAAO 1.9-m SpUpNIC grating spectrograph. The sources were observed in order to classify them and determine their redshifts where possible. Increasing the number of known γ-ray loud blazars will improve our understanding of blazar physics, in particular the identification of unusual sources such as misaligned AGN and γ-ray loud Seyfert galaxies. The distance to the source is also important since VHE emission ($\gtrsim 10$ GeV) from extragalactic sources is only detectable up to a redshift of $z \approx 1$ because of $\gamma\gamma$ absorption with EBL photons. It is therefore important to find the distance of γ-ray emitting sources if they are to be studied with IACTs. This chapter is set out as follows: Section 6.1 reviews the technical details of the SAAO 1.9-m telescope and SpUpNIC grating spectrograph; Section 6.2 details the procedures that were followed to reduce and extract the spectra of the sources observed; Sect 6.3 discusses the spectroscopy results.

6.1 Instrumentation

I undertook three observing campaigns with the SAAO 1.9-m SpUpNIC grating spectrograph located at the SAAO observatory 18 km east of Sutherland in order to classify 3FHL and 3FGL BCUs and unassociated sources. The campaigns were undertaken during July/August 2016, February 2017 and August/September 2017.

This section will present the details of the SAAO 1.9-m Cassegrain reflector and the SpUpNIC grating spectrograph.

6.1.1 SAAO 1.9-m telescope

The SAAO 1.9-m telescope was built by Grubb Parsons between 1938-48 for the Radcliffe Observatory, Pretoria, South Africa, and was moved to the SAAO Sutherland Observatory in 1976 (Glass, 1989). Observations are done from the Cassegrain focus (f/18, plate scale ~ 6 arcsec/mm). Three instruments are currently available: the HIgh speed Photo-POlarimeter (HIPPO); SHOC and the SpUpNIC grating spectrograph.

All observations with the SAAO 1.9-m telescope are carried out on the east side of the pier and the observing limits of the telescope are shown in Fig. 6.1. Caution must be taken when observing with SpUpNIC, since the large size of the instrument mounting will influence the observing limits and the instrument can potentially collide with the north pier when pointing east to declinations between $-60°$ and $-80°$.

The Telescope Control Software (TCS) user manual[1] was consulted for the use of the 1.9-m acquisition, guiding and telescope control procedures.

6.1.2 The SpUpNIC grating spectrograph

This section describes the instrumentation and operation of the upgraded grating spectrograph SpUpNIC (Spectrograph Upgrade: Newly Improved Cassegrain, Crause et al., 2016).

The basic elements of SpUpNIC's internal layout during arc and science exposures are presented in Fig. 6.2. Light entering the spectrograph passes through the central hole in the Guide mirror, used by the TCS to perform guiding, before passing through the order blocking filters and then the variable width entrance slit. The slit has a length corresponding to 2 arcminutes on the sky and the width can be adjusted from 0.15 to 4.2 arcseconds in 0.15 arcseconds increments. The light passing through the slit is collimated onto the diffraction grating before being re-focused onto an E2V CCD42-10 CCD (2048×512 pixels) which is cooled to ~ 168 K with liquid Nitrogen.

The Guide mirror (inclined at 45° to the beam) can be inserted into the beam, redirecting the light in the centre of the FoV to the Guide camera. This allows

[1]Available at `https://topswiki.saao.ac.za/index.php/74"_/_1.9m`

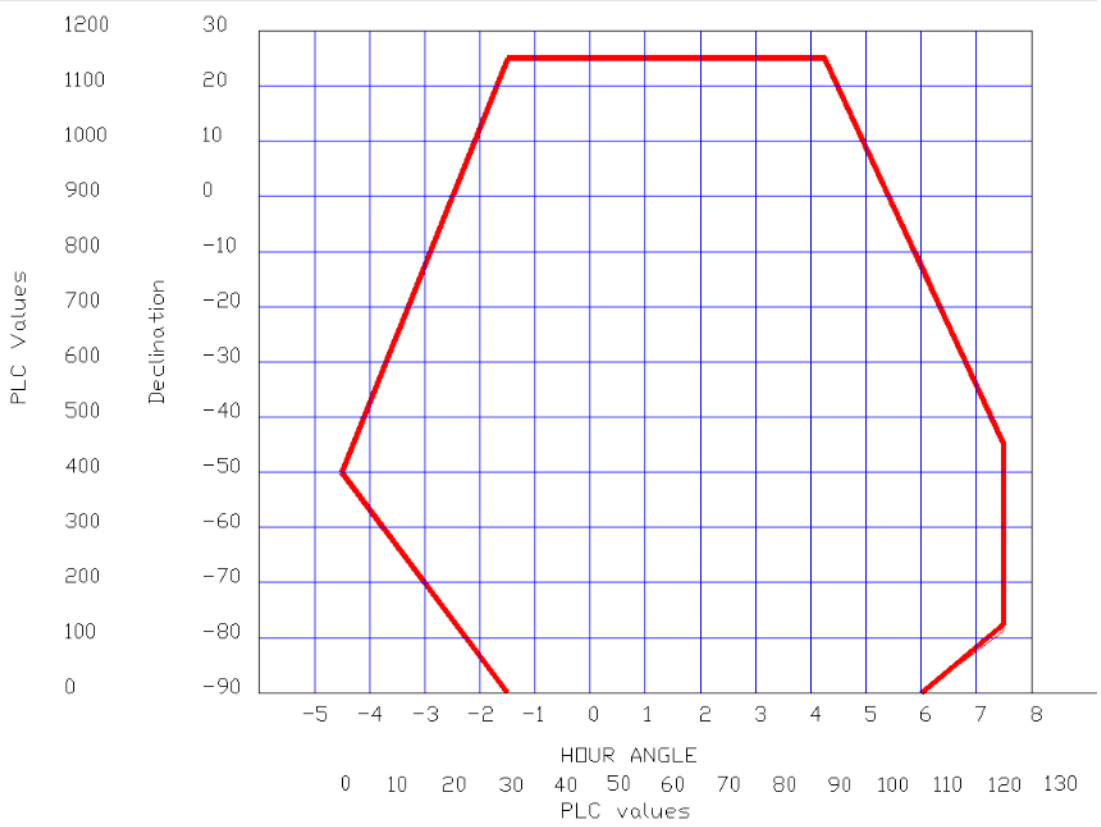

Figure 6.1: The observing limits of the SAAO 1.9-m telescope. Available at `www.saao.ac.za/science/facilities/telescopes/1-9m/`

the target to be easily positioned on the slit, or the pointing to be checked when the telescope is moved to a new target.

The spectrograph also has a rear-of-slit mirror, which can be used to view the slit from the rear. The rear-of-slit camera can be used to easily adjust the position of the target on the slit before exposures. Since the light paths to the rear-of-slit camera and the CCD are the same length, this also allows the rear-of-slit camera to be used to adjust the telescope focus.

Two hollow-cathode arc lamps (CuAr and CuNe) are permanently installed in the spectrograph. The arc mirror is moved into the beam by the control software when arc exposures are taken.

Access to the diffraction gratings is at the bottom of the spectrograph. The gratings are magnetically encoded to allow for automatic software identification when they are inserted. Control of the grating angles is motorised and the grating angle locked with a pneumatically-actuated locking clamp. Table. 6.1 shows the different diffraction gratings available for use with SpUpNIC. These gratings are the same as the ones used with the old Grating Spectrograph. The wavelength

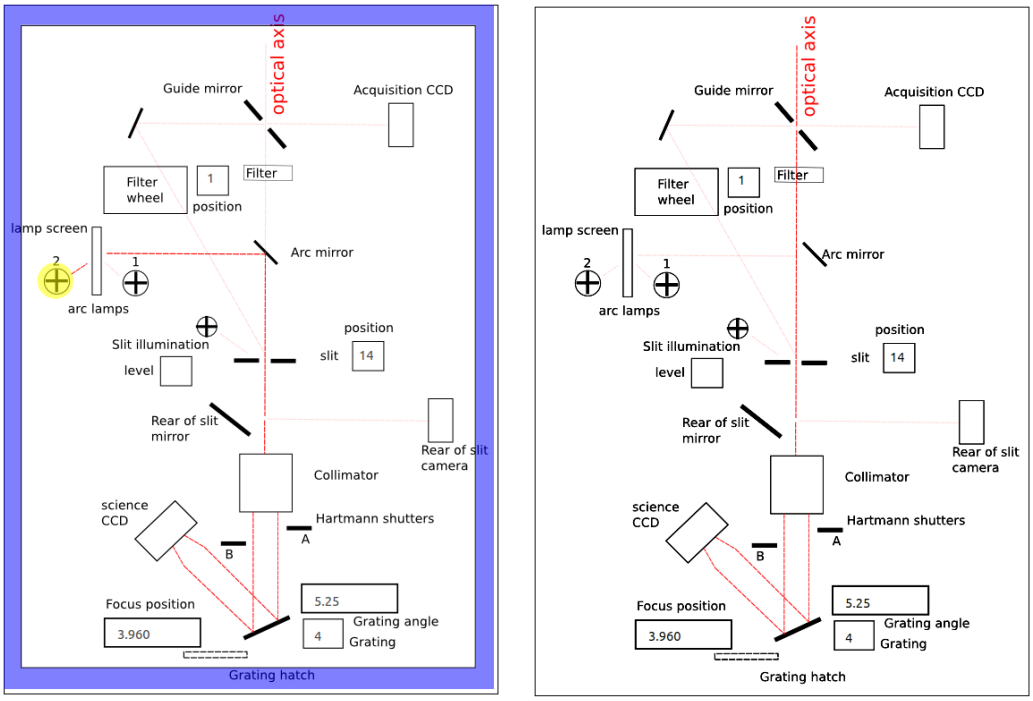

(a) GUI status when when arc exposures are being taken.

(b) GUI status when science exposures are being taken.

Figure 6.2: Two different states of SpUpNIC's interactive display of the controller status with the light path displayed (red dashed line) when arc exposures (a) and science exposures (b) are being taken. Available at `topswiki.saao.ac.za/index.php/SPUPNIC`.

range of diffraction gratings depend strongly on the grating angle as shown in Fig. 6.3 for grating 7.

6.1.3 The SpUpNIC control software

The spectrograph is controlled by the SpUpNIC control software, which controls the instrument and data acquisition. The main interface of the GUI is shown in Fig. 6.4 and consists of six panels:

- Target info,
- Instrument setup,
- Log/warnings,
- Exposure/CCD info, and
- a graphical view of all controllers' statuses.

Table 6.1: Grating characteristics of the available gratings for the SAAO 1.9-m SpUpNIC spectrograph. (Kilkenny & Worters, 2014, p. 71)

Grating	Lines (mm^{-1})	Order	Dispersion (Å mm^{-1})	Wavelength range (Å)	Blaze (Å)	Resolution (Å)
4	1200	1	50	800	4600	1
5	1200	1	50	800	6800	1
		2	20	350	3400	0.5
6	600	1	100	1600	4600	2
7	300	1	210	4200	4600	5
8	400	1	155	2300	7800	4
		2	75	1150	3900	2
9	830	1	65	690	7800	1.5
		2	30	480	3900	0.7
10	1200	1	50	800	10000	1
11	600	1	100	1600	10000	2
12	300	1	210	4200	10000	5

The Target info panel shows information regarding the object currently being observed with the current time (SAST and UT), observing catalogue, target name and coordinates displayed.

The Instrument setup panel displays information regarding the camera focus, slit width, grating, grating angle and order blocking filter. It also displays information regarding the Hartmann focusing procedure, used to find an optimal camera focus at the start of the observing run. The values in this panel can be changed. Changing the grating angle or slit width will also adjust them on the spectrograph itself. When gratings are changed, the control software will automatically select the correct blocking filters for the inserted grating.

The Log/warnings panel displays information regarding changes to individual spectrograph components and when the CCD begins an exposure or performs a readout. It also records any warnings or failures that occur. In addition, this panel indicates the current CCD temperature, which will change colour if the CCD temperature is outside the allowed range.

The Exposure/CCD info panel is used to perform the observations. It displays the observation information i.e. exposure type, exposure time, target name and remaining exposure time.

The last panel, displays a schematic of the spectrograph's status. Many of SpUpNIC's processes can be controlled from this panel simply by clicking on the appropriate icons. For example, by clicking the arc mirror icon, the software will insert the arc mirror into the beam, activate the arc lamp appropriate for the inserted grating and change the exposure type to Arc. Similarly, by again selecting

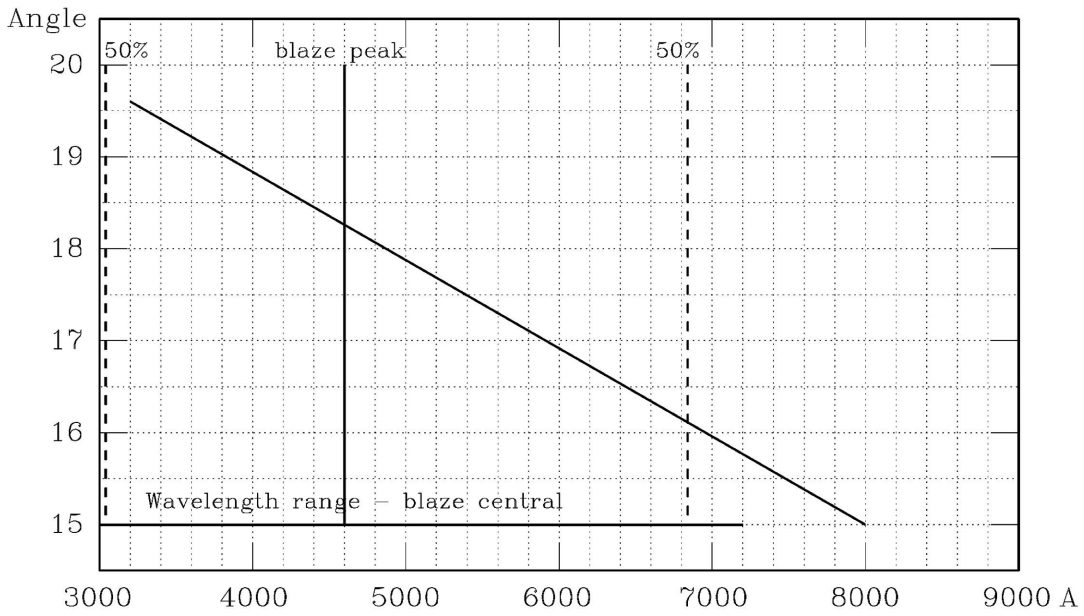

Figure 6.3: Grating 7's wavelength response to the grating angle (Kilkenny & Worters, 2014, fig. 9.5).

the arc mirror, the arc lamp is turned off, the arc mirror moved out of the beam and the exposure type changed back to the previous setting. The guide mirror and rear-of-slit mirror can also be inserted into or removed from the beam by simply clicking on it.

6.2 Data reduction of CCD spectroscopy

6.2.1 Pre-reduction

Before spectra can be extracted from the observations, the raw CCD data need to be pre-reduced. The procedures followed for spectroscopic observations differ slightly from the reduction procedures used when performing photometry (see Section 5.2). Bias and dark corrections applied to spectroscopic data is the same as those done for photometric data. A series of bias frames was taken at the beginning of the observations and combined into a master bias frame, which was subtracted from the flat, arc and science frames. No dark exposures were taken, since the dark current from the CCD is negligible.

Only the centre part of the CCD is exposed to light. Therefore, in order to remove the sections of the CCD not exposed to light, the images were trimmed using the **trimsec** parameter in the task **ccdproc** during the bias subtraction.

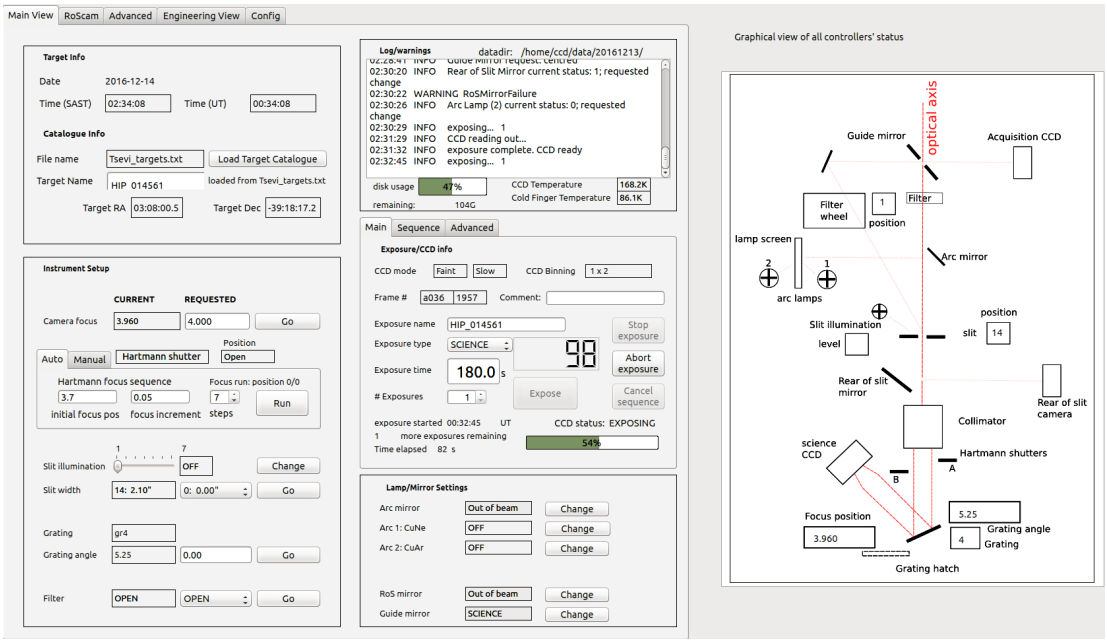

Figure 6.4: The main interface of the SpUpNIC Control Software GUI. The GUI consists of six panels: Target info; Instrument setup; Log/warnings; Exposure/CCD info and an interactive Graphical view of all controllers' status. Available at `topswiki.saao.ac.za/index.php/SPUPNIC`.

6.2.2 Flat correction

In order to perform flat field corrections for spectroscopy, light from a uniform flat field has to be dispersed with the diffraction grating. The flat field used consisted of an artificial light source projected onto a white screen inside the telescope dome. The light source used had a featureless thermal spectrum, which was taken into account when the flat corrections were performed. The dome flats were taken during the day, using the same instrument setup used for the science observations.

A master flat frame was created by combining several flat frames. The master flat frame was then normalized to correct for the shape of the flat field spectrum. The arc and science frames were then divided by the illumination corrected flat frame. This corrects for pixel-to-pixel Quantum Efficiency (QE) variations and illumination variations caused by dust, scattered light and fringing effects.

6.2.3 Wavelength calibration

The data recorded by the CCD are in pixel coordinates which need to be transformed to wavelength (Å) coordinates in the dispersion direction. Arc frames were taken before and after the science exposures. A CuAr arc lamp was used for all

observations during the observing campaigns. The arc frames consist of a measured spectrum of light from an arc lamp which produces emission lines at well calibrated wavelengths. SpUpNIC has two hollow-cathode arc lamps (CuAr and CuNe) with line identification plots available for several gratings at multiple grating angles from the SAAO Grating Spectrograph manual (pp. 85-99 Kilkenny & Worters, 2014).

The `IRAF` task **identify** was used to assign the correct wavelengths to the corresponding emission lines in the arc frames. The wavelengths of the CuAr lines are available in the `IRAF` "cuar.dat" linelist. The task **reidentify** was used to assign the correct wavelengths to all the rows in the two-dimensional arc spectrum and **fitcoords** was used to fit a two-dimensional polynomial to the arc frames, creating a transformation function for converting the $[x, y]$ pixel coordinates to $[\lambda, y]$ wavelength coordinates. This transformation function was applied to the appropriate science frames using the **transform** task to convert them to $[\lambda, y]$ wavelength coordinates.

The sky lines, which extend over the entire CCD image, are curved in the dispersion direction due to geometric distortions caused by the spectrograph optics. This should also be corrected when the **transform** task is run and should be perfectly aligned in the spatial direction of the 2-dimensional spectrum. This provides an additional check to ensure that the wavelength calibration was correctly applied.

6.2.4 Cosmic ray removal

Cosmic rays are recorded in long duration exposures and need to be removed from the data before the background is subtracted, since the column-wise background subtraction will include the cosmic rays in the subtraction, leading to an incorrect background subtraction in the target spectrum. The cosmic rays were removed from the CCD image using the `lacosmic` python module, which detects cosmic rays using Laplacian edge detection and is based on the L.A.Cosmic algorithm developed by (van Dokkum, 2001).[2]

6.2.5 Background subtraction

The background includes spectral lines originating from the Earth's atmosphere and scattered light. The strongest spectral lines are known as telluric lines and are

[2]Available from `https://github.com/larrybradley/lacosmic`

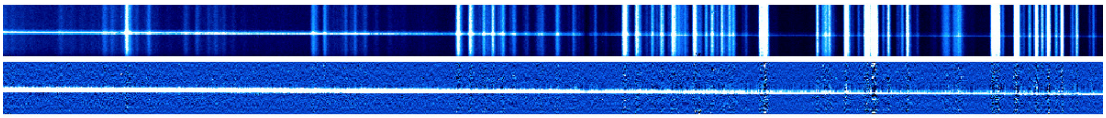

Figure 6.5: A comparison frame before and after background subtraction of 3FHL J0001.9-4155 after basic CCD reductions and cosmic ray cleaning obtained with the SAAO 1.9-m SpUpNIC spectrograph on 2017/08/25. The target spectrum is the bright trace in the x-direction and sky lines are visible in the y-direction of the top frame. The sky lines have been removed in the bottom frame.

produced by excited Oxygen, Nitrogen and Sodium in the atmosphere. Because the telluric lines and scattered background light originates from the atmosphere, they extend over the entire CCD image in the spatial dimension and should be removed from the target spectrum. This was done, for each target frame, using the **background** task. This task fits a polynomial to the image columns, excluding the target spectrum, and subtracts the calculated intensity from each column in the image. This successfully removed the telluric emission lines and scattered background light from the image. An example of the background subtraction results are presented in Fig. 6.5. The next step is to extract the target spectrum from the CCD image.

6.2.6 Extracting the spectra

Each spectrum was extracted using the task **apall** in the **twodspec.apextract** package. This task fits an aperature to the data in the spatial direction. The trace option was used to extract the spectra with optimal aperature sizes. With the trace option used, the position of the target on the 2-dimensional image is determined. The target position is then redetermined at other points along the dispersion axis in steps specified by the user in the **apall** task. A smooth fitting function is then fitted to the aperture positions.

6.2.7 Flux calibration

Several spectrophotometric standard stars were observed, with the same configuration as the science frames, at the start of each night. These standard stars were LTT 1788, 3864, LTT 7987, LTT 9491, Feige 67, EG 274 and CD -32 9927.[3] The standard stars were pre-reduced, wavelength calibrated and extracted using the same procedures as the target frames.

[3]The spectrophotometric standard star data can be found at `www.eso.org/sci/observing/tools/standards/spectra/stanlis.html`.

The **standard** task from the **NOAO.ONEDSPEC** package was used to create an output flux file from the standard star spectrum. A sensitivity curve was created using the **sensfunc** task, using the standard star flux file created in the previous step. The **calibrate** task was then used to apply the sensitivity curve to the science spectra, calibrating the target spectra to absolute physical fluxes.

6.2.8 Spectral analysis methods

The flux calibrated spectra were examined with **splot** and any residual cosmic rays removed. The spectra were also normalized using **splot** by fitting a high order Legendre function to the data and dividing the spectrum with the fitted continuum function.[4] The continuum fitting was performed with **splot** and not the **continuum** task, since **splot** allows residual cosmic rays to be removed during the continuum fitting procedures. The normalized and unnormalized spectra were then combined with the **scombine** task to increase the S/N of the spectra using average combining. The normalized spectra were used to perform the redshift calculations.

6.2.8.1 Redshift measurements

Target redshifts were calculated using the **xcsao** task from the **RVSAO** package (Kurtz & Mink, 1998), which implements the cross-correlation algorithm developed by Tonry & Davis (1979).[5] The **xcsao** task measures redshifts using cross-correlation measurements against template spectra.

The cross-correlation is a measure of similarity between two series as a function of the relative displacement between them. It is normally used in time series analysis, where the lag between two signals are investigated. The **rvsao** package uses cross-correlation to calculate the relative radial velocity displacement between two spectra, i.e. a template spectra with known radial velocity and a spectrum with an unknown radial velocity.

Sections of the target spectra containing telluric lines were masked by setting `fixbad=yes` in the **xcsao** task. A file specifying these sections was created and passed to **xcsao**. These sections were masked because they can influence the redshift measurements in low S/N spectra.

[4] An 8th order Legendre function was used to fit the continuum. No models were fitted to the continuum, therefore, a high order function was needed to remove localized residual excess in the continuum.

[5] The **rvsao** package is available at `tdc-www.harvard.edu/iraf/rvsao/`.

The **xcsao** task Fourier transforms both the target and template spectra. If absorption line templates are used, a high-stop Fourier filter is used to remove high spatial frequency information from the target spectra, thereby removing information which contains more noise than signal. If an emission line template is used, the high-stop filter is not used, as it seriously degrades the measured redshift. A second, low-stop filter is also used to remove any residual large-scale systematics from the target spectra remaining after continuum corrections.

The target spectra are then cross correlated against template spectra to measure the radial velocity difference between the target and template spectra. This method also allows a correlation error to be calculated, which is used to evaluate the confidence in the redshift measurement. The **xcsao** task returns this confidence as the R-value. The cross-correlation templates selected for the redshift analysis were the galaxy and artificial absorption line templates that are included with **RVSAO**. The cross-correlation calculations were performed using all the selected templates and the redshift from the template with the highest R-value was selected.

Kurtz & Mink (1998) recommends a minimum R-value $\gtrsim 3$ for accepting a redshift measurement. The sources observed during this project were mostly low S/N spectra of blazars. Therefore, the R-values returned by the **xcsao** were usually at or just below $R \approx 3$. I, therefore, also visually inspected the target spectra to ensure the redshift measurement was correct. If $R \leq 3$ and only a few lines are identifiable, only a tentative redshift was accepted for the source.

6.2.8.2 Equivalent Width measurements

The `pyspeckit` `Python` package was used to analyse emission lines in the spectra. The package contains tasks to subtract or normalize the spectrum with a fitted continuum. The spectra were normalized with the fitted continuum for this analysis. Spectral lines can also be fitted with Gaussian, Lorentz, Voigt or user defined functions. Various line measurements are automatically calculated for the fitted lines, including integrated flux, FWHM and equivalent widths (W_λ).

The measurements include a returned error if one is included in the spectrum when it is loaded. If no error was set for the spectrum, `pyspeckit` can calculate one, based on the error routines from the **MPFIT** suite (Markwardt, 2009). Of interest for source classification is the W_λ measurements of emission lines, which are used to classify blazars (See Section 2.2.2.2 p. 36). For emission line analysis, a continuum was fitted to spectra with identified emission lines, excluding the

sections with emission, absorption and telluric lines. A Gaussian function was fitted to each emission line and W_λ called from the fitting results.

6.2.8.3 The Ca H&K break

A useful feature in optical spectra often used to separate BL Lacs from normal elliptical galaxies is the Ca H&K break. The Ca H&K break is a stellar absorption feature caused by stars in the halo of giant elliptical galaxies. This feature is diluted by the strong non-thermal emission from the jet (see e.g. Landt et al., 2002). The strength of the Ca H&K break can be parametrized as

$$K_{4000} = \frac{f^+ - f^-}{f^+},$$

where f^- and f^+ are the average flux values between $3750\text{Å} - 3950\text{Å}$ and $4050\text{Å} - 4250\text{Å}$ respectively, in the rest-frame of the AGN (see e.g. Marcha et al., 1996). Dressler & Shectman (1987) defined the value separating AGN from normal elliptical galaxies to be $K_{4000} \sim 50\%$, while Marcha et al. (1996) proposed a value of less than 40% for BL Lacs.

Sources in this study will be classified as BL Lacs if they have emission lines with equivalent widths of $|W_\lambda| \leqslant 5\text{Å}$. A diluted Ca H&K break value of $K_{4000} \sim 40\%$ will be used to separate BL Lacs from non-active galaxies (e.g. Landt et al., 2002; Marcha et al., 1996).

6.3 Results

I observed a selection of 3FHL and 3FGL BCUs and unassociated sources in order to classify them, and if possible, measure their redshifts. Because the targets were faint (V $\sim$ 18) and the catalogue magnitudes were not recently obtained, the faint sources were observed for at least 3600 s in 1800 s exposures. The brighter sources were exposed for at least 2400 s in 1200 exposures. The sources were observed at least twice to allow cosmic ray identification in the spectra. All observations were carried out with grating 7 with a slit width of 1.5"- 1.6" and grating angle of $\approx 16°$, resulting in a wavelength range of $3500 - 9000$ Å and a spectral resolution of 5 Å. Because multiple observation campaigns were carried out, the grating angle could not be reset to the exact angle used previously. A CuAr arc lamp was used for wavelength calibration. Results are reported for the sources listed in Tab. 6.2

Table 6.2: Observation log of 3FHL BCUs and unassociated sources observed with the SpUpNIC spectrograph.

3FHL Name	Observation date	Start time UT	Exposures	Wavelength λ	⟨airmass⟩	⟨seeing⟩ arcsec
J0001.9-4155	2017/08/25	22:20:34	2x1800	4000 - 8500	1.12	1.5
J0002.1-6728	2017/08/25	23:34:10	2x1800	4000 - 8500	1.25	1.4
J0003.3-5248	2017/08/26	00:51:34	2x1800	4000 - 8500	1.08	1.4
J0115.9-2746	2017/08/26	22:52:00	2x1800	4000 - 8500	1.23	1.7
J0305.2-1609	2017/08/27	02:36:18	2x1800	4000 - 8500	1.08	2.2
J0647.0-5138	2017/02/17	19:22:49	2x1800	4000 - 8500	1.09	2.8
J0813.7-0353 C2	2017/02/25	19:48:18	2x1800	4000 - 8500	1.18	2.0
J0813.7-0353 C3	2017/02/25	21:43:41	2x1800	4000 - 8500	1.22	2.0
J0813.7-0353 C4	2017/02/27	20:00:57	2x1800	4000 - 8500	1.15	2.0
J0935.2-1735	2017/02/24	22:46:27	2x1800	4000 - 8500	1.09	1.1
J1042.2-4128	2017/02/25	00:03:33	2x1800	4000 - 8500	1.05	1.3
J1130.5-7801	2017/02/25	01:18:29	2x1800	4000 - 8500	1.6	1.3
J1212.1-2328	2017/02/24	00:53:45	4x1200	4000 - 8500	1.02	1.8
J1223.5-3033	2017/02/25	02:43:40	3x1800	4000 - 8500	1.13	1.3

Table 6.3: Observation log of 3FGL BCUs observed with the SpUpNIC spectrograph.

3FGL Name	Observation date	Start-time UT	Exposures	Wavelength range λ	⟨airmass⟩	⟨seeing⟩ arcsec
J0051.2-6241	2017/08/31	00:17:02	2x1800	3800 - 8500	1.18	1.4
J0256.3+0335	2017/08/31	01:30:45	3x1800	3800 - 8500	1.35	1.5
J1344.5-3655	2016/08/01	18:25:51	2x1200	4000 - 8500	1.23	1.0
J1406.0-2508	2016/07/30	19:36:44	1x1600, 2x1200	4000 - 8500	1.45	1.5
J1507.6-3710	2016/07/30	18:30:18	2x1200	4000 - 8500	1.06	1.8
J1842.3-5841	2017/08/31	19:29:55	3x1800	4000 - 8500	1.13	1.5
J1855.1-6008	2016/08/04	20:28:17	3x1800	4000 - 8500	1.15	1.5
J1944.1-4523	2016/08/01	22:43:27	5x1200	4000 - 8500	1.08	1.5
J1954.9-5640	2016/08/02	01:05:12	3x1200	4000 - 8500	1.36	1.5
J1959.8-4725	2016/08/04	21:38:04	2x1800	3500 - 8500	1.05	2.0
J2338.7-7401	2017/08/28	22:54:34	2x1800	3500 - 8500	1.4	2.0

and Tab. 6.3.

6.3.1 3FHL BCUs and unassociated sources

In this section, the results of the spectroscopic observations of the selection of 3FHL BCU sources are presented. The combined optical spectra of the sources observed with SpUpNIC are presented, with the identified lines indicated. The redshifts calculated by the **RVSAO** package are also indicated on the spectra.

6.3.1.1 3FHL J0001.9-4155

3FHL J0001.9-4155 (Fig. 6.6), observed on 2017/08/25, is a featureless BL Lac object. No redshift could be calculated for this source.

6.3.1.2 3FHL J0002.1-6728

3FHL J0002.1-6728 (Fig. 6.7) was observed on 2017/08/25. The optical spectrum does not exhibit any prominent features and can therefore be classified as a BL

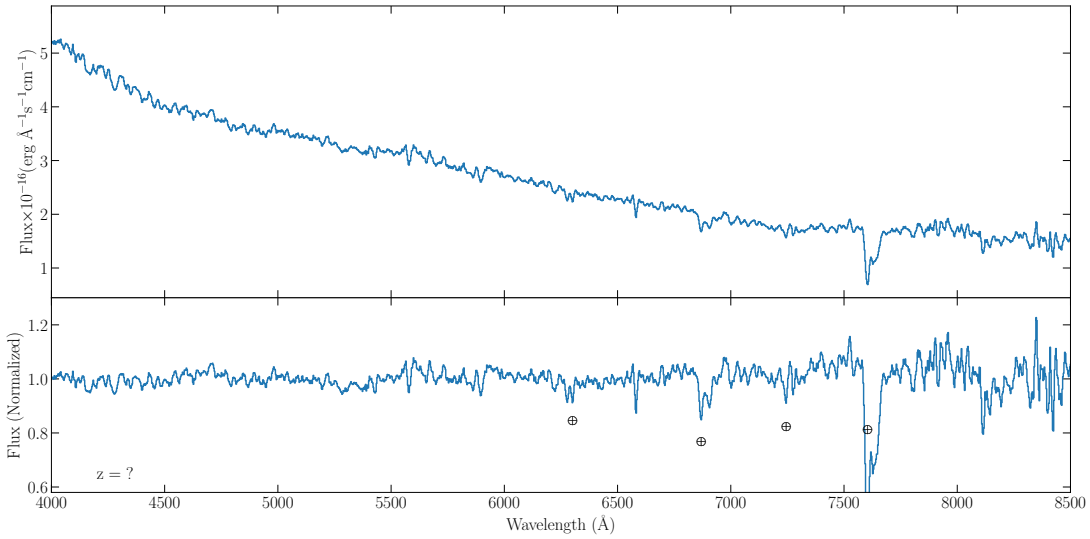

Figure 6.6: The average spectrum of 3FHL J0001.9-4155 observed with SpUpNIC using grating 7. Detected telluric lines are indicated with a $\oplus$. The spectrum has a resolution of ~ 5 Å and a S/N ≈ 29. The spectrum has been smoothed for display purposes using a smoothing box of 5 data points.

Lac object. No redshift could be calculated for this source.

6.3.1.3 3FHL J0003.3-5248

3FHL J0003.3-5248 (Fig. 6.8) was observed on 2017/08/26. No prominent features are present in the spectrum. Therefore, based on the featureless spectrum, the source can be classified as a BL Lac object. No redshift could be calculated for this source.

6.3.1.4 3FHL J0115.9-2746

3FHL J0115.9-2746 (Fig. 6.9) was observed on 2017/08/26. The optical spectrum does not exhibit any prominent features and can therefore be classified as a BL Lac object. No redshift could be calculated for this source.

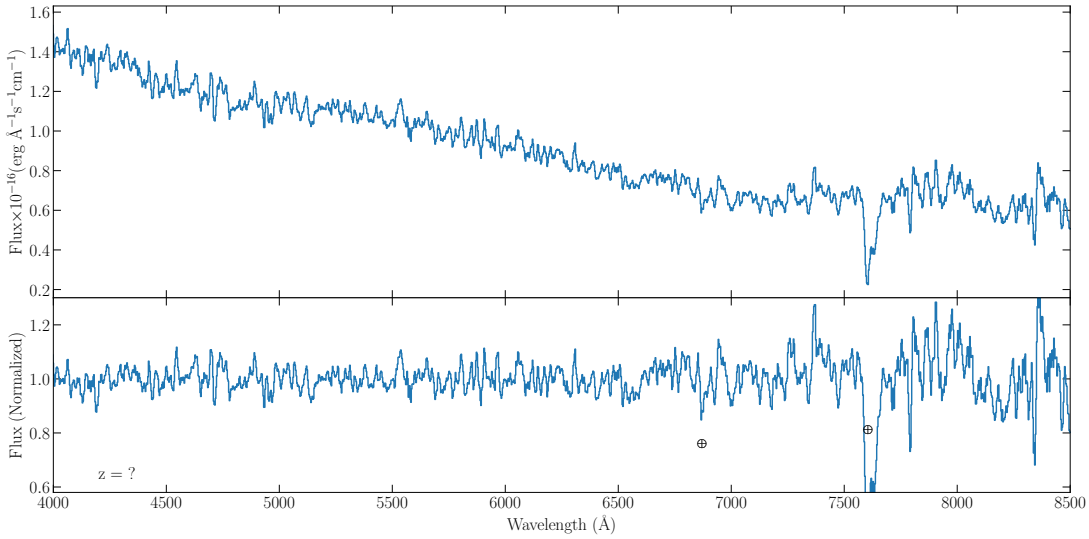

Figure 6.7: The average spectrum of 3FHL J0002.1-6728 observed with SpUpNIC using grating 7. Detected telluric lines are indicated with a ⊕. The spectrum has a resolution of ~ 5 Å and a S/N ≈ 15. The spectrum has been smoothed for display purposes using a smoothing box of 5 data points.

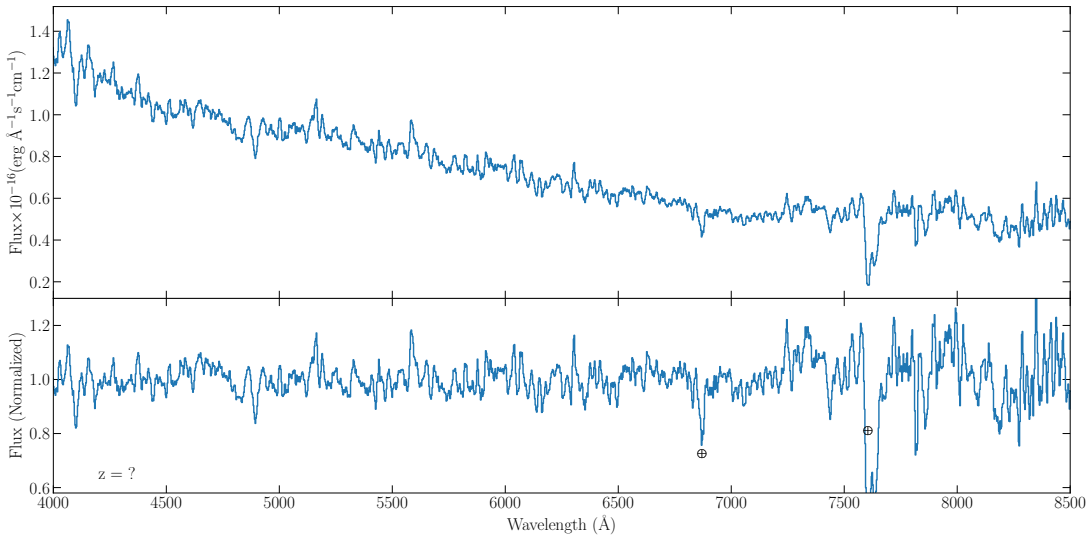

Figure 6.8: The average spectrum of 3FHL J0003.3-5248 observed with SpUpNIC using grating 7. Detected telluric lines are indicated with a ⊕. The spectrum has a resolution of ~ 5 Å and a S/N ≈ 14. The spectrum has been smoothed for display purposes using a smoothing box of 5 data points.

6.3.1.5 3FHL J0305.2-1609

3FHL J0305.2-1609 (Fig. 6.10) was observed on 2017/08/27. A redshift of $z = 0.312 \pm 0.001$ was obtained from the low S/N ~ 8 spectrum. The Ca II H&K,

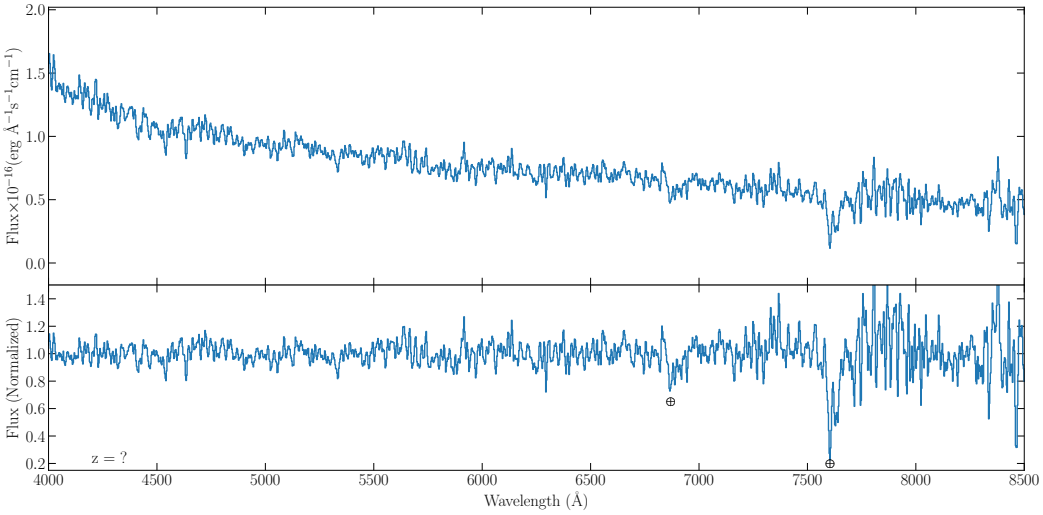

Figure 6.9: The average spectrum of 3FHL J0115.9-2746 observed with SpUpNIC using grating 7. Detected telluric lines are indicated with a $\oplus$. The spectrum has a resolution of ~ 5 Å and a S/N ≈ 11. The spectrum has been smoothed for display purposes using a smoothing box of 5 data points.

G-bandλ4306 and [MgI]λ5174 absorption lines were detected at 4445.0, 4484.3, 44865.8 and 6788.3 Å respectively. Also, the [O II]λ3729 emission line was detected at 4892 Å and has an equivalent width of $|W_\lambda| = 3.8 \pm 0.8$ Å. The source has a measured Ca H&K break of $K_{4000} = 0.21$.

While completing this dissertation, I discovered that the 3FGL counterpart to this source, 3FGL J0305.2-1607, was observed by Paiano et al. (2017) with the 10-m Gran Telescopio Canarias. Their spectrum of 3FGL J0305.2-1607 had a S/N ≈ 80 and is presented in Fig. 6.11. **RVSAO** was able to calculate a redshift from the S/N ~ 8 spectrum obtained during this project that matches their value of $z = 0.312$. The source can be classifed as a BL Lac object.

6.3.1.6 3FHL J0647.0-5138

3FHL J0647.0-5138 (Fig. 6.12), was observed on 2017/02/17. A redshift of $z = 0.2268 \pm 0.0003$ was calculated for this source. The Ca II H&K and G-bandλ4306 absorption lines were detected at 4825.8, 4868.5 and 5282.6 Å respectively. A [O III]4363λ emission line is also detected at 5363 Å with $|W_\lambda| < 4$ Å. A strong absorption feature coincident with LiIλ6707 can also be seen at 8228 Å however, the poor sky subtraction in this part of the spectrum makes the detection of the line uncertain. This source can be classified as a BL Lac object due to the small Ca H&K break ($K_{4000} = 0.15$) and absence of emission lines.

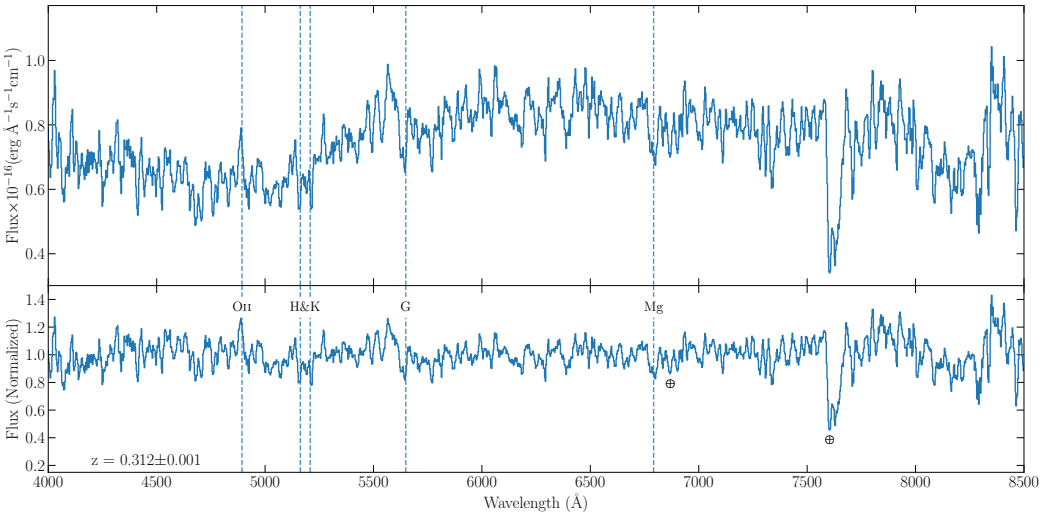

Figure 6.10: The average spectrum of 3FHL J0305.2-1609 observed with SpUpNIC using grating 7. Detected telluric lines are indicated with a ⊕. The spectrum has a resolution of ~ 5 Å and a S/N ≈ 8. The spectrum has been smoothed for display purposes using a smoothing box of 5 data points.

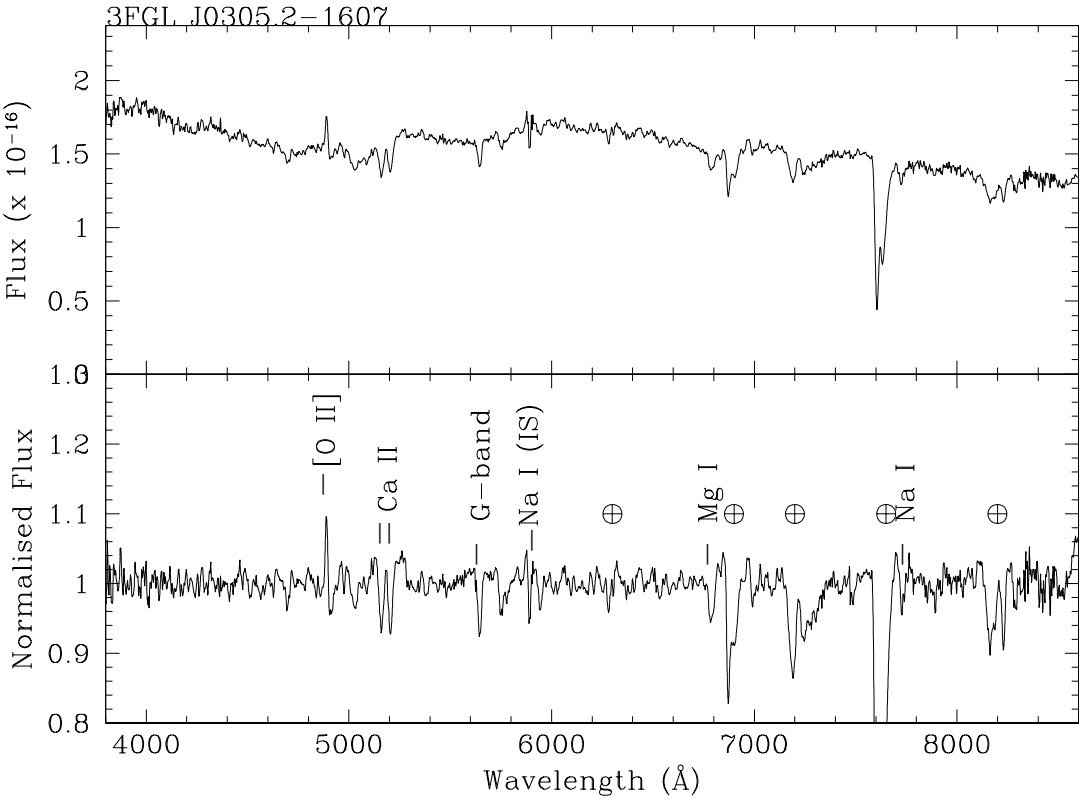

Figure 6.11: Optical spectrum of 3FGL J0305.2-1607 observed with the 10-m Gran Telescopio Canarias. Adopted from Paiano et al. (2017), fig. 2.

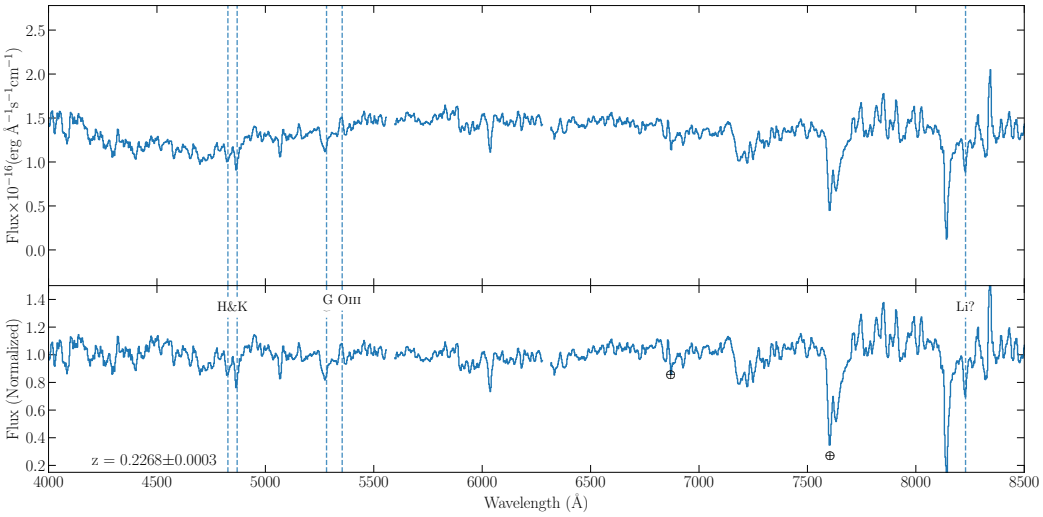

Figure 6.12: The average spectrum of 3FHL J0647.0-5138 observed with SpUpNIC using grating 7. Detected telluric lines are indicated with a $\oplus$. The spectrum has a resolution of ~ 5 Å and a S/N ≈ 13. The spectrum has been smoothed for display purposes using a smoothing box of 5 data points.

6.3.1.7 3FHL J0813.7-0353

Three of the five candidate optical counterparts to 3FHL J0813.7-0353 were observed with SpUpNIC on 2017/02/25 and 2017/02/27 (see 4.2.4, p. 64). Their spectra are presented in Fig. 6.13. A redshift was obtained for the 2nd candidate, while potential redshifts were obtained for the 3rd and 4th candidates.

A redshift of $z = 0.1954 \pm 0.0003$ was calculated for the 2nd candidate, based on the presence of the Ca II H&K and G-bandλ4306 absorption lines at 4703, 4744.7 an 5148.25 Å respectively. Potential OIIIλ5007, MgIλ5174 and NaIλ5894 features can also be seen in the spectrum. This source is not coincident with a radio or X-ray source. The source has a Ca II break of $K_{4000} = 0.28$ and can therefore be classified as a BL Lac.

A potential redshift of $z = 0.261$ was obtained for the 3rd candidate observed. A potential [OII]λ3729 emission line is detected at 4702.2 Å. Potential Ca II H&K, NaIλ5894 and OIλ6300 absorption lines are also detected in the spectrum. This source is not coincident with a radio or X-ray source. No Ca break is visible in the low S/N ≈ 14 spectrum but a higher S/N spectrum is needed for confirmation. Therefore I classify this source as a BL Lac.

The 4th candidate, which is coincident with a radio source, has a potential redshift of $z = 0.192$ based on the potential detection of the [OII]λ3729 emission line and Ca II H&K absorption lines at 4445, 4689 and 4730.4 Å respectively.

There is no Ca II H&K break and as such this source can be classified as a BL Lac object.

Observation of the 1st and 5th candidates are necessary to determine which source is associated with the 3FHL source. The 5th candidate is also coincident with a radio counterpart and could potentially be associated with the 3FHL source.

6.3.1.8 3FHL J0935.2-1735

3FHL J0935.2-1735 (Fig. 6.14), was observed on 2017/02/24. No redshift could be calculated for this source. 3FHL J0935.2-1735 can be classified as a BL Lac object due to the featureless spectrum.

6.3.1.9 3FHL J1042.2-4128

3FHL J1042.2-4128 (Fig. 6.15), was observed on 2017/02/16. A redshift could not be obtained for this BL Lac object, since the features present in the spectrum do not correspond to any absorption or emission lines.

6.3.1.10 3FHL J1130.5-7801

3FHL J1130.5-7801 (Fig. 6.16), was observed on 2017/02/25. A redshift of $z = 0.317 \pm 0.001$ was obtained for this source. The Ca II H&K absorption lines were detected at 5180.6 and 5226.5 Å respectively. A NeIII3869λ emission line was also detected in the spectrum with an equivalent width $|W_\lambda| = 1.6 \pm 0.42$ Å. Potential MgIλ5174 and NaIλ5894 lines can also be seen in the spectrum. The spectrum of 3FHL J1130.5-7801 is dominated by non-thermal emission and has no Ca H&K break. Based on the small W_λ of the NeII emission line and absent Ca H&K break this source can be classified as a BL Lac object.

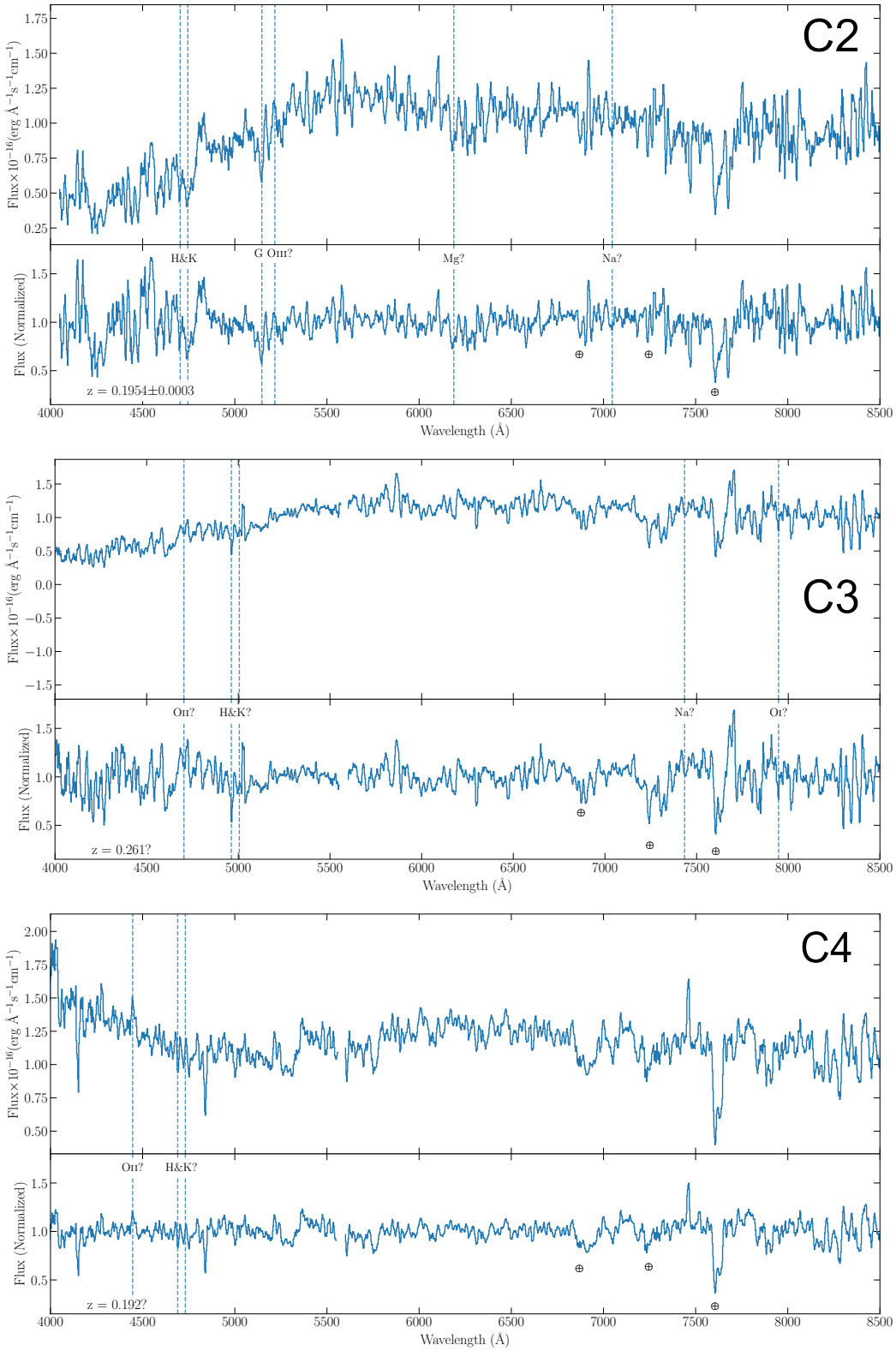

Figure 6.13: Flux calibrated spectra of the three optical candidates of 3FHL J0813.7-0353 observed with SpUpNIC. The candidate number and redshift are displayed on the spectra. The most prominent features in the spectra are also indicated. The telluric lines are indicated with a $\oplus$. The spectra has a resolution of $\sim$ 5 Å. The spectra has been smoothed for display purposes.

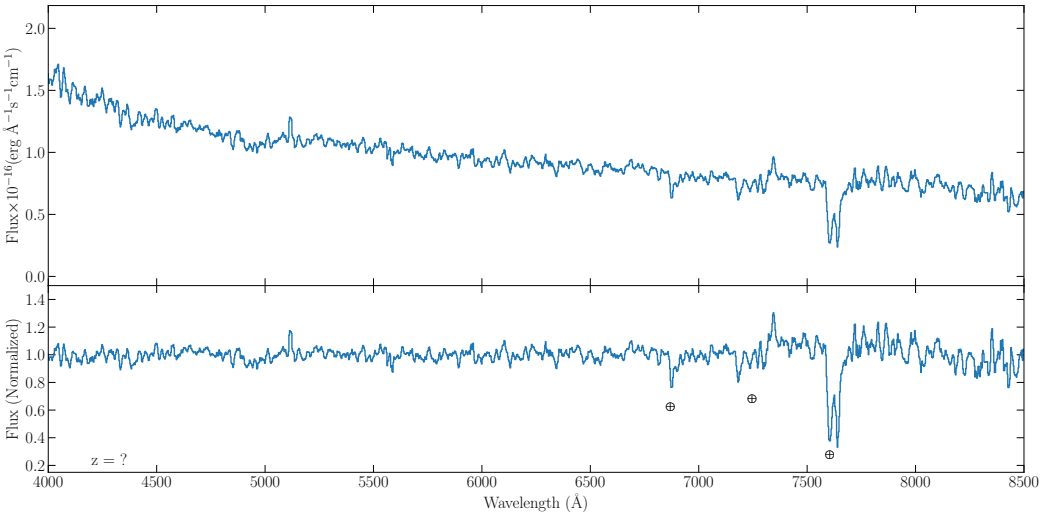

Figure 6.14: The average spectrum of 3FHL J0935.2-1735 observed with SpUpNIC using grating 7. Detected telluric lines are indicated with a $\oplus$. The spectrum has a resolution of ~ 5 Å and a S/N ≈ 16. The spectrum has been smoothed for display purposes using a smoothing box of 5 data points.

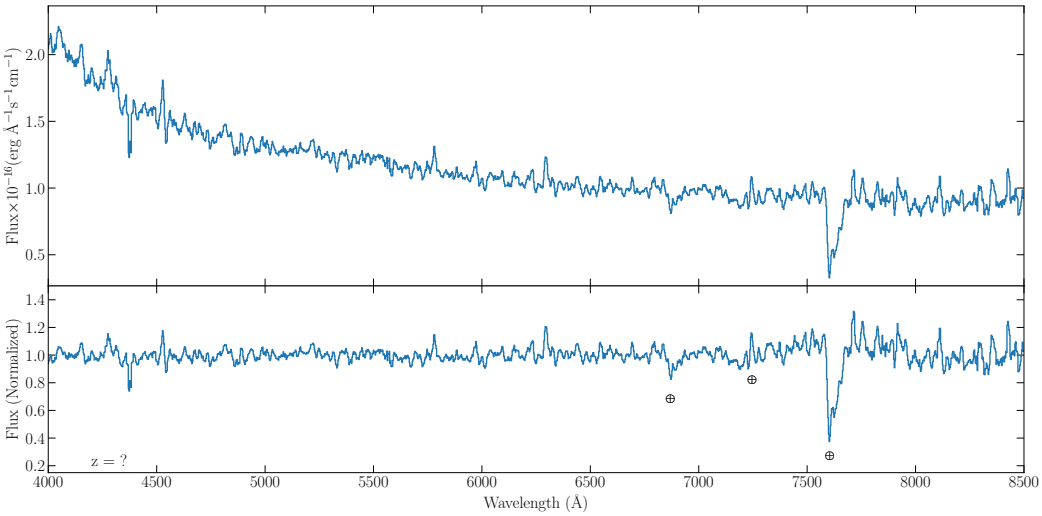

Figure 6.15: The average spectrum of 3FHL J1042.2-4128 observed with SpUpNIC using grating 7. Detected telluric lines are indicated with a $\oplus$. The spectrum has a resolution of ~ 5 Å and a S/N ≈ 16. The spectrum has been smoothed for display purposes using a smoothing box of 5 data points.

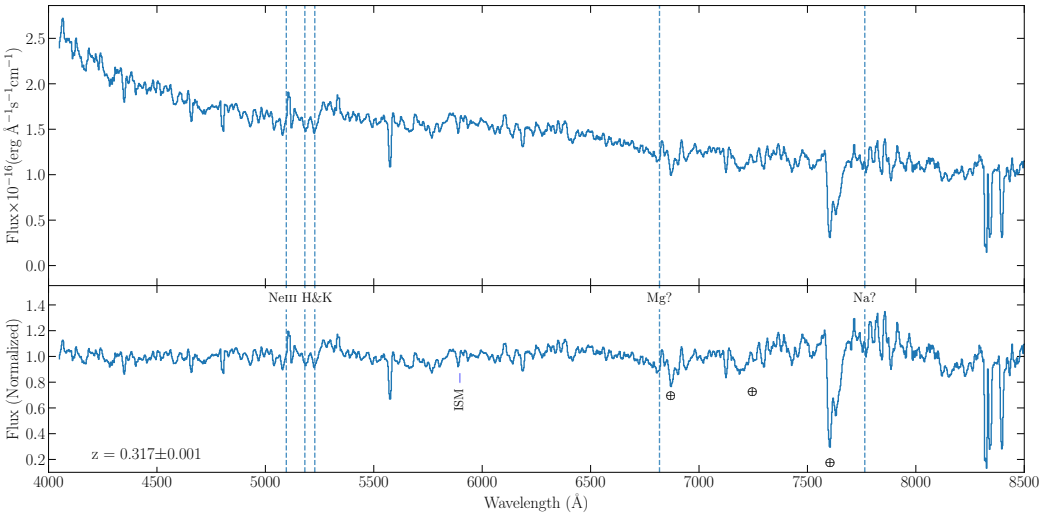

Figure 6.16: The average spectrum of 3FHL J1130.5-7801 observed with SpUpNIC using grating 7. Detected telluric lines are indicated with a $\oplus$. The spectrum has a resolution of ~ 5 Å and a S/N ≈ 16. The spectrum has been smoothed for display purposes using a smoothing box of 5 data points.

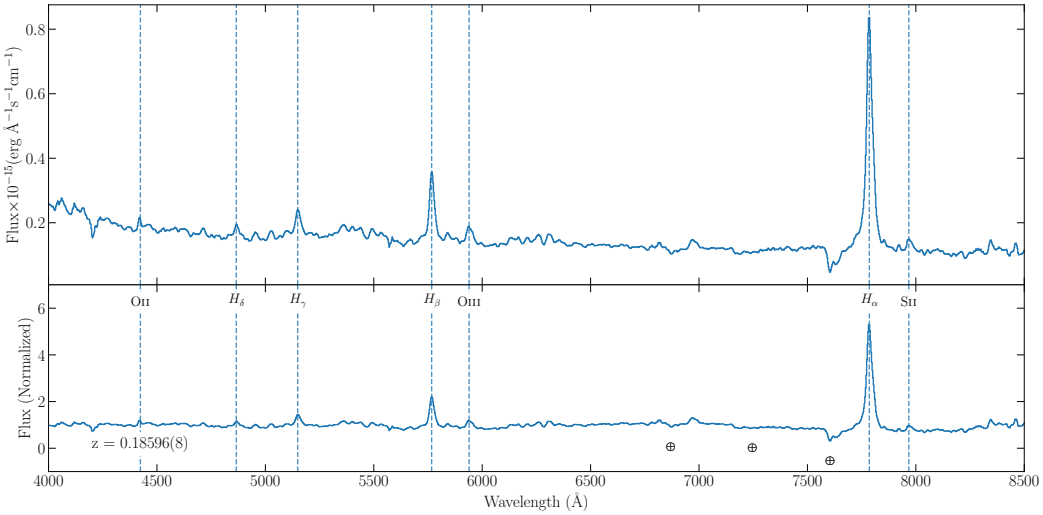

Figure 6.17: The average spectrum of 3FHL J1212.1-2328 observed with SpUpNIC using grating 7. Detected telluric lines are indicated with a $\oplus$. The spectrum has a resolution of ~ 5 Å and a S/N ≈ 50. The spectrum has been smoothed for display purposes using a smoothing box of 5 data points.

6.3.1.11 3FHL J1212.1-2328

There were two optical candidates for 3FHL J1212.1-2328. Unfortunately, the most probable optical candidate was too faint to observe with SpUpNIC. Therefore, the other optical candidate was observed instead in order to eliminate it as the

Table 6.4: Analysis of the brightest emission lines present in the spectrum of the observable optical candidate for 3FHL J1212.1-2328. The corrected integrated flux over the emission line, FWHM, luminosity and equivalent width (W_λ) of the lines are presented.

Line	$\lambda_{\rm rest}$	Flux	FWHM		Luminosity	W_λ
	Å	$\times 10^{-14}$ erg s^{-1} cm^{-2}	Å	km s^{-1}	$\times 10^{+41}$ erg s^{-1}	Å
H_α	6563	1.66 ± 0.01	15.92 ± 0.12	689 ± 5	16.349	-83.38 ± 8.75
[OIII]	5007	0.111 ± 0.007	21.86 ± 1.58	1277 ± 95	1.0916	-7.21 ± 2.98
H_β	4861	0.539 ± 0.004	21.69 ± 0.32	1303 ± 20	5.2893	-34.93 ± 5.29
H_γ	4340	0.224 ± 0.002	20.39 ± 0.87	1367 ± 60	2.2001	-11.86 ± 3.21

counterpart to 3FHL J1212.1-2328. The spectrum for the observed candidate, observed on 2017/02/24 are presented in Fig. 6.17. A redshift of $z = 0.18596$ was calculated. Numerous bright emission lines are present in the spectrum.

The emission lines include the $H_\alpha, H_\beta, H_\gamma$, [O II]$\lambda$3727, [O III]$\lambda$4959, [O III]$\lambda$5007, [Mg I]$\lambda$5174, Na I-D$\lambda$5894 and [S II]$\lambda$6731.

An analysis of the brighter emission lines were performed with `pyspeckit`. The lines were fitted with a Gaussian profile in order to calculate the flux, FWHM, luminosity and W_λ of the emission lines. The results are presented in Tab. 6.4. The emission line corresponding to H_α is actually a blend of three lines, H_α and the [NII]λ6548, 6584 doublet and was taken into account when the H_α emission line was fitted.

The source can be classified as a broadline AGN based on the width of the Hydrogen emission lines. A higher resolution spectrum is needed measure the [NII]λ6548, 6584 doublet and further refine the classification. Also, based on the absence of a radio counterpart for the optical source, and therefore the absence of a prominent jet, this object is most likely not associated with the 3FHL source.

6.3.1.12 3FHL J1223.5-3033

3FHL J1223.5-3033 (Fig. 6.18), was observed on 2017/02/25. A redshift of $z = 0.2193 \pm 0.0004$ was obtained for this source. The Ca II H&K and G-bandλ4306 absorption lines were detected at 4796.3, 4838.8 and 5250.3 Å respectively. A weak [O III]λ5007 emission line is also observed, with measured equivalent width of $|W_\lambda| < 2$ Å. Potential MgIλ5174 and NaIλ5894 can also be seen in the spectrum. The source has a measured Ca H&K break of $K_{4000} = 0.017$. Therefore, due to the weak [O III]λ5007 line and very weak Ca H&K break, I classify the source as a BL Lac object.

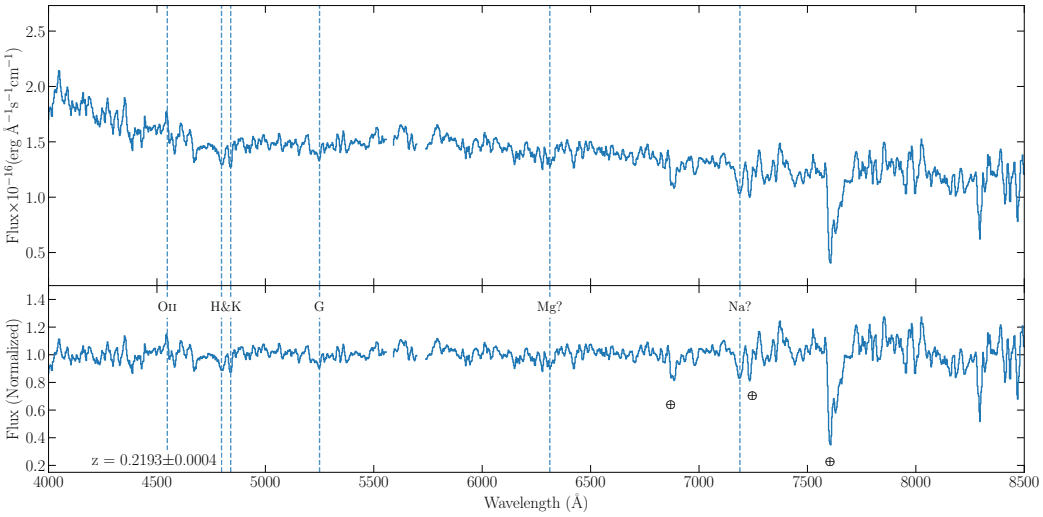

Figure 6.18: The average spectrum of 3FHL J1223.5-3033 observed with SpUpNIC using grating 7. Detected telluric lines are indicated with a $\oplus$. The spectrum has a resolution of ~ 5 Å and a S/N ≈ 16. The spectrum has been smoothed for display purposes using a smoothing box of 5 data points.

6.3.2 3FGL BCUs

In this section, the results of the spectroscopic observations of the selection of 3FGL BCUs are presented. The combined optical spectra of the sources observed with SpUpNIC are presented, with the identified lines indicated. The redshifts calculated by the **RVSAO** package are also indicated on the spectra.

6.3.2.1 3FGL J0051.2-6241

3FGL J0051.2-6241 (Fig. 6.19) was observed on 2017/08/31. A potential redshift of $z = 0.156$ was obtained from the nearly featureless spectrum. Potential absorption lines from Ca II H&K are detectable in the spectrum at 4547.3 and 4587.5 Å respectively. A faint emission features coincident with [NeV]λ3426 is also present. A potential NaIλ5894 absorption line is also present in the spectrum. Based on the nearly featureless spectrum, this source can be classified as a BL Lac object.

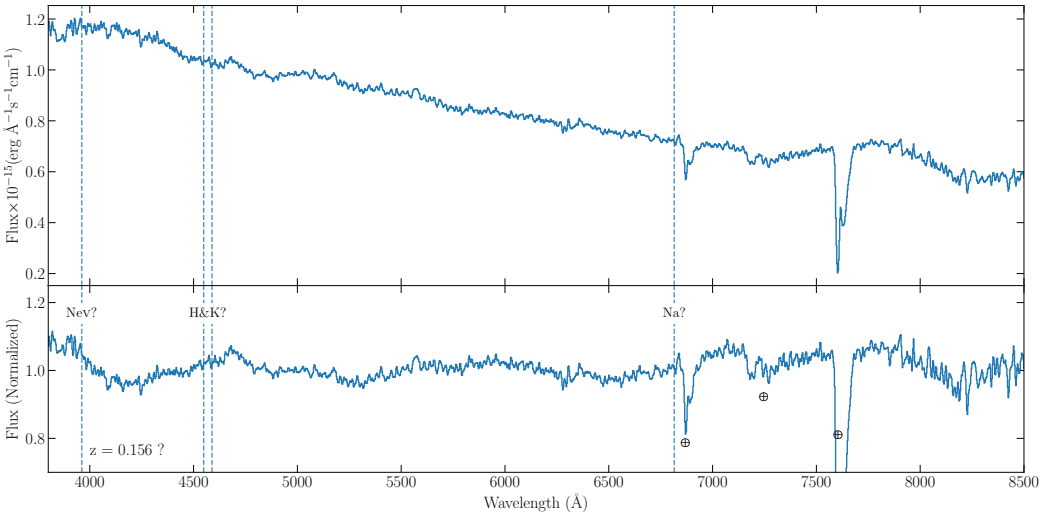

Figure 6.19: The average spectrum of 3FGL J0051.2-6241 observed with SpUpNIC using grating 7. Detected telluric lines are indicated with a ⊕. The spectrum has a resolution of ~ 5 Å and a S/N ≈ 45. The spectrum has been smoothed for display purposes using a smoothing box of 5 data points.

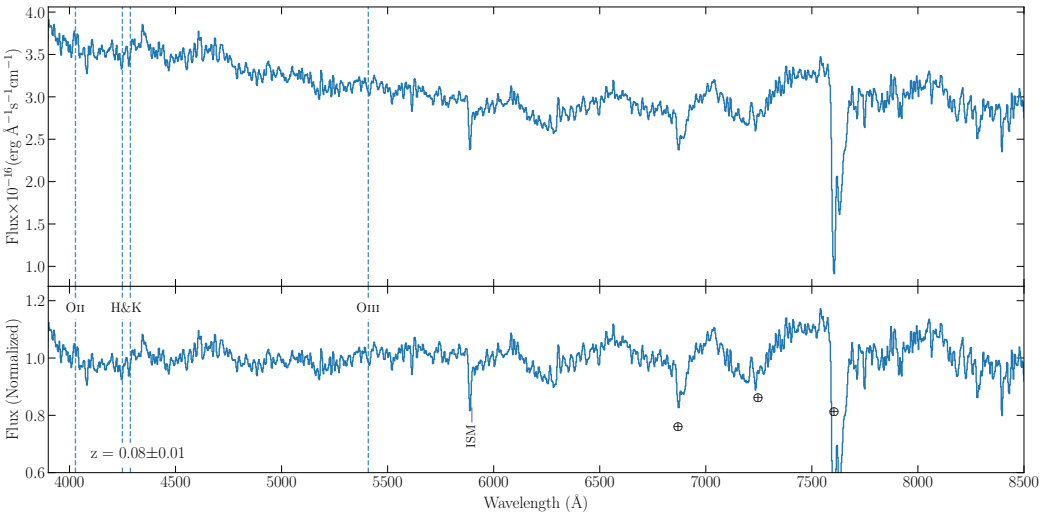

Figure 6.20: The average spectrum of 3FGL J0256.3+0335 observed with SpUpNIC using grating 7. Detected telluric lines are indicated with a ⊕. The spectrum has a resolution of ~ 5 Å and a S/N ≈ 27. The spectrum has been smoothed for display purposes using a smoothing box of 5 data points.

6.3.2.2 3FGL J0256.3+0335

3FGL J0256.3+0335 (Fig. 6.20) was observed on 2017/08/31. A redshift of $z = 0.08 \pm 0.01$ was obtained for this source. The Ca II H&K and [OIII]λ5007 absorption lines at 4248.4, 4286 and 5407.6 Å respectively. A weak emission line

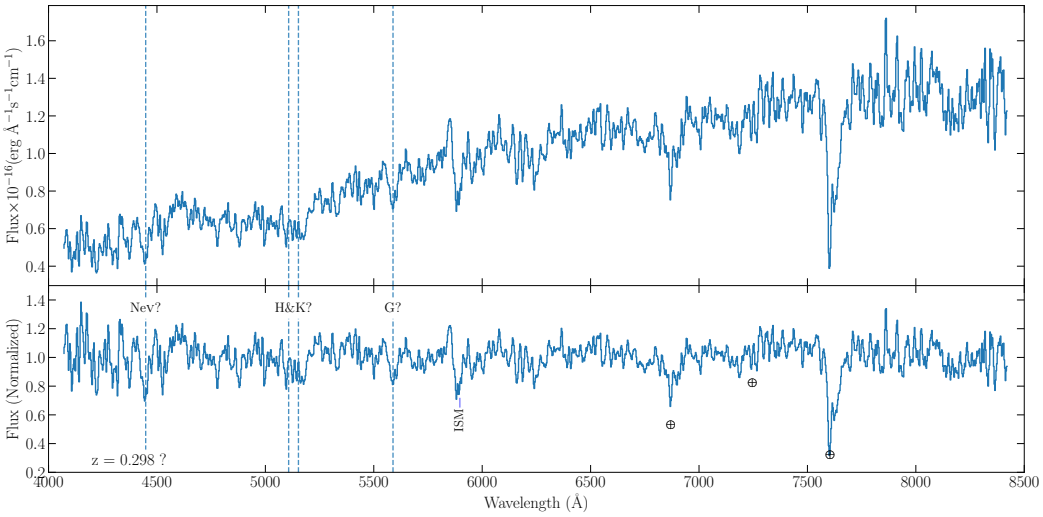

Figure 6.21: The average spectrum of 3FGL J1344.5-3655 observed with SpUpNIC using grating 7. Detected telluric lines are indicated with a $\oplus$. The spectrum has a resolution of ~ 5 Å and a S/N ≈ 11. The spectrum has been smoothed for display purposes using a smoothing box of 5 data points.

from [OII]λ3727 is also visible at 4025.2Å, with a measured equivalent width of $|W_\lambda| < 3$ Å. The spectrum of 3FGL J0256.3+0335 is dominated by non-thermal emission and has no Ca H&K break. Therefore, I classify this source as a BL Lac.

6.3.2.3 3FGL J1344.5-3655

3FGL J1344.5-3655 (Fig. 6.21) was observed on 2016/08/01. The spectrum has a very low S/N of ≈ 11, making the identification of features difficult. A potential redshift of $z = 0.298$ was calculated for this source based on the potential detection of the [NeV]λ3425, Ca II H&K and G-bandλ4306 absorption lines at 4445.6, 5105.8, 5151.1 and 5589 Å respectively. This source has a Ca H&K break of $K_{4000} = 0.21$. Based on the absence of any emission features, this source can be classified as a BL Lac object.

6.3.2.4 3FGL J1406.0-2508

3FGL J1406.0-2508 (Fig. 6.22) was observed on 2016/07/30. A potential redshift of $z = 0.153$ was obtained based on the presence of two features consistent with the Ca II H&K absorption lines at 4539.4 and 4579.6 Å. Also, based on the absence of any emission lines, the source can be classified as a BL Lac object.

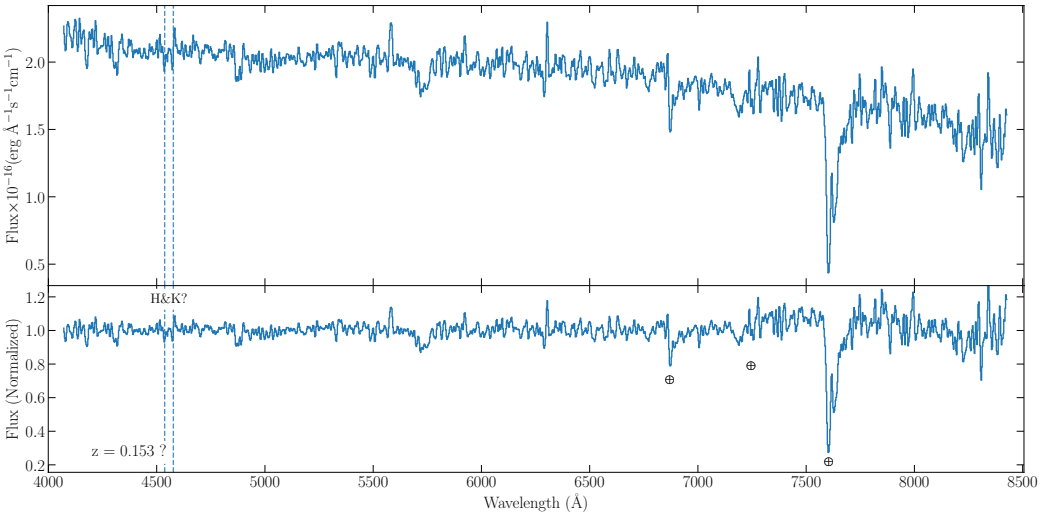

Figure 6.22: The average spectrum of 3FGL J1406.0-2508 observed with SpUpNIC using grating 7. Detected telluric lines are indicated with a $\oplus$. The spectrum has a resolution of ~ 5 Å and a S/N ≈ 21. The spectrum has been smoothed for display purposes using a smoothing box of 5 data points.

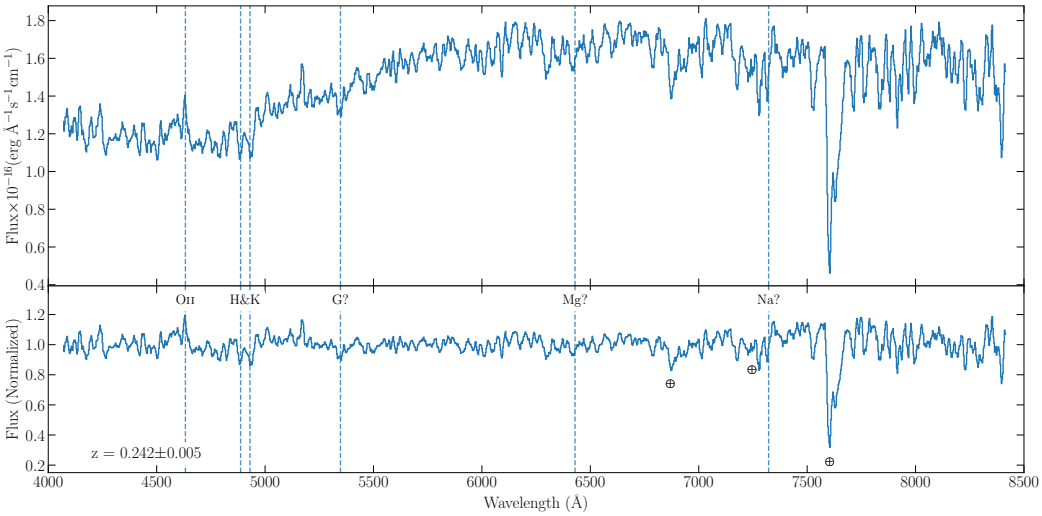

Figure 6.23: The average spectrum of 3FGL J1507.6-3710 observed with SpUpNIC using grating 7. Detected telluric lines are indicated with a $\oplus$. The spectrum has a resolution of ~ 5 Å and a S/N ≈ 15. The spectrum has been smoothed for display purposes using a smoothing box of 5 data points.

6.3.2.5 3FGL J1507.6-3710

3FGL J1507.6-3710 (Fig. 6.23) was observed on 2016/07/30. A redshift of $z = 0.242 \pm 0.005$ was obtained. The Ca II H&K and G-bandλ4306 absorption lines were detected at 4885.6, 4929.8 and 5348.0 Å respectively. A potential weak

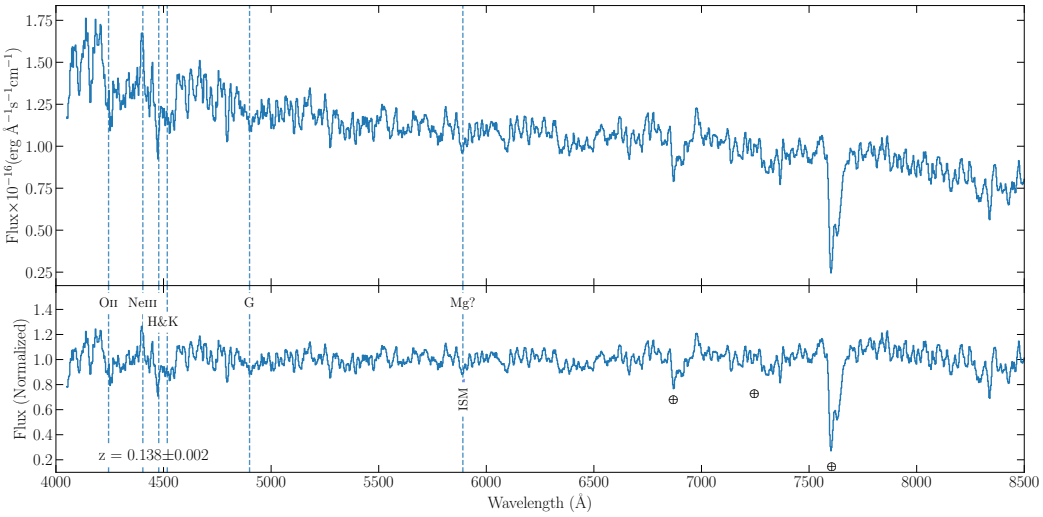

Figure 6.24: The average spectrum of 3FGL J1842.3-5841 observed with SpUpNIC using grating 7. Detected telluric lines are indicated with a $\oplus$. The spectrum has a resolution of ~ 5 Å and a S/N ≈ 12. The spectrum has been smoothed for display purposes using a smoothing box of 5 data points.

[MgI]λ5174 absorption line is also detected at 6426 Å. A potential [NaI]λ5894 absorption lines is also present at 7320 Å, however, this is next to a telluric line. A [OII]λ3729 emission line is also present with an equivalent width of $|W_\lambda| = 2.0 \pm 0.5$ Å. This source has a Ca H&K break of $K_{4000} = 0.16$ and can be classified as a BL Lac object.

6.3.2.6 3FGL J1842.3-5841

3FGL J1842.3-5841 (Fig. 6.24) was observed on 2017/08/31. A redshift of $z = 0.138 \pm 0.002$ was obtained. Absorption lines of [OII]λ3729, Ca II H&K and G-bandλ4306 were detected at 5146, 5428.4, 5476.5 and 5942.3 Å respectively. A potential MgIλ5174 absorption line is also detected at the location of the [NaI]λ5894 Interstellar Medium (ISM) absorption feature. The [NeIII]λ3869 emission line was also detected with an equivalent width of $|W_\lambda| = 3.53 \pm 0.6$ Å. The spectrum bluer than $< 4800\lambda$ is dominated by noise and no Ca H&K break could be calculated. The source can be classified as a BL Lac object based on the strength of the emission line.

6.3.2.7 3FGL J1855.1-6008

3FGL J1855.1-6008 (Fig. 6.25) was observed on 2016/08/04. A potential redshift of $z = 0.14$ was obtained. The redshift was calculated based on the potential

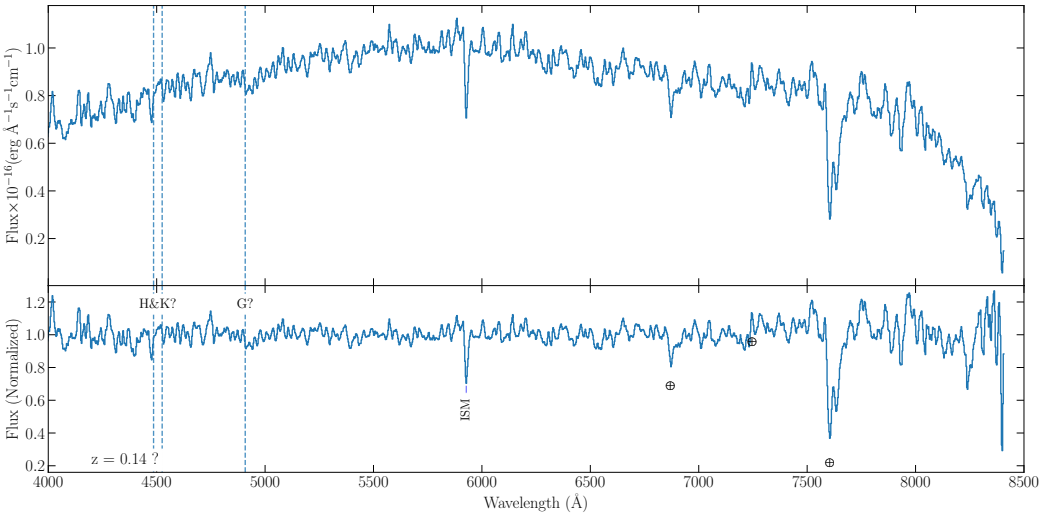

Figure 6.25: The average spectrum of 3FGL J1855.1-6008 observed with SpUpNIC using grating 7. Detected telluric lines are indicated with a $\oplus$. The spectrum has a resolution of ~ 5 Å and a S/N ≈ 18. The spectrum has been smoothed for display purposes using a smoothing box of 5 data points.

detection of the Ca II H&K and G-bandλ4306 absorption lines at 4484.3, 4524.1 and 4909 Å respectively. The Ca II H and G-band absorption lines are dominated by noise and are therefore not detected with certainty. Based on the absence of emission lines, the source can be classified as a BL Lac object.

6.3.2.8 3FGL J1944.1-4523

3FGL J1944.1-4523 (Fig. 6.26) was observed on 2016/08/01. A redshift of $z = 0.236 \pm 0.002$ was obtained based on the detection of the [NeV]λ3425 and [OII]λ3729 emission lines, the Ca II H&K and G-bandλ4306 and [MgI]λ5174 absorption lines at 4226.5, 4601.5, 4854.1, 4897.1, 5313.6 and 6384.7 Å respectively. A potential [NaI]λ5894 absorption lines is also present at 7273 Å, coincident with the location of a telluric line. An equivalent width of $|W_\lambda| = 1.4 \pm 0.6$ Å was calculated for the [OII]λ3729 emission line. The spectrum of 3FGL J1944.1-4523 is dominated by non-thermal emission and has no Ca H&K break. The source can be classified as a BL Lac object.

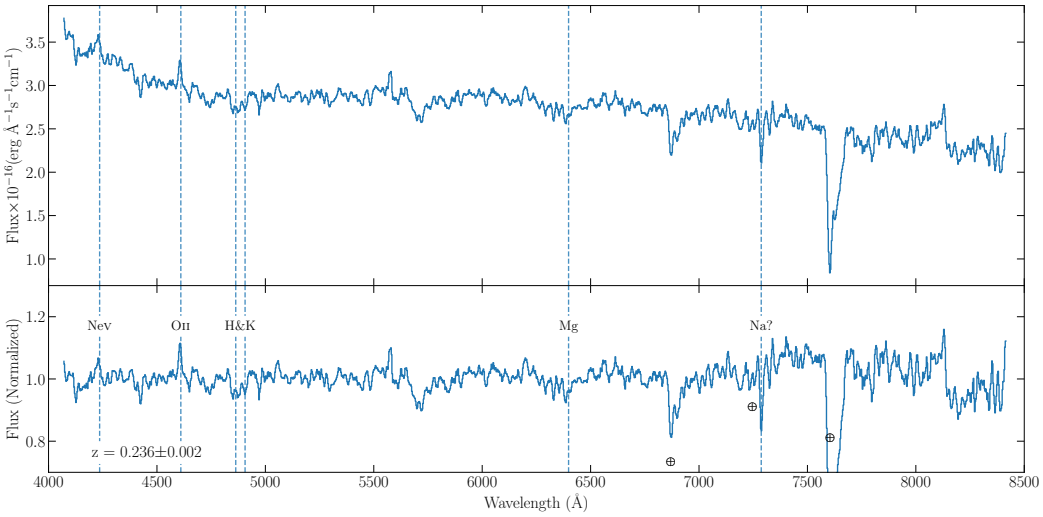

Figure 6.26: The average spectrum of 3FGL J1944.1-4523 observed with SpUpNIC using grating 7. Detected telluric lines are indicated with a $\oplus$. The spectrum has a resolution of ~ 5 Å and a S/N ≈ 30. The spectrum has been smoothed for display purposes using a smoothing box of 5 data points.

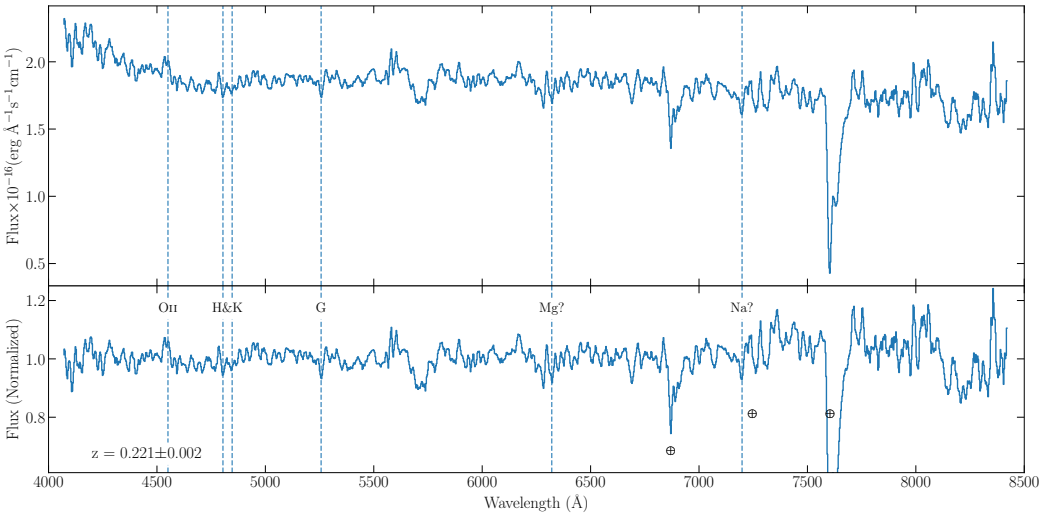

Figure 6.27: The average spectrum of 3FGL J1954.9-5640 observed with SpUpNIC using grating 7. Detected telluric lines are indicated with a $\oplus$. The spectrum has a resolution of ~ 5 Å and a S/N ≈ 25. The spectrum has been smoothed for display purposes using a smoothing box of 5 data points.

6.3.2.9 3FGL J1954.9-5640

3FGL J1954.9-5640 (Fig. 6.27) was observed on 2016/08/02. A redshift of $z = 0.221 \pm 0.002$ was calculated from the [OII]λ3729 emission line, the Ca II H&K and G-bandλ4306 absorption lines detected at 4553.1, 4803, 4845.5 and 5258 Å

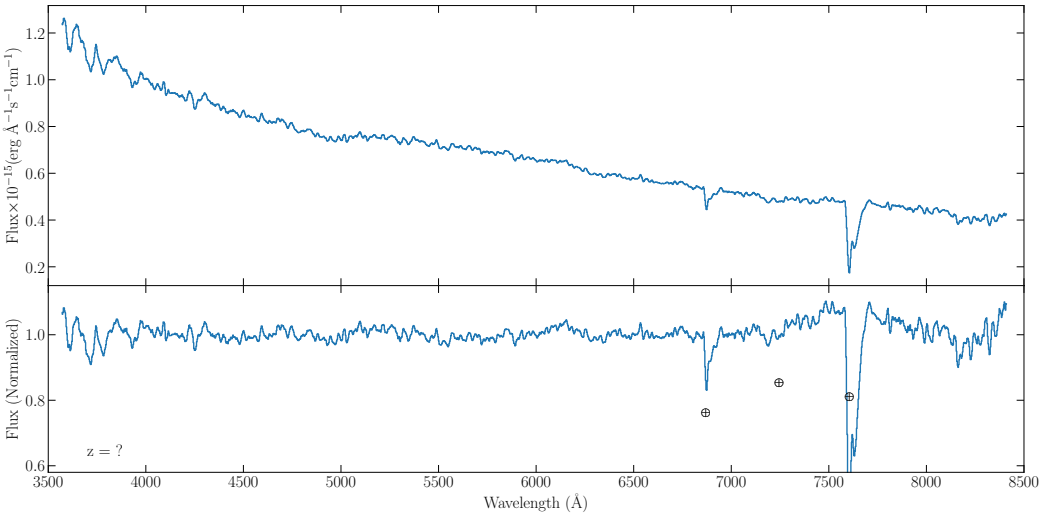

Figure 6.28: The average spectrum of 3FGL J1959.8-4725 observed with SpUpNIC using grating 7. Detected telluric lines are indicated with a $\oplus$. The spectrum has a resolution of ~ 5 Å and a S/N ≈ 54. The spectrum has been smoothed for display purposes using a smoothing box of 5 data points.

respectively. A weak potential [MgI]λ5174 absorption line is also detected at 6317.5 Å. A potential [NaI]λ5894 absorption lines is also present at 7197 Å, unfortunately coincident with the location of a telluric line. An equivalent width smaller than $|W_\lambda| < 1.5$ Å could be calculated for the [OII]λ3729 emission line, due to noise. This source has a Ca H&K break of $K_{4000} = 0.02$. Therefore, 3FGL J1954.9-5640 can be classified as a BL Lac object.

6.3.2.10 3FGL J1959.8-4725

3FGL J1959.8-4725 (Fig. 6.28) was observed on 2016/08/04. This BL Lac object has a featureless spectrum and no redshift could be calculated.

6.3.2.11 3FGL J2338.7-7401

3FGL J2338.7-7401 (Fig. 6.29) was observed on 2017/08/28. A redshift of $z = 0.1987 \pm 0.0004$ was obtained based on the presence of [OII]λ3729, Ca II H&K, [MgI]λ5174 and [NaI]λ5894 absorption lines at 4553.1, 4715.3, 4757.0 and 5161.6, 6317.5 and 7196.5 Å respectively. This source has a Ca H&K break of $K_{4000} = 0.04$. Based on the small Ca H&K break and absence of any emission features, this source can be classified as a BL Lac object.

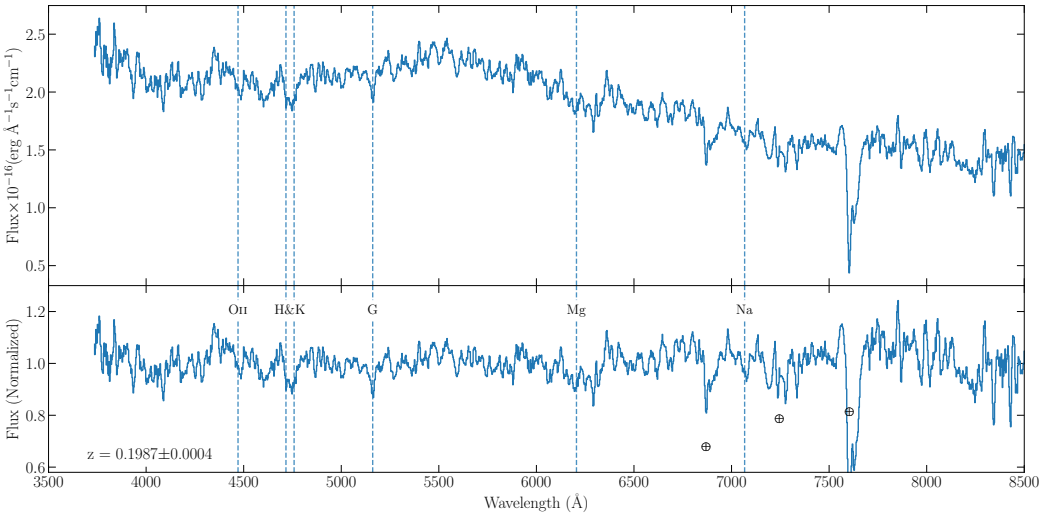

Figure 6.29: The average spectrum of 3FGL J2338.7-7401 observed with SpUpNIC using grating 7. Detected telluric lines are indicated with a ⊕. The spectra has a resolution of ~ 5 Å and a S/N ≈ 15. The spectra has been smoothed for display purposes using a smoothing box of 5 data points.

6.4 Summary of the spectroscopic observations of *Fermi* BCUs

This chapter presented the results of a campaign to classify eleven 3FHL BCUs, one unassociated 3FHL source and eleven 3FGL BCUs using the SpUpNIC grating spectrograph on the SAAO 1.9-m telescope. Tab. 6.5 summarizes the results of the 3FHL BCU and unassociated sources. All of the 3FHL BCUs were classified as BL Lac and potential BL Lacs, except 3FHL J1212.1-2328, with redshifts calculated for four of them. Redshifts were also found for the three observed optical candidates of 3FHL J0813.7-0353, but an optical counterpart could not be determinem.

Tab. 6.6 summarizes the results of the 3FGL BCUs. All the 3FGL BCUs observed were classified a BL Lac objects. Redshifts or tentative redshifts could be calculated for all but one source.

Table 6.5: A summary of the results obtained for the 3FHL BCUs and unassociated sources observed with SpUpNIC. The last source listed is the unassociated source observed with SpUpNIC

3FHL Name	Observation date	Classification	K_{4000}	Redshift
J0001.9-4155	2017/08/25	BL Lac	-	?
J0002.1-6728	2017/08/25	BL Lac	-	?
J0003.3-5248	2017/08/26	BL Lac	-	?
J0115.9-2746	2017/08/26	BL Lac	-	?
J0305.2-1609	2017/08/27	BL Lac	0.21	$z = 0.312 \pm 0.001$
J0647.0-5138	2017/02/17	BL Lac	0.15	$z = 0.2268 \pm 0.0003$
J0935.2-1735	2017/02/24	BL Lac	-	?
J1042.2-4128	2017/02/25	BL Lac	-	?
J1130.5-7801	2017/02/25	BL Lac	0	$z = 0.317 \pm 0.001$
J1212.1-2328	2017/02/24	Broadline AGN	-	$z = 0.18596$
J1223.5-3033	2017/02/25	BL Lac	-	$z = 0.2193 \pm 0.0004$
J0813.7-0353 C2	2017/02/25	BL Lac	0.28	$z = 0.1954 \pm 0.0003$
J0813.7-0353 C3	2017/02/25	BL Lac	-	$z = 0.261$?
J0813.7-0353 C4	2017/02/25	BL Lac	-	$z = 0.192$?

Table 6.6: A summary of the results obtained for the 3FGL BCUs observed with SpUpNIC.

3FGL Name	Observation date	Classification	K_{4000}	Redshift
J0051.2-6241	2017/08/31	BL Lac	-	$z = 0.156$?
J0256.3+0335	2017/08/31	BL Lac	0	$z = 0.08 \pm 0.01$
J1344.5-3655	2016/08/01	BL Lac	0.21	$z = 0.298$?
J1406.0-2508	2016/07/30	BL Lac	-	$z = 0.153$?
J1507.6-3710	2016/07/30	BL Lac	0.16	$z = 0.242 \pm 0.002$
J1842.3-5841	2017/08/31	BL Lac	-	$z = 0.138 \pm 0.002$
J1855.1-6008	2016/08/04	BL Lac	-	$z = 0.14$?
J1944.1-4523	2016/08/01	BL Lac	0	$z = 0.236 \pm 0.002$
J1954.9-5640	2016/08/02	BL Lac	0.02	$z = 0.221 \pm 0.002$
J1959.8-4725	2016/08/04	BL Lac	-	?
J2338.7-7401	2017/08/28	BL Lac	0.04	$z = 0.1987 \pm 0.0004$

Chapter 7

Discussion

This dissertation has focused on the observation of known and candidate VHE AGN. This has included the development of a photometric pipeline for rapid variability analysis, as well as the identification and optical follow-up observations of candidate VHE AGN.

Regularly monitoring sources using photometry provides a method to quickly detect any significant variability, e.g. flares and outbursts. Detecting flaring states as they develop enables multiwavelength monitoring campaigns to be initiated early to monitor the increased activity. The complete multiwavelength coverage of flares and outbursts provides the necessary information to model blazar variability in great detail.

Observing blazars in the VHE regime becomes difficult however, since the VHE detection of blazars are dependant on their distance, source class (FSRQ vs HSP BL Lac) and γ-ray flux. Performing multiwavelength modelling on blazars, therefore becomes import to predict the VHE γ-ray flux. The source class and distance to the blazar also heavily influence the model paramaters.

This discussion is structured as follows, in Section 7.1, the use of the pipeline developed for this project is briefly discussed and how it can be used to analyse flaring sources. Section 7.2 summarizes the results of the optical spectroscopy and the detectability of the 3FGL and 3FHL sources with IACTs, particularly H.E.S.S. and CTA South.

7.1 Photometry using the reduction and analysis pipeline

The Watcher Robotic Telescope has been regularly observing a number of H.E.S.S. detected TeV blazars since late 2015. This has resulted in a daunting amount of data to analyse. As such a reduction and analysis pipeline was developed to analyse this data using aperture photometry. During the course of the project the pipeline was extended to allow data analysis from other optical telescopes. Data collected using the SAAO 1.0-m SHOC instrument was analyzed using the pipeline and data obtained with the Las Cumbres Observatory (LCO) as part of a project to monitor flaring blazars has also been analyzed using the pipeline.

Most interesting phenomena in blazars occur during periods of high activity. It is therefore important to continually monitor known active blazars for flares or outbursts. However, this produces large amounts of data, which have to be analyzed, which takes a considerable amount of effort. This often results in flaring blazars being discovered after the flare has subsided, if no automatic reduction pipeline is available, leading to a search of incomplete archival data to analyze the flare. The pipeline alleviates this problem by enabling prompt analysis of photometric data from diverse optical telescopes. Performing an analysis of current data allows flares to be detected when they start and begin follow-up multiwavelength monitoring campaigns to monitor the flares. This is especially important regarding TeV observations, which provide the data used to model blazar emission up to the highest observable energies.

For this project, fourteen TeV detected blazars monitored by Watcher were analyzed for LTV. Variability was tested for using the χ^2-test, the F-test, scaled F-test and the power-enhanced F-test. All the sources observed, except 1ES 1101-232, showed variability in at least one filter. Also, as part of the project to classify 3FHL BCUs and unassociated sources, I also observed six sources, looking for IDV that might indicate the blazar origin of the optical emission. The tests found IDV for only one source, while possible IDV was found for the other sources. The tests generally agreed with each other, with the power-enhanced F-test returning the most robust results because of the increased degrees of freedom utilized by the test.

7.2 Source classification

The observablity of blazars with IACTs depend strongly on their flux and distance. It is therefore important to classify and measure the distance to unknown blazars. Blazars more distant than $z \sim 1$ become undectable to IACTs because VHE γ-ray are absorbed by the EBL. Also, FSRQs and low Synchrotron peaked blazars have lower intrinsic VHE emission than the High Synchrotron peaked blazar population. Optical spectroscopy is an efficient method to determine both the class and distance to blazars.

Optical spectroscopy was used to analyze ten 3FHL BCUs, two 3FHL unassociated sources and eleven 3FGL BCUs with the SAAO 1.9-m SpUpNIC grating spectrograph. All these sources were hard γ-ray sources, which increases their chances of being detected by IACTs, if their redshifts are less than $z \sim 1$. Of the twenty-one associated sources observed, all were classified as BL Lac objects. The unassociated 3FHL source requires further analysis before a final classification can be made, as only three of the five potential optical candidates of 3FHL J0813.7-0353 have been observed, while the optical candidate of 3FHL J1212.1-2328 inside the error circle has yet to be observed. Fig. 7.1 gives a summary of the redshifts calculated for the 3FHL and 3FGL sources observed. All sources in this sample, for which a redshift could be measured, lie at $z < 1$. This means the limit on observability depends on the flux of the source. There is, unfortunately, minimal multi-wavelength data available, and therefore I have estimated whether or not the sources will be observable by comparing the GeV flux to the instrumentational H.E.S.S. and CTA sensitivity curves to see whether the archival flux is higher than the predicted sensitivity.

The Space Science Data Center (SSDC) "Sky Explorer"[1] is a versatile online tool used to construct and model multiwavelength SEDs using public catalogues (e.g *Fermi*, Swift, AGILE, etc.), external archives (e.g. NED and CDS Vizier) and user supplied data. The SSDC Sky Explorer tool was used to retrieve achival data for the *Fermi* BCUs observed during this project. To determine if the observed BCUs are potentially detectable with H.E.S.S. and CTA South, multiwavelength SEDs were constructed and overlayed with the H.E.S.S and CTA South 50 h sensitivity curves. To highlight the lower energy and higher energy components of the SED, two smoothly broken power-law lines are shown in the figures. It is important to note that these lines are not fitted to the data or calculated from a model, and are only included to illustrate the two components. A detailed

[1] `https://tools.ssdc.asi.it`

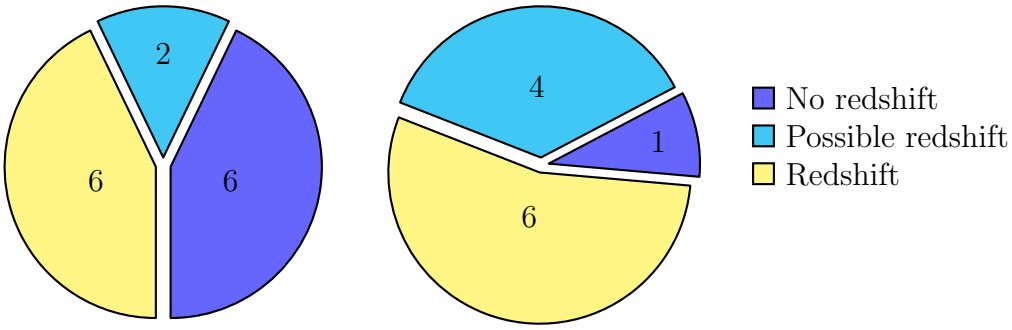

Figure 7.1: Left: Summary of the redshifts obtained for the eleven 3FHL BCUs and one unassociated source observed. Fourteen objects were observed, since three optical candidates for 3FHL 0813.7-0353 were observed. Right: Summary of the redshifts obtained for the 3FGL sources observed

summary of the 3FGL and 3FHL BCUs potentially visible with IACTs follows in Section 7.2.1 - 7.2.8. Appendix A presents the broadband SEDs for the observed sources I believe are not detectable with H.E.S.S or CTA South. These sources are not detectable due to low γ-ray flux and soft spectral indices, which puts their γ-ray flux below the sensitivity threshold of IACTs. Sources without available γ-ray data points above the sensitivity threshold are also included in Appendix A, since no modelling was performed to make predictions on their detectability.

7.2.1 3FGL J0051.2-6241

3FGL J0051.2-6241 is associated with the X-ray source 1RXS J005117.7-624154. It has a synchrotron peak frequency of $\log\nu_{\rm peak,Hz} = 15.9$ and a spectral power-law index of $\Gamma_{0.1-100\ \rm GeV} = 1.66 \pm 0.06$. The optical spectra taken with SpUpNIC classified this source as a BL Lac object with a potential redshift of $z = 0.156$, based on the presence of very faint features coincident with a [NeV]λ3426 emission line and Ca II H&K and NaIλ5894 absorption lines. The broadband SED is presented in Fig. 7.2. The flux of the VHE γ-ray emission extend above the sensitivitiy threshold of CTA South and should be detectable in $\lesssim 50$ h of observation.

7.2.2 3FHL J0305.2-1609

3FHL J0305.2-1609 is associated with the radio source PKS 0302-16. It has a synchrotron peak frequency of $\log\nu_{\rm peak,Hz} = 15.57$ and a spectral power-law index of $\Gamma_{0.1-100\ \rm GeV} = 1.69 \pm 0.19$. The source was classified as a BL Lac object with a redshift of $z = 0.312 \pm 0.001$. The Ca II H&K, G-bandλ4306 and [MgI]λ5174

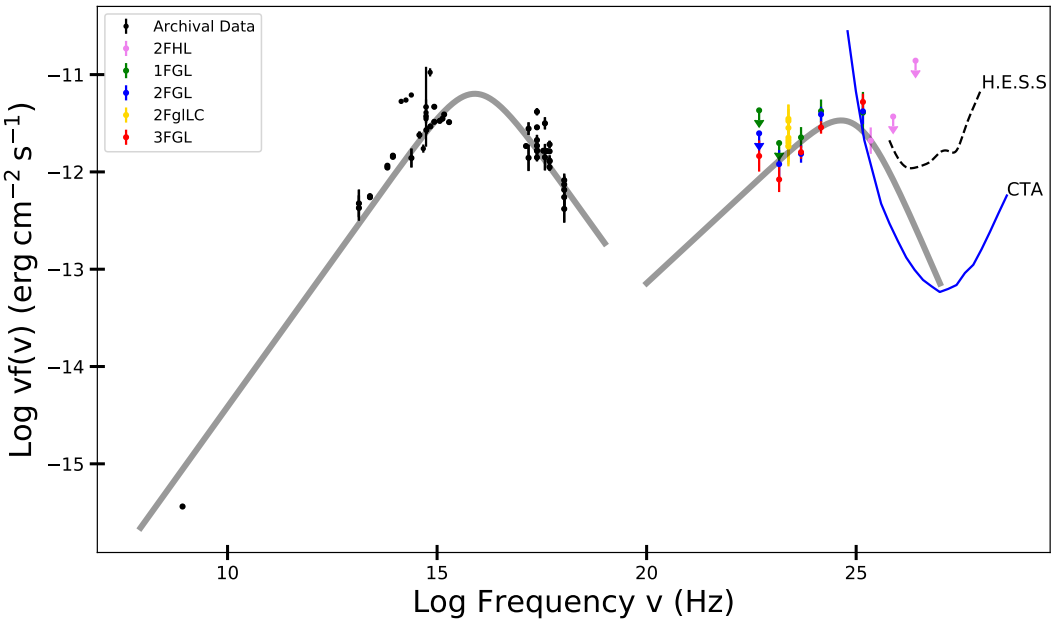

Figure 7.2: Broadband SED of 3FGL J0051.2-6241. The 50 h sensitivity curves of CTA South (sollid blue line) and H.E.S.S. (dashed black line) are overlayed on the SED. The γ-ray catalogues and colors are indicated in the SED legend. The low energy datapoints (black) is archival data retrieved from the NED and CDS Vizier services. Two smoothly broken power-laws (solid gray line) are overlayed on the SED to highlight the flux of the source.

absorption lines and [O II]λ3729 emission line was detected in the optical spectrum. This result agrees with results published by Paiano et al. (2017). The broadband SED is presented in Fig. 7.3. The source exhibit very hard γ-ray emission in both the 2FGL and 3FGL and should therefore be detectable by CTA South in $\lesssim 50$ h of observation.

7.2.3 3FHL J1130.5-7801

3FHL J1130.5-7801 is associated with the radio source SUMSS J113032-780105. It is a hard γ-ray source with a spectral power-law index of $\Gamma_{0.1-100\ \mathrm{GeV}} = 1.74 \pm 0.14$. This source is classified as a BL Lac object with a redshift of $z = 0.317 \pm 0.001$ based on the detection of Ca II H&K absorption lines and the NeIII3869λ emission line. It was also observed with the SAAO 1.0-m SHOC instrument for a period of $\approx$ 4h and IDV was found by the enhanced F-test. The broadband SED is presented in Fig. 7.4. 3FHL J1130.5-7801 may be observable by CTA South, since the flux measured by the 2FHL is above the sensitivitiy threshold of CTA, while the 3FGL emission is on the threshold.

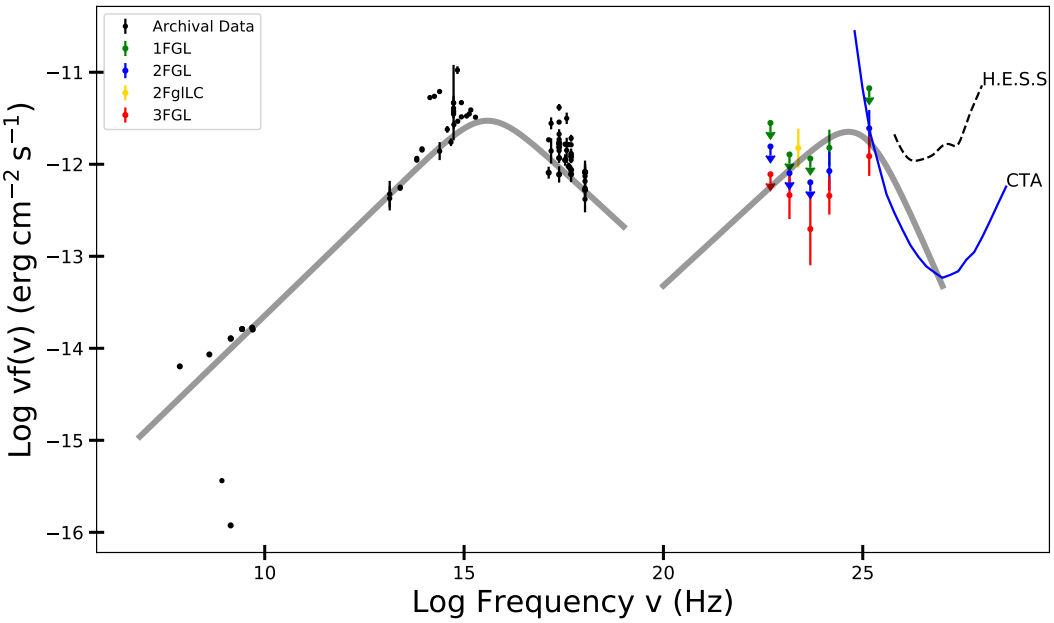

Figure 7.3: Broadband SED of 3FHL J0305.2-1609. The 50 h sensitivity curves of CTA South (sollid blue line) and H.E.S.S. (dashed black line) are overlayed on the SED. The γ-ray catalogues and colors are indicated in the SED legend. The low energy datapoints (black) is archival data retrieved from the NED and CDS Vizier services. Two smoothly broken power-laws (solid gray line) are overlayed on the SED to highlight the flux of the source.

7.2.4 3FGL J1406.0-2508

3FGL J1406.0-2508 is associated with the radio source NVSS J140609-250808. It has a synchrotron peak frequency of $\log\nu_{\rm peak,Hz} = 15.1$ and a spectral power-law index of $\Gamma_{0.1-100\ \rm GeV} = 1.89 \pm 0.11$. The optical spectra taken with SpUpNIC classified this source as a BL Lac object with a potential redshift of $z = 0.153$ based on the detection of features consistent with theCa II H&K absorption lines. The broadband SED is presented in Fig. 7.5. The γ-ray flux recorded in the 2FGL extends above the sensitivity threshold of CTA South. The VHE emission from this source is likely detectable in $\lesssim 50$ h of observation.

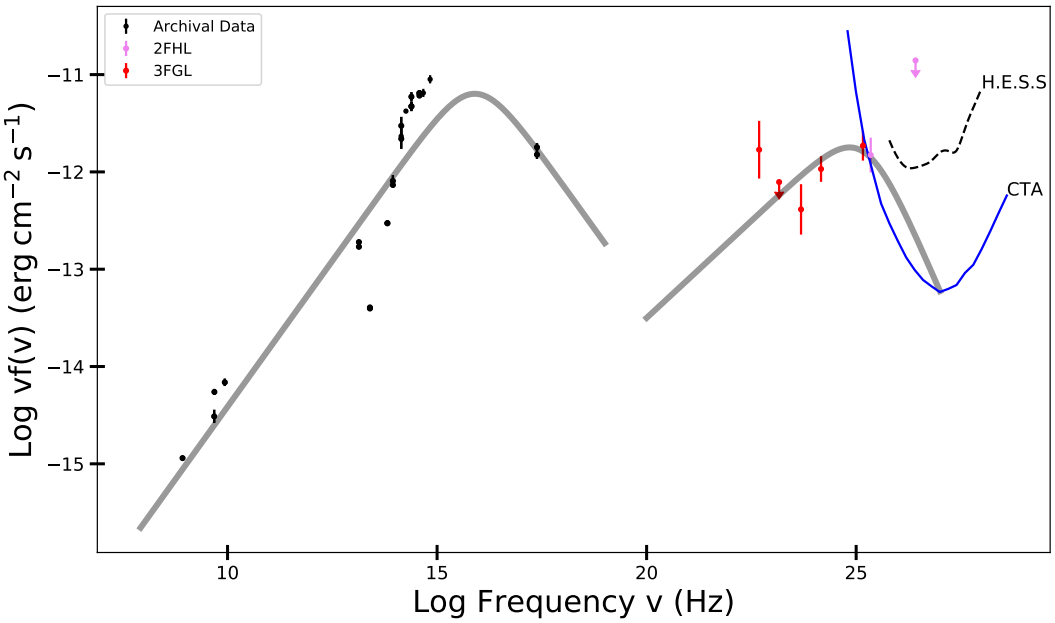

Figure 7.4: Broadband SED of 3FHL J1130.5-7801. The 50 h sensitivity curves of CTA South (sollid blue line) and H.E.S.S. (dashed black line) are overlayed on the SED. The γ-ray catalogues and colors are indicated in the SED legend. The low energy datapoints (black) is archival data retrieved from the NED and CDS Vizier services. Two smoothly broken power-laws (solid gray line) are overlayed on the SED to highlight the flux of the source.

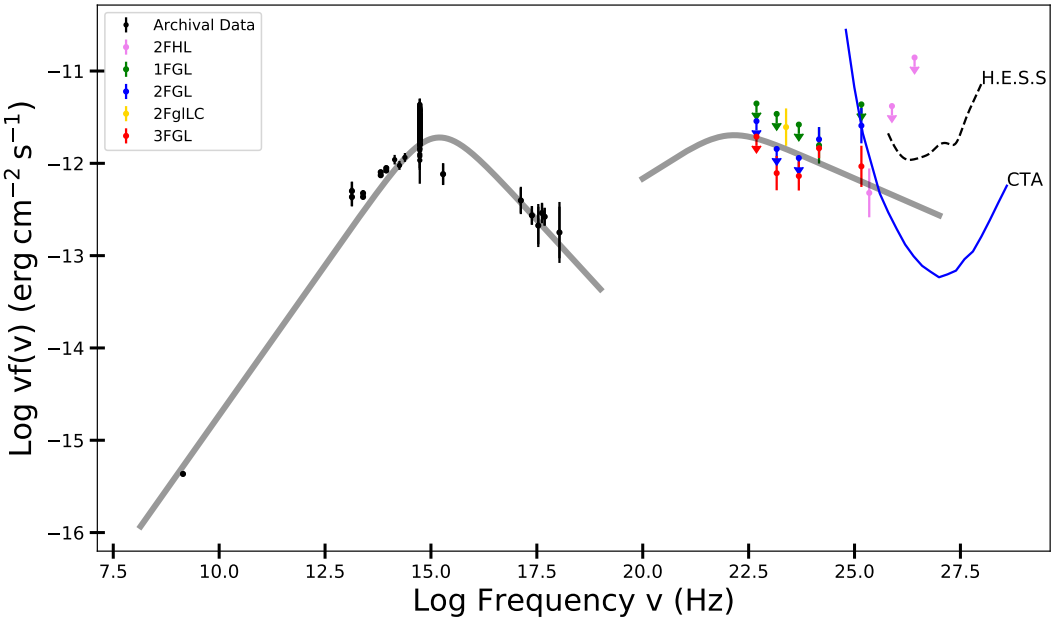

Figure 7.5: Broadband SED of 3FGL J1406.0-2508. The 50 h sensitivity curves of CTA South (sollid blue line) and H.E.S.S. (dashed black line) are overlayed on the SED. The γ-ray catalogues and colors are indicated in the SED legend. The low energy datapoints (black) is archival data retrieved from the NED and CDS Vizier services. Two smoothly broken power-laws (solid gray line) are overlayed on the SED to highlight the flux of the source.

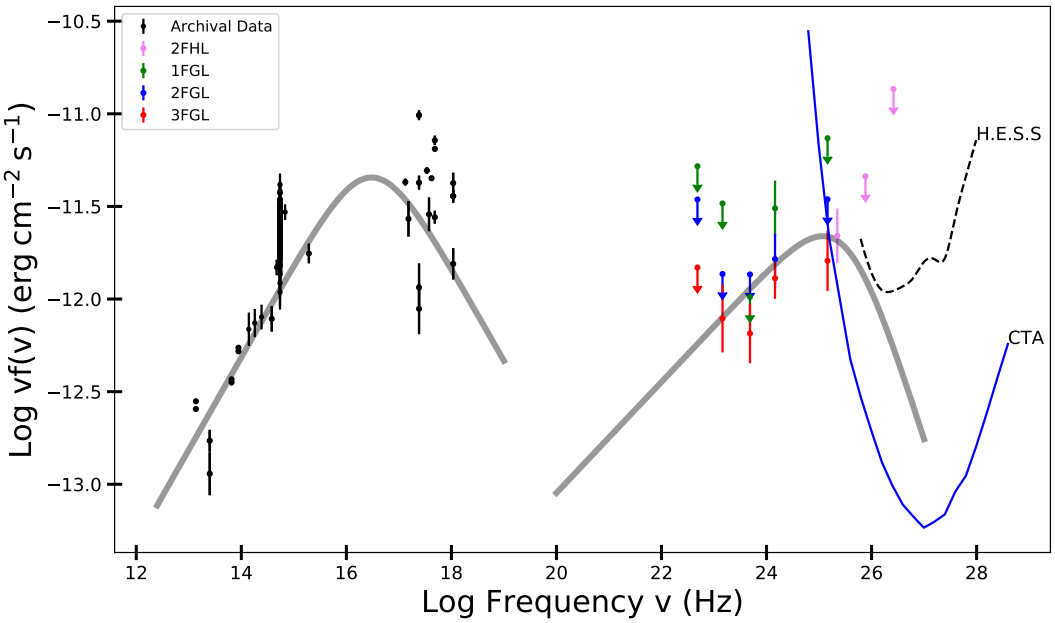

Figure 7.6: Broadband SED of 3FGL J1842.3-5841. The 50 h sensitivity curves of CTA South (sollid blue line) and H.E.S.S. (dashed black line) are overlayed on the SED. The γ-ray catalogues and colors are indicated in the SED legend. The low energy datapoints (black) is archival data retrieved from the NED and CDS Vizier services. Two smoothly broken power-laws (solid gray line) are overlayed on the SED to highlight the flux of the source.

7.2.5 3FGL J1842.3-5841

3FGL J1842.3-5841 is associated with the X-ray source 1RXS J184230.6-584202. It has a synchrotron peak frequency of $\log\nu_{\rm peak,Hz} = 16.476$ and a spectral power-law index of $\Gamma_{0.1-100\ \rm GeV} = 1.70 \pm 0.12$. The optical spectra taken with SpUpNIC classified this source as a BL Lac object with a redshift of $z = 0.138 \pm 0.002$. The [OII]λ3729, Ca II H&K and G-bandλ4306 absorption lines were detected, as well as a narrow [NeIII]λ3869 emission line with an equivalent width of $|W_\lambda| = 3.53 \pm 0.6$ Å. The broadband SED is presented in Fig. 7.6. The γ-ray flux recorded in the 2FGL extend above the sensitivitiy threshold of CTA South while the more complete 3FGL emission is just below the sensitivity threshold. The VHE emission from this source is likely detectable in $\lesssim 50$ h of observation.

7.2.6 3FGL J1944.1-4523

3FGL J1944.1-4523 is associated with the X-ray source 1RXS J194422.6-452326. It has a synchrotron peak frequency of $\log\nu_{\rm peak,Hz} = 16.14$ and a spectral power-law index of $\Gamma_{0.1-100\ \rm GeV} = 1.56 \pm 0.26$. The source has a redshift of $z = 0.236 \pm 0.002$

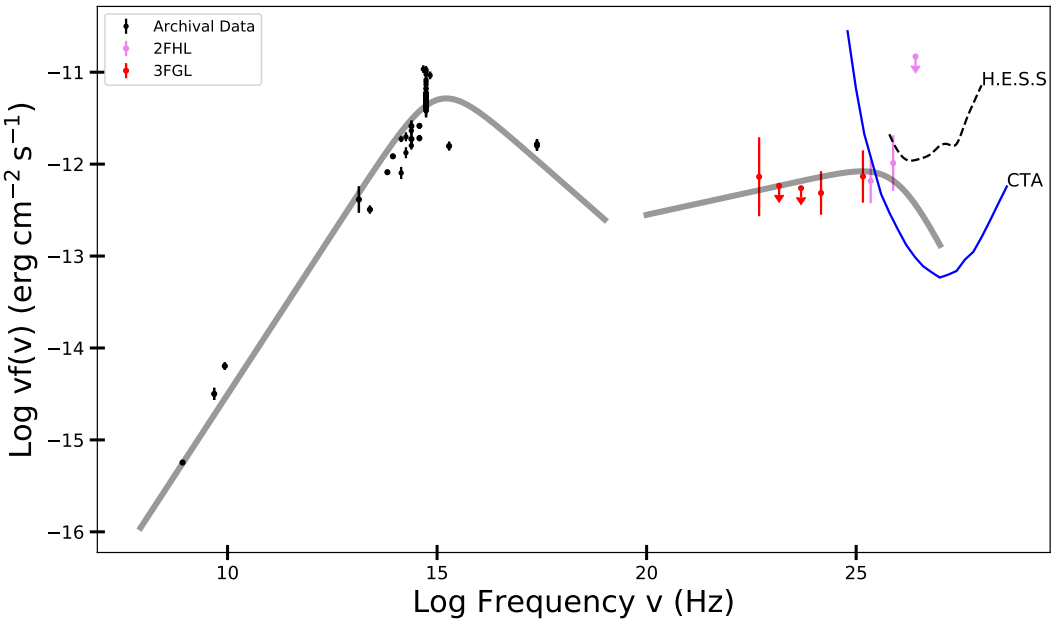

Figure 7.7: Broadband SED of 3FGL J1944.1-4523. The 50 h sensitivity curves of CTA South (sollid blue line) and H.E.S.S. (dashed black line) are overlayed on the SED. The γ-ray catalogues and colors are indicated in the SED legend. The low energy datapoints (black) is archival data retrieved from the NED and CDS Vizier services. Two smoothly broken power-laws (solid gray line) are overlayed on the SED to highlight the flux of the source.

based on the detection of the [NeV]λ3425 and [OII]λ3729 emission lines, the Ca II H&K and G-bandλ4306 and [MgI]λ5174 absorption lines. The broadband SED is presented in Fig. 7.7. 3FGL J1944.1-4523 is a newly detected source in the 3FGL. The VHE emission measured in the 2FHL is above the sensitivitiy threshold of CTA South. It should therefore be detectable in $\lesssim$ 50 h of observation.

7.2.7 3FGL J1954.9-5640

3FGL J1954.9-5640 is associated with the X-ray source 1RXS J195503.1-564031. It has a spectral power-law index of $\Gamma_{0.1-100\ \mathrm{GeV}} = 1.88 \pm 0.16$. The source has a redshift of $z = 0.221 \pm 0.002$ based on the detection of the [OII]λ3729 emission line, the Ca II H&K and G-bandλ4306 absorption lines. The broadband SED is presented in Fig. 7.8. The source is detected in the 2FHL catalog, but the γ-ray emission has very large errors, making detection of this source by CTA South uncertain.

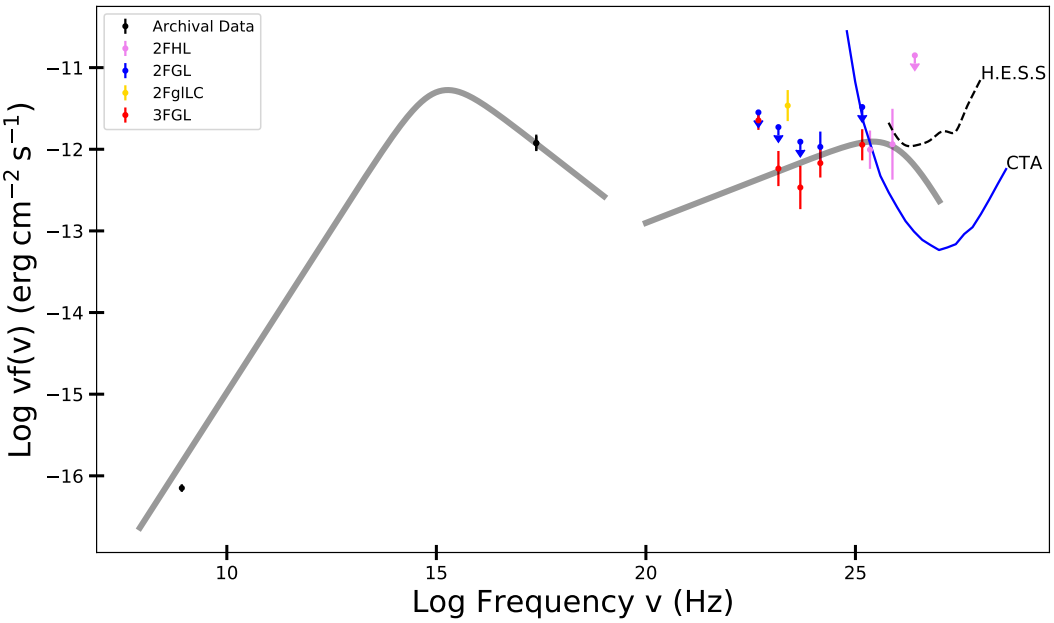

Figure 7.8: Broadband SED of 3FGL J1954.9-5640. The 50 h sensitivity curves of CTA South (sollid blue line) and H.E.S.S. (dashed black line) are overlayed on the SED. The γ-ray catalogues and colors are indicated in the SED legend. The low energy datapoints (black) is archival data retrieved from the NED and CDS Vizier services. Two smoothly broken power-laws (solid gray line) are overlayed on the SED to highlight the flux of the source.

7.2.8 3FGL J1959.8-4725

3FGL J1959.8-4725 is associated with the radio source SUMSS J195945-472519. It has a Synchrotron peak frequency of $\log\nu_{\mathrm{peak,Hz}} = 15.35$ and a spectral power-law index of $\Gamma_{0.1-100\ \mathrm{GeV}} = 1.81$. No redshift could be calculated for this featureless BL Lac. However, this source should be detectable by CTA South, since the VHE emission from various *Fermi* catalogs are above the CTA sensitivity threshold. The broadband SED is presented in Fig. 7.9.

Very view Blazars are detectable with IACTs due to low γ-ray flux and soft spectral indices. Therefore, blazars detected at VHE with IACTS should be studied in more detail to investigate why they are different from the larger population of γ-ray blazars. Table 7.1 lists the BCUs observed during this project that could be observable with IACTs.

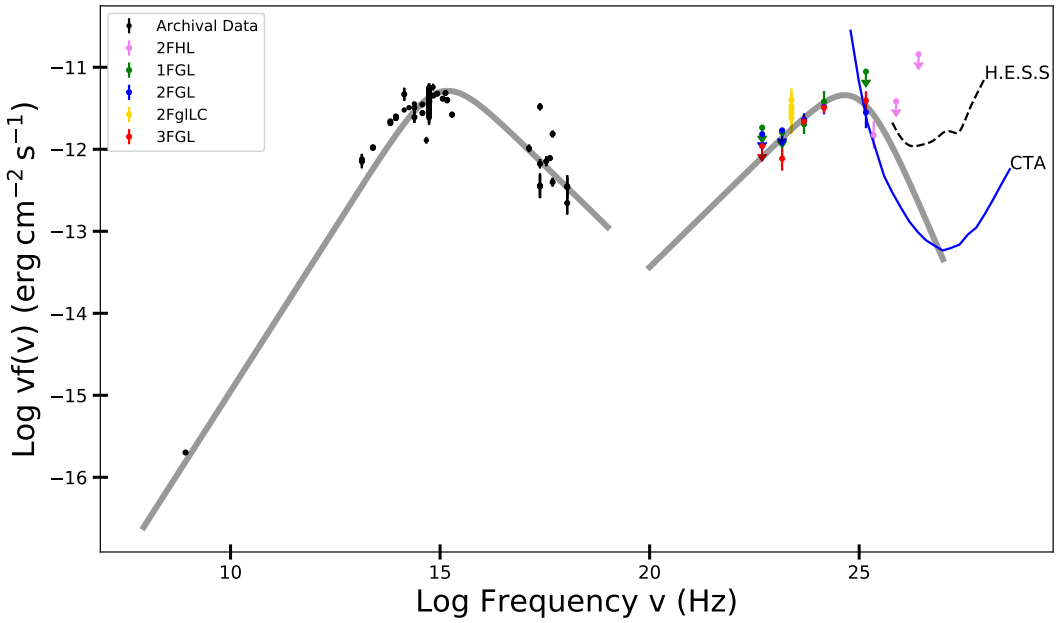

Figure 7.9: Broadband SED of 3FGL J1959.8-4725. The 50 h sensitivity curves of CTA South (sollid blue line) and H.E.S.S. (dashed black line) are overlayed on the SED. The γ-ray catalogues and colors are indicated in the SED legend. The low energy datapoints (black) is archival data retrieved from the NED and CDS Vizier services. Two smoothly broken power-laws (solid gray line) are overlayed on the SED to highlight the flux of the source.

Table 7.1: The BCUs observed during this project that could be detectable with IACTs. The source Name, source Class, redshift, Spectral index and the log of the synchrotron peak frequency are indicated.

Name	Class	z	Sp index	Syn peak log Hz
3FGL J0051.2-6241	HBL	0.156?	1.66 ± 0.06	15.99
3FHL J0305.2-1609	HBL	0.312 ± 0.001	1.69 ± 0.19	15.57
3FHL J1130.5-7801	-	0.317 ± 0.001	1.74 ± 0.14	-
3FGL J1406.0-2508	HBL	0.153?	1.89 ± 0.11	15.1
3FGL J1842.3-5841	HBL	0.138 ± 0.002	1.70 ± 0.12	16.476
3FGL J1944.1-4523	HBL	0.236 ± 0.002	1.56 ± 0.26	16.14
3FGL J1954.9-5640	-	0.221 ± 0.002	1.88 ± 0.16	-
3FGL J1959.8-4725	HBL	-	1.81	15.35

Chapter 8

Conclusion

To better understand and model blazar dynamics, the population of known FSRQs and BL Lac objects needs to be increased. These new AGN can be studied using multiwavelength observations, from radio to the very highest γ-ray energies. The VHE observations, carried out with IACTs such as H.E.S.S. and CTA South, will increase our understanding of the physical processes responsible for accelerating the emitting particles to energies required to emit VHE photons. The sample of detected VHE emitting blazars, although small, has already increased our understanding of blazar physics. Increasing the population of known blazars, and other novel AGN, that emit VHE γ-ray will provide additional data to test our current understanding of high energy processes.

A large number of the sources contained in the *Fermi*-LAT γ-ray catalogues remain unclassified or unassociated. Many of the brighter BCUs have already been classified since the release of the 3FGL and 3FHL catalogues. A large portion of the remaining unclassified sources are faint in all electromagnetic bands, making their classification and further study difficult. The classification and study of this population of faint γ-ray sources is still important, since new and novel classes of AGN might reside in this faint population. Even if no new AGN classes are discovered, increasing the number of classified blazars is still important for blazar population studies.

This project consisted of two parts: the first utilized $\sim$ 2 years of Watcher Robotic telescope observations to study the long-term behaviour of fourteen VHE blazars detected with H.E.S.S, while the second part consisted of classifying twelve faint 3FHL BCUs and unassociated sources and eleven 3FGL BCUs with optical spectroscopy using the SAAO 1.9-m SpUpNIC grating spectrograph.

8.1 Sample selection

The 16" Watcher Robotic telescope has been observing a number of H.E.S.S. detected TeV blazars since May 2015. Most of these sources are highly variable and are regularly observed with H.E.S.S. The sources were selected based on their observability with Watcher, and an upper magnitude limit $V_{mag} < 18$.

For the optical spectroscopic observations, selection criteria included observability from southern latitudes, high galactic latitudes ($|b| > 10°$), γ-ray photon indexes ($1.2 \gtrsim \Gamma \gtrsim 3$), blazar-like infrared spectra and $V_{mag} < 20$. X-ray and radio counterparts to the BCUS were also considered, but because all the sources considered are faint in much of the electromagnetic spectrum, the X-ray and radio flux of the sources were not considered during selection. All the selected sources lacked redshift measurements in their respective catalogues. An extensive search of the NED database was also performed to exclude sources with classifications and redshift measurements. However, after an extensive literature search when writing this dissertation, the 3FGL counterpart to 3FHL J0305.2-1609, 3FGL J0305.2-1607, was found to already be classified by Paiano et al. (2017), although the results were not yet added to the NED database when the source was observed. In addition, the unassociated source, 3FHL J0813.7-0353, had multiple optical candidates to which the γ-ray emission could be associated to. The source was constrained to five optical candidates. The most likely candidate was not detected during observations, therefore, the other candidates were observed to exclude them from the association.

8.1.1 Photometric results

Blazars are highly variable sources, exhibiting variability over the entire electromagnetic spectrum on timescales of hours to years. In order to study the optical variability of blazars on intra-day and long-term timescales observations were carried out with the SAAO 1.0-m SHOC instrument and the Watcher Robotic telescope.

During the observation campaign with the SAAO 1.9-m SpUpNIC grating spectrograph to classify *Fermi* 3FHL BCUs and unassociated sources during 2017, a selection of six of the sources were also observed with the SAAO 1.0-m SHOC instrument. Targets were observed in the clear filter for one to four hours in order to perform optical photometry. Exposure times were typically around 20 - 30 seconds, which resulted in a high S/N capable of being used to measure microvariability in

these sources.

Watcher observations from May 2015 to June 2017 were used to analyse the long-term variability of sources detected by H.E.S.S. These sources were observed in the V, R and i' filters with 30 second exposure times, which were stacked to 300 seconds to increase the S/N of the observations.

I conducted statistical variability tests to quantify the optical intra-day and long-term variability of the sources observed with SHOC and Watcher respectively. These tests included the F-test, the scaled F-test, the power-enhanced F-test and the χ^2-test. These tests generally agree with each other, with the power-enhanced F-test providing the most efficient detection of variability.

I observed six sources with SHOC, with one of the sources having multiple optical candidates, four of which were observed. All the tests detected variability or possible variability for four of the nine objects observed with SHOC. The power-enhanced F-test accepted variability for eight of the nine objects observed. This discrepancy can be attributed to the higher degrees of freedom in the power-enhanced F-test, which uses all the comparison stars when searching for variability and is therefore more sensitive to variability.

A search for LTV was also carried out for 14 of the H.E.S.S. detected sources observed with Watcher. Variability was detected for thirteen of the fourteen sources analysed. Of the eight sources with no flares or outbursts, LTV was detected for seven of the sources by all the tests.

From these results, it can be concluded that the majority of blazars are variable on diverse timescales. On short, intraday timescales the likelihood of detecting variability increases with the length of the observations. Long-term observation of blazars are likely to result in the detection of multiple outbursts, state changes and long-term variability, all of which will benefit from multiwavelength monitoring campaigns to investigate their cause.

8.1.2 Spectroscopic results

Longslit spectra of eleven 3FHL BCUs, a 3FHL unassociated source and eleven 3FGL BCUs were observed during 2016 and 2017 with the SAAO 1.9-m SpUpNIC grating spectrograph. The `IRAF` package **RVSAO** was used to measure the redshifts of the observed sources. The **RVSAO** package uses cross-correlation against template spectra to calculate the velocity offset between the target and the template, providing accurate redshift measurements of low S/N spectra. These measurements were further strengthened by the presence of emission and absorp-

tion lines in the measured spectra.

The strength of the characteristic emission lines (e.g. OII, NeII and OIII) are used to separate the BL Lacs and FSRQs. The absorption lines often detected in BL Lac spectra (e.g. Ca II H&K, G-band, MgI and NaI) originate from the stellar population and halo of the host galaxy and are often used to measure BL Lac redshifts.

Spectroscopic observation of BCUs is an efficient method to classify blazars based on the presence, or absence, of features characteristic of these sources. The strength of emission lines are an indicator of the strength of emission from the inner regions of the AGN, separating FSRQs and BL Lac objects. Finding absorption lines in blazar spectra or a diluted Ca H&K break gives an estimation of the power of the jet, since the non-thermal emission will dominate and dilute the thermal emission from the host galaxy.

This project was able to classify 10 of the 290 BCUs in the 3FHL and 11 of the 568 BCUs in the 3FGL ($\sim 3.4\%$ and $\sim 1.9\%$ respectively) as BL Lac objects. Although this only constitutes a small percentage in either catalogue, this project further reduced the number of sources yet to be classified.

8.1.3 Detectability of BCUs by IACTs

Broadband SEDs were constructed for all the 3FHL and 3FGL BCUs in order to determine if they can be observed by H.E.S.S.or CTA South. The H.E.S.S. and CTA 50 h sensitivity curves were overlayed on the SED to give an estimate of the detectability of the source. Of the 21 BCUs observed 8 of the sources have flux above the sensitivity threshold of CTA South, making their detection by CTA likely. No modelling has been performed for the observed sources, since most of them lack sufficient multiwavelength data to perform accurate modelling.

8.2 Future studies

AGN have been studied for many years, but questions still remain. Are leptonic and/or hadronic process involved in the non-thermal HE and VHE emission? What particles constitute the majority of the jet and are they the main emitters? These questions are difficult to answer with the current limited sample of VHE emitting AGN.

The Watcher Robotic Telescope is regularly monitoring seventeen TeV detected blazars. Only data from 2015 - 2017 for fourteen of these sources have been an-

alyzed for this project. Future studies will include data from all available observations. This increased dataset will provide more information concerning the long-term activity of these blazars, which will inform future long-term studies for the sources.

There are still many extragalactic γ-ray sources detected by *Fermi* that need to be classified. In this sample of unclassified sources, there are many blazars observable with the next generation IACTs like CTA. Future spectroscopic studies still need to be performed in order to observe a further thirty 3FHL BCUs that meet this project's selection criteria. These sources could not be observed due to time constraints during the observing campaigns. Some of these sources will be detectable by CTA South and need further study.

Bibliography

Abdo, A. A., Ackermann, M., Agudo, I., et al. 2010a, ApJ, 716, 30, doi: 10.1088/0004-637X/716/1/30

Abdo, A. A., Ackermann, M., Ajello, M., et al. 2010b, ApJ, 722, 520, doi: 10.1088/0004-637X/722/1/520

Abdo, A. A., Ackermann, M., Ajello, M., et al. 2011, ApJ, 736, 131, doi: 10.1088/0004-637X/736/2/131

Abdollahi, S., Ackermann, M., Ajello, M., et al. 2017, ApJ, 846, 34, doi: 10.3847/1538-4357/aa8092

Abeysekara, A. U., Alfaro, R., Alvarez, C., et al. 2013, Astroparticle Physics, 50, 26, doi: 10.1016/j.astropartphys.2013.08.002

Abeysekara, A. U., Archambault, S., Archer, A., et al. 2017, ApJS, 233, 7, doi: 10.3847/1538-4365/aa8d76

Acero, F., Ackermann, M., Ajello, M., et al. 2015, ApJS, 218, 23, doi: 10.1088/0067-0049/218/2/23

Ackermann, M., Ajello, M., Atwood, W. B., et al. 2015, ApJ, 810, 14, doi: 10.1088/0004-637X/810/1/14

Ackermann, M., Ajello, M., Atwood, W. B., et al. 2016, ApJS, 222, 5, doi: 10.3847/0067-0049/222/1/5

Agarwal, A., & Gupta, A. C. 2015, MNRAS, 450, 541, doi: 10.1093/mnras/stv625

Ajello, M., Atwood, W. B., Baldini, L., et al. 2017, ApJS, 232, 18, doi: 10.3847/1538-4365/aa8221

Aleksić, J., Ansoldi, S., Antonelli, L. A., et al. 2014, A&A, 567, A135, doi: 10.1051/0004-6361/201423364

Aleksić, J., Ansoldi, S., Antonelli, L. A., et al. 2016, Astroparticle Physics, 72, 76, doi: 10.1016/j.astropartphys.2015.02.005

Aloy, M.-Á., Martí, J.-M., Gómez, J.-L., et al. 2003, ApJ, 585, L109, doi: 10.1086/374543

Álvarez Crespo, N., Massaro, F., Milisavljevic, D., et al. 2016, AJ, 151, 95, doi: 10.3847/0004-6256/151/4/95

Antonucci, R. 1993, ARA&A, 31, 473, doi: 10.1146/annurev.aa.31.090193.002353

Antonucci, R. R. J. 1984, ApJ, 278, 499, doi: 10.1086/161816

Armstrong, T., Brown, A. M., & Chadwick, P. M. 2017, MNRAS, 470, 4089, doi: 10.1093/mnras/stx1309

Atwood, W. B., Abdo, A. A., Ackermann, M., et al. 2009, ApJ, 697, 1071, doi: 10.1088/0004-637X/697/2/1071

Bañados, E., Venemans, B. P., Mazzucchelli, C., et al. 2018, Nature, 553, 473, doi: 10.1038/nature25180

Baldwin, J. A., Phillips, M. M., & Terlevich, R. 1981, PASP, 93, 5, doi: 10.1086/130766

Barbary, K. 2016, The Journal of Open Source Software, 1, 58, doi: 10.21105/joss.00058

Barniol Duran, R., Tchekhovskoy, A., & Giannios, D. 2017, MNRAS, 469, 4957, doi: 10.1093/mnras/stx1165

Barth, A. J., Greene, J. E., & Ho, L. C. 2005, ApJ, 619, L151, doi: 10.1086/428365

Beckmann, V., & Shrader, C. R. 2012, Active Galactic Nuclei

Bennert, N., Falcke, H., Schulz, H., Wilson, A. S., & Wills, B. J. 2002, ApJ, 574, L105, doi: 10.1086/342420

Bentz, M. C., Denney, K. D., Grier, C. J., et al. 2013, ApJ, 767, 149, doi: 10.1088/0004-637X/767/2/149

Berger, K., Majumdar, P., Lindfors, E., et al. 2009, ArXiv e-prints, arXiv:0907.1046. https://arxiv.org/abs/0907.1046

Bertin, E., & Arnouts, S. 1996, Astronomy and Astrophysics Supplement Series, 117, 393, doi: 10.1051/aas:1996164

Blandford, R. D. 1976, MNRAS, 176, 465, doi: 10.1093/mnras/176.3.465

Blandford, R. D., & McKee, C. F. 1982, ApJ, 255, 419, doi: 10.1086/159843

Blandford, R. D., & Znajek, R. L. 1977, MNRAS, 179, 433, doi: 10.1093/mnras/179.3.433

Boller, T., Freyberg, M. J., Trümper, J., et al. 2016, A&A, 588, A103, doi: 10.1051/0004-6361/201525648

Böttcher, M. 2007, Ap&SS, 309, 95, doi: 10.1007/s10509-007-9404-0

Böttcher, M. 2010, ArXiv e-prints. https://arxiv.org/abs/1006.5048

Böttcher, M., Harris, D. E., & Krawczynski, H. 2012, Relativistic Jets from Active Galactic Nuclei

Böttcher, M., Reimer, A., & Marscher, A. P. 2009, ApJ, 703, 1168, doi: 10.1088/0004-637X/703/1/1168

Böttcher, M., Reimer, A., Sweeney, K., & Prakash, A. 2013, ApJ, 768, 54, doi: 10.1088/0004-637X/768/1/54

Böttcher, M., van Soelen, B., Britto, R., et al. 2017, Galaxies, 5, 52, doi: 10.3390/galaxies5030052

Brenneman, L. W., Reynolds, C. S., Nowak, M. A., et al. 2011, ApJ, 736, 103, doi: 10.1088/0004-637X/736/2/103

Brown, A. M. 2013, MNRAS, 431, 824, doi: 10.1093/mnras/stt218

Burdanov, A. Y., Krushinsky, V. V., & Popov, A. A. 2014, Astrophysical Bulletin, 69, 368, doi: 10.1134/S1990341314030122

Carmona-Loaiza, J. M., Colpi, M., Dotti, M., & Valdarnini, R. 2015, MNRAS, 453, 1608, doi: 10.1093/mnras/stv1749

Carnerero, M. I., Raiteri, C. M., Villata, M., et al. 2017, MNRAS, 472, 3789, doi: 10.1093/mnras/stx2185

Castignani, G., Pian, E., Belloni, T. M., et al. 2017, A&A, 601, A30, doi: 10.1051/0004-6361/201629775

Cerruti, M., Lenain, J.-P., Prokoph, H., & for the H. E. S. S. Collaboration. 2017, ArXiv e-prints. https://arxiv.org/abs/1708.00658

Cerruti, M., Zech, A., Boisson, C., & Inoue, S. 2011, in SF2A-2011: Proceedings of the Annual meeting of the French Society of Astronomy and Astrophysics, ed. G. Alecian, K. Belkacem, R. Samadi, & D. Valls-Gabaud, 555–558

Ciprini, S., Tosti, G., Raiteri, C. M., et al. 2003, A&A, 400, 487, doi: 10.1051/0004-6361:20030045

Condon, J. J. 1992, ARA&A, 30, 575, doi: 10.1146/annurev.aa.30.090192.003043

Condon, J. J., Cotton, W. D., Greisen, E. W., et al. 1998, AJ, 115, 1693, doi: 10.1086/300337

Coppejans, R., & Gulbis, A. A. S., SHOCnhelpful, a Guide to the Sutherland High-speed Optical Cameras. 2017. http://shoc.saao.ac.za/Documents/ShocnHelpful.pdf, accessed on 14/06/2018

Coppejans, R., Gulbis, A. A. S., Kotze, M. M., et al. 2013, Publications of the Astronomical Society of the Pacific, 125, 976, doi: 10.1086/672156

Corbett, E. A., Robinson, A., Axon, D. J., & Young, S. 2000, MNRAS, 319, 685, doi: 10.1046/j.1365-8711.2000.03658.x

Crause, L. A., Carter, D., Daniels, A., et al. 2016, in Ground-based and Airborne Instrumentation for Astronomy VI, Vol. 9908, 990827

Cutri, R. M., & et al. 2014, VizieR Online Data Catalog, II/328

Czerny, B., & You, B. 2016, Astronomische Nachrichten, 337, 73, doi: 10.1002/asna.201512268

D'Abrusco, R., Massaro, F., Ajello, M., et al. 2012, ApJ, 748, 68, doi: 10.1088/0004-637X/748/1/68

Daly, R. A., & Marscher, A. P. 1988, ApJ, 334, 539, doi: 10.1086/166858

de Diego, J. A. 2010, AJ, 139, 1269, doi: 10.1088/0004-6256/139/3/1269

de Diego, J. A. 2014, AJ, 148, 93, doi: 10.1088/0004-6256/148/5/93

de Diego, J. A., Polednikova, J., Bongiovanni, A., et al. 2015, AJ, 150, 44, doi: 10.1088/0004-6256/150/2/44

della Ceca, R., Lamorani, G., Maccacaro, T., et al. 1994, ApJ, 430, 533, doi: 10.1086/174428

Dobler, G., Finkbeiner, D. P., Cholis, I., Slatyer, T., & Weiner, N. 2010, ApJ, 717, 825, doi: 10.1088/0004-637X/717/2/825

Donato, D., Ghisellini, G., Tagliaferri, G., & Fossati, G. 2001, A&A, 375, 739, doi: 10.1051/0004-6361:20010675

Done, C. 2010, ArXiv e-prints. https://arxiv.org/abs/1008.2287

Dressler, A., & Shectman, S. A. 1987, AJ, 94, 899, doi: 10.1086/114524

Dwek, E., & Krennrich, F. 2013, Astroparticle Physics, 43, 112, doi: 10.1016/j.astropartphys.2012.09.003

Evans, P. A., Osborne, J. P., Beardmore, A. P., et al. 2013, VizieR Online Data Catalog, IX/43

Everett, M. E., & Howell, S. B. 2001, Publications of the Astronomical Society of the Pacific, 113, 1428, doi: 10.1086/323387

Fabian, A. C. 2008, Astronomische Nachrichten, 329, 155, doi: 10.1002/asna.200710902

Fabian, A. C., Iwasawa, K., Reynolds, C. S., & Young, A. J. 2000, PASP, 112, 1145, doi: 10.1086/316610

Fabian, A. C., Vaughan, S., Nandra, K., et al. 2002, MNRAS, 335, L1, doi: 10.1046/j.1365-8711.2002.05740.x

Fanaroff, B. L., & Riley, J. M. 1974, MNRAS, 167, 31P, doi: 10.1093/mnras/167.1.31P

Feltre, A., Hatziminaoglou, E., Fritz, J., & Franceschini, A. 2012, MNRAS, 426, 120, doi: 10.1111/j.1365-2966.2012.21695.x

Filippenko, A. V., & Halpern, J. P. 1984, ApJ, 285, 458, doi: 10.1086/162521

Fischer, J. U., Hasinger, G., Schwope, A. D., et al. 1998, Astronomische Nachrichten, 319, 347, doi: 10.1002/asna.2123190603

Fossati, G., Maraschi, L., Celotti, A., Comastri, A., & Ghisellini, G. 1998, MNRAS, 299, 433, doi: 10.1046/j.1365-8711.1998.01828.x

Fritz, J., Franceschini, A., & Hatziminaoglou, E. 2006, MNRAS, 366, 767, doi: 10.1111/j.1365-2966.2006.09866.x

García-González, J., Alonso-Herrero, A., Hönig, S. F., et al. 2017, MNRAS, 470, 2578, doi: 10.1093/mnras/stx1361

Gaskell, C. M. 1988, ApJ, 325, 114, doi: 10.1086/165986

Gaur, H., Gupta, A., Bachev, R., et al. 2017, Galaxies, 5, 94, doi: 10.3390/galaxies5040094

Gaur, H., Gupta, A. C., Strigachev, A., et al. 2012a, MNRAS, 425, 3002, doi: 10.1111/j.1365-2966.2012.21583.x

Gaur, H., Gupta, A. C., Strigachev, A., et al. 2012b, MNRAS, 420, 3147, doi: 10.1111/j.1365-2966.2011.20243.x

Ghisellini, G. 2016, Galaxies, 4, 36, doi: 10.3390/galaxies4040036

Ghisellini, G., Celotti, A., Fossati, G., Maraschi, L., & Comastri, A. 1998, MNRAS, 301, 451, doi: 10.1046/j.1365-8711.1998.02032.x

Gilmore, R. C., Somerville, R. S., Primack, J. R., & Domínguez, A. 2012, MNRAS, 422, 3189, doi: 10.1111/j.1365-2966.2012.20841.x

Giomi, M., Bühler, R., Sgrò, C., Longo, F., & Atwood, W. B. 2017, in American Institute of Physics Conference Series, Vol. 1792, 6th International Symposium on High Energy Gamma-Ray Astronomy, 070022

Glass, I. S. 1989, Quarterly Journal of the Royal Astronomical Society, 30, 33

Goodrich, R. W. 1989, ApJ, 342, 224, doi: 10.1086/167586

Goyal, A., Gopal-Krishna, Wiita, P. J., et al. 2012, A&A, 544, A37, doi: 10.1051/0004-6361/201218888

Goyal, A., Stawarz, Ł., Ostrowski, M., et al. 2017, ApJ, 837, 127, doi: 10.3847/1538-4357/aa6000

Granato, G. L., & Danese, L. 1994, MNRAS, 268, 235, doi: 10.1093/mnras/268.1.235

Gupta, A. C., & Joshi, U. C. 2005, A&A, 440, 855, doi: 10.1051/0004-6361:20042370

Gupta, A. C., Kalita, N., Gaur, H., & Duorah, K. 2016, MNRAS, 462, 1508, doi: 10.1093/mnras/stw1667

Hansen, J. E., & Travis, L. D. 1974, Space Sci. Rev., 16, 527, doi: 10.1007/BF00168069

Hartman, R. C., Bertsch, D. L., Bloom, S. D., et al. 1999, ApJS, 123, 79, doi: 10.1086/313231

Holder, J. 2017, in American Institute of Physics Conference Series, Vol. 1792, 6th International Symposium on High Energy Gamma-Ray Astronomy, 020013

Hönig, S. F., Beckert, T., Ohnaka, K., & Weigelt, G. 2006, A&A, 452, 459, doi: 10.1051/0004-6361:20054622

Hönig, S. F., & Kishimoto, M. 2017, ApJ, 838, L20, doi: 10.3847/2041-8213/aa6838

Howell, S. B. 2006, Handbook of CCD Astronomy, 2nd edn., Vol. 5 (Cambridge, UK: Cambridge University Press)

Howell, S. B., Mitchell, K. J., & Warnock, A., I. 1988, AJ, 95, 247, doi: 10.1086/114634

Hummel, C. A., Schalinski, C. J., Krichbaum, T. P., et al. 1992, A&A, 257, 489

Ingram, A., & Done, C. 2012, MNRAS, 427, 934, doi: 10.1111/j.1365-2966.2012.21907.x

Isler, J. C., Urry, C. M., Coppi, P., et al. 2017, ApJ, 844, 107, doi: 10.3847/1538-4357/aa79fc

Jones, D. L., & Wehrle, A. E. 1994, ApJ, 427, 221, doi: 10.1086/174134

Jorstad, S. G., Marscher, A. P., Lister, M. L., et al. 2005, AJ, 130, 1418, doi: 10.1086/444593

Joshi, R., Chand, H., Gupta, A. C., & Wiita, P. J. 2011, MNRAS, 412, 2717, doi: 10.1111/j.1365-2966.2010.18099.x

Jun, H. D., Im, M., Kim, D., & Stern, D. 2017, ApJ, 838, 41, doi: 10.3847/1538-4357/aa63f9

Kawabata, K. S., Okazaki, A., Akitaya, H., et al. 1999, PASP, 111, 898, doi: 10.1086/316387

Kharb, P., Lister, M. L., & Cooper, N. J. 2010, ApJ, 710, 764, doi: 10.1088/0004-637X/710/1/764

Kilkenny, D., & Worters, H., The SAAO 1.9-m Telescope and Grating spectrograph, version 6.5. 2014. https://www.saao.ac.za/wp-content/uploads/sites/5/spmanv6.5.pdf, accessed on 25/10/2018

Kimball, A. E., & Ivezić, Ž. 2008, AJ, 136, 684, doi: 10.1088/0004-6256/136/2/684

Koratkar, A., & Blaes, O. 1999, PASP, 111, 1, doi: 10.1086/316294

Korista, K. T., Alloin, D., Barr, P., et al. 1995, ApJS, 97, 285, doi: 10.1086/192144

Kotze, M., A data reduction pipeline for SHOC. 2013. http://shoc.saao.ac.za/Pipeline/SHOCpipeline.pdf, accessed on 10/03/2017

Kurtz, M. J., & Mink, D. J. 1998, Publications of the Astronomical Society of the Pacific, 110, 934, doi: 10.1086/316207

Kushwaha, P., Sinha, A., Misra, R., Singh, K. P., & de Gouveia Dal Pino, E. M. 2017, ApJ, 849, 138, doi: 10.3847/1538-4357/aa8ef5

Landt, H., & Bignall, H. E. 2008, MNRAS, 391, 967, doi: 10.1111/j.1365-2966.2008.13967.x

Landt, H., Padovani, P., & Giommi, P. 2002, MNRAS, 336, 945, doi: 10.1046/j.1365-8711.2002.05832.x

Landt, H., Ward, M. J., Baloković, M., et al. 2017, MNRAS, 464, 2565, doi: 10.1093/mnras/stw2447

Maini, A., Prandoni, I., Norris, R. P., Giovannini, G., & Spitler, L. R. 2016, A&A, 589, L3, doi: 10.1051/0004-6361/201628305

Manganaro, M., Becerra, J., Nievas, M., et al. 2016, in Journal of Physics Conference Series, Vol. 718, Journal of Physics Conference Series, 052022

Marcha, M. J. M., Browne, I. W. A., Impey, C. D., & Smith, P. S. 1996, MNRAS, 281, 425, doi: 10.1093/mnras/281.2.425

Markwardt, C. B. 2009, in Astronomical Data Analysis Software and Systems XVIII, ed. D. A. Bohlender, D. Durand, & P. Dowler, Vol. 411, 251

Marocco, J., Hache, E., & Lamareille, F. 2011, A&A, 531, A71, doi: 10.1051/0004-6361/201016143

Massey, P., & Lindsey, L. E. 1992, A User's Guide to Stellar CCD Photometry with IRAF. iraf.noao.edu/iraf/ftp/iraf/docs/daophot2.ps.Z

Mauch, T., Murphy, T., Buttery, H. J., et al. 2003, MNRAS, 342, 1117, doi: 10.1046/j.1365-8711.2003.06605.x

Miley, G. 1980, ARA&A, 18, 165, doi: 10.1146/annurev.aa.18.090180.001121

Mushotzky, R. F., Done, C., & Pounds, K. A. 1993, ARA&A, 31, 717, doi: 10.1146/annurev.astro.31.1.717

Nakagawa, K., & Mori, M. 2013, ApJ, 773, 177, doi: 10.1088/0004-637X/773/2/177

Netzer, H. 2006, Active Galactic Nuclei: Basic Physics and Main Components, ed. D. Alloin, 1

Osterbrock, D. E. 1989, Annals of the New York Academy of Sciences, 571, 99, doi: 10.1111/j.1749-6632.1989.tb50500.x

Osterbrock, D. E. 1991, Reports on Progress in Physics, 54, 579, doi: 10.1088/0034-4885/54/4/002

Paiano, S., Falomo, R., Franceschini, A., Treves, A., & Scarpa, R. 2017, ApJ, 851, 135, doi: 10.3847/1538-4357/aa9af4

Peterson, B. M., Ferrarese, L., Gilbert, K. M., et al. 2004, ApJ, 613, 682, doi: 10.1086/423269

Pica, A. J., & Smith, A. G. 1983, ApJ, 272, 11, doi: 10.1086/161257

Pier, E. A., & Krolik, J. H. 1992, ApJ, 401, 99, doi: 10.1086/172042

Pühlhofer, G. 2018, arXiv e-prints, arXiv:1801.06074. https://arxiv.org/abs/1801.06074

Raiteri, C. M., Villata, M., Acosta-Pulido, J. A., et al. 2017, Nature, 552, 374, doi: 10.1038/nature24623

Rani, B., Gupta, A. C., Joshi, U. C., Ganesh, S., & Wiita, P. J. 2011, MNRAS, 413, 2157, doi: 10.1111/j.1365-2966.2011.18288.x

Rees, M. J. 1982, in IAU Symposium, Vol. 97, Extragalactic Radio Sources, ed. D. S. Heeschen & C. M. Wade, 211–221

Rees, M. J., Netzer, H., & Ferland, G. J. 1989, ApJ, 347, 640, doi: 10.1086/168155

Romoli, C., Zacharias, M., Meyer, M., et al. 2017, ArXiv e-prints. https://arxiv.org/abs/1708.00882

Rovero, A. C., Donzelli, C., Pichel, A., & Muriel, H. 2015, ArXiv e-prints. https://arxiv.org/abs/1509.08377

Rowan-Robinson, M. 1995, MNRAS, 272, 737, doi: 10.1093/mnras/272.4.737

Ruffini, R., & Wheeler, J. A. 1971, Physics Today, 24, 30, doi: 10.1063/1.3022513

Rybicki, G., & Lightman, A. 2008, Radiative Processes in Astrophysics, Physics textbook (Wiley). https://books.google.co.za/books?id=eswe2StAspsC

Schmidt, G. D., & Smith, P. S. 2000, ApJ, 545, 117, doi: 10.1086/317811

Schmidt, M. 1963, Nature, 197, 1040, doi: 10.1038/1971040a0

Schneider, P. 2015, Extragalactic Astronomy and Cosmology: An Introduction, doi: 10.1007/978-3-642-54083-7

Sergeev, S. G., Pronik, V. I., Sergeeva, E. A., & Malkov, Y. F. 1999, ApJS, 121, 159, doi: 10.1086/313192

Seyfert, C. K. 1943, ApJ, 97, 28, doi: 10.1086/144488

Shakura, N. I., & Sunyaev, R. A. 1973, A&A, 24, 337

Shen, Z.-Q., Jiang, D. R., Kameno, S., & Chen, Y. J. 2001, A&A, 370, 65, doi: 10.1051/0004-6361:20010193

Singh, K. K., Sahayanathan, S., Tickoo, A. K., & Bhatt, N. 2014, New A, 27, 34, doi: 10.1016/j.newast.2013.08.004

Smith, P. S., Schmidt, G. D., & Jannuzi, B. T. 2011, ArXiv e-prints. https://arxiv.org/abs/1110.6040

Sokolov, A., Marscher, A. P., & McHardy, I. M. 2004, ApJ, 613, 725, doi: 10.1086/423165

Sramek, R. A., & Weedman, D. W. 1980, ApJ, 238, 435, doi: 10.1086/158000

Stalevski, M., Ricci, C., Ueda, Y., et al. 2016, MNRAS, 458, 2288, doi: 10.1093/mnras/stw444

Stanley, E. C., Kharb, P., Lister, M. L., et al. 2015, ApJ, 807, 48, doi: 10.1088/0004-637X/807/1/48

Stenholm, L. 1994, A&A, 290, 393

Stickel, M., Padovani, P., Urry, C. M., Fried, J. W., & Kuehr, H. 1991, ApJ, 374, 431, doi: 10.1086/170133

Strom, R. G., & Willis, A. G. 1980, A&A, 85, 36

Tadhunter, C. 2008, New A Rev., 52, 227, doi: 10.1016/j.newar.2008.06.004

Tchekhovskoy, A., Narayan, R., & McKinney, J. C. 2011, MNRAS, 418, L79, doi: 10.1111/j.1745-3933.2011.01147.x

Teukolsky, S. A. 2015, Classical and Quantum Gravity, 32, 124006, doi: 10.1088/0264-9381/32/12/124006

Thompson, D. J., Bertsch, D. L., Fichtel, C. E., et al. 1993, ApJS, 86, 629, doi: 10.1086/191793

Tonry, J., & Davis, M. 1979, AJ, 84, 1511, doi: 10.1086/112569

Tramacere, A., Giommi, P., Perri, M., Verrecchia, F., & Tosti, G. 2009, A&A, 501, 879, doi: 10.1051/0004-6361/200810865

Urry, C. M., & Padovani, P. 1995, PASP, 107, 803, doi: 10.1086/133630

van Dokkum, P. G. 2001, Publications of the Astronomical Society of the Pacific, 113, 1420, doi: 10.1086/323894

Veilleux, S., Shopbell, P. L., Rupke, D. S., Bland-Hawthorn, J., & Cecil, G. 2003, AJ, 126, 2185, doi: 10.1086/379000

Voges, W., Aschenbach, B., Boller, T., et al. 1999, A&A, 349, 389. https://arxiv.org/abs/astro-ph/9909315

Voges, W., Aschenbach, B., Boller, T., et al. 2000, International Astronomical Union Circular, 7432, 1

Völk, H. J., & Bernlöhr, K. 2009, Experimental Astronomy, 25, 173, doi: 10.1007/s10686-009-9151-z

Wagner, S. J., & Witzel, A. 1995, ARA&A, 33, 163, doi: 10.1146/annurev.aa.33.090195.001115

Wardle, J. F. C., & Aaron, S. E. 1997, MNRAS, 286, 425, doi: 10.1093/mnras/286.2.425

Wilson, A. S., Braatz, J. A., Heckman, T. M., Krolik, J. H., & Miley, G. K. 1993, ApJ, 419, L61, doi: 10.1086/187137

Wilson, A. S., & Colbert, E. J. M. 1995, ApJ, 438, 62, doi: 10.1086/175054

Wilson, A. S., Young, A. J., & Shopbell, P. L. 2001, ApJ, 547, 740, doi: 10.1086/318412

Wodaski, R. 2002, The new CCD astronomy, 2nd edn., Vol. 1 (Duvall: New Astronomy Press)

Wright, A., & Otrupcek, R. 1990, PKS Catalog (1990), 0

Wright, A. E., Griffith, M. R., Burke, B. F., & Ekers, R. D. 1994, The Astrophysical Journal Supplement Series, 91, 111, doi: 10.1086/191939

Wright, E. L., Eisenhardt, P. R. M., Mainzer, A. K., et al. 2010, AJ, 140, 1868, doi: 10.1088/0004-6256/140/6/1868

Xu, C., Baum, S. A., O'Dea, C. P., Wrobel, J. M., & Condon, J. J. 2000, AJ, 120, 2950, doi: 10.1086/316842

Yan, D., Wu, Q., Fan, X., Zhang, L., & Wang, J. 2017, ArXiv e-prints. https://arxiv.org/abs/1711.05939

Yang, J., Wang, J., Dai, B., & Gao, X. 2009, PASJ, 61, 1153, doi: 10.1093/pasj/61.5.1153

Yuan, F., & Narayan, R. 2014, ARA&A, 52, 529, doi: 10.1146/annurev-astro-082812-141003

Zhang, H., & Böttcher, M. 2013, ApJ, 774, 18, doi: 10.1088/0004-637X/774/1/18

Zhang, H., Chen, X., & Böttcher, M. 2014, ApJ, 789, 66, doi: 10.1088/0004-637X/789/1/66

Appendix A

3FHL and 3FGL BCUs not detectable by IACTs

The 3FHL and 3FGL BCUs observed with SpUpNIC are faint in γ-ray, and therefore most of them will not be detectable by IACTs in $\lesssim 50$ h of observation. The broadband SEDs of these sources are presented in this Appendix.

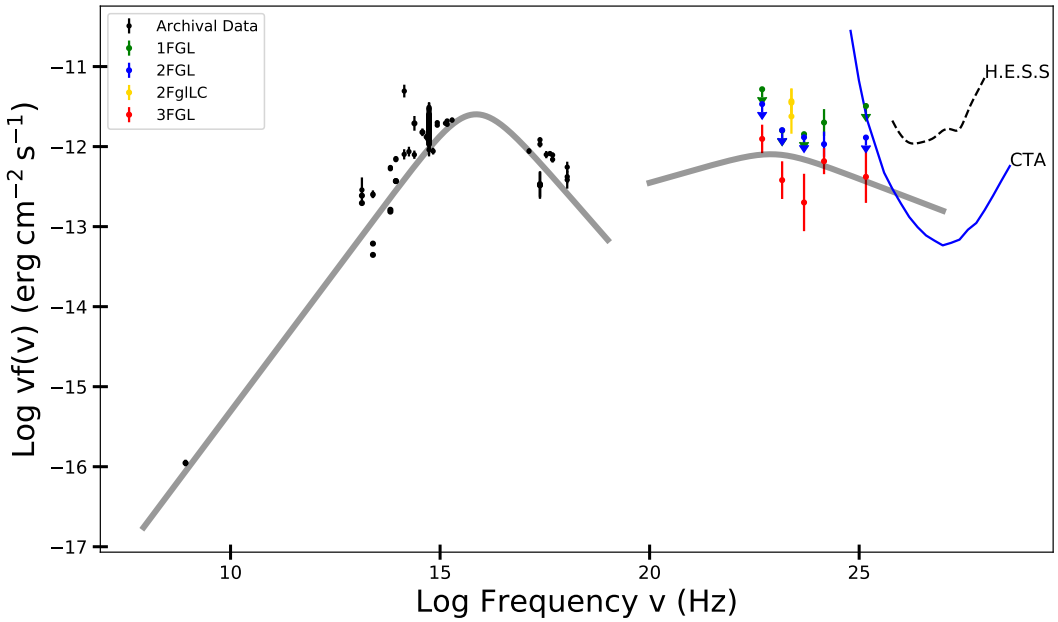

Figure A.1: Broadband SED of 3FHL J0001.9-4155. The 50 h sensitivity curves of CTA South (sollid blue line) and H.E.S.S. (dashed black line) are overlayed on the SED. The γ-ray catalogues and colors are indicated in the SED legend. The low energy datapoints (black) is archival data retrieved from the NED and CDS Vizier services. Two smoothly broken power-laws (solid gray line) are overlayed on the SED to highlight the flux of the source.

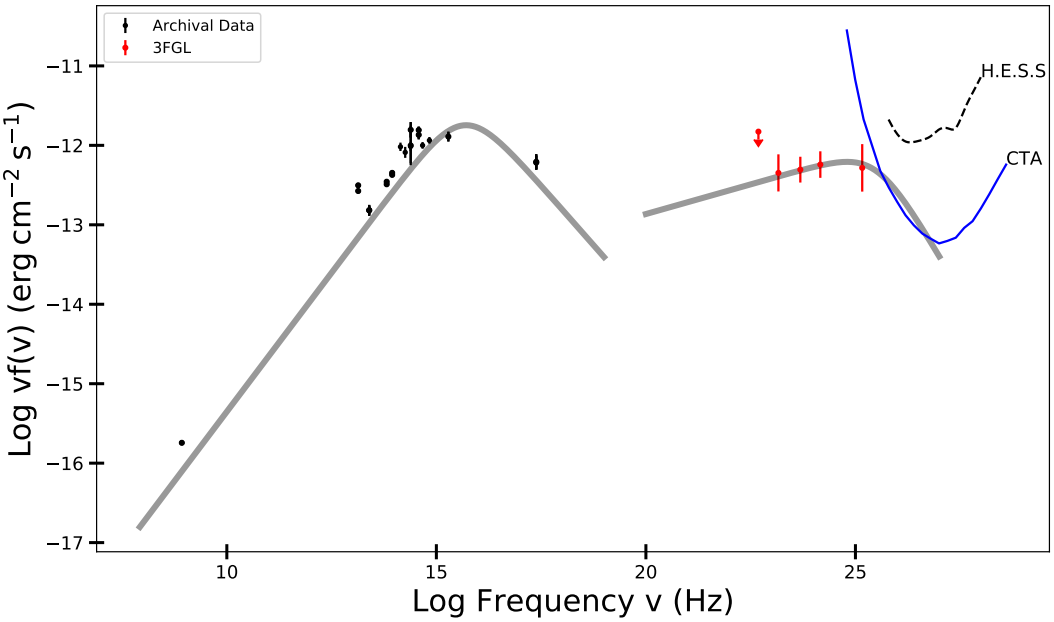

Figure A.2: Broadband SED of 3FHL J0002.1-6728. The 50 h sensitivity curves of CTA South (sollid blue line) and H.E.S.S. (dashed black line) are overlayed on the SED. The γ-ray catalogues and colors are indicated in the SED legend. The low energy datapoints (black) is archival data retrieved from the NED and CDS Vizier services. Two smoothly broken power-laws (solid gray line) are overlayed on the SED to highlight the flux of the source.

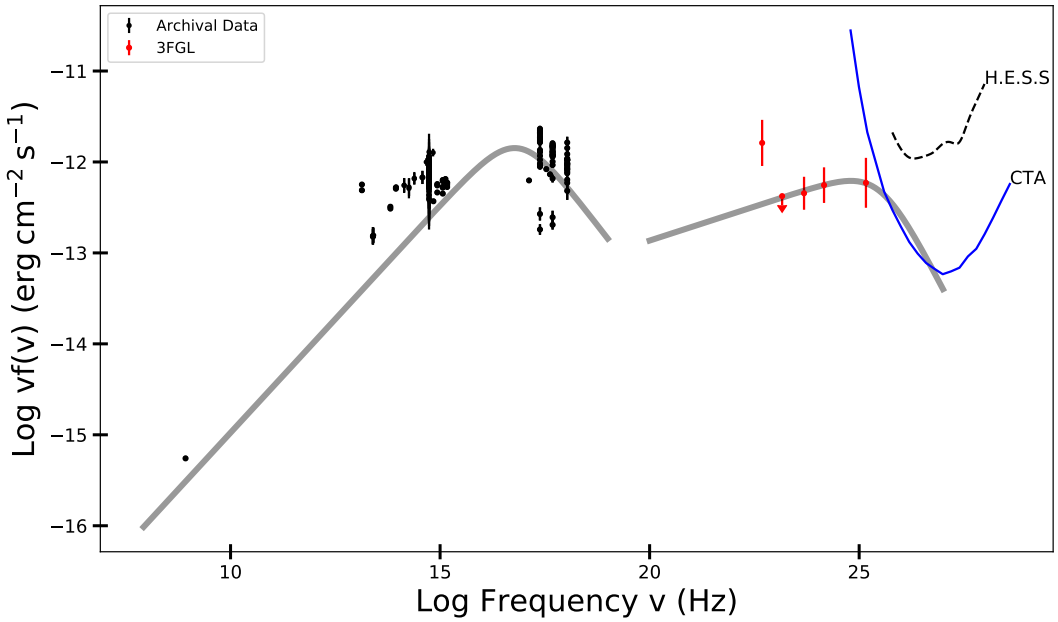

Figure A.3: Broadband SED of 3FHL J0003.3-5248. The 50 h sensitivity curves of CTA South (sollid blue line) and H.E.S.S. (dashed black line) are overlayed on the SED. The γ-ray catalogues and colors are indicated in the SED legend. The low energy datapoints (black) is archival data retrieved from the NED and CDS Vizier services. Two smoothly broken power-laws (solid gray line) are overlayed on the SED to highlight the flux of the source.

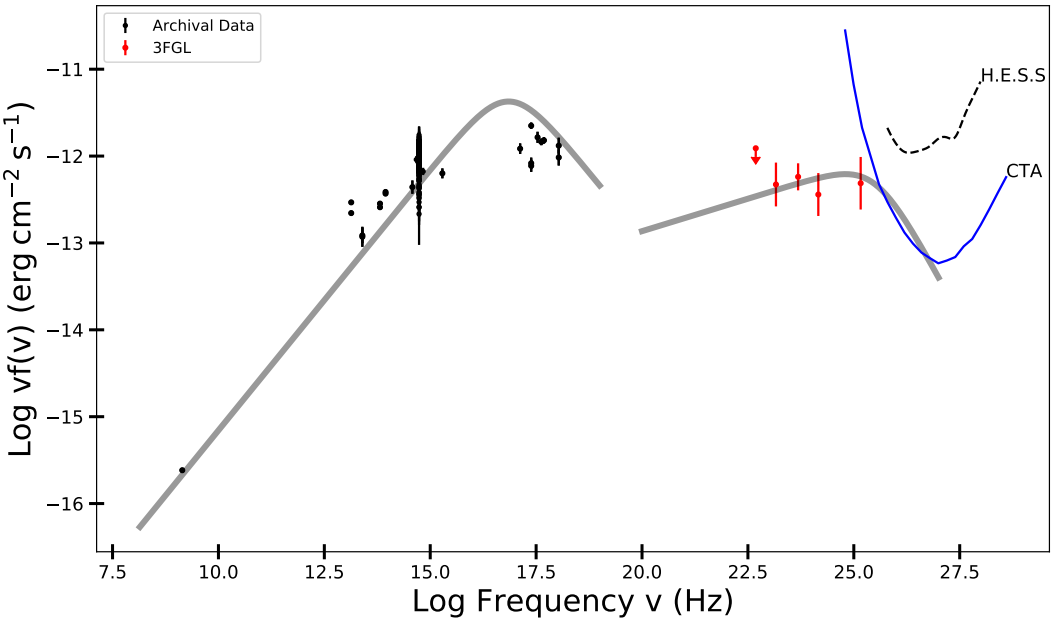

Figure A.4: Broadband SED of 3FHL J0115.9-2746. The 50 h sensitivity curves of CTA South (sollid blue line) and H.E.S.S. (dashed black line) are overlayed on the SED. The γ-ray catalogues and colors are indicated in the SED legend. The low energy datapoints (black) is archival data retrieved from the NED and CDS Vizier services. Two smoothly broken power-laws (solid gray line) are overlayed on the SED to highlight the flux of the source.

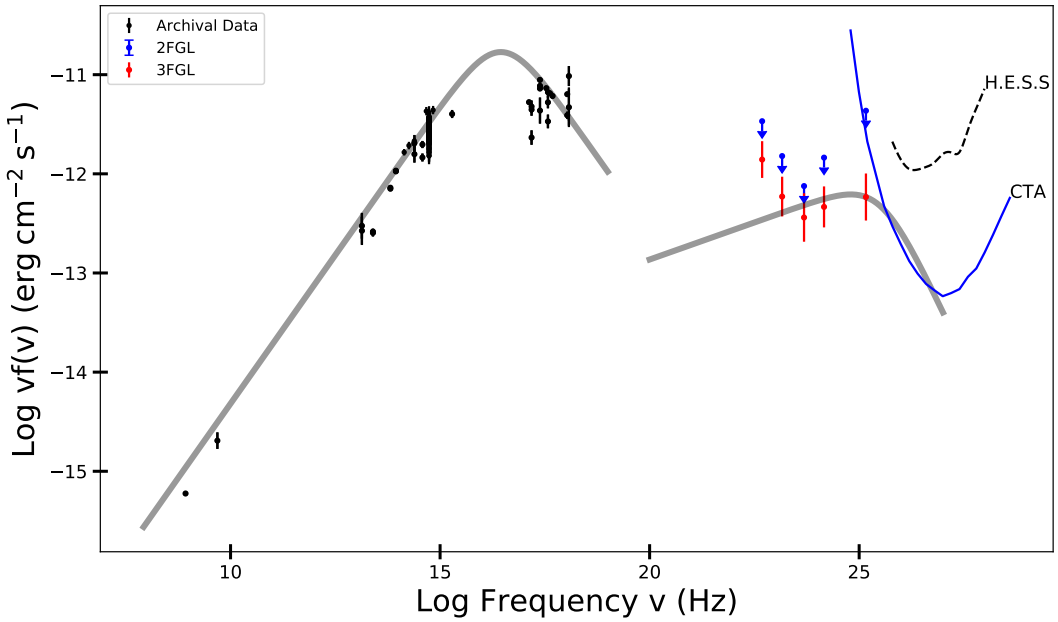

Figure A.5: Broadband SED of 3FHL J0647.0-5138. The 50 h sensitivity curves of CTA South (sollid blue line) and H.E.S.S. (dashed black line) are overlayed on the SED. The γ-ray catalogues and colors are indicated in the SED legend. The low energy datapoints (black) is archival data retrieved from the NED and CDS Vizier services. Two smoothly broken power-laws (solid gray line) are overlayed on the SED to highlight the flux of the source.

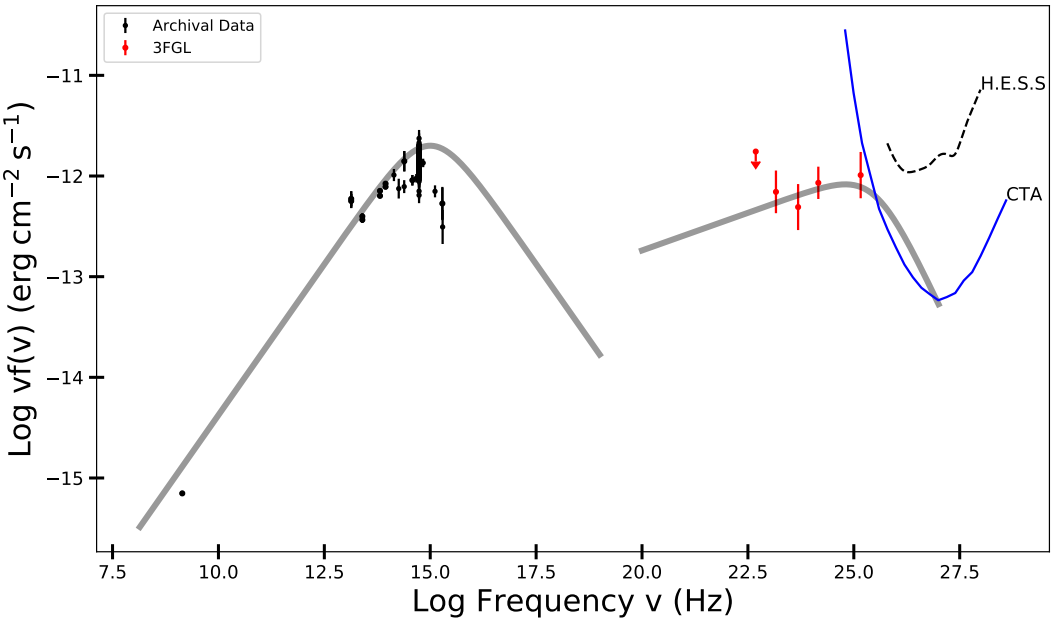

Figure A.6: Broadband SED of 3FHL J0935.2-1735. The 50 h sensitivity curves of CTA South (sollid blue line) and H.E.S.S. (dashed black line) are overlayed on the SED. The γ-ray catalogues and colors are indicated in the SED legend. The low energy datapoints (black) is archival data retrieved from the NED and CDS Vizier services. Two smoothly broken power-laws (solid gray line) are overlayed on the SED to highlight the flux of the source.

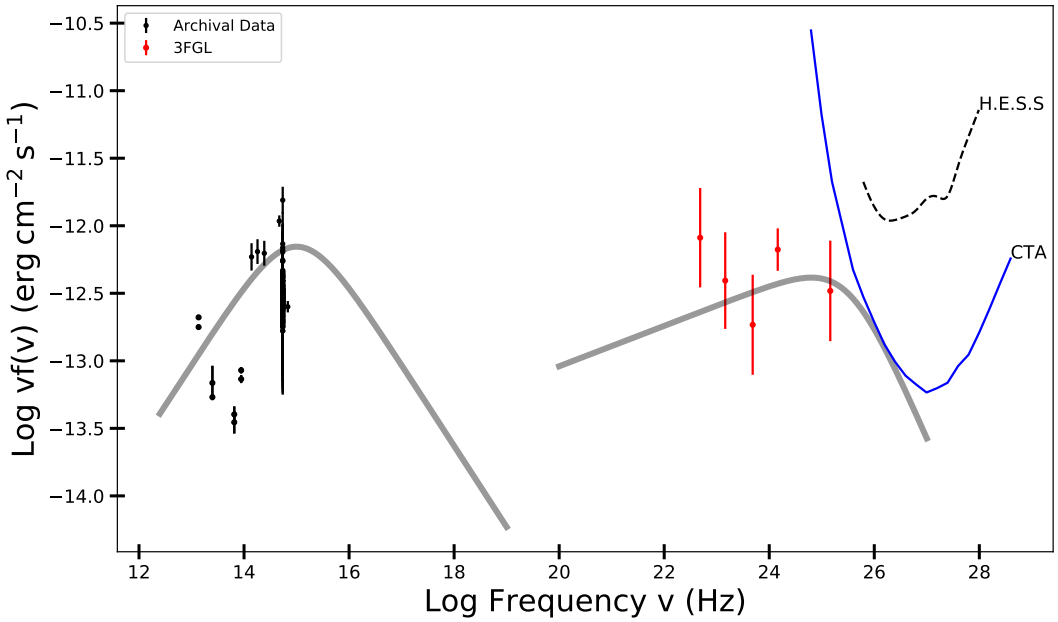

Figure A.7: Broadband SED of 3FHL J1042.2-4128. The 50 h sensitivity curves of CTA South (sollid blue line) and H.E.S.S. (dashed black line) are overlayed on the SED. The γ-ray catalogues and colors are indicated in the SED legend. The low energy datapoints (black) is archival data retrieved from the NED and CDS Vizier services. Two smoothly broken power-laws (solid gray line) are overlayed on the SED to highlight the flux of the source.

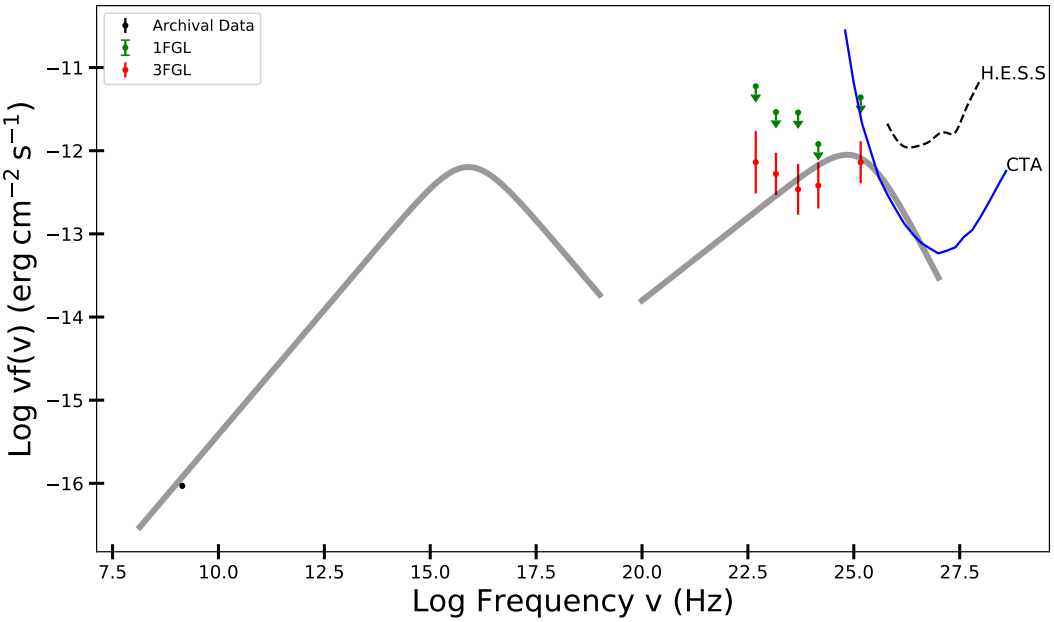

Figure A.8: Broadband SED of 3FHL J1123.5-3033. The 50 h sensitivity curves of CTA South (sollid blue line) and H.E.S.S. (dashed black line) are overlayed on the SED. The γ-ray catalogues and colors are indicated in the SED legend. The low energy datapoints (black) is archival data retrieved from the NED and CDS Vizier services. Two smoothly broken power-laws (solid gray line) are overlayed on the SED to highlight the flux of the source.

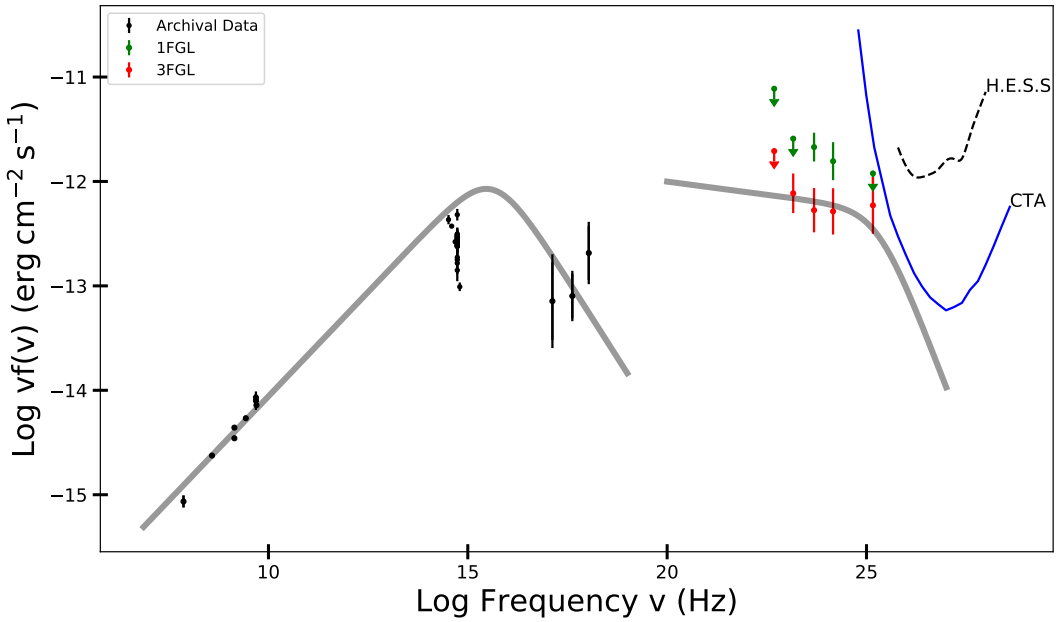

Figure A.9: Broadband SED of 3FGL J0256.3+0335. The 50 h sensitivity curves of CTA South (sollid blue line) and H.E.S.S. (dashed black line) are overlayed on the SED. The γ-ray catalogues and colors are indicated in the SED legend. The low energy datapoints (black) is archival data retrieved from the NED and CDS Vizier services. Two smoothly broken power-laws (solid gray line) are overlayed on the SED to highlight the flux of the source.

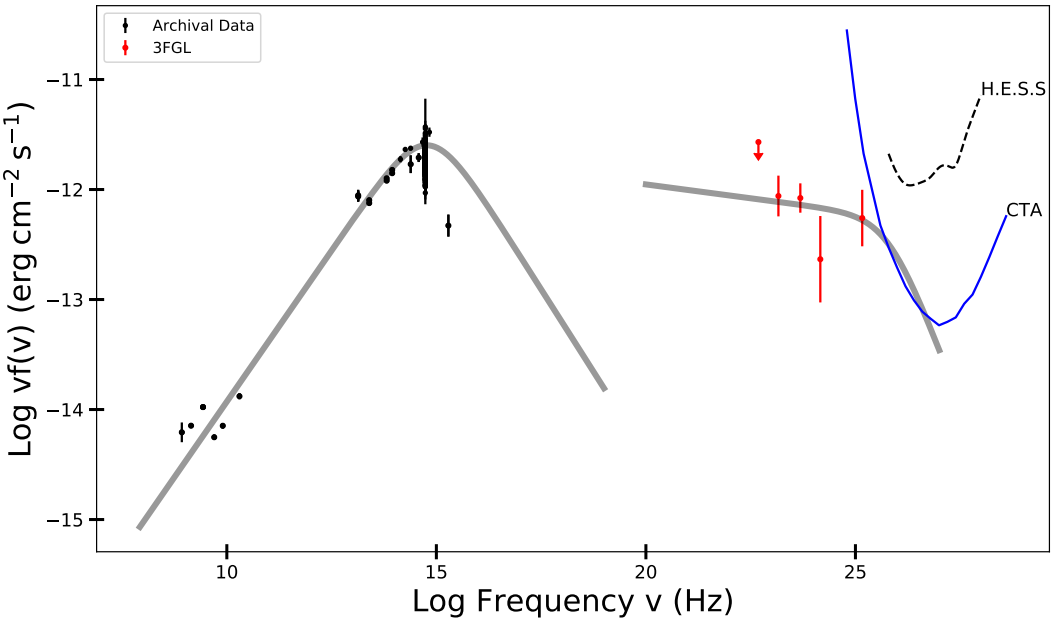

Figure A.10: Broadband SED of 3FGL J1344.5-3655. The 50 h sensitivity curves of CTA South (sollid blue line) and H.E.S.S. (dashed black line) are overlayed on the SED. The γ-ray catalogues and colors are indicated in the SED legend. The low energy datapoints (black) is archival data retrieved from the NED and CDS Vizier services. Two smoothly broken power-laws (solid gray line) are overlayed on the SED to highlight the flux of the source.

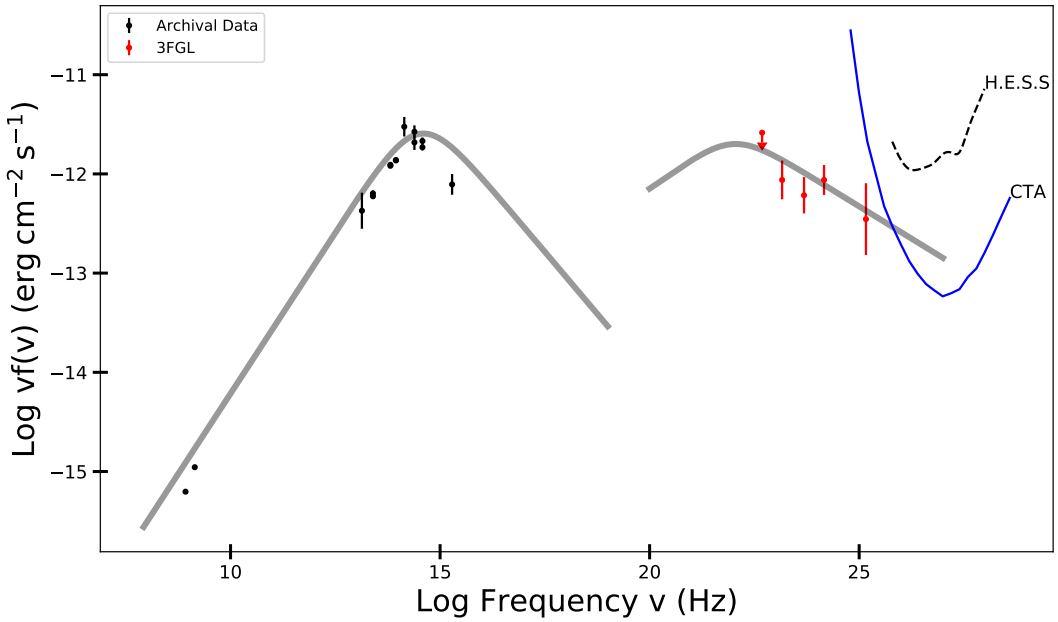

Figure A.11: Broadband SED of 3FGL J1507.6-3710. The 50 h sensitivity curves of CTA South (sollid blue line) and H.E.S.S. (dashed black line) are overlayed on the SED. The γ-ray catalogues and colors are indicated in the SED legend. The low energy datapoints (black) is archival data retrieved from the NED and CDS Vizier services. Two smoothly broken power-laws (solid gray line) are overlayed on the SED to highlight the flux of the source.

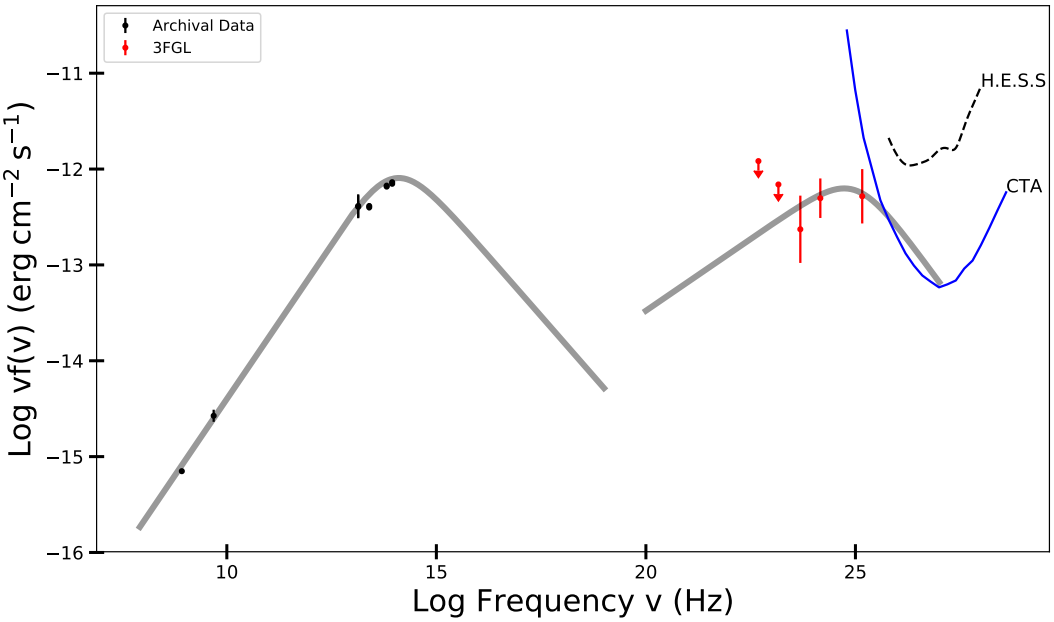

Figure A.12: Broadband SED of 3FGL J1855.1-6008. The 50 h sensitivity curves of CTA South (sollid blue line) and H.E.S.S. (dashed black line) are overlayed on the SED. The γ-ray catalogues and colors are indicated in the SED legend. The low energy datapoints (black) is archival data retrieved from the NED and CDS Vizier services. Two smoothly broken power-laws (solid gray line) are overlayed on the SED to highlight the flux of the source.

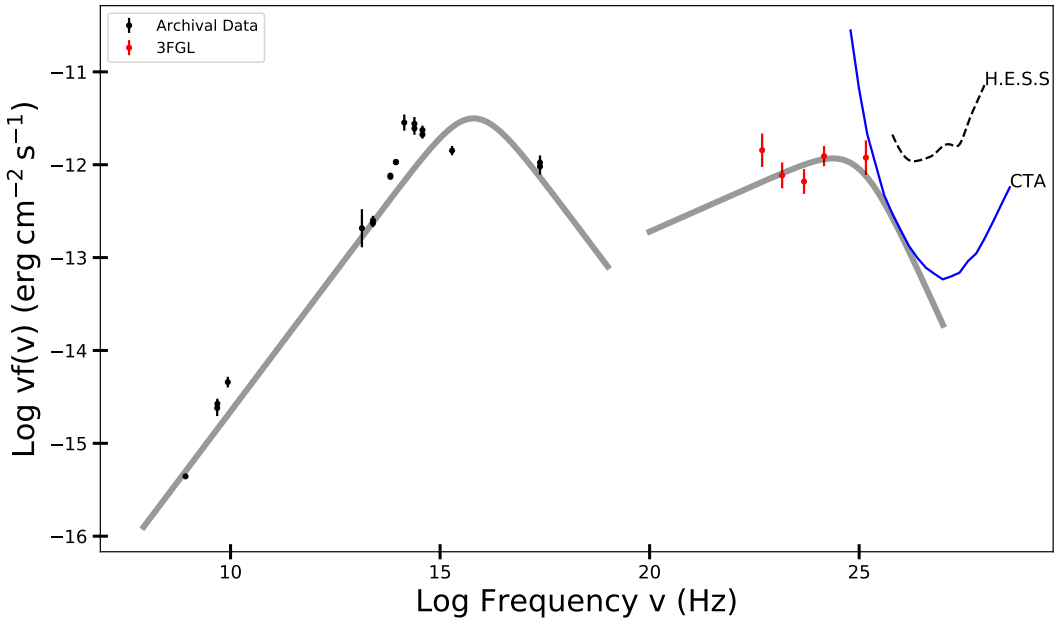

Figure A.13: Broadband SED of 3FGL J2338.7-7401. The 50 h sensitivity curves of CTA South (sollid blue line) and H.E.S.S. (dashed black line) are overlayed on the SED. The γ-ray catalogues and colors are indicated in the SED legend. The low energy datapoints (black) is archival data retrieved from the NED and CDS Vizier services. Two smoothly broken power-laws (solid gray line) are overlayed on the SED to highlight the flux of the source.

Appendix B

Peer-reviewed contributions

This research has been presented at both national and international conferences and associated research published in peer-reviewed proceedings and journals. The peer-reviewed conference proceedings and journals are listed below:

- J.P. Marais, B. van Soelen, R.J. Britto and P.J. Meintjes. Long-term monitoring of TeV Blazars with the Watcher Robotic Telescope. In *Proceedings of South African Institute of Physics (SAIP) 2016, University of Cape Town, South Africa, 4 - 8 July 2016,* SA Institute of Physics, ISBN:78-0-620-77094-1, 237. *Contriution: Main Author.*

- B. van Soelen, J.P. Marais, R.J. Britto, G. Chiaro, L. Klindt, P.J. Meintjes and D. Salvetti. Characterising the Fermi-LAT BCUs: Optical Spectroscopy and Neural Networks. In *4th Annual Conference on High Energy Astrophysics in South Africa*, PoS(HEASA 2016)19, 2016. *Contriution: Data Analysis.*

- R.J. Britto, J.P. Marais, P.J. Meintjes, B. van Soelen, Markus Böttcher, D.A.H. Buckley, S. Crawford and A. Rajoelimanana. Observations of the flaring Fermi-LAT blazar 4C +01.02 and prospects in spectro-polarimetry with SALT-RSS. In *4th Annual Conference on High Energy Astrophysics in South Africa*, PoS(HEASA 2016)21, 2016. *Contriution: Data Analysis.*

- R.J. Britto, J.P. Marais, P.J. Meintjes, B. van Soelen, Markus Böttcher, H. Schutte, D.A.H. Buckley, A. Falcone. Studies of optical/gamma-ray flares of blazar 4C +01.02: recent updates from the 2016-2017 observations. In *5th Annual Conference on High Energy Astrophysics in South Africa*, PoS(HEASA 2017)013, 2017. *Contriution: Data Analysis.*

- J.P.Marais, B. van Soelen. Searching for new TeV blazars in the 3rd Fermi-LAT catalogue of hard gamma-ray sources. In *5th Annual Conference on High Energy Astrophysics in South Africa*, PoS(HEASA 2017)014, 2017. *Contriution: Main Author.*

- B. van Soelen, L. Klindt, J.P. Marais, R.J. Britto, P.J. Meintjes, P.Väisänen, L. Hanlon and D. Murphy. New Discoveries and Surprises Revealed through SALT Spectroscopy of the Unclassified Fermi-LAT Sources. *Frontier Research in Astrophysics - II*, PoS(FRAPWS 2016)034, 2016. *Contriution: Data Analysis.*

- M. Böttcher, B. van Soelen, R. J. Britto, D.A.H. Buckley, J.P. Marais and H. Schutte. SALT Spectropolarimetry and Self-Consistent SED and Polarization Modeling of Blazars. *Galaxies*, 2017, 5, 52, doi: 10.3390/galaxies5030052. *Contriution: Data Analysis.*

- M. Böttcher, H. Schutte, B. van Soelen, R.J. Britto, J.P. Marais and D.A.H. Buckley. SALT Spectropolarimetry and Self-Consistent SED and Polarization Modeling of Blazars. In *4th International Fermi Symposium*, PoS(IFS 2017)021, 2017. *Contriution: Data Analysis.*

Long-term monitoring of TeV Blazars with the Watcher Robotic Telescope

J P Marais B van Soelen, R J Britto and P J Meintjes

Department of Physics, University of the Free State, Bloemfontein, 9301, South Africa

E-mail: MaraisJP@ufs.ac.za

Abstract. Blazars are known to show large-scale multi-wavelength variability on the order of sub-hours to years. This variability often manifests as rapid flares that can show correlation over a broad wavelength range. Since flares happen suddenly, rapid follow-up observations must be scheduled if a more detailed multi-wavelength observation campaign is to be started. We report on the long term optical photometric monitoring of a selection of known TeV blazars observed with the Watcher Robotic Telescope since May 2015 in the V, R and i' filters and present results of five well known sources: PKS 1510-089; AP Librae; PG 1553+113; PKS 2005-489 and PKS 2155-304. A reduction pipeline is currently in development to help identify potential sources for rapid follow-up multi-wavelength observations and provide optical light-curves to complement multi-wavelength observations. During the observation period PKS 1510-089 showed two outbursts and a $\Delta m_V = 1.7$ mag. Analysis with the Discrete Correlation Function between optical and γ-rays for PKS 1510-089 showed that all the flares are well correlated, suggesting a common origin for the optical and γ-ray emission. PKS 2155-304 showed a $\Delta m_V = 1$ magnitude difference and a steady increase in magnitude. PG 1553+113 exhibits an outburst with a total magnitude change of $\Delta m_V \sim 0.6$, while PKS 2005-489 shows a general magnitude increase toward the middle of the campaign and a decrease toward the end. No flare events were observed for AP Librae.

1. Introduction

Blazars are a class of Active Galactic Nuclei (AGN) which have a jet orientation which lies very close to the observer's line of sight ($\lesssim 10^\circ$) and they can be subdivided into Flat Spectrum Radio Quasars (FSRQ) and BL Lacertae objects (BL Lac). BL Lacs and FSRQs are characterized by their rapid multi-wavelength variability on the order of sub-hours to years, high polarization (radio to optical) and highly Doppler boosted emission from the jet. The Spectral Energy Distribution (SED) of blazars show a "double-humped" profile, with the low energy component (radio to UV/X-ray) produced by synchrotron radiation and high energy component (X-ray to γ-ray) produced by inverse Compton (IC) emission in the leptonic scenario [1] [2]. There is still some debate as to the origin of the high energy component, whether leptonic, hadronic or lepto-hadronic (see e.g. [3], [4] or [5]).

The Watcher Robotic Telescope, situated at the Boyden Observatory, South Africa is currently undertaking long-term observation of a selection of blazars detected with the High Energy Stereoscopic System (H.E.S.S.) telescope. The observational campaign began in December 2014. We present light-curves for five of these sources: PKS 1510-089; AP Librae; PG 1553+113; PKS 2005-489 and PKS 2155-304, from May (MJD = 57154) to November (MJD = 57335) 2015 in

the R, V and i' filters. In this short proceedings we analyse the long-term light-curves for these five sources to investigate their long-term variability. Aperture photometry was performed on *Fermi*-LAT ($0.1 \leq \mathrm{E}_\gamma \leq 300$ GeV) data for PKS 1510-089 to investigate any correlation between its optical and γ-ray light-curves.

2. Data reduction pipeline and method

The goal of an automatic reduction pipeline is to reduce and analyse observational data with as little input by the user as possible. The reduction pipeline being developed in the `Python Programming Language` for the reduction of the Watcher Robotic Telescope data, uses output from various `Python` packages, such as `sep`, a module that uses `SExtractor` algorithms in `Python` to help analyse data [6], `pyRAF`, which allows `Python` programs to be executed in `IRAF` and `Astropy`, which reads the fits file headers during the `IRAF` reduction process [7] [8], allowing the pipeline to reduce long-term data with locally (daily) applicable bias, dark and flat files.

The reduction pipeline uses the output of the `Astropy` and `sep` modules as the input for `pyRAF`, which then performs the reduction and photometry with the standard `IRAF ccdred/ccdproc` and `daophot/phot` tasks. To ensure the quality of the data being reduced, the `sep` module is used to analyse the quality of the data and extracted sources. Frames are rejected if the background counts and total background noise (rms) is more than twice the average of all the data. This allows anomalous frames to to be rejected, while still keeping the overall data quality approximately the same. Frames are also rejected if the eccentricity of the extracted sources are more than $e = 0.9$.

The data obtained from the Watcher Robotic Telescope was run through the reduction pipeline and photometric results obtained from the `daophot/phot` task. Differential photometry was performed using the method outlined in Everett and Howell [9]. The corrected magnitude is calculated by:

$$m = m_{\mathrm{obs}} - \left(\langle m_i \rangle - \frac{1}{M} \sum_{j=1}^{M} \langle m_i \rangle_j \right). \tag{1}$$

Here m_{obs} is the observed instrumental magnitude per frame. The average instrumental magnitude of the N comparison stars, weighted by their variance, per frame is $\langle m_i \rangle$, M is the total the number of frames and $\langle m_i \rangle_j$ is the average magnitude of the comparison stars on frame j. The uncertainty in the corrected magnitude is determined by:

$$\sigma = \sqrt{\sigma_*^2 + \sigma_{ens}^2} \tag{2}$$

where σ_* is the error calculated by `IRAF` for the star and σ_{ens} is the ensemble error, given by

$$\sigma_{ens} = \left[\sum_{i=1}^{N} \left(\frac{1}{\sigma_{*i}^2} \right) \right]^{-\frac{1}{2}} \tag{3}$$

The Discrete Correlation Function (DCF) [10] was used to calculate correlations between the optical and γ-ray ($\mathrm{E}_\gamma < 1$ GeV) flares in May and August 2015 and lower ($\mathrm{E}_\gamma < 1$ GeV) and higher ($1 \leq \mathrm{E}_\gamma \leq 300$ GeV) components of the flare detected by the LAT in August 2015 for PKS 1510-089.

3. Results and discussion

During the observation period PKS 1510-089 showed three flares detected in γ-rays, two of which were detected by the Watcher Robotic Telescope. The May 2015 flare was also detected

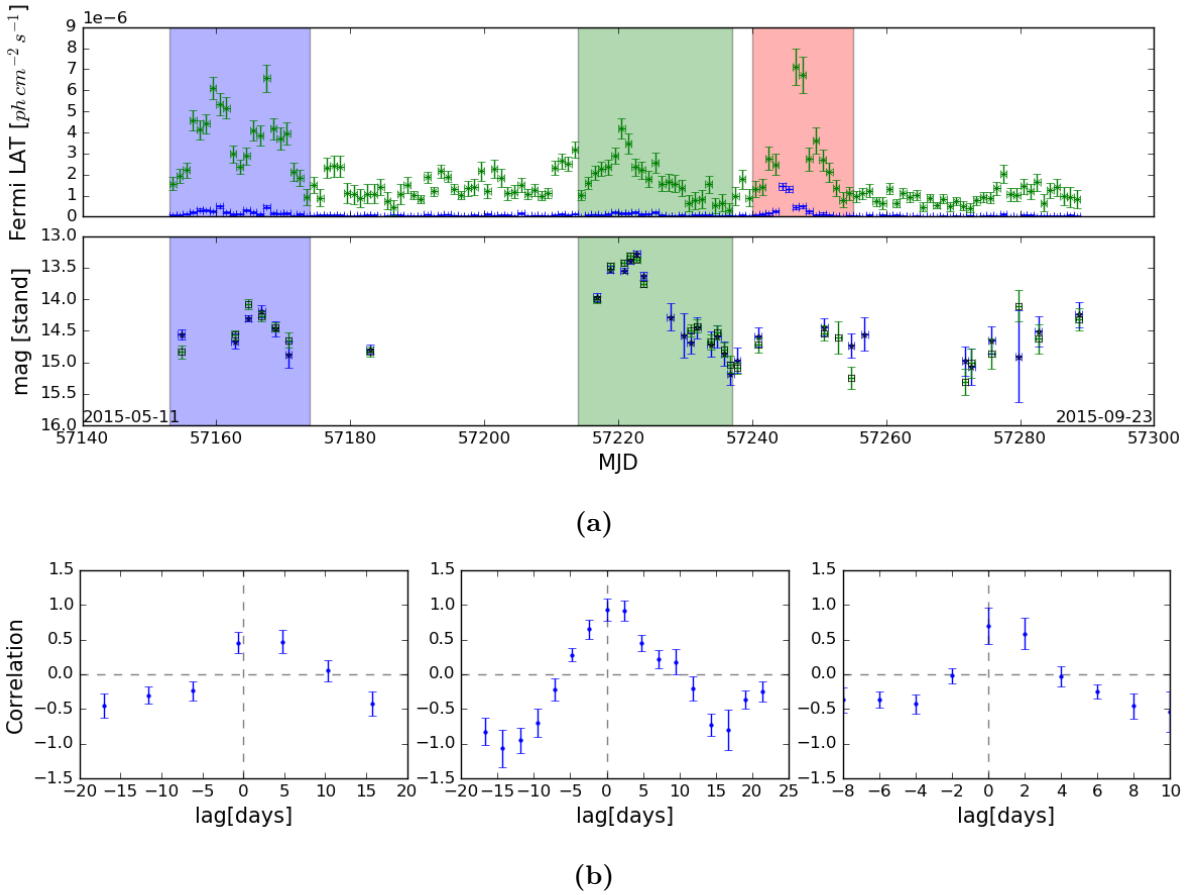

Figure 1: Light-curve and DCF for PKS 1510-089. Frame a) is the light-curve for PKS 1510-089. The top panel is the γ-ray light-curve from $E_\gamma < 1$ GeV (green crosses) and $1 \leq E_\gamma \leq 300$ GeV (blue plusses) emission. The green squares and blue stars are the R and V magnitudes respectively. Frame b) shows the correlations between the flares. Left and middle: May and July flares receptively. Correlations are calculated between E_γ (< 1 GeV) emission and R filter, right: August flare. Correlations are between the ($1 \leq E_\gamma \leq 300$ GeV) and ($E_\gamma \leq 1$ GeV) γ-ray emission.

by M.A.G.I.C. (Major Atmospheric Gamma Imaging Cherenkov) [11] and the July flare was detected by the 0.6m telescope of the Belogradchik observatory, situated in Bulgaria [12]. The light-curve and DCFs for the three flares are shown in figure 1. The third flare was not observed by Watcher, but was detected in γ-rays by *Fermi*-LAT. The first flare, in May 2015, had a $\Delta m_V \approx 1$ magnitude change with a maximum daily γ-ray flux of $F(E_\gamma < 1\ \text{GeV}) = (6.57 \pm 0.635) \times 10^{-6}$ ph cm^{-2} s^{-1}.

The DCF calculations suggest a positive correlation with a lag of $\tau = 2.07 \pm 2.73$ days between the $E_\gamma < 1$ GeV emission and R filter. However, this ~ 20 day flare only has optical data every $\sim$ 4th day, so any information regarding short term correlation between the gamma-ray and optical emission should be treated with caution. The second flare in July 2015 showed a $\Delta m_V \approx 1.9$ with a maximum daily γ-ray flux of $F(E_\gamma < 1\ \text{GeV}) = (4.13 \pm 0.500) \times 10^{-6}$ ph cm^{-2} s^{-1}. A DCF calculation showed a positive correlation with a $\tau = 1.19 \pm 1.19$ day lag between the γ-ray ($E_\gamma < 1$ GeV) emission and R filter. The third flare, in August, was not observed by Watcher, but a γ-ray flare was recorded with the LAT ($0.1 \leq E_\gamma \leq 300$ GeV). Maximum

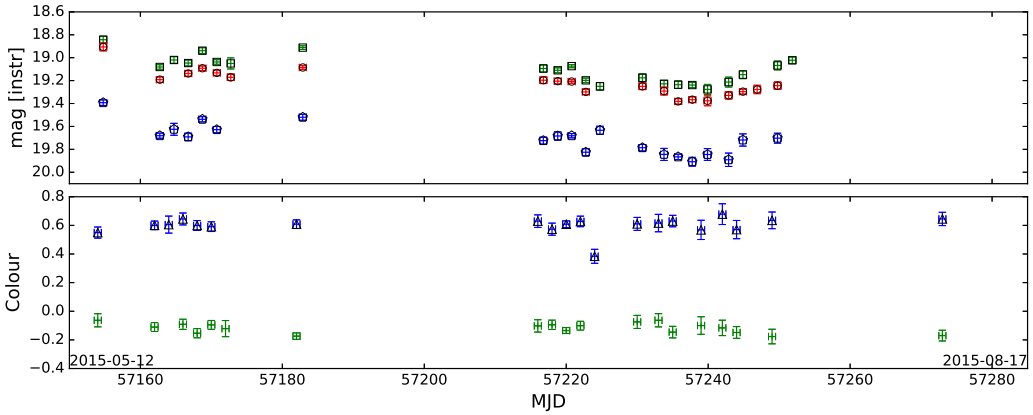

Figure 2: Light-curve for AP Lib. The light-curves show the data for the V(blue pentagons), R(green squares) and i'(red circles) filters in the top panels. The colour curves are shown in the bottom panels, with R-V(blue triangles) and R-i'(green plusses)

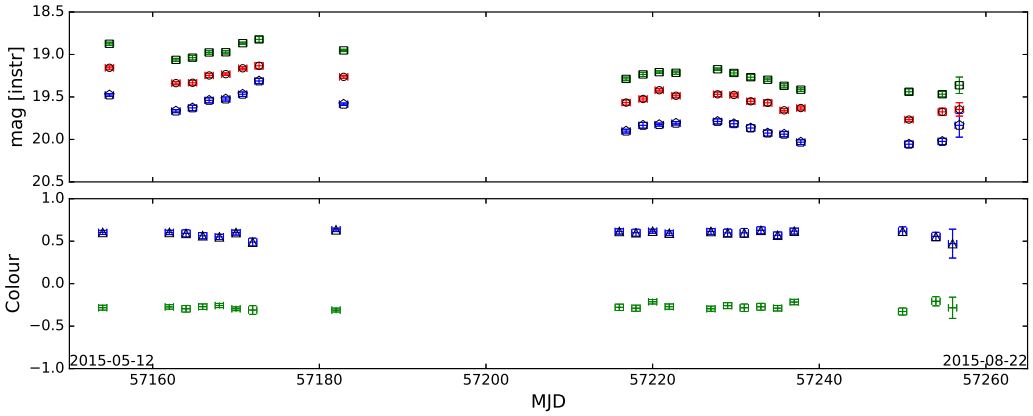

Figure 3: Light-curves for PG 1553+113. See figure 2 for description of symbols.

daily fluxes of $F(\mathrm{E}_\gamma < 1\ \mathrm{GeV}) = (7.125 \pm 0.864) \times 10^{-6}$ ph cm^{-2} s^{-1} and $F\ (\mathrm{E}_\gamma > 1\ \mathrm{GeV}) = (1.437 \pm 0.150) \times 10^{-6}$ ph cm^{-2} s^{-1} were recorded with the LAT. There was a lag of $\tau = 1 \pm 1$ days between the $1 \leq \mathrm{E}_\gamma \leq 300$ GeV and $\mathrm{E}_\gamma < 1$ GeV emission, calculated with the DCF.

AP Librae[1] showed a $\Delta m_V \approx 0.35$ magnitude change over the course of the observation campaign, with no sudden magnitude changes. Its R-V colour stayed constant (~ 0.6), but its R-i' colour varied slightly around ~ -0.1. Its light-curve is shown in figure 2.

PG 1553+113 (figure 3) showed a overall decrease in magnitude with a $\Delta m_V \approx 1$ change. The R-V and R-i' colours stayed constant during the whole observation campaign with ~ 0.6 and ~ -0.2 respectively.

PKS 2005-489 showed a slight increase in magnitude toward the middle of the campaign, then a slight decrease toward the end, with an overall $\Delta m_V \approx 0.4$ magnitude change. The light-curve is shown in figure 4.

PKS 2155-304, shown in figure 5, displayed an overall magnitude increase during the campaign, with a $\Delta m_V \approx 1$ increase. It showed small variability ($\Delta m_R \approx 0.3$) in the R filter during the

[1] Please note that the instrumental magnitudes are used for AP Librae, PG 1553+113, PKS 20115-489 and PKS 2155-304.

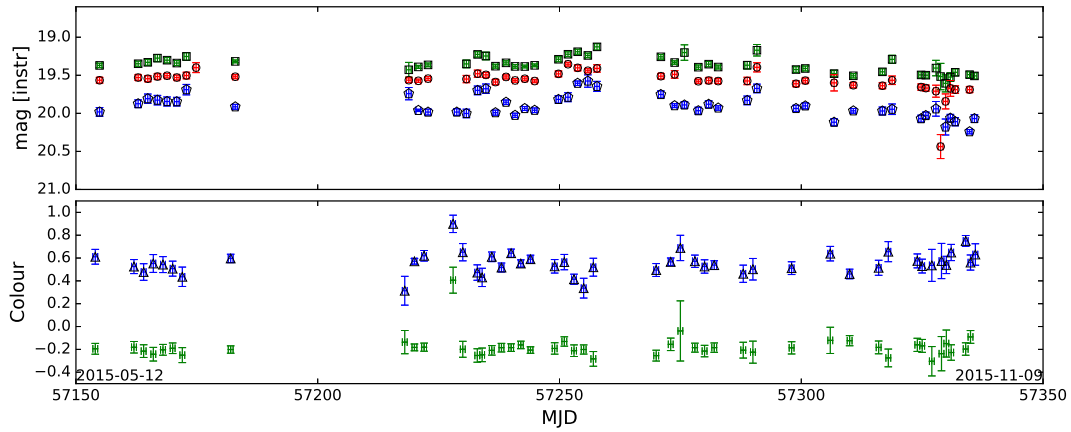

Figure 4: Light-curves for PKS 2005-489. See figure 2 for description of symbols.

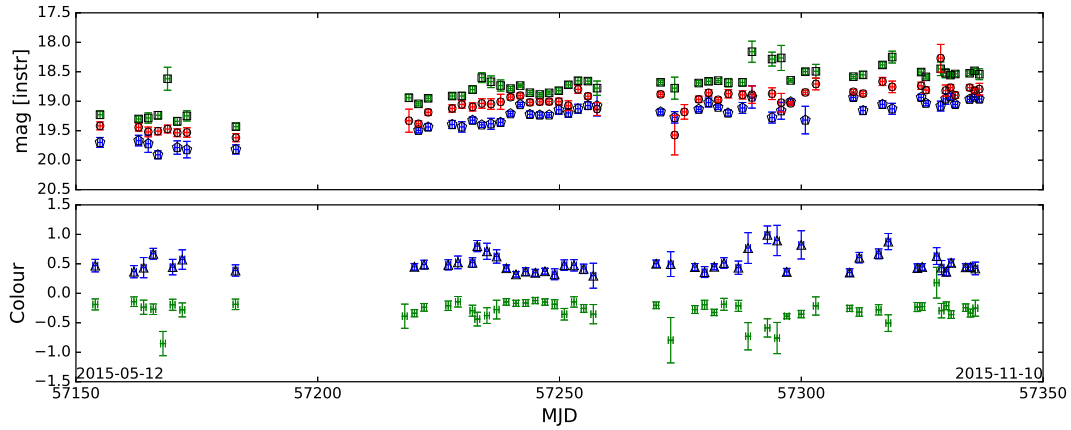

Figure 5: Light-curves for PKS 2155-304. See figure 2 for description of symbols.

middle of the campaign, but no corresponding change in magnitude was noted for the V and i' filters.

4. Conclusion

In this paper we presented light-curves on 5 well known TeV blazars observed with the Watcher Robotic Telescope for the period between May 2015 and November 2015. During this campaign, the FSRQ PKS 1510-089 ($z = 0.361$), which was discovered to be a TeV emitter in 2009 [13], experienced three flares during the observation period, two optical and γ-ray flares during May and July 2015 and a flare in August 2015 that was not detected by the Watcher Robotic Telescope, which was not observing the source during the flaring period. The August flare was detected *Fermi*-LAT in the $1 \leq E_\gamma \leq 300$ and $E_\gamma \leq 1$ GeV range.

AP Librae ($z = 0.049$), PG 1553+113 ($z = 0.43 - 0.58$); PKS 2005-489 ($z = 0.071$) and PKS 2155-304 ($z = 0.116$) are BL Lacs observed in the TeV range by H.E.S.S. [14]. The rapid flares of PKS 1510-089 hint that the emission during the flares originate from a small region in the jet and the small time lags between the γ-ray and optical emission has previously been shown to agree well with a Shock-in-Jet Model (see e.g. [15]). *Fermi*-LAT aperture photometry for AP Librae, PG 1553+113, PKS 2005-489 and PKS 2155-304 was also performed, but did not show any γ-ray

variability flaring events. The automatic reduction pipeline, currently in development, used to reduce the data and perform photometry, gave reasonable results, although more development and testing, under different conditions, still needs to be carried out. A more rigorous γ-ray analysis still need to carried out on the flares detected by the *Fermi*-LAT to explore the emission regions and conditions during the flares. The preliminary results show the importance of long-term monitoring and the rigorousness of the reduction pipeline.

Acknowledgments
The financial assistance of the National Research Foundation (NRF) towards this research, funded in part for the grant: Unique Grant No. 87919, is hereby acknowledged. Opinions expressed and conclusions arrived at, are those of the author and are not necessarily to be attributed to the NRF. This research has made use of the SIMBAD database, operated at CDS, Strasbourg, France. pyRAF is a product of the Space Telescope Science Institute, which is operated by AURA for NASA. We thank the Watcher Group for providing the optical data used in this analysis.

References

[1] Beckmann V and Shrader C 2012 *Active Galactic Nuclei* Physics textbook (Wiley) ISBN 9783527410910 chapter 4 pp 116-120
[2] Schneider P 2014 *Extragalactic astronomy and cosmology : an introduction.* (Berlin : Springer, 2014.) ISBN 9783642540820 chapter 5 pp 215-223
[3] Cerruti M, Zech A, Boisson C and Inoue S 2011 *SF2A-2011: Proceedings of the Annual meeting of the French Society of Astronomy and Astrophysics* ed Alecian G, Belkacem K, Samadi R and Valls-Gabaud D pp 555–558
[4] Böttcher M, Reimer A, Sweeney K and Prakash A 2013 *ApJ* **768** 54
[5] Cerruti M, Zech A, Boisson C and Inoue S 2015 *MNRAS* **448** 910–927
[6] Barbary K, Boone K and Deil C 2015 sep: v0.3.0 URL `http://dx.doi.org/10.5281/zenodo.15669`
[7] Massey P and Davis L E 1992 *NOAO Laboratory*
[8] Massey P 1997 *NOAO, Arizona, Tucson*
[9] Everett M E and Howell S B 2001 *PASP* **113** 1428–1435
[10] Edelson R A and Krolik J H 1988 *ApJ* **333** 646–659
[11] Mirzoyan R and MAGIC Collaboration 2015 *The Astronomer's Telegram* **7542**
[12] Bachev R 2015 *The Astronomer's Telegram* **7829**
[13] HESS Collaboration *et al.* 2013 *A&A* **554** A107
[14] Cerruti M 2011 *Proceedings of the 32nd International Cosmic Ray Conference* **8** 109
[15] Spada M, Ghisellini G, Lazzati D and Celotti A 2001 *MNRAS* **325** 1559–1570

PROCEEDINGS OF SCIENCE

Characterising the *Fermi*-LAT BCUs: Optical Spectroscopy and Neural Networks

Brian van Soelen*, **Johannes P Marais, Richard J Britto**
Department of Physics, University of the Free State, 9300, Bloemfontein, South Africa
E-mail: vansoelenb@ufs.ac.za,maraisjp@ufs.ac.za, brittor@ufs.ac.za

Graziano Chiaro
Dip. Fisica & Astronomia G. Galilei - Università di Padova, I-35131, Padova, Italy
E-mail: chiaro@pd.infn.it

Lizelke Klindt, Pieter J. Meintjes
Department of Physics, University of the Free State, 9300, Bloemfontein, South Africa
E-mail: lizelkeklindt@gmail.com, meintjpj@ufs.ac.za

David Salvetti
INAF - Istituto di Astrofisica Spaziale e Fisica Cosmica , I-20133, Milano, Italy
E-mail: salvetti@iasf-milano.inaf.it

The *Fermi*-LAT telescope has provided an unprecedented view of the GeV gamma-ray sky since its launch in 2008. The latest *Fermi*-LAT catalogue of Active Galactic Nuclei lists 1591 sources associated with AGN, of which 460 are classified as blazar candidates of uncertain type (BCU). The characterisation of the physical properties of these BCU sources is important for observational cosmology and fundamental physics, as these sources and their environments constitute a natural laboratory to study particle acceleration and matter/radiation interactions in extreme conditions. Of particular interest is the search for new and interesting/unusual sources that may be observable at very high energies by ground-based imaging atmospheric Cherenkov telescopes. Based on the observed gamma-ray properties, a number of machine learning techniques are being investigated to classify these sources. However, the classification of a blazar as a FSRQ or BL Lac depends on the optical spectral properties. Here we discuss the work that we have thus far undertaken to optically characterise a selection of sources as well as future plans to undertake classification to help calibrate an artificial neural network method.

4th Annual Conference on High Energy Astrophysics in Southern Africa
25-27 August, 2016
Cape Town, South Africa

*Speaker.

PoS(HEASA 2016)019

1. Introduction

Blazars are radio loud Active Galactic Nuclei (AGN) where the propagation direction of the relativistic jet lies close to our line of sight. This results in the thermal component of the active galaxy being overpowered by the highly Doppler boosted non-thermal emission produced in the jet. As a result, blazars are the most numerous, non-transient, γ-ray sources detected by *Fermi*-LAT. In the third *Fermi*-LAT catalogue (3FGL), of the 1785 catalogued γ-ray sources, 1088 ($\sim 61\%$) are listed as blazars, with a further 568 ($\sim 32\%$) listed as blazar candidates [1].

Blazars are sub-divided into flat spectrum radio quasars (FSRQs) or BL Lacs based on their spectral properties. FSRQs show strong emission lines, while BL Lacs show mainly featureless spectra with weak or no emission lines. Typically, a source is classified as an FSRQ if it shows emission lines with equivalent widths $|W_\lambda| > 5$ Å, while it is classified as a BL Lac if the equivalent widths are $|W_\lambda| < 5$ Å (e.g. [2, 3]). This can be understood as FSRQs having a higher accretion rate than BL Lacs (and hence more luminous accretion discs), which leads to a greater ionization of the broad and narrow line regions (see e.g. [4, 5, 6] and reference therein). Blazars can also be further subdivided into low-, intermediate- or high-synchrotron peaked blazars based on where the synchrotron component of the spectral energy distribution (SED) peaks. The limits are $\nu_{\rm peak} < 10^{14}$ Hz, 10^{14} Hz $< \nu_{\rm peak} < 10^{15}$ Hz and $\nu_{\rm peak} > 10^{15}$ Hz, respectively (e.g. [7]).

The *Fermi*-LAT 3LAC includes 1444 extra-galactic sources (in the clean sample) which are above $|b| > 10^\circ$ [7]. This includes 402 sources which are listed as blazar candidates of unknown type or BCUs (table 1). There are three different BCUs types, depending on whether the source has a published optical spectrum, which is not sensitive enough for classification (BCU I), whether there is no optical spectrum but the synchrotron peak in the SED can be found, (BCU II) or if there is no spectrum, but the source shows a blazar-like multi-wavelength SED (BCU III). These sources are an important sample to identify new TeV candidate sources that can be observed with ground-based imaging atmospheric Cherenkov telescopes (IACTs). This is particularly true for the 60 BCUs which are included in 2nd catalogue of Hard Fermi-LAT sources (2FHL) detected above 50 GeV [8].

In order to search for new sources we are currently undertaking a project to obtain optical spectra of a selection of BCUs in order to classify the sources and determine their redshifts. The redshift is particularly important for TeV observations since sources beyond $z \gtrsim 1$ are unobservable at TeV energies due to attenuation from the extragalactic background light (EBL; [9, 10, 11]). Of particular interest is the search for non-blazar sources, since only a few of these have been detected at TeV energies. Currently only 6 FSRQs and 4 radio galaxies are listed in TeVCat, compared to 57 BL Lacs.[1]

However, the large number of sources can make detailed spectroscopic follow-up of all sources difficult. For this reason, machine learning techniques are currently been developed to classify *Fermi*-LAT sources based on their γ-ray properties. Recently an artificial neural network (ANN), based on the γ-ray flaring pattern was presented by Chiaro et al. [12]. However, such methods are dependent on having classified sources that can be used to train the network. Increasing the number of classifications will significantly assist with the training of these ANNs.

[1] http://tevcat.uchicago.edu/: accessed 22 November 2016.

AGN classification	Entire 3LAC	Clean sample	Low-latitude sample
FSRQs	467	414	24
BL Lacs	632	604	30
BCUs	460	402	2
Total	**1591**	**1444**	**182**

Table 1: Summary of the source classification in the *Fermi*-LAT 3LAC [7].

This paper is structured as follows: section 2 briefly summarizes the B-FlaP method, section 3 summarizes our previous observations as well as presenting preliminary results for 3FGL J1507.6-3710, while the discussion and final conclusions are presented in section 4.

2. B-FlaP method- artificial neural networks

Chiaro et al. [12] have developed an ANN method to distinguish between FSRQ and BL Lac sources in the 3LAC catalogue based on the observed flaring pattern. The method is based on an analysis of the Empirical Cumulative Distribution Function (ECDF) of the gamma-ray light curves. These should differ in shape due to the brightness and frequency of flares observed from these sources. This classification scheme is based upon the hypothesis that BL Lacs will have fewer large flares, and smoother light curves than FSRQs.

The ANN is constructed using a two-layer feed-forward network, which consists of 10 input nodes, 6 hidden nodes and 2 output nodes. The input nodes are the flux values of the ECDFs at the 10, 20, 30, 40, 50, 60, 70, 80, 90 & 100th percentiles. The ANN assigns a likelihood (L_{BLL}) for a sources to be a BL Lac or an FSRQ ($L_{FSRQ} = 1 - L_{BLL}$). After training the ANN on $\sim 70\%$ of classified sources, a 90% accurate classification of the testing sample was obtained by assigning limits of $L_{BLL} > 0.566$ for BL Lacs and $L_{BLL} < 0.230$ for FSRQs. No classification is made for sources that are in between these limits. The ANN was applied to the *Fermi*-LAT BCUs and classified 342 BL Lacs and 154 FSRQs.

3. Optical classification

Our optical observations to classify *Fermi*-LAT BCUs started with sources listed in the previous *Fermi*-LAT 2LAC catalogue [13]. In our initial observations we focused on selecting candidate sources from the *Fermi*-LAT 2LAC that were unclassified, and had no redshift measurement (or had redshifts from low quality spectra) [14]. The selected candidates were limited to sources observable with South Africa based telescopes and spectroscopic observations have been undertaken with the Southern African Large Telescope (SALT; [15, 16, 17]), and the SAAO 1.9-m telescope, located at the South African Astronomical Observatory (SAAO) near Sutherland. So far 7 sources from the 2LAC catalogue have been classified as summarized in table 2 [14]. In addition, photometric observations to search for short and long term variability have been undertaken with the Sutherland High Speed Camera (SHOC; [18]) and the Watcher Robotic Telescope, respectively [19, 20].

2LAC name	Optical	ANN
J0044.7-3702	FSRQ	FSRQ
J0201.5-6626	FSRQ	-
J0644.2-6713	FSRQ	FSRQ
J0730.6-6607	BL Lac	BL Lac
J1218.8-4827	BL Lac	-
J1407.5-4257	BL Lac	BL Lac
J2049.8+1001	BL Lac	-

Table 2: Summary of source classification from the optical spectra [14], with a comparison to the results predicted by the ANN [12].

Our observation campaign has been extended to include unclassified sources listed in the 3LAC with priority given to sources included in the 2FHL catalogues. Below we briefly summarized the preliminary results for one source included it the 3LAC catalogue.

3.1 3FGL J1507.6-3710

3FGL J1507.6-3710 is listed as a BCU II in the 3LAC catalogue, and is characterised as an intermediate synchrotron peak blazar ($\nu_{\rm peak} = 3 \times 10^{14}$ Hz). The source is detected at a 5.5σ significance with an average flux of $F(1-100\,\mathrm{GeV}) = (4.4 \pm 0.9) \times 10^{-10}$ cm^{-2} s^{-1} with a photon index of $\Gamma = 2.13 \pm 0.15$.

3FGL J1507.6-3710 was observed with the SpUpNIC spectrograph on the SAAO 1.9-m telescope on 2016 July 30. The spectra was reduced following the standard IRAF procedures and the preliminary, normalized spectrum is shown in figure 1. Based on the identified Ca H&K and G-band this source is at a redshift of $z = 0.240 \pm 0.001$. We also calculated a Ca H&K break value of $C = (f_+ - f_-)/f_+ \sim 0.13$ where the fluxes are measured between 3750–3950 Å and 4050–4250 Å in the galaxy rest frame [21, 22]. Non-active galaxies have a Ca H&K break which is $C \gtrsim 0.5$ [21], which indicates that the source has a non-thermal component. This, combined with the lack of strong emission lines, indicates that 3FGL J1507.6-3710 is a BL Lac. This confirms the classification predicted by the ANN [12].

4. Discussion and conclusions

Our on-going programme to increase the number of classified AGN sources continues to make progress. Thus far 7 new sources have been successfully classified and new observations of a selection of candidates were undertaken over three weeks in July/August 2016 with the SpUpNIC spectrograph. Here we have shown the preliminary results for one of these sources, 3FGL J1507.6-3710, which we have classified as a BL Lac at a redshift of $z = 0.240 \pm 0.001$. Further observation programmes are planned. In addition, these results can be used to help improve the accuracy of the machine learning technique developed by Chiaro et al. [12] since a larger number of classified sources will improve the training and increase the accuracy of the ANN.

Increasing the number of classified extra-galactic sources is important to improve our understanding of the origin of extra-galactic γ-ray emission. Given the large number of extra-galactic

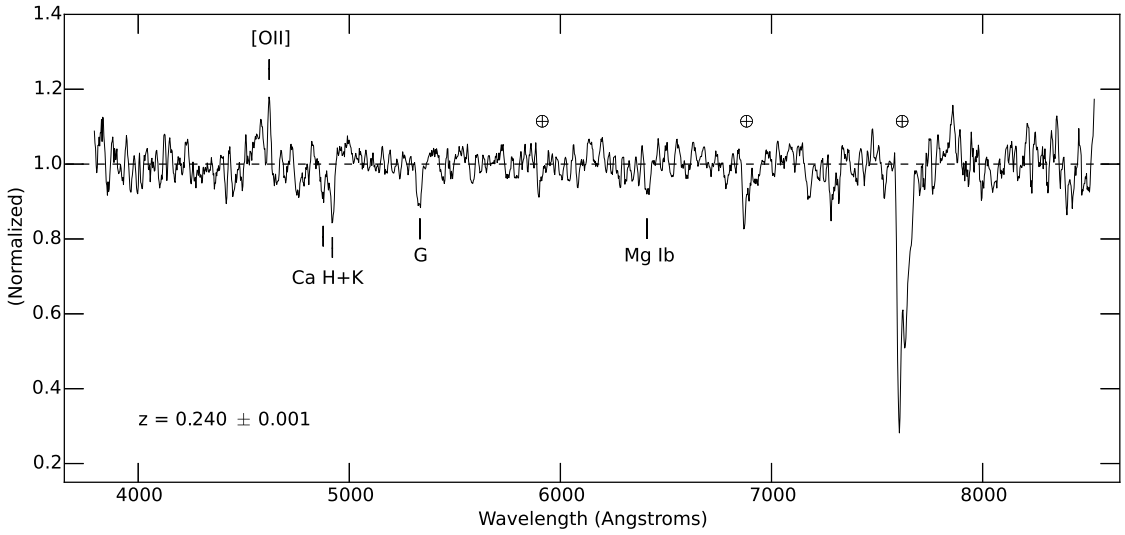

Figure 1: Combined optical spectrum for 3FGL J1507.6-3710, with the identified features marked. Telluric lines are marked with a $\oplus$.

sources, and the anticipated increase in sensitivity at TeV energies that will be possible with the Cherenkov Telescope Array (CTA; [23]), it is important to obtain classifications for the current BCUs. Optical spectroscopic programmes and machine learning techniques, such as briefly summarized here, are important tools for undertaking such classifications.

Acknowledgments

This work is based on the research supported in part by the National Research Foundation (NRF) of South Africa for the grant No. 87919.

References

[1] F. Acero et al. (*Fermi* Collaboration), *Fermi Large Area Telescope Third Source Catalog*, *ApJS* **218** (2015) 23

[2] M.J.M. Marcha et al., *Optical spectroscopy and polarization of a new sample of optically bright flat radio spectrum sources*, *MNRAS* **281** (1996) 425

[3] H. Landt et al., *A physical classification scheme for blazars*, *MNRAS* **351** (2004) 83

[4] M. Böttcher and C.D. Dermer, *An Evolutionary Scenario for Blazar Unification*, *ApJ* **564** (2002) 86

[5] A. Cavaliere and V. D'Elia, *The Blazar Main Sequence*, *ApJ* **571** (2002) 226

[6] G. Ghisellini et al., *General physical properties of bright Fermi blazars*, *MNRAS* **402** (2010) 497

[7] M. Ackermann et al. (*Fermi* Collaboration), *The Third Catalog of Active Galactic Nuclei Detected by the Fermi Large Area Telescope*, *ApJ* **810** (2015) 14

[8] M. Ackermann et al. (*Fermi* Collaboration), *2FHL: The Second Catalog of Hard Fermi-LAT Sources*, *ApJS* **222** (2016) 5

[9] R.J. Gould and G. Schréder, *Opacity of the Universe to High-Energy Photons*, *Physical Review Letters* **16** (1966) 252

[10] M.G. Hauser and E. Dwek, *The Cosmic Infrared Background: Measurements and Implications*, *ARA&A* **39** (2001) 249

[11] F. Aharonian et al. (H.E.S.S. Collaboration), *A low level of extragalactic background light as revealed by γ-rays from blazars*, *Nature* **440** 1018

[12] G. Chiaro et al. *Blazar flaring patterns (B-FlaP) classifying blazar candidate of uncertain type in the third Fermi-LAT catalogue by artificial neural networks*, *MNRAS* **462** (2016) 3180

[13] M. Ackermann et al. (*Fermi* Collaboration), *The Second Catalog of Active Galactic Nuclei Detected by the Fermi Large Area Telescope*, *ApJ* **743** (2011) 171

[14] L. Klindt et al., *Optical spectroscopic classification of a selection of Southern Hemisphere Fermi-LAT unclassified blazars*, *MNRAS* **467** (2017) 2537

[15] D.A.H. Buckley et al., *Completion and commissioning of the Southern African Large Telescope*, *SPIE* **6267** (2006) 32

[16] E.B. Burgh et al., *Prime Focus Imaging Spectrograph for the Southern African Large Telescope: optical design*, *SPIE* **4841** (2003) 1463

[17] H.A. Kobulnicky et al., *Prime focus imaging spectrograph for the Southern African large telescope: operational modes*, *SPIE* **4841** (2003) 1634

[18] R. Coppejans et al., *Characterizing and Commissioning the Sutherland High-Speed Optical Cameras (SHOC)*, *PASP* **125** (2013) 976

[19] L. Klindt et al., *Optical variability of unidentified Active Galactic Nuclei with blazar characteristics in the Fermi-2LAC catalogue* in proceedings of *3rd Annual Conference on High Energy Astrophysics in Southern Africa*, PoS(HEASA2015)008 (2015)

[20] B. van Soelen et al., *Optical observations of Very High Energy Sources from the Boyden Observatory* in proceedings of *3rd Annual Conference on High Energy Astrophysics in Southern Africa*, PoS(HEASA2015)007 (2015)

[21] A. Dressler and S.A. Shectman, *Systematics of the 4000 Ångström break in the spectra of galaxies*, *AJ* **94** (1987) 899

[22] H. Landt et al., *The classification of BL Lacertae objects: the Ca H&K break*, *MNRAS* **336** (2002) 945

[23] M Actis et al. (CTA Consortium), *Design Concepts for the Cherenkov Telescope Array*, *Experimental Astronomy* **32** (2011) 193

PROCEEDINGS OF SCIENCE

Observations of the flaring *Fermi*-LAT blazar 4C +01.02 and prospects in spectro-polarimetry with SALT-RSS

Richard J. Britto (on behalf of the *Fermi*-LAT Collaboration)*
Department of Physics, University of the Free State, PO Box 339, Bloemfontein 9300, South Africa
E-mails: brittor@ufs.ac.za, dr.richard.britto@gmail.com

Johannes P. Marais, Pieter J. Meintjes, Brian van Soelen
Department of Physics, University of the Free State, PO Box 339, Bloemfontein 9300, South Africa
E-mails: maraisjp@ufs.ac.za, meintjpj@ufs.ac.za, vansoelenb@ufs.ac.za

Markus Böttcher
Centre for Space Research, North-West University, Potchefstroom 2520, South Africa
E-mail: markus.bottcher@nwu.ac.za

David A. H. Buckley, Steve Crawford
South African Astronomical Observatory, PO Box 9, Observatory 7935, Cape Town, South Africa
E-mail: dibnob@saao.ac.za, crawford@saao.ac.za

Andry Rajoelimanana
Department of Physics, University of the Free State, PO Box 339, Bloemfontein 9300, South Africa
E-mail: andry@saao.ac.za

The *Fermi* Gamma-Ray Space telescope has identified 1741 active galactic nuclei during its first four years of observation (2008–2012) and detected 1145 blazars and 573 blazar candidates of uncertain type (BCUs) as listed in the Third *Fermi*-LAT Point Source Catalog (3FGL). Since *Fermi* typically operates in survey mode, sources from the whole sky are monitored almost continuously. Daily or sub-daily *Fermi*-LAT binned light-curves of bright blazars above 100 MeV can be produced for any given time range since August 2008. It is thus possible to identify flaring periods of blazars and trigger observations with South Africa-based optical telescopes to perform γ-ray *versus* optical correlation studies of flux variability. Also, the recently commissioned polarisation capability of the Robert Stobie Spectrograph (RSS) on the 10-meter class *Southern African Large Telescope (SALT)* at the *South African Astronomical Observatory (SAAO)*, Sutherland, is expected to contribute to the characterisation of the wavelength dependent radiation emission mechanisms of these objects. We report our preliminary studies on the blazar 4C +01.02 and discuss the prospects for spectro-polarimetry of a broader sample of flaring blazars.

4th Annual Conference on High Energy Astrophysics in Southern Africa
25-27 August, 2016
Cape Town, South Africa

PoS(HEASA 2016)021

1. Introduction

The Large Area Telescope onboard the *Fermi* Gamma-Ray Space Telescope (*Fermi*-LAT), operating since 2008, is sensitive to γ-ray photons between ~ 20 MeV and > 300 GeV [1]. Among the 1591 sources of the Third *Fermi*-LAT AGN Catalog (3LAC) [2], constructed using the first four years of *Fermi*-LAT data (3FGL [3]), 1559 objects are classified as *blazars* (632 BL Lacs, 467 flat spectrum radio quasars [FSRQs], and 460 blazar candidates of uncertain type [BCUs]). Operating in survey mode for most of its observation strategy, *Fermi* is able to provide a consistent monitoring of the whole sky every three hours.

Several South Africa-based optical telescopes are used for joint optical/γ-ray observations of blazars during outbursts. Most of them are based near Sutherland (32° 23' 14" S, 20° 48' 42" E; altitude:1798 m), the main observation site of the *South African Astronomical Observatory (SAAO)*. We use the *Robert Stobie Spectrograph (RSS)* on the 10-m *Southern African Large Telescope (SALT)* [4, 5, 6] for optical spectroscopy with good sensitivity for blazar observations. Due to the design of the telescope, observations with SALT-RSS are constrained to be performed for sources within the $-75°$ to $+10°$ declination range. We also use the *SpUpNIC spectrograph* [7] on the 1.9-m *Radcliffe* Telescope, based on the same site. The *Boyden* Observatory (29° 02' 19.7" S; 26° 24' 17.0" E; altitude:1372 m) of the University of the Free State, near Bloemfontein, also hosts the Boyden 1.5-m Telescope and the Irish *Watcher Robotic Telescope*.[1] Both these telescopes are used for photometric observations. Besides the project presented in this paper, more details on our blazar programmes using *Fermi*-LAT and South Africa-based telescopes can be found in [8, 9, 10].

Blazar 4C +01.02 (PKS B0106+013) is a distant FSRQ (radio coord.: R.A.=01h 08m 38.8s, Decl. =+01° 35' 00"; redshift z=2.099) monitored by *Fermi*[2] and the radio *Very-Long-Baseline Interferometry (VLBI)* under the *MOJAVE* project.[3] Kharb et al [11] presented an interesting multi-wavelength study of the source in 1988–1989, using data from the *Hubble Space Telescope (HST)*, MOJAVE and the *Chandra* X-ray space telescope. Following *Fermi*-LAT reports on outbursts in March/April 2016, we started optical monitorings of 4C +01.02. We also performed spectroscopic observations with both SpUpNIC and SALT-RSS.

We present a time-domain study of 4C +01.02 in Section 2, then our project using spectroscopy and spectro-polarimetric observations from South Africa-based telescopes in Section 3, and our conclusions in Section 4.

2. Time-domain study of FSRQ 4C +01.02

We analysed *Fermi*-LAT data from 11 May till 15 August 2016 (MJD 57519–57615), in the 100 MeV–300 GeV range, using the Pass 8 data representation and the *Fermi* Science Tools version v10r0p5.[4] We produced one-day binned light-curves using the unbinned likelihood algorithm (gtlike/pyLikelihood Science Tool) with the following standard analysis cuts applied to point

*Speaker.

[1] http://watchertelescope.ie

[2] http://fermi.gsfc.nasa.gov/ssc/data/access/lat/msl_lc/

[3] http://www.physics.purdue.edu/MOJAVE/sourcepages/0106+013.shtml

[4] http://fermi.gsfc.nasa.gov/ssc/data/analysis/

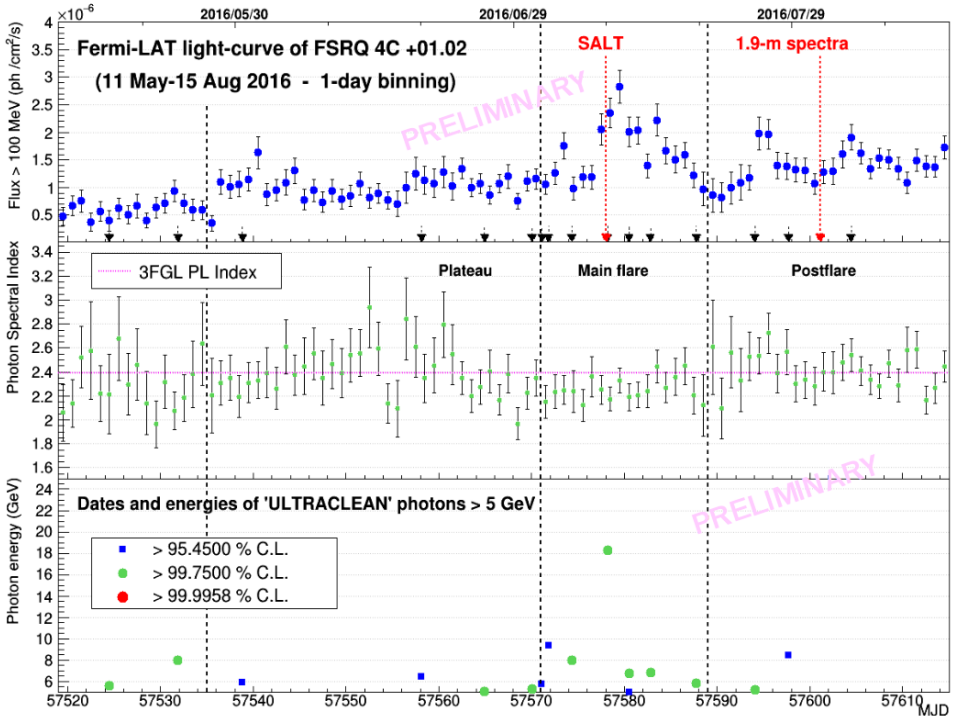

Figure 1: Upper panel: *Fermi*-LAT light-curve of 4C +01.02 above 100 MeV between 11 May and 29 August 2016 in one-day binning. Vertical dashed lines indicate separations between three phases of the outburst: plateau, flare and postflare, whose spectral parameters are presented in Table 1. Black arrow indicated the arrival time of photons above 5 GeV. Middle panel: Optimised value of the photon index of the source. The magenta horizontal dashed-line indicates the value of the PL photon index of 3FGL. Lower panel: Arrival time and energies of high energy photons ("ULTRACLEAN" photon class, > 5 GeV). Three levels of confidences of the association of the photon with 4C +01.02 are indicated.

Table 1: Spectral parameters obtained by running the likelihood analysis over four periods of this outburst. We model the spectral shape of 4C +01.02 by a the power-low function (PL — characterised by the photon index Γ), then by a log-parabola (LP — characterised by the α and β parameters. What is labeled as "preflare" (MJD 57519-57571) is also characterised by a hardening of the PL photon index (Γ).

Period	Γ	α	β	Flux (ph cm^{-2} s^{-1})
11 May-28 May (Pre-flare)	2.26 ± 0.06	2.04 ± 0.09	0.19 ± 0.06	5.35e-07 $\pm$ 4.38e-08
28 May-02 Jul (Plateau)	2.36 ± 0.03	2.27 ± 0.04	0.11 ± 0.03	9.94e-07 $\pm$ 3.50e-08
02 Jul -20 Jul (Flare)	2.26 ± 0.03	2.11 ± 0.04	0.16 ± 0.03	1.56e-06 $\pm$ 5.71e-08
20 Jul -15 Aug (Postflare)	2.41 ± 0.03	2.32 ± 0.04	0.12 ± 0.03	1.38e-06 $\pm$ 4.40e-08

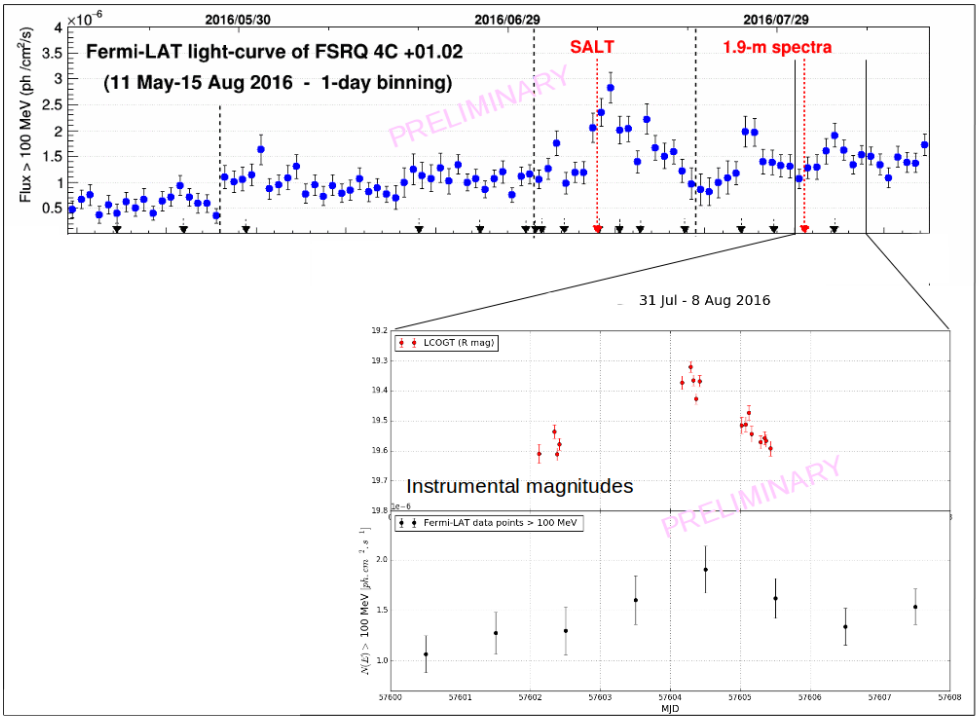

Figure 2: *Fermi*-LAT light-curve of 4C +01.02 above 100 MeV between 11 May and 29 August 2016 in one-day binning, as in Figure 1. The lower panels contain a zoom on the *Fermi*-LAT light-cuve during 31 July–8 August 2016, compared to the optical light-curve with LCO in the R-band.

source analysis: radius of the *Region of interest* (ROI)=15°; Source region=ROI+10°; SOURCE class; event type = 3; zenith angle $< 90°$; DATA_QUAL=1, LAT_CONFIG=1; Diffuse emission: `gll_iem_v06.fits` (Galactic) and `iso_P8R2_SOURCE_V6_v06.txt` (extragalactic) templates. The source of interest is modeled by a single power law (PL) of photon index Γ. Eight parameters defining the spectral shapes of the brightest point sources of the ROI and the two diffuse templates are kept free in the likelihood analyis.

We present in Figure 1 the daily light-curve of 4C +01.02 (upper panel). According to the flux level and variability, we defined four episodes that we refered to as *pre-flare*, *plateau*, *(main) flare* and *postflare*, sucessively. In Table 1 are presented the spectral parameters optimised during the likelihood analysis of our data for each of the four episodes, using successively the PL and log-parabola models. The *plateau–flare–post-flare* pattern was previously observed for FSRQ 3C 454.3 during several of its outbursts (eg Britto et al [12] and references therein). The dates of observations with SALT and the 1.9-m telescope are labeled in red. The variation of the spectral photon index Γ (middle panel) shows evidence of hardening when the source is brighter — during the main flare. This is a common feature reported for bright FSRQs during outbursts. An unusual feature is that the pre-flare period (corresponding to a relatively quiescent state of the source) is also characterised by a hardening of the spectrum, as also reported in Table 1.

High cadence monitoring of 4C +01.02, with short exposure times, was performed with the

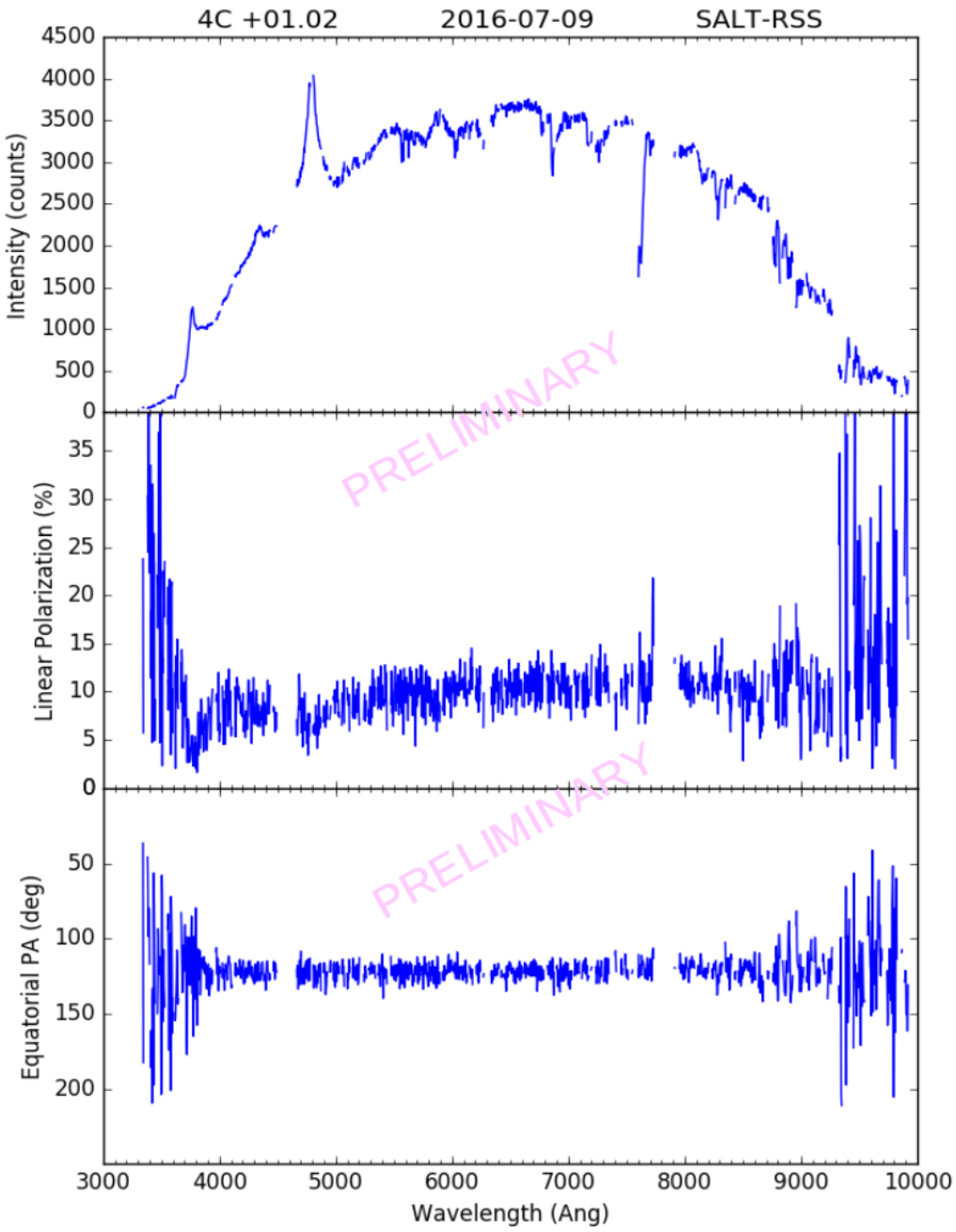

Figure 3: 4C +01.02 SALT-RSS count spectrum in the 3500–10000 Å range (grating PG0300) and polarised parameters, obtained on 9 July 2016 (3:15–3:56 UT), combining four exposures of 600 s each.

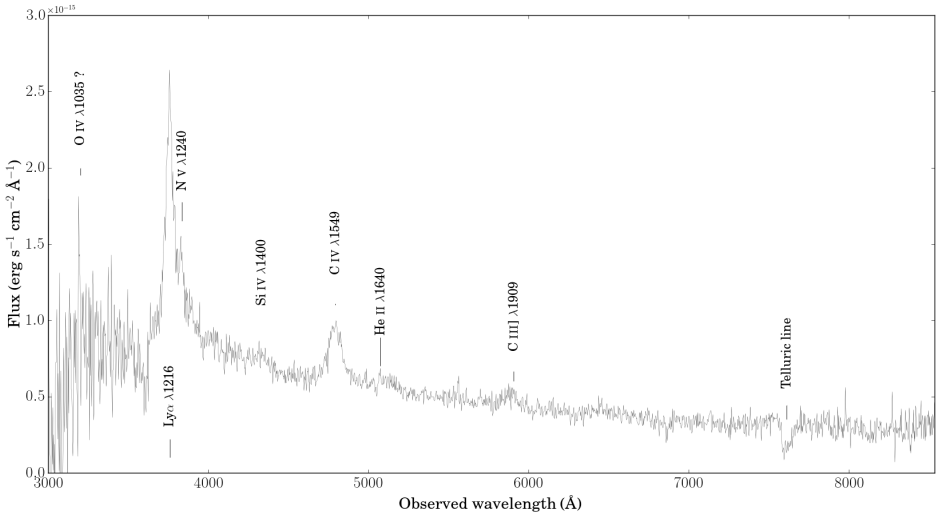

Figure 4: 4C +01.02 spectrum from SpUpNIC (1.9 m telescope/SAAO/Sutherland) in the 3000–8500 Å range, taken on 1 August 2016, at 2:30 UT, combining two exposures of 600 seconds, grating 7.

Las Cumbres Observatory (LCO) global network of telescopes[5] during 2–5 August 2016 (MJD 57602–57605). Monitoring continued with both the LCO instruments and the Watcher telescope for several weeks beyond these dates. We present in Figure 2 a highlight of the 31 July–8 August (MJD 57600–57608) period of the *Fermi*-LAT daily light-curve (lower panel), along with our first LCO data, presented in this figure for the R-band only (upper panel). Data collected during a longer period and in the B and V bands are expected to be presented in Britto et al [13]. Also, near simultaneous and complementary observations by Watcher and the 1.5-m Boyden telescope are still being processed. However, the preliminary data presented in Figure 2 gives a first insight of a day-scale correlation between optical and γ-ray light-curves.

3. Perspectives of spectroscopy and polarimetry measurements with SALT-RSS

Constraining the physical processes that power blazar jets is a current challenge, though the unified model of AGN [14] provides a basic picture concerning the emission of non-thermal radiation. Radiation is expected to be emitted at different distances from the central supermassive black hole, depending on its frequency. If absorption of radiation can be observed, it may constrain the location (or locations) of this emission. Also, the nature of the non-thermal X-ray and γ-ray emission remains to be understood (leptonic *versus* hadronic scenarios). Among the methods used for all these investigations are the monitoring of fast variability [15, 12, 8], absorption of γ rays in the broad-line region (BLR) [16, 17, 18] and the measurement of polarisation [19]. In particular, the measurement of optical polarisation allows constraints on the strength and geometry of the magnetic field of the AGN (linear polarisation), and constraints on the location of the γ-ray emiting region (polarisation angle change — see Trippe [19] and references therein).

[5] previously called LCOGT, https://lco.global

A recent feature of SALT-RSS is the polarimetry capability [20]. We have collected spectro-polarimetry data with SALT-RSS from blazar PKS 2023-07, 4C +01.02 and PKS 1510-089. The spectrum of 4C +01.02 (obtained on 9 July 2016) is presented in Figure 3 (upper panel) along with the measurements of the linear polarisation and polarisation angle as a function of the wavelength (middle and lower panels respectively). This spectrum was obtained during the γ-ray *main flare* reported in Section 2). We note a polarisation degree in the 5–10 % interval, remaining quite stable on the whole wavelength range. The dip around 3700–3800 Å corresponds to the position of the Lyα 1216 Å line, where the percentage of thermal radiation is higher. However, further studies are needed to discard eventual instrumental/analysis systematic effects. The polarisation angle also remains constant.

An optical spectrum of 4C +01.02 in the 3000–8500 Å range was taken with the SpUpNIC spectrograph of the SAAO 1.9-m telescope, on 1 August 2016 (Figure 4). This spectrum was taken during the *post-flare* phase of the outburst, when the γ-ray flux was about half what it was during the SALT-RSS acquisition, as indicated in Figures 1 and 2. We also expect to reduce additional observations that were performed at later stages in order to monitor and quantify the spectral changes in 4C +01.02 during different phases of the outburst.

Other flaring blazars are also being observed with SALT-RSS and SpUpNIC, and similar studies are expected to be undertaken, specifically multi-wavelength studies of lower redshift blazars as potential targets for TeV telescopes and the upcoming *Cherenkov Telescope Array* (CTA) [21, 22, 23, 10].

4. Conclusions

We have observed FSRQ 4C +01.02 over several months (and continued till early December 2016) and were able to report the γ-ray variability pattern of the source during the May–August 2016 period, for which we got quasi-simultaneous optical observations. A correlation between the R and high energy spectral bands was observed within a common limited range. The sensitivity of the SpUpNIC spectrograph and SALT-RSS give interesting perspectives to monitor the temporal variability of both the spectrum and polarisation parameters of 4C +01.02. Spectro-polarimetic measurements of this source and other flaring blazars at different phases during outbursts are expected to constrain models of radiation production mechanisms that power the blazar engine.

Acknowledgements

The Fermi-LAT Collaboration acknowledges support for LAT development, operation and data analysis from NASA and DOE (United States), CEA/Irfu and IN2P3/CNRS (France), ASI and INFN (Italy), MEXT, KEK, and JAXA (Japan), and the K.A. Wallenberg Foundation, the Swedish Research Council and the National Space Board (Sweden). Science analysis support in the operations phase from INAF (Italy) and CNES (France) is also gratefully acknowledged.

The authors acknowledge support from the National Research Foundation, South Africa and the South African Gamma-ray Astronomy Programme (SA-GAMMA).

We thank the HESS Collaboration for allowing us to use LCOGT data that are part of its proposal.

References

[1] W. B. Atwood, A. A. Abdo, M. Ackermann, et al., *The Large Area Telescope on the* Fermi *Gamma-Ray Space Telescope Mission*, *ApJ*, **697** (2009), pp. 1071–1102

[2] M. Ackermann, M. Ajello, W. B. Atwood et al., *The Third Catalog of Active Galactic Nuclei Detected by the* Fermi *Large Area Telescope*, *ApJ*, **810** (2015), pp. 14–47, arXiv:1501.06054 [astro-ph.HE]

[3] F. Acero, M. Ackermann, M. Ajello, et al., Fermi *Large Area Telescope Third Source Catalog*, *ApJ*, **218**, 23 (2015), arXiv:1501.02003 [astro-ph.HE]

[4] D. A. H. Buckley, G. P. Swart and J. G. Meiring, *Completion and commissioning of the Southern African Large Telescope*, *Ground-based and Airborne Telescopes. Edited by Stepp, Larry M.. Proceedings of the SPIE*, **66267** (2006), 62670Z

[5] E. B. Burgh, K. H. Nordsieck, H. A. Kobulnicky et al., *Prime Focus Imaging Spectrograph for the Southern African Large Telescope: optical design*, *Instrument Design and Performance for Optical/Infrared Ground-based Telescopes. Edited by Iye, Masanori; Moorwood, Alan F. M. Proceedings of the SPIE*, **4841** (2003), pp. 1463–1471

[6] H. A. Kobulnicky, K. H. Nordsieck, E. B. Burgh et al., *Prime focus imaging spectrograph for the Southern African large telescope: operational modes*, *Instrument Design and Performance for Optical/Infrared Ground-based Telescopes. Edited by Iye, Masanori; Moorwood, Alan F. M. Proceedings of the SPIE*, **4841** (2003), pp. 1634–1644

[7] L. A. Crause, D. Carter, A. Daniels et al., *SpUpNIC (Spectrograph Upgrade: Newly Improved Cassegrain) on the South African Astronomical Observatory's 74-inch Telescope*, Proceeding of the *SPIE Astronomical Telescopes and Instrumentation* conference in Edinburgh in June 2016, `http://www.saao.ac.za/wp-content/uploads/sites/5/SpUpNIC_2016-1.pdf`

[8] R. J. Britto (on behalf of the *Fermi*-LAT Collaboration), J. P. Marais, P. J. Meintjes and B. van Soelen, *Blazar variability and gamma-ray emission – signatures for leptonic and hadronic jet gamma-ray production models*, FRAPWS2016: Frontier Research in Astrophysics – II, 23–28 May 2016, Mondello (Palermo), Italy, submitted to *Proceedings of Science*

[9] R. J. Britto, E. Bottacini, M. Böttcher et al (on behalf of the *Fermi*-LAT Collaboration), *Multiwavelength Study of Fermi-LAT blazars Variability and Radiation Production Mechanisms*, SF2A-2016: Proceedings of the Annual meeting of the French Society of Astronomy and Astrophysics. Eds.: C. Reylé, J. Richard, L. Cambrésy, M. Deleuil, E. Pécontal, L. Tresse and I. Vauglin, held 14–17 June, 2016 at the *Centre de Recherche Astrophysique de Lyon*, pp.93–101, `http://adsabs.harvard.edu/abs/2016sf2a.conf...93B`

[10] B. van Soelen et al, *Characterising the* Fermi-*LAT BCUs: Optical Spectroscopy and Neural Networks*, in these proceedings

[11] P. Kharb, M. L. Lister, H. L. Marshall & B. S. Hogan, Chandra *and* HST *imaging of the quasars PKS B0106+013 and 3C345: Inverse compton X-rays and magnetized jets*, *ApJ*, **748** (2012), 81 (13 pp)

[12] R. J. Britto, E. Bottacini, B. Lott, S. Razzaque & S. Buson, Fermi-*LAT Observations of the 2014 May–July Outburst from 3C 454.3*, *ApJ*, **830** (2016), 162 (15 pp), arXiv:1511.02280 [astro-ph.HE]

[13] R. J. Britto et al., in preparation

[14] C. M. Urry & P. Padovani, *Unified Schemes for Radio-Loud Active Galactic Nuclei*, *Publications of the Astronomical Society of the Pacific*, **107** (1995), pp. 803–845

[15] R. J. Britto, *Study of flaring quasars using optical/gamma-ray correlations*, *Proceedings of Science: SALT Science Conference 2015*, [PoS(SSC2015)032], STIAS, Stellenbosch, South Africa, 1–5 June 2015.

[16] R. J. Britto, S. Razzaque & B. Lott, (on behalf of the *Fermi*-LAT Collaboration), *Spectral Studies of Flaring FSRQs at GeV Energies Using Pass 8* Fermi-*LAT Data*, *Proceedings of the Fifth* Fermi-*LAT Symposium*, Nagoya, Japan, 20–24 October 2014, eConf C14102.1 (2015), arXiv:1502.07624 [astro-ph.HE]

[17] J. Poutanen & B. Stern, *GeV Breaks in Blazars as a Result of Gamma-ray Absorption Within the Broad-line Region*, *ApJL*, **717** (2010), L118, arXiv:1005.3792 [astro-ph.HE]

[18] B. Stern & J. Poutanen, *The Mystery of Spectral Breaks: Lyman Continuum Absorption by Photon-Photon Pair Production in the Fermi GeV Spectra of Bright Blazars*,*ApJ*, **794** (2014), 8, arXiv:1408.0793 [astro-ph.HE]

[19] S. Trippe, *Polarization and Polarimetry: A Review*, *Journal of The Korean Astronomical Society*, **47** (2014), pp. 15–39, arXiv:1401.1911 [astro-ph.IM]

[20] S. B. Potter, K. Nordsieckb, E. Romero-Colmeneroa et al., *Commissioning the polarimetric modes of the Robert Stobie spectrograph on the Southern African Large Telescope*, *Proceedings of SPIE 9908: Ground-based and Airborne Instrumentation for Astronomy VI*, **99082K** (August 9, 2016), DOI: 10.1117/12.2232391

[21] A. Reimer & M. Böttcher, *Studies of active galactic nuclei with CTA*, *Astrop. Physics*, **43** (2013), pp. 103–111

[22] T. Takahashi, Y. Uchiyama & Ł. Stawarz, *Multiwavelength Astronomy and CTA: X-rays*, *Astrop. Physics*, **43** (2013), pp. 142–154

[23] H. Sol, A. Zech, C. Boisson et al., *Active Galactic Nuclei under the scrutiny of CTA*, *Astrop. Physics*, **43** (2013), pp. 215–240

PROCEEDINGS OF SCIENCE

Studies of optical/gamma-ray flares of blazar 4C +01.02: recent updates from the 2016-2017 observations*

Richard J. Britto (on behalf of the *Fermi*-LAT Collaboration)†
Department of Physics, University of the Free State, PO Box 339, Bloemfontein 9300, South Africa
E-mails: brittor@ufs.ac.za, dr.richard.britto@gmail.com

Johannes P. Marais, Brian van Soelen
Department of Physics, University of the Free State, PO Box 339, Bloemfontein 9300, South Africa
E-mails: maraisjp@ufs.ac.za, vansoelenb@ufs.ac.za

Markus Böttcher, Hester Schutte
Centre for Space Research, North-West University, Potchefstroom 2520, South Africa
E-mail: markus.bottcher@nwu.ac.za, schuttehester1@gmail.com

David A. H. Buckley
South African Astronomical Observatory, PO Box 9, Observatory 7935, Cape Town, South Africa
E-mail: dibnob@saao.ac.za

Abe Falcone
Department of Astronomy and Astrophysics, Penn State University, 516 Davey Lab, University Park, PA 16802, USA
E-mail: adf15@psu.edu

The flat spectrum radio quasar 4C +01.02 became one of the brightest active galactic nuclei detected at high redshift ($z = 2.1$) in gamma rays when it underwent a series of outbursts during several months in 2016. We monitored this source in gamma rays using the Large Area Telescope onboard of the *Fermi* spacecraft (*Fermi*-LAT), and in optical using the Las Cumbres Observatory (LCO). The highest peak flux detected was $F(E > 100\ \mathrm{MeV}) = (2.8 \pm 0.3)\ 10^{-6}$ ph cm^{-2} s^{-1} on 10 July 2016 (MJD 57579, daily average). We also obtained optical spectropolarimetry with the Robert Stobie Spectrograph on the Southern African Large Telescope (SALT-RSS) and observed a degree of linear polarisation of up to 10% during flaring states, and ∼1% during a quiescent period. We report recent updates we obtained in our time-domain and spectral studies of this source in July–August 2016, November–December 2016, and July 2017.

5th Annual Conference on High Energy Astrophysics in Southern Africa
4-6 October, 2017
University of the Witwatersrand (Wits), South Africa

*based on observations made with the Southern African Large Telescope (SALT)
†Speaker.

PoS(HEASA2017)013

1. Introduction

The flat spectrum radio quasar 4C +01.02 (PKS B0106+013) is a high redshift blazar (optical coord: R.A. = 01h 08m 38.8s, Decl. = +01° 35' 00", $z = 2.099$). This source has shown two relatively bright outbursts, in April and November 2016. Near-simultaneous optical data were obtained in optical and gamma rays.

Multiwavelength observations of flaring blazars can provide information on particle acceleration occurring in the relativistic plasma jets [4]. Optical polarisation and spectropolarimetry (wavelength dependent polarisation) are crucial tools to probe the ratio of synchrotron radiation (polarised) from the jet over thermal radiation (unpolarised) emitted by radiation fields surrounding the central supermassive black hole of the AGN. Such radiation fields are the ultraviolet-blue emission from the disk and the broad-line region (BLR), the red emission from the host galaxy and the infrared emission from the dust torus. Furthermore, the degree of order of the magnetic fields surrounding the emitting region can be constrained through spectropolarimetry ([3] and references therein).

We present in this paper updates on our on-going study of 4C +01.02 during its 2016 long lasting outburst [5], using new observational data collected from August 2016 to July 2017. We used the *Fermi*-Large Area Telescope [1], the Southern African Large Telescope–Robert Stobie Spectrograph (SALT-RSS) [7, 10] and the Las Cumbres Observatory (LCO) [6]. Details on these intruments and on the data reductions are given in [5].

We present our updated gamma-ray and three-band filter optical light-curves in section 2, followed by the SALT-RSS observations in section 3. Finally, we conclude with the summary of the status of our project in section 4.

2. Gamma-ray/optical light-curves

We analysed *Fermi*-LAT data from 20 October 2014 to 28 April 2017 (MJD 56954–57871), in the 100 MeV–300 GeV range, using the Pass 8 data representation and the *Fermi* Science Tools version v10r0p5[1], running the unbinned likelihood algorithm (gtlike/pyLikelihood Science Tool) with the following standard analysis cuts applied to point source analysis: radius of the *Region of interest* (ROI)=15°; Source region=ROI+10°; SOURCE class; event type = 3; zenith angle $<$ 90°; DATA_QUAL=1, LAT_CONFIG=1; Diffuse emission: `gll_iem_v06.fits` (Galactic) and `iso_P8R2_SOURCE_V6_v06.txt` (extragalactic) templates. We used the user contributed `make3FGLxml.py` script[2] to prepare the source model from the *Fermi*-LAT Third Source Catalog (3FGL, [2]).The source of interest was modelled by a single power law (PL). We produced a three-day binned *Fermi*-LAT light-curve for this whole period, plotted in Figure 1 (upper panel), where the four SALT-RSS observations taken during high gamma-ray states are indicated with dashed-red arrows. In the middle and lower panels, the values of the photon indices and energies of the individual photons above 5 GeV are shown.

During most of this 2.5 year period, the source was in a high state, with a maximum observed on 10 July (MJD 57579, daily average) F(E$>$ 100 MeV) = (2.8 $\pm$ 0.3) 10^{-6} ph cm^{-2} s^{-1}. The

[1] http://fermi.gsfc.nasa.gov/ssc/data/analysis/

[2] https://fermi.gsfc.nasa.gov/ssc/data/analysis/user/

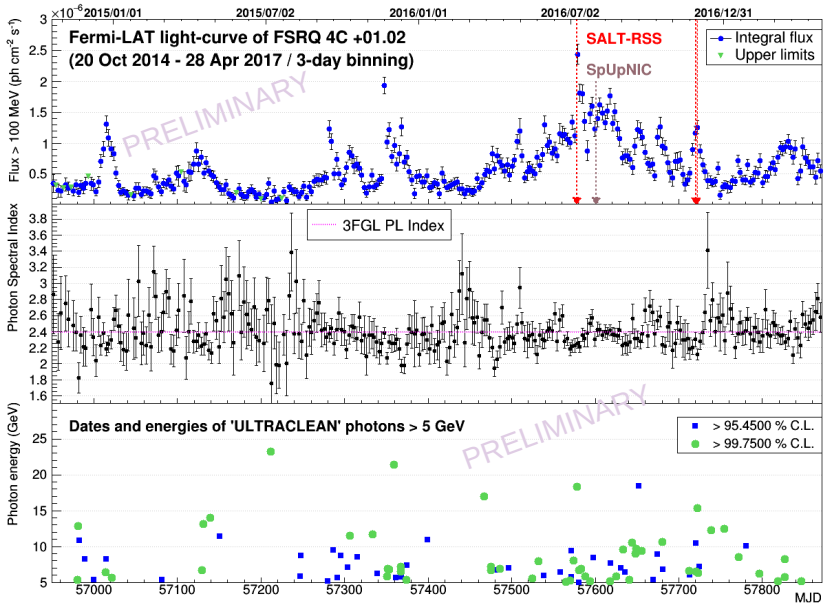

Figure 1: Upper panel: *Fermi*-LAT light-curve of 4C +01.02 above 100 MeV between 20 October 2014 and 28 April 2017 in a one-day binning. Middle panel: Optimised value of the photon index of the source. The magenta horizontal dashed-line indicates the value of the PL photon index of 3FGL. Lower panel: Arrival time and energies of high energy photons ("ULTRACLEAN" photon class, > 5 GeV). Two levels of confidences of the association of the photon with 4C +01.02 are indicated.

one-day binned *Fermi*-LAT light-curve during the 11 May–12 September 2016 period is plotted in Figure 2, along with LCO photometry data obtained in the B, V and R Johnson-Cousins filters. However, since we could not obtain a full LCO coverage during this flaring period, we can not really discuss light-curve correlations.

3. Optical spectropolarimetry with SALT-RSS

Spectropolarimetry observations were obtained with SALT-RSS in the whole optical range, using the PG 300 grating, in the "LINEAR" spectropolarimetry mode, and reduced using the `pySALT` pipeline [8] and `polsalt` package.[3] Four consecutive exposures of 600 s were triggered for each of the five observations we performed, which started on 9 July 2016 at 3:15 UT, 27 November 2016 at 19:15 UT, 28 November 2016 at 19:15 UT, 29 November 2016 at 19:36 UT and 25 July 2017 at 2:43 UT. The first four observations were obtained during flaring activity, and are labeled in Figure 1, while the fifth observation (25 July 2017) was obtained during quiescence (corresponding to a gamma-ray flux $F(E > 100\ \mathrm{MeV}) \sim 0.1 \times 10^{-6}$ ph cm^{-2} s^{-1}). The *Swift*-XRT telescope detected 0.04 ± 0.006 counts s^{-1} in the 0.3–10 keV range[4] on 2 August 2017 (MJD 57967.91), when the gamma-ray flux was at the same level as on 25 July 2017. Count rates from *Swift*-XRT on this source ranges from ∼0.03 to 0.08 counts s^{-1}.

[3] https://github.com/saltastro/polsalt

[4] http://www.swift.psu.edu/monitoring/source.php?source=PKS0106+01

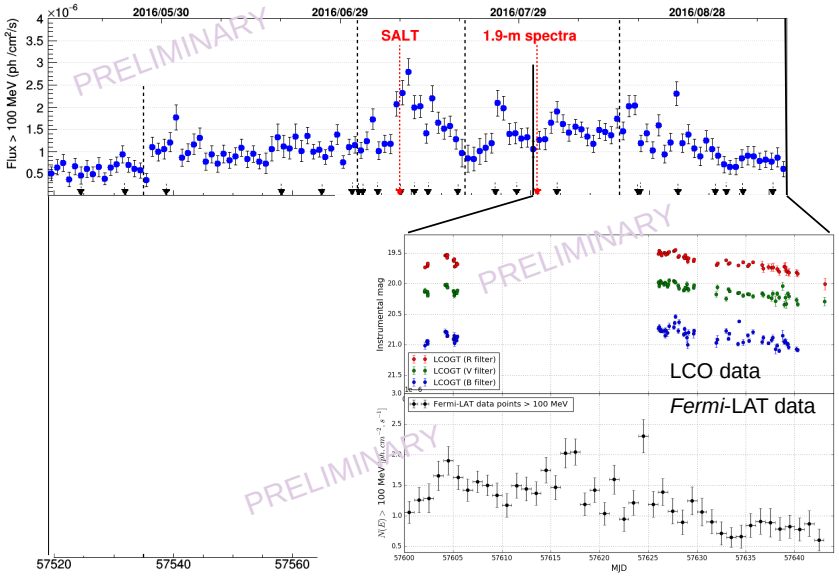

Figure 2: Upper panel: *Fermi*-LAT light-curve of 4C +01.02 above 100 MeV between 11 May and 12 September 2016, in a one-day binning. Vertical dashed arrow indicate separations between three phases of the outburst: plateau, flare and postflare. Small black arrow indicate the arrival times of high energy photons (> 5 GeV). Zoom panel: LCO data in the B, V and R Johnson-Cousins filters, compared to the *Fermi*-LAT data points from the upper panel, in the MJD 57600–57643 range.

In Figure 3, preliminary results from the five SALT-RSS observations are presented. The percentage of linear polarisation remained between 5-10% during the flare, after which it decreases to $\sim$1% when it was observed during a quiescent phase. This matches our expectation of observing a significant increase of synchrotron radiation emission from the jet, characteristic of blazar outbursts. Furthermore, a decrease of the polarisation degree is observed at the position of strong emission lines, since these originate from non-thermal emission from ther BLR.

We show in Figure 4 the normalized count spectra of the five observations. We notice a significant increase of the equivalent widths of the emission lines during quiescence. This is often observed, due to jet emission that outshines the BLR radiation field, though it has also been observed that BLR emission lines may become more luminous during flares (See [9] in the case of the FSRQ 3C 454.3).

4. Summary

We reported updates on our optical/gamma-ray observations of 4C +01.02 during its long lasting outburst in 2016, where significant flux variability was recorded, both in gamma ray and optical bands. We also compared the spectral and polarisation features observed by SALT-RSS with the observation performed on 25 July 2017 during its quiescent state. A negligeable degree of polarisation was reported at this date, compared to previous values that were observed up to $\sim$10 % during flaring activity. Broadband SED modelling is also being undertaken, considering

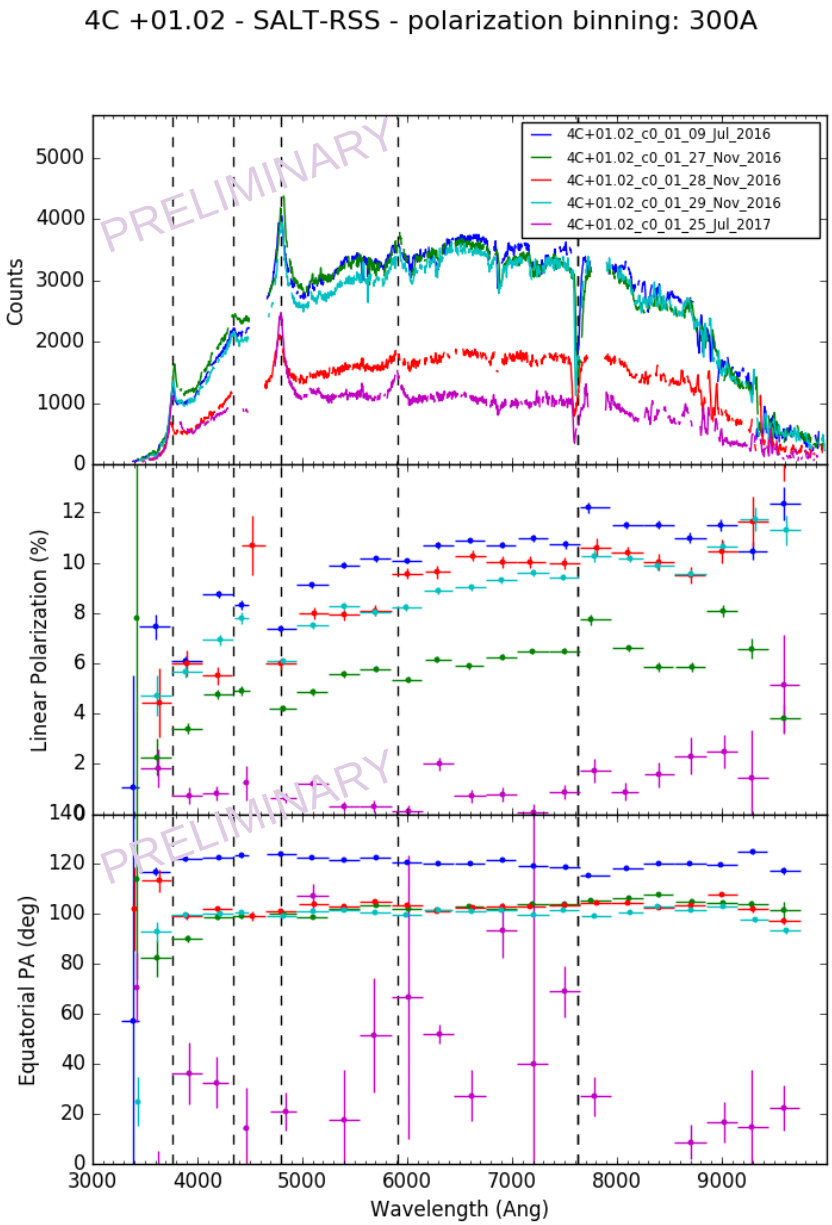

Figure 3: Preliminary SALT-RSS data reductions from 4C +01.02 data obtained on 9 July, 27, 28, 29 November 2016 and 25 July 2017 (grating PG 300 in "LINEAR" spectropolarimetry mode), combining four exposures of 600 s for each data set. Upper panel: count spectra in the ∼3500–10000 Å range. Middle panel: linear polarisation degree. Lower panel: position angle.

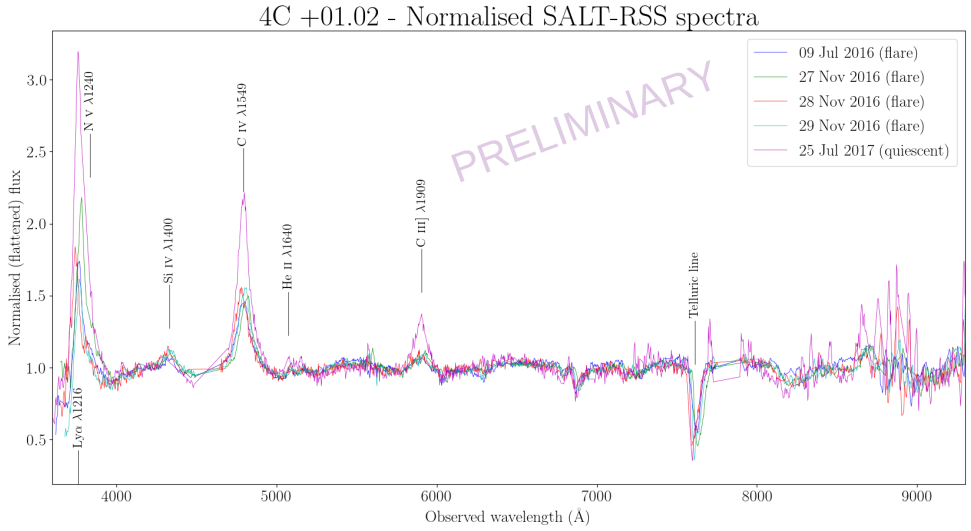

Figure 4: 4C +01.02 SALT-RSS count spectrum from Figure 3 after normalisation of the continuum to 1.

the wavelength dependence of the linear polarisation degree, providing constraints on the degree of order of the magnetic field and the mass of the supermassive black hole.

Acknowledgements

The *Fermi*-LAT Collaboration acknowledges support for LAT development, operation and data analysis from NASA and DOE (United States), CEA/Irfu and IN2P3/CNRS (France), ASI and INFN (Italy), MEXT, KEK, and JAXA (Japan), and the K.A. Wallenberg Foundation, the Swedish Research Council and the National Space Board (Sweden). Science analysis support in the operations phase from INAF (Italy) and CNES (France) is also gratefully acknowledged. This work performed in part under DOE Contract DE-AC02-76SF00515.

Some of the observations reported in this paper were obtained with the Southern African Large Telescope (SALT), under program 2016-2-LSP-001 (PI: David A. H. Buckley).

The authors affiliated to South African institutions acknowledge support from the National Research Foundation, South Africa and the South African Gamma-ray Astronomy Programme (SA-GAMMA).

We thank the HESS Collaboration for allowing us to use LCO data that are part of its proposal (PI: B. van Soelen).

References

[1] W. B. Atwood, A. A. Abdo, M. Ackermann, et al., *The Large Area Telescope on the* Fermi *Gamma-Ray Space Telescope Mission*, *ApJ*, **697** (2009), pp. 1071–1102

[2] F. Acero, M. Ackermann, M. Ajello, et al., Fermi *Large Area Telescope Third Source Catalog*, *ApJ*, **218** (2015), 23

[3] M. Böttcher, B. van Soelen, R. J. Britto et al., *SALT Spectropolarimetry and Self-Consistent SED and Polarization Modeling of Blazars*, Galaxies 2017, **5**(3), 52

[4] R. J. Britto, *Study of flaring quasars using optical/gamma-ray correlations*, *Proceedings of Science: SALT Science Conference 2015*, [PoS(SSC2015)032], STIAS, Stellenbosch, South Africa, 1–5 June 2015.

[5] R. J. Britto (on behalf of the *Fermi*-LAT Collaboration), J. P. Marais, P. J. Meintjes, B. van Soelen, M. Böttcher, D. A. H. Buckley, S. Crawford, A. Rajoelimanana, *Observations of the flaring* Fermi*-LAT blazar 4C +01.02 and prospects in spectropolarimetry with SALT-RSS*, Proccedings of the 4th Annual Conference on High Energy Astrophysics in Southern Africa (HEASA 2016), 25–26 August 2016, SAAO, Cape Town, South Africa, Eds. M. Boettcher, D. Buckley, S. Colafrancesco, P. Meintjes and S. Razzaque, [PoS(HEASA 2016)021]

[6] T. M. Brown, N. Baliber, F. B. Bianco, et al., *Las cumbres observatory global telescope network*, Publ. Astron. Soc. Pac., **125** (2013), 1031

[7] D. A. H. Buckley, G. P. Swart and J. G. Meiring, *Completion and commissioning of the Southern African Large Telescope*, *Ground-based and Airborne Telescopes. Edited by Stepp, Larry M.. Proceedings of the SPIE*, **66267** (2006), 62670Z

[8] S. M. Crawford, M., Still, P., Schellart et al., *PySALT: the SALT Science Pipeline*, SPIE Astronomical Instrumentation, **7737** (2010), 82

[9] J. León-Tavares, V. Chavushyan, V. Patiño-Álvarez et al. *Flare-like Variability of the Mg*II λ *2800 Emission Line in the γ-Ray Blazar 3C 454*, ApJL, **763** (2013), L36

[10] S. B. Potter, K. Nordsieck, E. Romero-Colmeneroa et al., *Commissioning the polarimetric modes of the Robert Stobie spectrograph on the Southern African Large Telescope*, *Proceedings of SPIE 9908: Ground-based and Airborne Instrumentation for Astronomy VI*, **99082K** (August 9, 2016), DOI: 10.1117/12.2232391

PROCEEDINGS OF SCIENCE

Searching for new TeV blazars in the 3rd Fermi-LAT catalogue of hard gamma-ray sources

J.P. Marais* **and B. van Soelen**
University of the Free State
E-mail: maraisjp@ufs.ac.za, vansoelenb@ufs.ac.za

The 3rd Fermi catalogue of Hard *Fermi*-LAT Sources (3FHL), which detected 1556 sources above 10 GeV, provides an important resource for finding new candidate TeV sources for follow-up observations with the H.E.S.S. telescopes. To search for potential TeV emitting extragalactic sources, we observed a sample of five 3FHL sources classified as Blazars of unknown type (BCU) and two 3FHL sources without initial associations at other wavelengths with the SAAO 1.9-m telescope. The observations were performed during February 2017, with the SpUpNIC spectrograph on the 1.9-m telescope. Possible counterparts for the unassociated sources were determined by cross-matching objects using archival multi-wavelength data from Radio, Infrared and X-ray catalogues. Classifications were obtained for all the observed BCUs and redshifts were determined for two of them. Redshift measurements were obtained for the optical candidates of both the unassociated sources observed. Further analysis is necessary to confirm their association to the 3FHL γ-ray sources.

5th Annual Conference on High Energy Astrophysics in Southern Africa
4-6 October, 2017
University of the Witwatersrand (Wits), South Africa

*Speaker.

PoS(HEASA2017)014

1. Introduction

The most numerous extragalactic source class detected by *Fermi* are blazars. Blazars are radio-loud Active Galactic Nuclei (AGN) with relativistic jets closely orientated towards the observer's line of sight. The non-thermal emission from the closely orientated jet is Doppler boosted, greatly increasing the measured flux at all wavelengths and dominates over the thermal emission from the host galaxy and inner regions of the AGN. The Spectral Energy Distributions (SEDs) of AGN display a double humped shape consisting of a low energy component extending from radio to X-ray energies and a High Energy (HE) component that can extend from X-ray up to TeV energies. The low energy emission is considered to be synchrotron emission from a population of relativistic electrons moving along the jet. The source of the HE and Very High Energy (VHE) emission is more difficult to determine, with leptonic Inverse Compton (IC) emission and hadronic processes, such as proton synchrotron and neutral pion decay, being considered [1].

The 3rd catalogue of Hard *Fermi*-LAT Sources (3FHL) list 1556 sources detected above 10 GeV with the *Fermi*-LAT of which 76% are extragalactic in nature. This makes the extragalactic source population the most significant contributor to the HE γ-ray sky above 10 GeV seen by *Fermi* [2]. The 3FHL catalogue provides an extensive list of potential VHE emitting objects, which can be studied with Imaging Air Cherenkov Telescopes (IACT), such as the H.E.S.S. telescope. Classification and redshift measurements of 290 of these extragalactic sources, classified as blazar candidates of unknown type (BCU), still have to be made in order to constrain the γ-ray population. There are also a further 177 sources which have yet to be associated with objects at other wavelengths. Classifying the sources responsible for the γ-ray emission can potentially bring to light new source classes of γ-ray emitting objects, such as the extreme blazars [3], Dark Matter candidates [4] and even unexpected HE phenomena.

Blazars can be classified as BL Lac or Flat Spectrum Radio Quasars (FSRQ) by measuring the Equivalent Widths (EW) of their optical emission lines, with the divide set at 5 Å: BL Lacs EW < 5 Å and FSRQs EW > 5 Å [5]. This classification scheme takes advantage of the properties of the central regions of the AGN. BL Lacs have radiatively inefficient accretion flows which are unable to sustain a Broad Line Region (BLR), while FSRQs can sustain a BLR and illuminate the torus surrounding the AGN [6]. Measuring emission lines in optical spectra can then give an indication of the strength of the BLR emission, allowing the blazar to be classified as either a BL Lac or FSRQ.

The difference in BLR strengths between these two blazar classes also determines the processes responsible for the HE and VHE emission. In the leptonic scenario the bright FSRQ BLR and torus provide seed photons (produced external to the jet) that can be upscattered to HE and VHE γ-rays; this is known as the External Compton (EC) process. This EC emission radiatively cools the relativistic electrons before the majority of the electron population can be accelerated to very high energies. The HE and VHE emission from BL Lacs, on the other hand can also be produced from synchrotron photons upscattered to HE and VHE energies, produced through the so called Synchrotron Self Compton (SSC) emission. BL Lac jets exhibit weak radiative cooling, so their electron population can reach much higher energies than those in FSRQ jets [6, 7].

Detailed studies of γ-ray emission from blazars can provide constraints on particle acceleration and emission mechanisms in the jet environment predicted by models [8, 9, 10]. Classifying the

Fermi-LAT BCUs and unassociated sources will increase the number of blazars that can be used to constrain the mechanisms responsible for the HE emission. These constraints, applied to very distant blazars, can be used for example, to place limits on the Extragalactic Background Light (EBL), which is the integrated emission from all emitting gas, dust, stars and galaxies since the epoch of recombination and is important for the study of cosmology. The EBL provides key information about stellar and galactic evolution throughout cosmic history [11]. The EBL affects VHE γ-rays through attenuation by $\gamma\gamma$ interactions. Knowledge of the intrinsic blazar spectrum can be used to measure the amount of γ-ray attenuation by the EBL.

Classifying and measuring the redshifts of BCUs detected in the 3FHL catalogue will provide candidates for follow-up studies with H.E.S.S. and CTA. Observations with IACTs extend the broadband SEDs of blazars beyond $E > 2$ TeV and provides important constraints on blazar emission models [12]. VHE emission from blazars with a redshift $z \gtrsim 1$ are not detectable by IACTs due to $\gamma\gamma$ attenuation by the EBL. Determining the redshift of potential VHE blazars will, therefore, reduce the number of possible counterparts.

We searched for candidates for follow-up observations with IACTs by performing optical spectroscopy on a sample of five 3FHL BCUs and two unassociated 3FHL sources using the SpUpNIC spectrograph on the South African Astronomical Observatory (SAAO) 1.9-m telescope [13]. This paper is structured as follows: in Section 2, we describe the selection of optical candidates using multi-wavelength archival data; Section 3 describes the observation and analysis of the sources; while Section 4 describes the results obtained on individual sources.

2. Multi-wavelength candidate identification

The poor spatial resolution of the *Fermi*-LAT, although better than earlier γ-ray instruments like the *Energetic Gamma-ray Experiment Telescope* (EGRET), makes it difficult to determine the exact position of potential HE and VHE emitters for follow-up studies. The *Fermi*-LAT source localization is also highly dependant on the spectral index of the γ-ray detections, making the localization of sources with a softer spectral index more difficult [14]. Many methods have been used to identify likely counterparts of unassociated *Fermi* sources. These methods include, but are not limited to: multiwavelength monitoring of sources inside the *Fermi*-LAT error ellipses in order to search for correlated multi-wavelength variability (a hallmark of blazars) [15]; using broadband SED characterization to find blazar-like sources [16, 17]; searching for radio counterparts inside the *Fermi*-LAT error ellipses [18]; and using machine-learning techniques to search for blazars among multi-wavelength data [19, 20].

Many of the brighter unassociated γ-ray sources have already been associated by the methods mentioned above. Using multiwavelength monitoring to associate potential electromagnetic (radio, optical, etc.) counterparts with previously unassociated *Fermi*-LAT sources, requires variable sources continuously monitored over long periods of time. Fainter sources are more difficult to continuously monitor. Broadband SED characterisation requires fairly complete coverage over the entire energy range to successfully characterise the sources. This is difficult for the fainter sources with limited data. Machine learning can be used to study the fainter sources, but requires large datasets to successfully train the algorithms. We, therefore, identified potential candidates of two unassociated 3FHL sources observable from the SAAO Sutherland Observatory, using archival

ALLWISE and DSS[1] data [21]. The ALLWISE data allowed non-thermal dominated sources to be identified, while DSS and NOMAD[2] data were used to constrain our candidates to objects observable in the optical band, with $V \lesssim 18$. To further constrain the number of candidates, we also used X-ray and radio data where possible. We also observed five 3FHL BCUs, confirming the optical counterparts using the same methods used to select the unassociated 3FHL optical candidates.

2.1 ALLWISE blazar strip

The infrared colours of blazars are dominated by their non-thermal synchrotron emission, clearly separating them from normal galaxies, stars and non-jetted AGN [24]. To constrain the number of optical candidates to observe, for both the unassociated sources and BCUs, we selected ALLWISE infrared sources inside, or slightly outside the *Fermi* 95% error ellipses and whose infrared colours put them inside or near the ALLWISE blazar strip. For the BCUs, this provided an initial confirmation for the optical counterpart to the γ-ray source. For the unassociated sources, without firm multiwavelength associations, this drastically reduced the number of sources that could be the source of the γ-rays.

2.2 X-ray and Radio counterparts

Further constraints were applied, using archival X-ray and radio data. Potential optical candidates were selected based on the presence of X-ray and radio sources. Unfortunately, for many of the BCUs and unassociated sources considered, X-ray and radio sources were not located close to the optical candidates, and in some instances were either absent or outside the *Fermi* error ellipses. Since all of our 3FHL targets are also weak γ-ray emitters, this could potentially indicate that their X-ray and radio emission is below the threshold of the surveys considered. This agrees with the results of Schinzel et al. [25], whose follow-up radio observations in the 4-10 GHz range, found 245 unassociated 3FGL γ-ray sources without compact radio counterparts above 2 mJy within 3σ of the γ-ray localization. Therefore, for the candidates without close X-ray or radio counterparts, all observable optical candidates were considered for follow-up observations.

3. Observations and Analysis

We performed optical spectroscopy on five Fermi 3FHL BCUs and two unassociated Fermi 3FHL sources using the SpUpNIC spectrograph on the SAAO 1.9-m Cassegrain reflector during February 2017. The observations were obtained with Grating 7 and a usable wavelength range between 3000 Å and 9000 Å. A series of bias and dome flat field exposures were taken at the start of each night. Spectrophotometric standard stars were also observed each night for flux calibration of the optical spectra. The total integration time per target varied between 3600 and 7200 seconds, in separate, consecutive 1800 second exposures, depending on source brightness and sky conditions.

Standard `IRAF/NOAO`[3] spectrophotometry reduction routines were performed on the data. `IRAF/NOAO` routines were also used for the wavelength calibration, background subtraction, spec-

[1]The Digitized Sky Survey data is accessible from http://archive.eso.org/dss/dss

[2]Naval Observatory Merged Astrometric Dataset [22] is accessible from the CDS/Vizier [23] catalog service at http://vizier.u-strasbg.fr/viz-bin/VizieR

[3]The Image Reduction and Analysis Facility can be downloaded from http://iraf.noao.edu/

3FHL Name	3FHL Type	Association	Class	Redshift
3FHL J0647.0-5138	BCU	1ES 0646-515	BL Lac	0.22687(3)
3FHL J0813.7-0353	unassociated	-	?	~ 0.3
3FHL J0935.2-1735	BCU	NVSS J093514-173658	BL Lac	-
3FHL J0937.8-1434	unassociated	-	BL Lac	-
3FHL J1042.2-4128	BCU	1RXS J104204.1-412936	BL Lac	-
3FHL J1130.5-7801	BCU	SUMSS J113032-780105	BL Lac	0.31504(2)
3FHL J1223.5-3033	BCU	NVSS J122337-303246	BL Lac	0.21935(4)

Table 1: Table of sources observed during our 2017 Feb observation campaign. The 3FHL names, source type, counterparts (if associated) are given, as well as the preliminary classification and redshift determined in this work.

tra extraction and spectra calibration using the spectrophotometric standard stars. After spectrophotometric calibration of the targets, the frames were examined and cleaned of cosmic rays and median combined to produce higher Signal-to-Noise (S/N) spectra used to determine the redshift of the source. Redshifts were determined using the `XCSAO` cross-correlation task from the `RVSAO` [26]. The observed spectra were cross-correlated against the SDSS Data Release 5 cross-correlation templates.[4]

4. Results

Table 1 lists the BCUs and unassociated sources we observed during our campaign along with, where possible, the classification and redshift measurements determined from these observations. The flux-calibrated optical spectra of our targets are presented in Figures 1. All redshift measurements were manually checked to see if the calculated redshifts matched any feature seen in the spectra. These included the 3933 and 3970 Å Ca H&K and $\sim$ 4300 Å G band features.

4.1 3FHL J0647.0-5138

The spectrum of the optical counterpart of this sources is rather flat with a Ca H&K break, at a redshift of $z = 0.22687(3)$. The absence of any emission lines is consistent with a BL Lac object. The spectrum suffers from sky contamination at wavelengths $\lambda \gtrsim 8000$ Å that could not be completely removed, but did not influence the redshift calculation.

4.2 3FHL J0813.7-0353

This source is unassociated in both the 3FHL and 3FGL catalogues. There are a total of 9 optical candidates which lie inside the ALLWISE blazar strip that were observable during our campaign. All the sources that we observed displayed BL Lac-like spectra, all with redshifts z $\sim$ 0.3 (a representative spectrum is shown in Fig. 1). A single $F_{1.4\ \mathrm{GHz}} \sim 30$ mJy radio source lies inside the 3FHL error ellipse, but not near any of the observable candidates. No X-ray sources are detected inside the 3FHL error ellipse. Further observations are needed to associate the source to an optical counterpart.

[4]The SDSS cross-correlation templates can be downloaded from http://classic.sdss.org/dr5/algorithms/spectemplates/

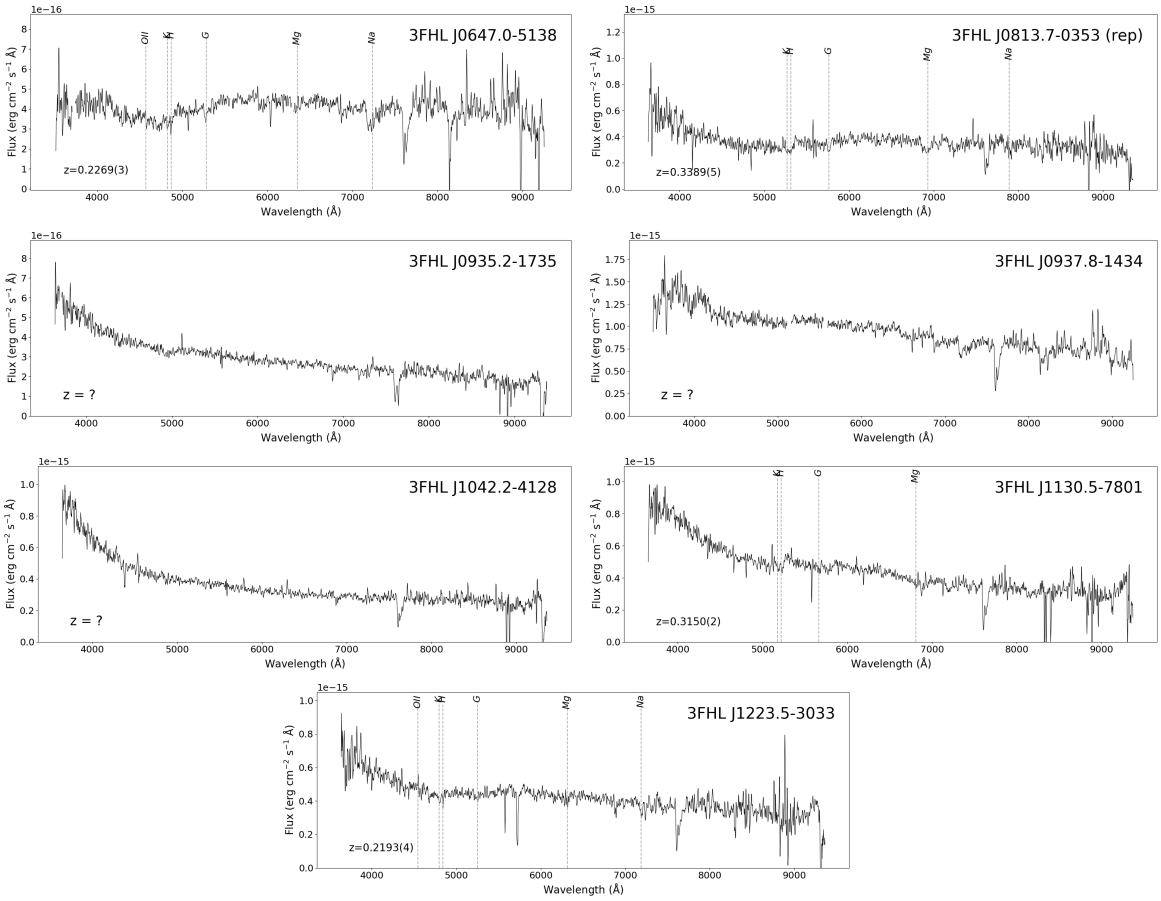

Figure 1: Calibrated spectra for our selection of 3FHL BCUs and unassociated sources that were classified as being extragalactic in nature. Their 3FHL designations and redshifts are labelled.

4.3 3FHL J0935.2-1735

The optical spectrum of the counterpart to the BCU source J0935.2-1735 shows no discernible features and no redshift could be calculated. The spectrum is blue, consistent with a non-thermal origin of the emission. We therefore tentatively classify the source as a BL Lac.

4.4 3FHL J0937.8-1434

This source is unassociated in the 3FHL catalogue, but our best optical candidate lies within the error ellipse of a $F_{1.4\ \mathrm{GHz}} \sim 5$ mJy radio source, NVSS J093754-143350. The low S/N of this spectra, prevented us from determining a redshift for this source, but the spectrum is consistent with non-thermal emission. We classified this source as BL Lac in nature due to the absence of any emission lines.

4.5 3FHL J1042.2-4128

Due to the non-thermal featureless spectrum we obtained for this source we have classified it as a BL Lac. A redshift determination was not possible due to the featureless spectrum. The optical

counterpart of this source was listed in D'Abrusco et al. [27] as a potential blazar-like source, which is consistent with our observations.

4.6 3FHL J1130.5-7801

We obtained a lower S/N spectrum for this sources, but it shows the Ca H&K break and G band features consistent with a redshift of $z = 0.31504(2)$ determined from the cross-correlation. The low S/N spectrum prohibits us from determining a firm classification for this source but we tentatively classify this source as a BL Lac-type object due to the lack of emission lines.

4.7 3FHL J1223.5-3033

We calculated a tentative redshift of $z = 0.21935(4)$, via cross-correlation, for 3FHL J1223.5-3033. The low S/N of this source and weak nature of the possible [OIII] 3727 Å emission line prevents us from determining the EW of the line. Based on the presence of only the one very weak emission line, this source can be classified as BL Lac in nature.

5. Conclusion

The *Fermi* 3FHL catalogue, consisting of sources emitting above 10 GeV, is a great resource to find TeV emitting blazars for follow-up studies with IACTs. To find sources for potential follow-up studies with IACTs, we performed optical spectroscopy on five Fermi 3FHL BCUs and two unassociated Fermi 3FHL sources using the SpUpNIC spectrograph on the SAAO 1.9-m Cassegrain reflector during February 2017. Optical candidates were selected based on their ALLWISE infrared colors, which place them in well defined classes. We considered optical candidates whose ALLWISE colors put them in the so-called blazar strip, the region in infrared color space that corresponds to a non-thermal origin of the infrared emission, consistent with blazar jet dominated emission [24].

We classified six of the observed Fermi 3FHL sources as BL Lacs based on the absence of strong emission features. Redshift measurements were made for three of the 3FHL sources. All nine of the observed candidates for 3FHL J0813.7-0353, showed a non-thermal spectrum, at a redshift of $z \sim 0.3$. Further observations are necessary to determine the optical association of this source.

Acknowledgments

The financial assistance of the National Research Foundation (NRF) towards this research is hereby acknowledged. Opinions expressed and conclusions arrived at, are those of the author and are not necessarily to be attributed to the NRF.
This paper uses observations made at the South African Astronomical Observatory (SAAO).

References

[1] M. Böttcher, A. Reimer, K. Sweeney and A. Prakash, *Leptonic and Hadronic Modeling of Fermi-detected Blazars*, ApJ **768** (May, 2013) 54, [1304.0605].

[2] M. Ajello, W. B. Atwood, L. Baldini, J. Ballet, G. Barbiellini, D. Bastieri et al., *3FHL: The Third Catalog of Hard Fermi-LAT Sources*, ApJS **232** (Oct., 2017) 18, [1702.00664].

[3] G. Bonnoli, F. Tavecchio, G. Ghisellini and T. Sbarrato, *An emerging population of BL Lacs with extreme properties: towards a class of EBL and cosmic magnetic field probes?*, MNRAS **451** (July, 2015) 611–621, [1501.01974].

[4] A. V. Belikov, M. R. Buckley and D. Hooper, *Searching for dark matter subhalos in the Fermi-LAT second source catalog*, Phys.~Rev.~D **86** (Aug., 2012) 043504, [1111.2613].

[5] C. M. Urry and P. Padovani, *Unified Schemes for Radio-Loud Active Galactic Nuclei*, PASP **107** (Sept., 1995) 803, [astro-ph/9506063].

[6] G. Ghisellini, A. Celotti, G. Fossati, L. Maraschi and A. Comastri, *A theoretical unifying scheme for gamma-ray bright blazars*, MNRAS **301** (Dec., 1998) 451–468, [astro-ph/9807317].

[7] G. Ghisellini, *The Blazar Sequence 2.0*, *Galaxies* **4** (Sept., 2016) 36, [1609.08606].

[8] M. Böttcher, M. G. Baring, E. P. Liang, E. J. Summerlin, W. Fu, I. A. Smith et al., *Diagnosing particle acceleration in relativistic jets*, in *Extragalactic Jets from Every Angle* (F. Massaro, C. C. Cheung, E. Lopez and A. Siemiginowska, eds.), vol. 313 of *IAU Symposium*, pp. 153–158, Mar., 2015, DOI.

[9] B. Khiali, E. M. de Gouveia Dal Pino and H. Sol, *Particle Acceleration and gamma-ray emission due to magnetic reconnection around the core region of radio galaxies*, *ArXiv e-prints* (Apr., 2015) , [1504.07592].

[10] M. Zacharias and S. J. Wagner, *The extended jet of AP Librae: Origin of the very high-energy γ-ray emission?*, A&A **588** (Apr., 2016) A110, [1602.03430].

[11] E. Dwek and F. Krennrich, *The extragalactic background light and the gamma-ray opacity of the universe*, *Astroparticle Physics* **43** (Mar., 2013) 112–133, [1209.4661].

[12] A. A. Abdo, M. Ackermann, M. Ajello, L. Baldini, J. Ballet, G. Barbiellini et al., *Fermi Large Area Telescope Observations of Markarian 421: The Missing Piece of its Spectral Energy Distribution*, ApJ **736** (Aug., 2011) 131, [1106.1348].

[13] L. A. Crause, D. Carter, A. Daniels, G. Evans, P. Fourie, D. Gilbank et al., *SpUpNIC (Spectrograph Upgrade: Newly Improved Cassegrain) on the South African Astronomical Observatory's 74-inch telescope*, in *Ground-based and Airborne Instrumentation for Astronomy VI*, vol. 9908 of Proc. SPIE, p. 990827, Aug., 2016, DOI.

[14] W. B. Atwood, A. A. Abdo, M. Ackermann, W. Althouse, B. Anderson, M. Axelsson et al., *The Large Area Telescope on the Fermi Gamma-Ray Space Telescope Mission*, ApJ **697** (June, 2009) 1071–1102, [0902.1089].

[15] A. Bayirli, T. Ergin and T. Guver, *Correlating between the Optical and Gamma-ray Light Curves of Fermi-LAT Unassociated Sources*, in *40th COSPAR Scientific Assembly*, vol. 40 of *COSPAR Meeting*, 2014.

[16] S. Paiano, A. Franceschini and A. Stamerra, *A new method to unveil blazars among multiwavelength counterparts of unassociated Fermi γ-ray sources*, MNRAS **468** (July, 2017) 4902–4937, [1703.09143].

[17] G. La Mura, G. Chiaro, S. Ciroi, P. Rafanelli, D. Salvetti, M. Berton et al., *Optical Counterparts of Undetermined Type γ-Ray Active Galactic Nuclei with Blazar-Like Spectral Energy Distributions*, *Journal of Astrophysics and Astronomy* **36** (Dec., 2015) 447–455, [1510.00960].

[18] Y. Fujinaga, K. Niinuma, A. Kimura, K. Fujisawa, T. Oyama, S. Mizuno et al., *The discovery of new AGN candidates within the field of Fermi unassociated γ-ray sources*, PASJ **68** (Oct., 2016) 70.

[19] J. Lefaucheur and S. Pita, *Research and characterisation of blazar candidates among the Fermi/LAT 3FGL catalogue using multivariate classifications*, A&A **602** (June, 2017) A86, [1703.01822].

[20] J. Lefaucheur, C. Boisson, P. Goldoni and S. Pita, *Looking for infrared counterparts of Fermi/LAT blazar candidates*, *ArXiv e-prints* (Sept., 2017) , [1709.10168].

[21] R. M. Cutri and et al., *VizieR Online Data Catalog: AllWISE Data Release (Cutri+ 2013)*, *VizieR Online Data Catalog* **2328** (Jan., 2014) .

[22] N. Zacharias, D. G. Monet, S. E. Levine, S. E. Urban, R. Gaume and G. L. Wycoff, *The Naval Observatory Merged Astrometric Dataset (NOMAD)*, in *American Astronomical Society Meeting Abstracts*, vol. 205, p. 48.15, Dec., 2004.

[23] F. Ochsenbein, P. Bauer and J. Marcout, *The VizieR database of astronomical catalogues*, *Astronomy and Astrophysics Supplement Series* **143** (Apr., 2000) 23–32, [astro-ph/0002122].

[24] R. D'Abrusco, F. Massaro, M. Ajello, J. E. Grindlay, H. A. Smith and G. Tosti, *Infrared Colors of the Gamma-Ray-detected Blazars*, ApJ **748** (Mar., 2012) 68, [1203.0568].

[25] F. K. Schinzel, L. Petrov, G. B. Taylor and P. G. Edwards, *Radio Follow-up on All Unassociated Gamma-Ray Sources from the Third Fermi Large Area Telescope Source Catalog*, ApJ **838** (Apr., 2017) 139, [1702.07036].

[26] M. J. Kurtz and D. J. Mink, *RVSAO 2.0: Digital Redshifts and Radial Velocities*, PASP **110** (Aug., 1998) 934–977, [astro-ph/9803252].

[27] R. D'Abrusco, F. Massaro, A. Paggi, H. A. Smith, N. Masetti, M. Landoni et al., *The WISE Blazar-like Radio-loud Sources: An All-sky Catalog of Candidate γ-ray Blazars*, ApJS **215** (Nov., 2014) 14, [1410.0029].

PROCEEDINGS OF SCIENCE

New Discoveries and Surprises Revealed through SALT Spectroscopy of the Unclassified Fermi-LAT Sources

B. van Soelen[*†]
University of the Free State, Bloemfontein, South Africa
E-mail: vansoelenb@ufs.ac.za

L. Klindt, J.P. Marais, R.J. Britto, P.J. Meintjes

University of the Free State, Bloemfontein, South Africa

P. Väisänen

South African Astronomical Observatory, Cape Town, South Africa

L. Hanlon, D. Murphy
University College Dublin, Dublin, Ireland

The *Fermi* Space Telescope has detected 1444 objects which in the Fermi-3LAC catalogue are associated with extra-galactic sources (above galactic latitudes of $|b| > 10^{\circ}$). While most are already associated with Flat Spectrum Radio Quasars (FSRQs) and BL Lacs, a significant fraction are associated with blazar-like sources that remain unclassified. We have undertaken optical spectroscopy and photometry of a selection of these sources from South African based telescopes. Optical spectroscopy has been used to classify these sources into FSRQs and BL Lac type objects as well as establish their redshifts. Photometric observations have searched for intraday and short–term variability in these sources. The results for four sources, 2FGL J0044.7-3702, 2FGL J0201.5-6626, 2FGL J0644.2-671 and 2FGL J0730.6-6607 are presented. In addition, long–term optical monitoring of known and candidate TeV blazars is being performed with the Watcher Robotic Telescope and a new photometric pipeline is being developed to allow for automated alerts of flaring sources which may be used to trigger follow-up observations. The preliminary results from this pipeline for PKS 1510-089 during 2015 are presented.

Frontier Research in Astrophysics – II
23-28 May 2016
Mondello (Palermo), Italy

[*]Speaker.
[†]This paper uses observations made at the South African Astronomical Observatory (SAAO)

PoS(FRAPWS2016)034

1. Introduction

Since operation began in 2008, the Large Area Telescope (LAT) on-board the *Fermi* Space Telescope has been continuously observing the whole sky in the MeV and GeV energy range. This is an invaluable tool for the detection of new extra-galactic gamma-ray sources and the continuous monitoring of known sources. The recent improvement in the *Fermi*-LAT data analysis with the development of Pass 8 has increased the system's sensitivity over the whole energy range, and has raised the high energy detection limit. This improves the ability of *Fermi*-LAT to identify sources both below 100 MeV and above 50 GeV. In addition, the improvement in sensitivity at the lower energies by Imaging Air Cherenkov Telescopes (IACTs) allows an overlap to be made between these instruments (see e.g. [1] for preliminary comparison between *Fermi*-LAT and H.E.S.S.).

The 3rd Catalogue of Active Galactic Nuclei Detected by the Fermi Large Area Telescope (3LAC) [2] lists all sources detected by the instrument above a Galactic latitude of $|b| > 10^{\circ}$. The *clean sample* contains 1444 objects, which includes 414 Flat Spectrum Radio Quasars (FSRQs) 604 BL Lacs and 24 non-blazar AGNs. The catalogue also lists 402 sources which are classified as *blazar candidates of uncertain type* (BCUs). This provides a wealth of new objects which may be observed at TeV energies with ground based IACTs. Sixty of these BCUs are detected above 50 GeV [3] which may make them excellent new candidates if they are at redshifts $z \lesssim 1$.

As part of an on-going project we are undertaking to spectroscopically classify a selection of BCUs as well as undertake long–term photometric observations of known and candidate TeV sources. Below we briefly discuss recent results from this project.

2. Spectroscopic and photometric observations of 2LAC candidate sources

Optical spectroscopic observations have thus far been undertaken of sources which were originally selected from the 2nd Catalogue of Active Galactic Nuclei Detected by the Fermi Large Area Telescope (2LAC) [4]. These sources all remained unclassified in the updated 3LAC. The sources were selected based on being unclassified, (mainly) radio bright (>100 mJy), observable from South Africa (latitude and magnitude limitations), and having no redshift measurement. Based on these criteria we selected thirteen sources for spectroscopic and photometric observations.

2.1 Spectroscopic observations

Optical spectroscopy of our sample was performed with the South African Astronomical Observatory SAAO 1.9-m telescope using the grating spectrograph between 21 May 2014 and 3 June 2014. The grating spectrograph was utilized with a wavelength coverage of 3700 – 7900 Å with a resolution of ~ 5 Å. Further observations were made with the Southern African Large Telescope (SALT) [5] using the Robert Stobie Spectrograph (RSS) [6] between November 2014 and October 2015 (2014-Semester II and 2015-Semester I). SALT/RSS observations were performed with two different instrument configurations: during 2014-Semester II grating pg0300 (wavelength range $\sim$990–11 000 Å, $R \sim 530$) was used, which covers all observable wavelengths, and during 2015-Semester I grating pg0900 (wavelength range $\sim$4000–8700 Å, $R \sim 860$) was used.

Data reductions followed the standard IRAF [7] procedures, and the redshifts and classifications were determined for five sources with three additional determinations based on the most likely line identification.

2.2 SHOC Photometric observations

Rapid photometric observations for nine sources were obtained using the Sutherland High Speed Optical Camera (SHOC) [8] on the SAAO 1.9-m telescopes during three observing periods (13 – 19 August 2014, 10 – 31 December 2014 and 13 – 26 May 2015). Observations were undertaken with the clear filter, with exposure times between $\sim$ 10–200 seconds. Data reductions were performed using the SHOC data reduction pipeline[1], and differential photometry was performed using at least two comparison stars in the field-of-view following a similar method to [9].

Intraday and short-term ($\sim$few days) variability was searched for by using the power-enhanced F-test ($F_{\rm enh}$) analysis of variance technique [10]. Sources were classified as variable if $F_{\rm enh} > F_{\alpha=0.001}$, as possibly variable if $F_{\alpha=0.01} < F_{\rm enh} < F_{\alpha=0.001}$, and non-variable if $F_{\rm enh} < F_{\alpha=0.01}$. Here, α is the critical value (see [10] and references therein).

2.3 2LAC results

While results have been obtained for all sources, here we briefly summarize the results for four interesting sources, with the important results summarized in Table 1. The spectra for the four sources are shown in Fig. 1.

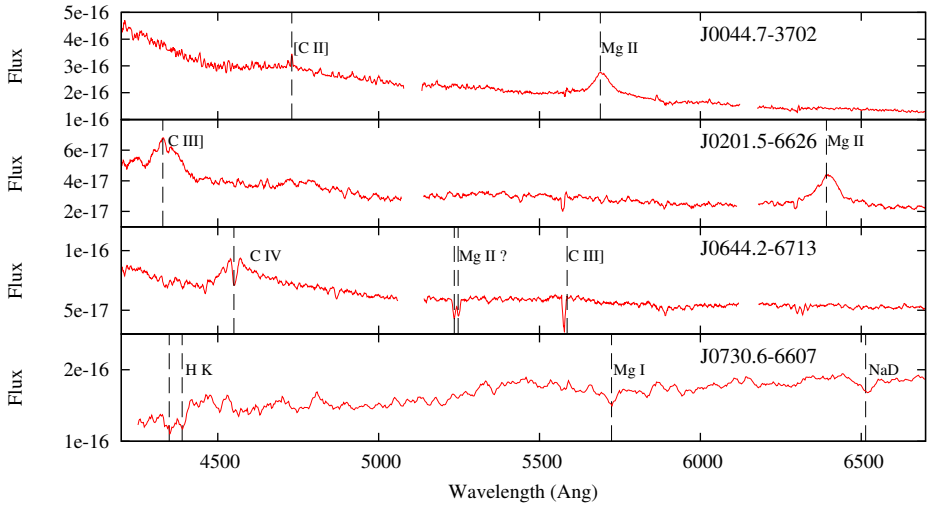

Figure 1: SALT spectra of, from top to bottom, 2FGL J0044.7-3702, 2FGL J0201.5-6626, 2FGL J0644.2-67132 and 2FGL J0730.6-6607. The spectra have been shape corrected but the flux is in arbitrary units. The lines used for classification and redshift determinations are indicated. Please see the text for details.

2.3.1 2FGL J0044.7-3702

This source showed strong [C II] and Mg II emission lines which places it at a redshift of $z = 1.0331 \pm 0.0004$. Based on the strength of the Mg II line, which has an equivalent width of

[1]The SHOC data reduction pipeline by M. Kotze can be accessed at http://shoc.saao.ac.za/Pipeline/

$W_\lambda = 17.9 \pm 3.4$ Å, we classify it as an FSRQ. While five nights of optical observations showed no clear variability, this source has shown clear gamma-ray variability over the four year period covered by the 3LAC, having a variability index of 173.747 [2],[2] and it is a relatively bright radio source ($\sim$ 330 mJy at 4.85 GHz).

2.3.2 2FGL J0201.5-6626

This source also exhibits strong emission lines, namely C III] and Mg II, at a redshift of $z = 1.28 \pm 0.01$. The equivalent widths ($W_{\lambda,C\ III]} = 31 \pm 13$ Å and $W_{\lambda,MgII} = 42 \pm 12$ Å) classify the source as an FSRQ. While gamma-ray variability was not significantly detected, 6 nights of observations showed clear optical variability.

2.3.3 2FGL J0644.2-6713

This source exhibits broad C IV and C III] emissions lines at a redshift of $z = 1.930 \pm 0.004$ (which is the highest redshift in our sample). The equivalent width ($W_{\lambda,CIV} = 24 \pm 13$ Å) classifies this as an FSRQ. However, this source also exhibits two intervening absorption lines in the spectra. One lies over the broad C IV line, which suggest absorption for material further out from the galactic nucleus. The second is a double absorption feature at ~ 5240 Å which may be due to absorption from an intervening galaxy. We suggest that this is Mg II at a redshift of $z \approx 0.9$. Gamma-ray variability has been reported for this sources in the 3LAC and observations over 8 nights with SHOC showed variability on 5 nights and clear variability over the whole observing period.

2.3.4 2FGL J0730.6-6607

The spectrum of 2FGL J0730.6-6607 is mainly featureless, which classifies this as a BL Lac, and Ca II H&K, Mg I and NaD absorption lines place the source at $z = 0.106 \pm 0.001$. The weak Ca II depression is consistent with a significant non-thermal contribution to the observed spectrum. Optical photometric observations showed intraday variability over three nights and overall short–term variability. While there was no reported gamma-ray variability in the 3LAC this is the hardest source in our sample ($\Gamma = 1.34$). Since the source lies at a relatively low redshift this is our best candidate for IACT observations at TeV energies.

3. Long-term monitoring optical monitoring

In addition to the follow-up studies on candidates TeV sources we are also undertaking long–term optical monitoring of known and candidate TeV blazars with the Watcher Robotic Telescope [11]. As part of this process an automated pipeline is being developed in Python to undertake rapid photometric reduction of the sources.

[2]A variability index > 72.44 indicates the source has a probability of $> 99\%$ of being variable over the 4-year timescale considered in the 3LAC.

Table 1: Summary of the measured properties for four sources classified as part of this study. The table list the lines identified, the redshift, the classification based on the line profiles, the number of nights that show variability (V), potential variability (PV), no variability (N) and whether short–term variability was detected (STV).

Source	Lines	Redshift	Classification	V	PV	N	STV
2FGL J0044.7-3702	[C II], Mg II	1.0331 ± 0.0004	FSRQ	0	2	3	no
2FGL J0201.5-6626	C III], Mg II	1.280 ± 0.010	FSRQ	2	0	4	yes
2FGL J0644.2-6713	C IV, C III]	1.930 ± 0.004	FSRQ	5	1	2	yes
2FGL J0730.6-6607	Ca II H&K, Mg I, NaD	0.1063 ± 0.0009	BL Lac	3	2	1	yes

3.1 Pipeline procedure

The photometric pipeline being developed makes use of PYRAF, an IRAF interpreter written in Python. For all data frames bias and flat field correction is first performed (the dark current is negligible), after which all frames are corrected to the same orientation. Next the SEP module [12], using the *Source Extractor* [13] program, determines the properties of the sources and background sky. This includes, for example, source positions, source ellipticity[3] and the sky background level and standard deviation. Data frames are rejected if the sources have an ellipticity $e > 0.9$, (indicating poor tracking due to e.g. wind), or if the sky background is more than twice the global average (which indicates, for example, that the target was too close to the Moon).

All accepted frames are then analysed using the IRAF tasks DAOPHOT/PHOT to perform aperture photometry on all objects in the field of view using input parameters determined from the SEP package. Differential photometry of selected sources is then performed following [9].

3.2 Photometric monitoring of PKS 1510-089

As an example of the output from the pipeline, Fig. 2 shows the long–term V, R and V-R light curves for PKS 1510-089 during 2015. The source shows large variability as is expected for this well known blazar and there is some indication of the colour variations.

The pipeline is still under development and we intend to improve the aperture optimization. However, this example demonstrates the ability of the Watcher telescope to undertake this long–term monitoring campaign.

4. Discussion and Conclusion

Thus far, through the BCU follow-up programme we have been able to classify approximately 8 new blazar sources into FSRQs and BL Lac type objects and establish their redshifts. These are crucial in searching for new potential TeV sources that are close enough to be observed with ground based IACTs. We have identified at least one source, namely 2FGL J0730.6-6607, which has a hard gamma-ray photon index ($\Gamma = 1.34$) and lies close enough ($z = 0.106 \pm 0.001$) to be considered for TeV observations. The BCU classification is part of an on-going programme that has now been expanded with the updated 3LAC and 2FHL catalogues, which have increased the

[3]Here ellipticity refers to the shape of the sources on the image.

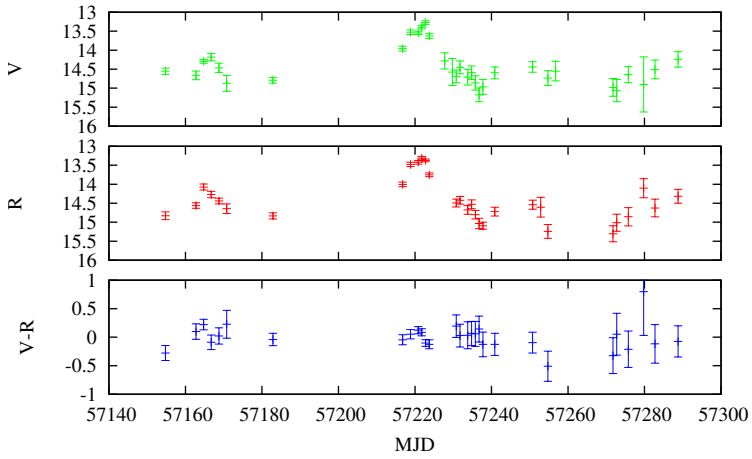

Figure 2: Long term optical light curve in V (top), R (middle) and V-R (bottom) during 2015. These data are analysed with the new data reduction and analysis pipeline.

number of BCU sources. Of particular interest is the search for rarer TeV candidate sources. For example, TeVCat currently[4] only lists five known TeV FSRQ systems, in comparison to the more than 50 BL Lacs. A more detailed discussion of the spectroscopic observations of seven candidate sources is reported in [14].

The classification of *Fermi*-LAT sources is also currently being investigated using machine learning techniques [15, 16]. Such techniques provide important methods to search for potential sources based on e.g. gamma-ray variability and photon index. However, these methods are dependent on having sources with known optical classifications and the observations discussed here can be used to improve their calibration.

In addition, the long-term optical monitoring campaign with the Watcher telescope of both the known and candidate blazar sources will allow for multi-wavelength correlations studies to be undertaken. A new pipeline is currently under development, the aim of which, is to allow for automated alerts of flaring sources which may be used to trigger follow-up observations.

The current development of the Cherenkov Telescope Array (CTA), will greatly increase the sensitivity of TeV observations and this on-going project aims to identify new sources that will be important candidates for future TeV observations.

Acknowledgments

This work is based on the research supported in part by the National Research Foundation of South Africa for the grant 87919. Some of the observations reported in this paper were obtained with the Southern African Large Telescope (SALT).

References

[1] D. Zaborov et al. *AGN observations with a less than 100 GeV threshold using H.E.S.S. II* in proceedings of the *34th International Cosmic Ray Conference (ICRC2015)*, arXiv/1509.06509

[4] http://tevcat.uchicago.edu/ as of 30 July 2016

[2] M. Ackermann et al. *The Third Catalog of Active Galactic Nuclei Detected by the Fermi Large Area Telescope, ApJ* **810** (2015) 14

[3] M. Ackermann et al. *2FHL: The Second Catalog of Hard Fermi-LAT Sources, ApJS* **222** (2016) 5

[4] M. Ackermann et al. *The Second Catalog of Active Galactic Nuclei Detected by the Fermi Large Area Telescope, ApJ* **743** (2011) 171

[5] D.A.H. Buckley, G.P. Swart, J.G Meiring *Completion and commissioning of the Southern African Large Telescope, SPIE* **6267** (2006) 32

[6] E.B. Burgh et al. *Prime Focus Imaging Spectrograph for the Southern African Large Telescope: optical design, SPIE* **4841** (2003) 1463

[7] D. Tody *The IRAF Data Reduction and Analysis System, SPIE* **627** (1986) 733

[8] R. Coppejans et al. *Characterizing and Commissioning the Sutherland High-Speed Optical Cameras (SHOC), PASP* **125** (2013) 976

[9] M. Everett and S.B. Howell, *A Technique for Ultrahigh-Precision CCD Photometry, PASP* **113** (2001) 1428

[10] J.A. De Diego *On the Reliability of Microvariability Tests in Quasars, AJ* **148** (2014) 93

[11] M. Topinka et al. *Status update of the Watcher Robotic Telescope, EAS* **61** (2013) 487

[12] K. Barbary, K. Boone and C. Deil SEP: v0.3.0 URL http://dx.doi.org/10.5281/zenodo.15669 (2015)

[13] E. Bertin and S. Arnouts *SExtractor: Software for source extraction, A&AS* **117** (1996) 393

[14] L. Klindt, B. van Soelen, P.J. Meintjes, P. Väisänen *Optical spectroscopic classification of a selection of Southern hemisphere Fermi-LAT unclassified blazars, MNRAS* **467** (2017) 2537

[15] S. Parkinson *Classification and Ranking of Fermi LAT Gamma-ray Sources from the 3FGL Catalog using Machine Learning Techniques, ApJ* **820** (2016) 8

[16] G. Chiaro et al. (2016) *Blazar Flaring Patterns (B-FlaP): Classifying Blazar Candidates of Uncertain type in the third Fermi-LAT catalog by Artificial Neural Networks,* arXiv/1607.07822

MDPI

Article

SALT Spectropolarimetry and Self-Consistent SED and Polarization Modeling of Blazars*

Markus Böttcher[1] 0000-0002-8434-5692, Brian van Soelen[2], Richard J. Britto[2]†, David A. H. Buckley[3], Johannes P. Marais[2] and Hester Schutte[1]

1 Centre for Space Research, North-West University, Potchefstroom, South Africa; Markus.Bottcher@nwu.ac.za
2 Department of Physics, University of the Free State, Bloemfontein, South Africa
3 South African Astronomical Observatory, Cape Town, South Africa
* Correspondence: Markus.Bottcher@nwu.ac.za; Tel.: +27-18-299-2418

Academic Editor: name
Version August 1, 2017 submitted to Galaxies

Abstract: We report on recent results from a target-of-opportunity program to obtain spectropolarimetry observations with the Southern African Large Telescope (SALT) on flaring gamma-ray blazars. SALT spectropolarimetry and contemporaneous multi-wavelength spectral energy distribution (SED) data are being modelled self-consistently with a leptonic single-zone model. Such modeling provides an accurate estimate of the degree of order of the magnetic field in the emission region and the thermal contributions (from the host galaxy and the accretion disk) to the SED, thus putting strong constraints on the physical parameters of the gamma-ray emitting region. For the specific case of the γ-ray blazar 4C+01.02, we demonstrate that the combined SED and spectropolarimetry modeling constrains the mass of the central black hole in this blazar to $M_{\rm BH} \sim 10^9\,M_\odot$.

Keywords: active galaxies — blazars; gamma-rays; polarization — optical; spectropolarimetry

1. Introduction

Blazars are a class of radio-loud, jet-dominated active galactic nuclei whose jets are closely aligned with our line of sight. Due to relativistic Doppler boosting, they are bright and often rapidly variable sources across the entire electromagnetic spectrum. Their spectral energy distribution (SED) is dominated by two broad non-thermal components. The low-frequency component (radio through optical – X-rays) is well understood as synchrotron radiation from relativistic electrons, while for the high-energy component (X-rays through γ-rays) both leptonic and hadronic emission mechanisms are possible [e.g., 3,4,14]. In leptonic models, the high-energy emission is produced by Compton scattering of soft radiation fields off the same relativistic electrons producing the synchrotron emission. A variety of target photon fields are possible, including the co-spatially produced synchrotron radiation and external photon fields from the accretion disk, the broad-line region, and/or the infrared-emitting dust torus around the central engine [3,4,10]. In the infrared through UV, also thermal components from the host galaxy and the accretion-disk + dust-torus system add to the SED. Due to the multitude of plausibly contributing radiation components and our lack of knowledge of the dominant particle acceleration mechanism, there is significant ambiguity concerning the underlying particle distributions and the

*based on observations made with the Southern African Large Telescope (SALT) under programme 2016-2-LSP-001 (PI: D. A. H. Buckley)
†for the Fermi-LAT collaboration

location of and physical conditions within the γ-ray emission zone [e.g., 4,10]. These degeneracies can generally not be broken by SED modeling alone.

An additional aspect of radiation, which provides important information, is polarization. While radio polarization is routinely employed to diagnose magnetic-field topologies in the large-scale jets of radio-loud AGN (one of the main topics of this conference), the utility of optical and high-energy (X-ray / γ-ray) polarimetry as a disgnostic for the physical conditions in the high-energy emission region has only recently begun to be considered [e.g., 12,17–19]. In view of a multitude of on-going optical polarimetric blazar monitoring programs, this provides a promising avenue for progress in our understanding of the physical conditions in AGN jets. Specifically, the optical emission from blazars is often dominated by synchrotron emission from the jet, which is well-known to be polarized at a degree $\Pi_{\rm sy}$ related to the spectral index p of the underlying non-thermal electron distribution (resulting in a synchrotron radiation spectral index $\alpha = (p-1)/2$) and the degree of order of the magnetic field $f_{\rm B,order}$ through

$$\Pi_{\rm sy} = f_{\rm B,order}\,\frac{p+1}{p+7/3} = f_{\rm B,order}\,\frac{\alpha+1}{\alpha+5/3} \quad (1)$$

Additional contributions to the optical spectrum may arise from the host galaxy and a dust torus, which may be dominant towards the red, and from the accretion disk, which may contribute significantly towards the blue end of the spectrum. These thermal contributions are expected to be unpolarized and will reveal their presence through a decline of the degree of polarization (compared to pure synchrotron emission) in spectropolarimetric observations.

The above considerations motivated us to use the Southern African Large Telescope (SALT — see Section 2.2) for spectropolarimetry of flaring *Fermi*-detected γ-ray blazars in order to constrain the degree of ordering of the magnetic field in the emission region and the contribution of thermal radiation components to the optical spectrum. We focus on the specific example of the high-redshift ($z = 2.1$) blazar 4C+01.02, which underwent a large γ-ray flare in July 2016. The resulting SEDs and spectropolarimetry results were modelled with a leptonic single-zone model that self-consistently calculates the SEDs along with the expected optical spectropolarimetry signatures (see Section 3). Results from this combined fitting procedure for the case of 4C+01.02 are presented and discussed in Sections 4 and 5.

2. Observations

Our observations were conducted in the framework of a SALT Large Program on high-energy transients (PI: D. Buckley). This program aims at target-of-opportunity (ToO) spectroscopy and spectropolarimetry observations of various transients, including cataclysmic variables, novae, microlensing events, X-ray binaries, tidal disruption events, gamma-ray bursts, and flaring blazars. In the case of blazars, ToO observations are triggered by flaring activity detected by *Fermi*-LAT and, when possible, complemented by optical photometry using the Las Cumbres Observatory (LCO) network and X-ray observations with *Swift*. Within the first year of this program (April 2016 – May 2017), 14 ToO spectropolarimetry observations targeting 7 different blazars (5 Flat Spectrum Radio Quasars [FSRQs] and 2 BL Lac objects) were conducted, revealing generally frequency-dependent polarization degrees in the range $\sim 5-25$ %. In the following we focus on the particularly interesting case of the FSRQ 4C +01.02 (PKS B0106+013; $z = 2.1$), which underwent a large γ-ray flare in July 2016.

2.1. Fermi-LAT

The *Fermi* Large Area Telescope (LAT), is observing the whole sky every 3 hr, which enables an almost continuous monitoring of the flux variability of bright sources. *Fermi*-LAT is sensitive to photons from 20 MeV to $>$ 300 GeV [1]. We analysed data from 4C+01.02 between 100 MeV and 300 GeV during its high state in 2016, using the *Pass 8* data representation [2] and the *Fermi* Science

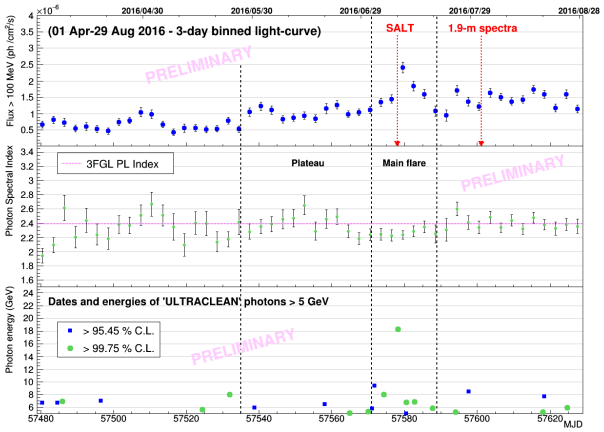

Figure 1. *Top panel:* 3-day binned *Fermi*-LAT light curve at $E > 100$ MeV of 4C+01.02 for the period 2016 April – June. *Middle panel: Fermi*-LAT spectral index light curve for a power-law fit to the 3-day binned spectra. *Bottom panel:* Arrival times and energies of high-energy ($E > 5$ GeV) photons.

Tools version v10r0p5.[1] We applied the following standard analysis cuts: radius of the *Region of interest* (ROI)=15°; Source region=ROI+10°; SOURCE class; front + back event type; zenith angle $< 90°$; DATA_QUAL=1, LAT_CONFIG=1; Diffuse emission: `gll_iem_v06.fits` (Galactic) and `iso_P8R2_SOURCE_V6_v06.txt` (extragalactic) templates. In the light-curve processing, we used the unbinned likelihood gtlike/pyLikelihood tool, and modeled the source of interest by a single power law spectrum of photon index Γ. In the SED processing, we used the binned likelihood analysis from the same tool, within the *Enrico* Python package [15], for a preliminary SED construction. Fig. 1 shows the light curve of 4C+01.02 during 11 April – 29 August, 2016. We labeled the July 2 – 20 period as "Main flare" as it contains the highest peak in flux for the considered high state, which also was the highest flux ever detected with *Fermi*-LAT for this source to date ($\simeq 2.810^{-6} \pm 0.3$ ph cm^{-2} s^{-1} $>$ 100 MeV on 10 July [MJD 57579], daily average). The SED of the *main flare* is plotted in Fig. 3 along with multiwavelength data.

2.2. SALT

The Southern African Large Telescope (SALT) is a 10-m class telescope, located at the South African Astronomical Observatory (SAAO), near Sutherland, South Africa [7]. One of its main instruments is the *Robert Stobie Spectrograph (RSS)*, located at the telescope's prime focus. The RSS is capable of performing spectroscopy in various modes, including long-slit, multi-object slit, polarimetry, and Fabry-Pérot, and is sensitive to wavelengths from ∼3200 Å to ≥9000 Å [8,11]. The results presented in Fig. 2 were obtained using RSS in the spectropolarimetry "LINEAR" mode [13] on 2016 July 9 and November 27, 28 and 29. Each spectrum, along with the polarization degree and polarization angle as a function of wavelength, was obtained through four exposures of 600 s, one for each of the four orientations of the half-wave plates (0°, 45°, 22.5° and 67.5° respectively). Data reduction was performed using the POLSALT reduction pipeline.[2]

2.3. LCO

The Las Cumbres Observatory (LCO) is a global network of 18 telescopes located at eight different locations [6]. Observations were undertaken with the 1-m class telescopes using the SBIG CCD. Data reduction followed the standard procedures using the IRAF/NOAO packages. Differential photometry

[1] http://fermi.gsfc.nasa.gov/ssc/data/analysis/
[2] https://github.com/saltastro/polsalt

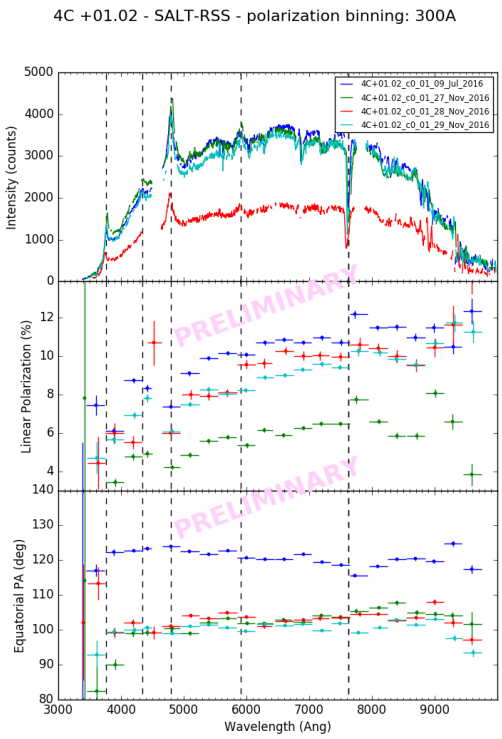

Figure 2. *Top panel:* SALT RSS count spectra of 4C+01.02 during four observing windows, including the 2016 July 9 flare indicated in Fig. 1 (blue). Dashed vertical lines indicate the positions of the following lines: Lyα 1216 Å, Si IV 1400 Å, C IV 1549 Å, C III] 1909 Å and a telluric absorption line. *Middle panel:* Linear polarization degree as function of wavelength from SALT spectropolarimetry for the four SALT observing windows, as in the top panel. *Bottom panel:* Polarization angle as a function of wavelength for the four SALT observations.

was performed using four nearby comparison stars whose magnitudes were taken from the NOMAD catalog [16]. The photometric data points included in Fig. 3 were taken on 2016, August 2.

3. SED and Spectropolarimetry Modeling

The SEDs of blazars are often successfully modelled with simple single-zone leptonic radiation models. In this paper, we adopt the time-independent leptonic blazar emission model described in detail in [4]. The code evaluates the non-thermal synchrotron + Compton radiation spectrum based on an equilibrium solution for the electron spectrum, assuming a rapid acceleration mechanism that provides a power-law injection spectrum with index q between cut-off energies $\gamma_{\rm min}$ and $\gamma_{\rm max}$ that is balanced by self-consistent radiative losses and escape on a time scale $t_{\rm esc} = \eta_{\rm esc}\, R/c$ where R is the size of the spherical emission region. The non-thermal jet emission, direct accretion-disk emission, plus the dominant Lyα and C IV emission lines from the BLR (see Fig. 2, top panel), are added up to yield the total SED.

The degree of polarization of the synchrotron emission is evaluated based on the local synchrotron spectral index α through Equ. (1). The frequency-dependent degree of polarization of the total observed optical spectrum is then calculated assuming that the direct accretion-disk ($F_{\rm AD}$) + BLR line ($F_{\rm line}$) emissions are unpolarized, so that

$$\Pi(\nu) = \frac{\Pi_{\rm sy}(\nu)\, F_{\rm sy}(\nu)}{F_{\rm sy}(\nu) + F_{\rm AD}(\nu) + F_{\rm line}(\nu)} \qquad (2)$$

Our fitting procedure consists of adjusting parameters of the model to obtain simultaneous agreement with the SED and spectropolarimetry data of 4C+01.02 during the γ-ray flare of July 2016. Since only the optical and γ-ray data are contemporaneous, we include the archival *Swift*-XRT X-ray spectrum from summed observations in 2007 and 2008 [9] as a guide for our spectral fit since they also correspond to a moderately high γ-ray flux state of the source.

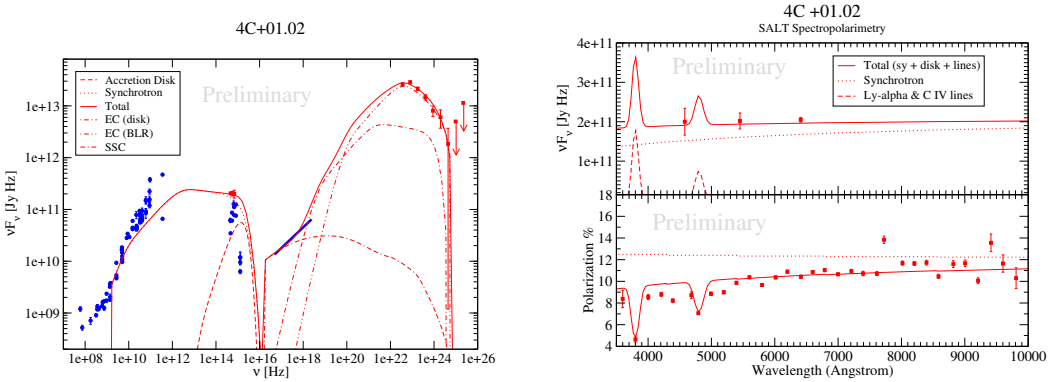

Figure 3. *Left panel:* Contemporaneous optical + γ-ray SED (red) of 4C+01.02, along with archival data (from NED[1] – blue), and our SED model (solid red). *Right panel: Top:* Optical spectrum with the 3 LCO photometry points, with our model (red lines). *Bottom:* SALT spectropolarimetry (data points), along with our model prediction (solid red line), and the degree of polarization of the synchrotron radiation component (red dotted).

Table 1. Model parameters.

Parameter	Value
Electron injection $\gamma_{\rm min}$	230
Electron injection $\gamma_{\rm max}$	6×10^3
Electron injection index q	2.1
Kinetic power in radiating electrons L_e	2.5×10^{45} erg/s
Doppler factor δ	35
Magnetic field B	1 G
Magnetic-field order $f_{\rm B,order}$	0.16
Energy partition ratio L_B/L_e	0.45
Escape time-scale parameter $\eta_{\rm esc}$	1
Emission-region radius R	2.2×10^{16} cm
Emission-region distance from BH	0.2 pc
Black-hole mass $M_{\rm BH}$	$10^9\ M_\odot$
Accretion-disk luminosity L_d	1.26×10^{47} erg/s = $L_{\rm Edd}$
External radiation field $u_{\rm ext}$	5×10^{-3} erg/cm^3

4. Results

Fig. 3 shows the result of our combined SED + spectropolarimetry fit to 4C+01.02 in July 2016. The parameters used for this fit are listed in Table 1.

The chosen parameters result in a minimum allowed variability time scale from causality arguments of $t_{\rm var,min} = R/(\delta\, c) = 18$ hr, consistent with the lack of evidence for intra-day variability.

The peak of the accretion-disk emission is well constrained by the spectropolarimetry results to be located near or beyond the blue end of the optical spectrum, requiring a central black-hole mass of $M_{\rm BH} \leq 10^9\ M_\odot$. On the other hand, its significant contribution to the observed spectrum requires a luminosity of the order of the Eddington luminosity for a $10^9\ M_\odot$ black hole. Thus, the mass of the central black hole in 4C+01.02 is well constrained to be $M_{\rm BH} \sim 10^9\ M_{\rm BH}$.

[1] `https://ned.ipac.caltech.edu/`

5. Summary and Conclusions

We have presented results of ToO spectropolarimetry observations using the SALT RSS, focusing on the case of the high-redshift FSRQ 4C+01.02 during a large γ-ray flare in July 2016. The contemporaneous SED and spectropolarimetry data were fitted in a consistent way with a single-zone leptonic model. This combined fitting constrained the accretion-disk contribution to the SED and, in particular, the black-hole mass in the center of 4C+01.02 to $M_{\rm BH} \sim 10^9\,M_\odot$. This is in tension with the claim by [9] who modelled the entire optical – UV spectrum of the source to be dominated by direct accretion-disk emission, requiring a black-hole mass of $M_{\rm BH} = 5 \times 10^9\,M_\odot$. If such an interpretation of the optical – UV emission from 4C+01.02 is correct, the degree of polarization in the optical should be close to zero. This contradicts our SALT spectropolarimetry results which indicate that even in the moderate-activity state in November 2016, the optical polarization is still of the order of ~ 5 – 10 %. Our combined SED + spectropolarimetry modeling therefore strongly favours a synchrotron-dominated optical emission scenario with the accretion-disk contributing only towards the blue end of the spectrum, requiring a black-hole mass of $M_{\rm BH} \sim 10^9\,M_\odot$.

Acknowledgments: The work of M.B. is supported through the South African Research Chairs Initiative (SARChI) of the South African Department of Science and Technology (DST) and National Research Foundation[3]. The authors acknowledge further support by the South African DST through the South African Gamma-Ray Astronomy Programme. The authors are grateful for the support provided by S. Crawford and K.H. Nordsieck with reducing the spectropolarimetry observations. This work makes use of observations from the LCO network. Some of the observations reported in this paper were obtained with the Southern African Large Telescope (SALT).

The Fermi-LAT Collaboration acknowledges support for LAT development, operation and data analysis from NASA and DOE (United States), CEA/Irfu and IN2P3/CNRS (France), ASI and INFN (Italy), MEXT, KEK, and JAXA (Japan), and the K.A. Wallenberg Foundation, the Swedish Research Council and the National Space Board (Sweden). Science analysis support in the operations phase from INAF (Italy) and CNES (France) is also gratefully acknowledged.

References

1. Atwood, W. B., et al., *ApJ*, **2009**, *697*, 1071.
2. Atwood, W. B., et al., *2012 Fermi Symposium proceedings*, eprint arXiv:1303.3514.
3. Böttcher, M., *Ap&SS*, **2007**, *309*, 95.
4. Böttcher, M., Reimer, A., Sweeney, K., & Prakash, A., *ApJ*, **2013**, *768*, 54.
5. Britto, R. J., et al., *Proceedings of (HEASA2016), Cape Town, South Africa*, **2017**, PoS(HEASA 2016)021.
6. Brown, T.M., et al., *PASP*, **2013**, *125*, 1031
7. Buckley, D. A. H., Swart, G. P. & Meiring, J. G., *SPIE*, **2006** *6267*, 32
8. Burgh, E. B., et al., *Proceedings of the SPIE*, **4841** (2003), pp. 1463–1471
9. Ghisellini, G., et al., *MNRAS*, **2011**, *411*, 901.
10. Ghisellini, G., et al., *MNRAS*, **2010**, *402*, 497.
11. Kobulnicky, H. A.. et al., *Proceedings of the SPIE*, **4841** (2003), pp. 1634–1644.
12. Marscher, A. P., *ApJ*, **2014**, *780*, 87.
13. Potter, S. B., et al.,*Proceedings of SPIE 9908* **99082K** (August 9, 2016), DOI: 10.1117/12.2232391
14. Romero, G. E., Böttcher, M., Markoff, S., & Tavecchio, F., *SSRv*, **2017**, *207*, 5.
15. Sanchez, D. A. & Deil, C., *In Proceedings of the 33rd ICRC, Rio de Janeiro (Brazil)*, eprint arXiv:1307.4534.
16. Zacharias, N. et al., *American Astronomical Society Meeting Abstracts*, **2004**, *36*, 1418
17. Zhang, H., & Böttcher, M., *ApJ*, **2013**, *774*, 18.
18. Zhang, H., Chen, X., & Böttcher, M., *ApJ*, **2014**, *789*, 66.
19. Zhang, H., et al., *ApJ*, **2015**, *804*, 58.

[3] Any opinion, finding and conclusion or recommendation expressed in this material is that of the authors, and the NRF does not accept any liability in this regard.

PROCEEDINGS OF SCIENCE

SALT Spectropolarimetry and Self-Consistent SED and Polarization Modeling of Blazars*

Markus Böttcher†, Hester Schutte
Centre for Space Research, North-West University, Potchefstroom, South Africa
E-mail: Markus.Bottcher@nwu.ac.za

Brian van Soelen, Richard J. Britto‡, Johannes P. Marais

Department of Phyics, Bloemfontein, South Africa

David A. H. Buckley

South African Astronomical Observatory, Cape Town, South Africa

We report on results from a target-of-opportunity program to obtain optical spectropolarimetry of flaring γ-ray blazars with the Southern African Large Telescope (SALT). SALT spectropolarimetry and contemporaneous multi-wavelength spectral energy distributions (SEDs) are modelled self-consistently with a leptonic single-zone model. Such modeling provides an accurate estimate of the degree of order of the magnetic field in the emission region and the thermal contributions from the host galaxy and the accretion disk to the SED, thus putting strong constraints on the physical parameters of the gamma-ray emitting region. For the specific case of the γ-ray blazar 4C+01.02 ($z = 2.1$), which underwent a large γ-ray flare in July 2016, we demonstrate that the combined SED and spectropolarimetry modeling provides an estimate of the mass of the central black hole in this blazar to $M_{\rm BH} \sim 2 \times 10^9 M_\odot$.

7th Fermi Symposium 2017
15-20 October 2017
Garmisch-Partenkirchen, Germany

*based on observations made with the Southern African Large Telescope (SALT) under programme 2016-2-LSP-001 (PI: D. A. H. Buckley)

†Speaker.

‡for the Fermi-LAT collaboration

PoS(IFS2017)021

1. Introduction

Blazars are the most abundant extragalactic source class detected by *Fermi*-LAT. Their spectral energy distribution (SED) is dominated by two broad non-thermal components. The low-frequency component is synchrotron radiation from relativistic electrons, while for the high-energy component both leptonic and hadronic emission mechanisms are possible (e.g., [4, 5]). In leptonic models, the high-energy emission is produced by Compton scattering of soft radiation fields off relativistic electrons [4, 10, 5]. In the infrared through UV, also thermal components from the host galaxy and the accretion-disk, broad-line-region (BLR) and dust-torus system add to the SED. There is significant ambiguity concerning the underlying particle distributions and the location of and physical conditions within the γ-ray emission zone (e.g., [10, 5]), which can generally not be broken by SED modeling alone.

In this paper, we demonstrate how optical polarization can help to break some of these degeneracies (see also, [11, 19, 20]). The optical emission from blazars is often dominated by polarized jet synchrotron emission. Additional contributions to the optical spectrum may arise from the host galaxy, a dust torus, and from the accretion disk. These thermal contributions are expected to be unpolarized and will reveal their presence through a decline of the degree of polarization (compared to pure synchrotron emission) in spectropolarimetric observations (e.g., [17, 12]).

The above considerations motivated us to use the Southern African Large Telescope (SALT) for spectropolarimetry of flaring γ-ray blazars to constrain the contribution of thermal components to the optical spectrum. We focus on the blazar 4C+01.02, a high-polarization flat-spectrum radio quasar (FSRQ) at a redshift of $z = 2.1$. which underwent a large γ-ray flare in July 2016 [6]. The resulting SEDs and spectropolarimetry results were modelled with a leptonic single-zone model that self-consistently calculates the SED along with the expected optical spectropolarimetry signatures (see Section 3).

2. Observations

Our observations were conducted in the framework of a SALT Large Program on high-energy transients (PI: D. Buckley). This program aims at target-of-opportunity (ToO) spectroscopy and spectropolarimetry observations of various transients, including flaring blazars. Within the first year of this program (April 2016 – May 2017), 14 ToO spectropolarimetry observations targeting 7 different blazars were conducted, revealing generally frequency-dependent polarization degrees in the range $\sim 5 - 25$ %. In the following we focus on the particularly interesting case of the FSRQ 4C +01.02 (PKS B0106+013; $z = 2.1$).

2.1 Fermi-LAT

We analysed *Fermi*-LAT data from 4C+01.02 between 100 MeV and 300 GeV during its high state in 2016, using the *Pass 8* data representation [2] and the *Fermi* Science Tools version v10r0p5.[1] We applied the following standard analysis cuts: radius of the *Region of interest* (ROI)=15°; Source region=ROI+10°; SOURCE class; front + back event type; zenith angle $< 90°$;

[1] http://fermi.gsfc.nasa.gov/ssc/data/analysis/

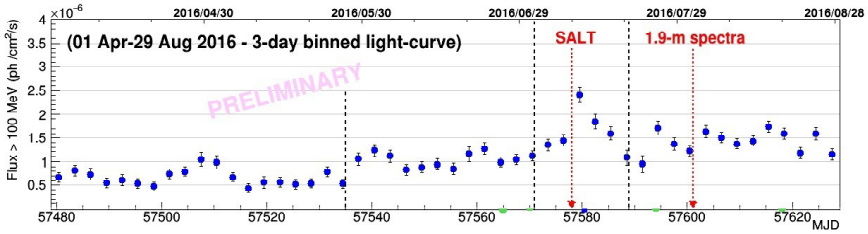

Figure 1: 3-day binned *Fermi*-LAT light curve at $E > 100$ MeV of 4C+01.02 for 2016 April – August. The vertical dashed lines demarcate the period July 2 – 20, used for the extraction of the spectral points in Fig. 3.

DATA_QUAL=1, LAT_CONFIG=1; Diffuse emission: `gll_iem_v06.fits` (Galactic) and `iso_P8R2_SOURCE_V6_v06.txt` (extragalactic) templates. In the light-curve processing, we used the unbinned likelihood gtlike/pyLikelihood tool, and modeled the source of interest with a single power law spectrum. In the SED processing, we used the binned likelihood analysis within the *Enrico* Python package [14]. Figure 1 shows the light curve of 4C+01.02 during 1 April – 29 August, 2016. The July 2 – 20 period contains the highest peak flux for the considered high state, which also was the highest flux ever detected with *Fermi*-LAT for this source to date (daily average $F_{>100\,\mathrm{MeV}} \simeq (2.8 \pm 0.3) \times 10^{-6}$ ph cm^{-2} s^{-1} on 10 July [MJD 57579]). The SED of the *main flare* is plotted in Fig. 3 along with multiwavelength data.

2.2 SALT

SALT is a 10-m class telescope, located at the South African Astronomical Observatory (SAAO), near Sutherland, South Africa. One of its main instruments, the *Robert Stobie Spectrograph (RSS)*, is capable of performing spectroscopy in various modes and is sensitive to wavelengths from ∼3200 Å to ≥9000 Å [8]. The results presented in Fig. 2 were obtained using RSS in the spectropolarimetry "LINEAR" mode [13] on 2016 July 9 and November 27, 28 and 29. Each spectrum, along with the polarization degree and polarization angle as a function of wavelength, was obtained through four exposures of 600 s, one for each of the four orientations of the half-wave plates (0°, 45°, 22.5° and 67.5° respectively). Data reduction was performed using the POLSALT reduction pipeline, version 0.2.dev0-py2.7.[2]

2.3 LCO

The Las Cumbres Observatory (LCO) is a global network of 18 telescopes located at 8 different locations on different continents in both hemispheres [7]. Observations were undertaken with the 1-m class telescopes using the SBIG CCD. Data reduction followed the standard procedures using the IRAF/NOAO packages. Differential photometry was performed using four nearby comparison stars whose magnitudes were taken from the NOMAD catalog [18]. The photometric data points included in Fig. 3 were taken on 2016, August 2.

[2]https://github.com/saltastro/polsalt

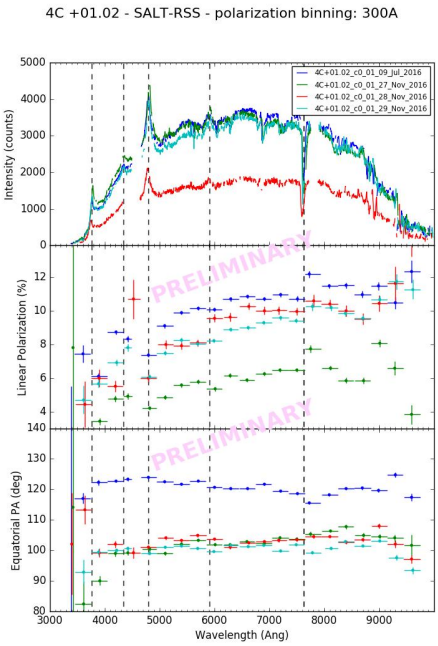

Figure 2. *Top panel:* SALT RSS count spectra of 4C+01.02 during four observing windows, including the 2016 July 9 flare indicated in Fig. 1 (blue). Dashed vertical lines indicate the positions of the following lines: Lyα 1216 Å, Si IV 1400 Å, C IV 1549 Å, C III] 1909 Å and a telluric absorption line. *Middle panel:* Linear polarization degree as function of wavelength from SALT spectropolarimetry for the four SALT observing windows, as in the top panel. *Bottom panel:* Polarization angle as a function of wavelength for the four SALT observations.

3. SED and Spectropolarimetry Modeling

The simultaneous fitting of the SED and spectropolarimetry data on 4C+01.02 is done by a combination of the leptonic single-zone model of [5] with a newly developed spectropolarimetry fitting routine. The code of [5] evaluates the non-thermal synchrotron and Compton radiation spectrum based on an equilibrium solution for the electron spectrum, assuming a rapid acceleration mechanism that provides a power-law injection spectrum with index q between cut-off energies $\gamma_{\rm min}$ and $\gamma_{\rm max}$ that is balanced by self-consistent radiative losses and escape. This code is used to determine down a first iteration of the radiating electron distribution. A newly developed code (Schutte & Böttcher 2018, in preparation) is then used for a combined fit of the radio – optical SED and the optical spectropolarimetry data. It calculates the synchrotron spectrum, based on the broken power-law distribution found from the SED fit and adds unpolarized contributions from a Shakura-Sunyaev [16] type accretion disk, $F_{\rm AD}$, and the prominent C IV and Lyα emision lines, $F_{\rm lines}$ to the spectrum. The degree of polarization of the synchrotron emission is evaluated using the full energy integrals over the modified Bessel functions (Equ. 6.37 in [15]), with a correction factor $f_{\rm B,order}$ to account for not perfectly ordered B-fields. The frequency-dependent degree of polarization of the total observed optical spectrum is then calculated as

$$\Pi(\nu) = \frac{\Pi_{\rm sy}(\nu) F_{\rm sy}(\nu)}{F_{\rm sy}(\nu) + F_{\rm AD}(\nu) + F_{\rm lines}(\nu)}. \tag{3.1}$$

A simultaneous fit to the radio – optical SED and the optical spectropolarimetry data of 4C+01.02 during the 2016 July flare is obtained by adjusting the parameters of the radiating electron distribution, the B-field ordering parameter $f_{\rm B,order}$, and the black-hole mass and accretion-disk luminosity. Since only the optical and γ-ray data are contemporaneous, we include the archival *Swift*-XRT X-ray spectrum from summed observations in 2007 and 2008 [9] as a guide for our spectral fit since they also correspond to a moderately high γ-ray flux state of the source.

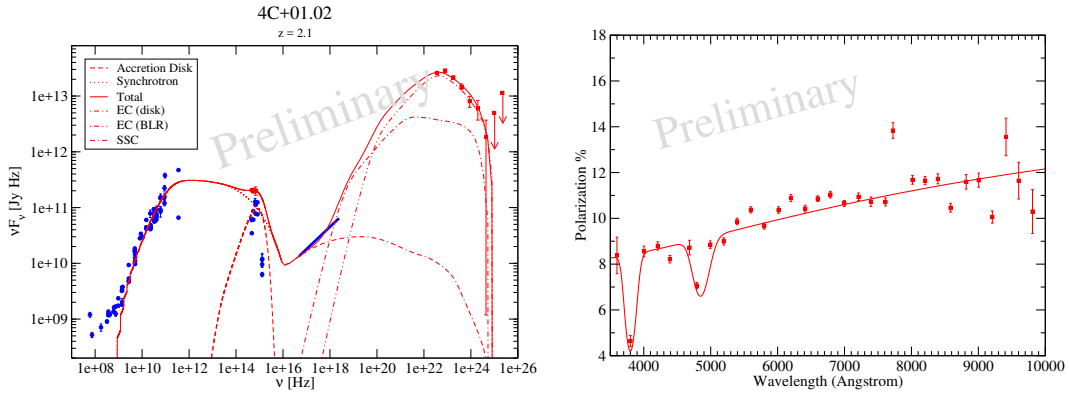

Figure 3: *Left:* Contemporaneous optical + γ-ray SED (red) of 4C+01.02, along with archival data (from NED[3] – blue), and our SED model (solid red). *Right:* Fit to the SALT spectropolarimetry data.

4. Results

Figure 3 shows the result of our combined SED + spectropolarimetry fit to 4C+01.02 in July 2016. The most relevant parameters used for this fit are listed in Table 1. All of the listed parameters are free parameters, varied to obtain a simultaneous fit to the SED and spectropolarimetry data, with the energy partition ratio being calculated from the kinetic and magnetic powers in the jet, which, in turn, are free input parameters.

Table 1: Model parameters.

Parameter	Value
Kinetic power in radiating electrons L_e	2.5×10^{45} erg/s
Magnetic field B	1 G
Magnetic-field order $f_{\rm B,order}$	0.21
Energy partition ratio L_B/L_e	0.45
Emission-region distance from BH	0.2 pc
Black-hole mass $M_{\rm BH}$	$2.4 \times 10^9\, M_\odot$
Accretion-disk luminosity L_d	1.3×10^{46} erg/s
External radiation field $u_{\rm ext}$	5×10^{-3} erg/cm^3

The peak of the accretion-disk emission is well constrained by the spectropolarimetry results to be located near or beyond the blue end of the optical spectrum, requiring a central black-hole mass of $M_{\rm BH} \sim 2 \times 10^9\, M_\odot$.

5. Summary and Conclusions

We have presented results of ToO spectropolarimetry observations of the high-redshift FSRQ 4C+01.02 during a large γ-ray flare in July 2016. The contemporaneous SED and spectropolarimetry data were fitted in a consistent way with a single-zone leptonic model. This combined fitting

[3] https://ned.ipac.caltech.edu/

constrained the accretion-disk contribution to the SED and, in particular, the black-hole mass in the center of 4C+01.02 to $M_{\rm BH} \sim 2 \times 10^9\,M_\odot$. This is in tension with the result of [9] who modelled the entire optical – UV spectrum of the source as dominated by accretion-disk emission, requiring a black-hole mass of $M_{\rm BH} = 5 \times 10^9\,M_\odot$. If such an interpretation of the optical – UV emission from 4C+01.02 is correct, the degree of polarization in the optical should be close to zero. This contradicts our SALT spectropolarimetry results which indicate that even in the moderate-activity state in November 2016, the optical polarization is still of the order of ~ 5 – 10 %. Our combined SED + spectropolarimetry modeling therefore strongly favours a synchrotron-dominated optical emission scenario with the accretion-disk contributing only towards the blue end of the spectrum, requiring a black-hole mass of $M_{\rm BH} \sim 2 \times 10^9\,M_\odot$.

Acknowledgments

The work of M.B. is supported through the South African Research Chairs Initiative of the South African Department of Science and Technology and National Research Foundation[4]. The authors acknowledge further support by the South African DST through the South African Gamma-Ray Astronomy Programme. The authors are grateful for the support provided by S. Crawford and K. H. Nordsieck with reducing the spectropolarimetry observations. This work makes use of observations from the LCO network. Some of the observations were obtained with the Southern African Large Telescope (SALT).

The Fermi-LAT Collaboration acknowledges support for LAT development, operation and data analysis from NASA and DOE (United States), CEA/Irfu and IN2P3/CNRS (France), ASI and INFN (Italy), MEXT, KEK, and JAXA (Japan), and the K.A. Wallenberg Foundation, the Swedish Research Council and the National Space Board (Sweden). Science analysis support in the operations phase from INAF (Italy) and CNES (France) is also gratefully acknowledged.

References

[1] Atwood, W. B., et al., *ApJ*, **2009**, *697*, 1071.

[2] Atwood, W. B., et al., *2012 Fermi Symposium proceedings*, eprint arXiv:1303.3514.

[3] Barres de Almeida, U., et al., *MNRAS*, **2014**, *441*, 2885.

[4] Böttcher, M., *Ap&SS*, **2007**, *309*, 95.

[5] Böttcher, M., Reimer, A., Sweeney, K., & Prakash, A., *ApJ*, **2013**, *768*, 54.

[6] Britto, R. J., et al., *Proceedings of HEASA2016, Cape Town, South Africa,* **2017**, PoS(HEASA 2016)021.

[7] Brown, T.M., et al., *PASP*, **2013**, *125*, 1031.

[8] Burgh, E. B., et al., *Proceedings of the SPIE*, **4841** (2003), 1463.

[9] Ghisellini, G., et al., *MNRAS*, **2011**, *411*, 901.

[10] Ghisellini, G., et al., *MNRAS*, **2010**, *402*, 497.

[4] Any opinion, finding and conclusion or recommendation expressed in this material is that of the authors, and the NRF does not accept any liability in this regard.

[11] Marscher, A. P., *ApJ*, **2014**, *780*, 87.

[12] Palma, N., et al., *ApJ*, **2011**, *735*, 60.

[13] Potter, S. B., et al., *Proceedings of SPIE 9908* **99082K** (August 9, 2016), DOI: 10.1117/12.2232391

[14] Sanchez, D. A. & Deil, C., *In Proceedings of the 33rd ICRC, Rio de Janeiro (Brazil)*, eprint arXiv:1307.4534.

[15] Rybicki, G. B., & Lightman, A. P., *Radiative Processes in Astrophysics*, **1979**, John Wiley & Sons

[16] Shakura, N. I., & Sunyaev, R. A., 1973, *A&A*, **1973**, *24*, 337.

[17] Smith, P., et al., *ApJ*, **1986**, *305*, 484.

[18] Zacharias, N. et al., *American Astronomical Society Meeting Abstracts*, **2004**, *36*, 1418

[19] Zhang, H., Chen, X., & Böttcher, M., *ApJ*, **2014**, *789*, 66.

[20] Zhang, H., et al., *ApJ*, **2015**, *804*, 58.